

# ***PHOTON FACTORY ACTIVITY REPORT***

***1992***

**#10**



NATIONAL LABORATORY FOR HIGH ENERGY PHYSICS, KEK





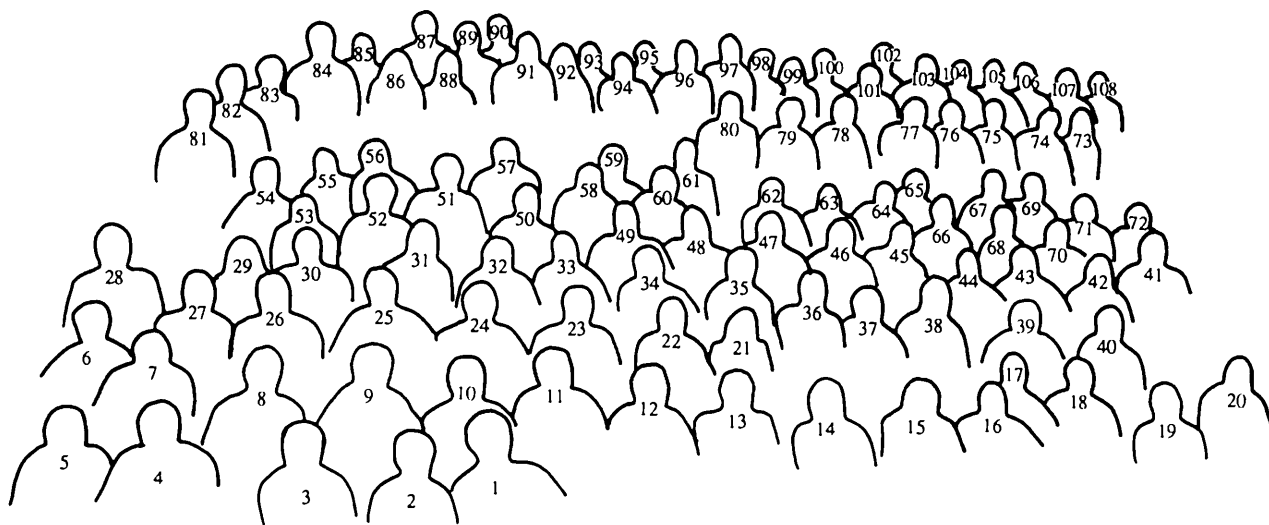




# ***Photon Factory Activity Report 1992***



*Staff members and visitors of the Photon Factory gathered in front of the PF office building.*



- |                   |                   |                   |                    |
|-------------------|-------------------|-------------------|--------------------|
| 1. T. Kosuge      | 28. S. Muto       | 55. K. Usami      | 82. N. Kanaya      |
| 2. N. Usami       | 29. R. Watanabe   | 56. H. Kimura     | 83. T. Katsura     |
| 3. H. Kobayakawa  | 30. Y. Kagoshima  | 57. T. Miyahara   | 84. Y. Kitajima    |
| 4. K. Kakihara    | 31. S. Saigusa    | 58. T. Nogami     | 85. S. Wilkins     |
| 5. K. Ito         | 32. H. Shiwaku    | 59. J. D. Wang    | 86. S. Takano      |
| 6. J. H. Chen     | 33. T. Jin        | 60. Y. Saito      | 87. G. Foran       |
| 7. S. Anami       | 34. Y. Amemiya    | 61. Z. L. Cao     | 88. Y. Hakuta      |
| 8. M. Tanaka      | 35. A. Hosoya     | 62. H. Katagiri   | 89. K. Ohsumi      |
| 9. T. Kikuchi     | 36. A. Nakagawa   | 63. M. Yokota     | 90. L. Winton      |
| 10. N. Watanabe   | 37. T. Oogoe      | 64. H. Honma      | 91. K. Nasu        |
| 11. Y. Uchida     | 38. M. Sato       | 65. A. Ueda       | 92. A. Kikuchi     |
| 12. T. Kamitani   | 39. K. Mori       | 66. C. O. Pak     | 93. A. Iida        |
| 13. H. Iwasaki    | 40. S. Fukuda     | 67. Y. Sato       | 94. A. Mikuni      |
| 14. I. Sato       | 41. H. Maezawa    | 68. S. Asaoka     | 95. M. Nomura      |
| 15. H. Kitamura   | 42. K. Haga       | 69. T. Tsuchiya   | 96. T. Shidara     |
| 16. H. Nakamura   | 43. Y. Takiyama   | 70. M. Isawa      | 97. P. Rehse       |
| 17. T. Honda      | 44. K. Furukawa   | 71. N. Nakamura   | 98. T. Kurihara    |
| 18. M. Kobayashi  | 45. K. Tanaka     | 72. Y. Kobayashi  | 99. M. Kimura      |
| 19. T. Matsushita | 46. S. Yagi       | 73. K. Nakamura   | 100. Y. Koyama     |
| 20. H. Kobayashi  | 47. S. Y. Paik    | 74. T. Suwada     | 101. T. Shioya     |
| 21. H. Ando       | 48. V. Belyakov   | 75. T. Urano      | 102. Y. Hori       |
| 22. N. Sakabe     | 49. A. V. Khmelev | 76. A. Higuchi    | 103. T. Mitsuhashi |
| 23. S. Ohsawa     | 50. T. Noma       | 77. S. Kamada     | 104. M. Katoh      |
| 24. K. Kobayashi  | 51. H. Kawata     | 78. S. Yamamoto   | 105. T. Iwazumi    |
| 25. I. Frolov     | 52. E. Arakawa    | 79. N. Kamikubota | 106. T. Mori       |
| 26. I. Abe        | 53. T. Oguchi     | 80. S. J. Xia     | 107. A. Koyama     |
| 27. H. Hanaki     | 54. Y. Hirano     | 81. T. Kikegawa   | 108. A. Yagishita  |

## PREFACE

The Photon Factory celebrated the 10th anniversary of its first emission of synchrotron radiation. It was on 10th March, 1982, that radiation was observed from the bending magnets in the 2.5-GeV ring in which the electron beam was successfully stored. Since then, the Photon Factory has been a central synchrotron-radiation facility for researchers from universities, government institutions and electronic industrial companies in Japan. It has also been open to researchers from overseas. On the 3rd and 4th of last December a symposium was held at KEK in celebration of the 10th anniversary. It was attended by more than 150 persons from Tsukuba, from various parts of the country and from overseas. At the symposium talks were presented concerning the history of the establishment of the Photon Factory by Professors K. Kohra, T. Nishikawa, J. Tanaka, K. Huke and T. Sasaki. These were followed by other talks by Professors H. Winick, Y. Sato, J. Harada, S. Suga, T. Ohta and Dr. M. Oshima, who reviewed the research activities during the past 10 years. In the final part of the symposium a panel discussion session was organized in which the prospects of future developments of the Photon Factory were featured. This facility will exist continuously as an active Japanese center for providing radiation with an improved brightness, stability and lifetime.

At the beginning of fiscal year 1992 Professor A. Asami retired from his post as Head of the Injector Linac Division; Professor I. Sato succeeded to his position. At the same time, Professor T. Yamakawa retired; he has been in charge of the superconducting wiggler at the 2.5-GeV ring. Dr. K. Nasu was appointed as Professor of solid state physics theory. He will contribute to the development of synchrotron-radiation science in collaboration with the staff in the various experimental groups in the Instrumentation Division.

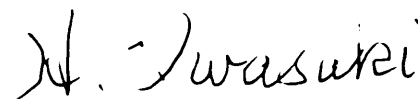
A reorganization was made of the categories of synchrotron radiation experiments to be performed at the Photon Factory. In addition to the existing categories of the G-type (general) and U-type (urgent) proposals, two new categories were created: an S-type proposal for experiments which, for example, will explore new fields of application with a special mode of ring operation, and a P-type proposal for experiments by users who have had little experience, or for test experiments. Users can choose any of the categories according to the aim of their investigations.

Australia-Japan collaborative research in synchrotron-radiation science and technology was started and has reached such a stage that test diffraction experiments using monochromatized X-radiation were carried out at the newly constructed branch beamline BL-20B. Two young Australian researchers are staying at the Photon Factory in order to maintain the equipment and to carry out additional, construction work. The branch beamline will begin full operation this coming October.

A new building with a large hall for setting up and repairing various kinds of instruments was constructed at the site just beside the Photon Factory office building. It has more than ten subsidiary rooms which can be used for designing instruments and staff office space. The increase in the area of the working space of the Photon Factory is expected to result in a further increase in research activity.

Five students who have studied in the department of synchrotron-radiation science of the Graduate University for Advanced Studies obtained doctoral degrees and started their new life as well-trained researchers in the newly developed interdisciplinary field of science and technology. The Photon Factory will continue its efforts to educate more students, not only from Japan, but also from other countries.

Two international conferences, Biophysics and Synchrotron Radiation (BSR92) and X-ray Absorption Fine Structure (XAFS VII), were held, in which a number of papers were presented by the staffs and users of the Photon Factory.



Director of the Photon Factory

## Editorial Board

HYODO, Kazuyuki  
ISAWA, Masaaki  
KANAYA, Noriichi  
KOBAYASHI, Hitoshi  
KOBAYASHI, Katsumi\*  
YAGISHITA, Akira  
YAMAMOTO, Shigeru  
(\*Chief editor)

## Acknowledgments

The editors would like to thank Ms. Miyako Kimura and Sumie Imai for their help in editing this issue.

KEK Progress Report 93-1 A/M

© National Laboratory for High Energy Physics, 1993

KEK Reports are available from:

Technical Information & Library  
National Laboratory for High Energy Physics  
1-1 Oho, Tsukuba-shi  
Ibaraki-ken, 305  
JAPAN

Phone: 0298-64-1171  
Telex: 3652-534 (Domestic)  
(0)3562-534 (International)  
Fax: 0298-64-2801  
Cable: KEKOH

## CONTENTS

	Page
<b>PREFACE</b>	
<b>CONTENTS</b>	G – 1
<b>OUTLINE OF THE PHOTON FACTORY</b>	G – 2
<b>INJECTOR LINAC</b>	
A. Introduction	L – 1
B. Operation	L – 1
C. Progress and Improvements	L – 2
D. Research	L – 5
E. R & D Regarding B-factory	L – 7
<b>LIGHT SOURCE</b>	
A. Introduction	R – 1
B. Single-bunch Operation	R – 3
C. Improvements and Developments	R – 5
D. Light Source Specifications	R – 22
<b>BEAMLINES AND INSTRUMENTATION</b>	
A. Introduction	I – 1
B. Beamlines	I – 2
C. New Instrumentation	I – 6
D. Selected Experiments	I – 7
E. Summary of Experimental Stations and Beamline Optics	I – 12
<b>THE TRISTAN SYNCHROTRON RADIATION FACILITY AT THE ACCUMULATION RING</b>	
A. Introduction	A – 1
B. Operation of the TRISTAN Accumulation Ring for SR Experiments	A – 2
C. Beamlines	A – 2
D. New Results of Experiments	A – 6
E. Specifications of the TRISTAN Accumulation Ring	A – 11
F. Specifications of Experimental Stations	A – 13
<b>THE TRISTAN SUPER LIGHT FACILITY</b>	
A. Introduction	S – 1
B. TRISTAN MR as a Very Low-emittance Machine	S – 2
C. R&D Studies on New Insertion Devices for the Project	S – 7
D. Experimental Stations and Instrumentation for the TSLF	S – 10
E. Coherent X-ray Sources	S – 13
F. Scientific Case	S – 15
<b>USERS' SHORT REPORTS</b>	
Contents	i
Users' Short Reports	1
Author Index	436
<b>LIST OF PUBLISHED PAPERS 1991/92</b>	454

# OUTLINE OF THE PHOTON FACTORY

## INTRODUCTION

The Photon Factory (PF) is a national synchrotron radiation research facility affiliated with the National Laboratory for High Energy Physics (KEK) supervised by the Ministry of Education, Science and Culture. It is located at the northern end of Tsukuba Science City, which is about 60 km north-east of Tokyo. The PF consists of a 2.5-GeV electron/positron linear accelerator, a 2.5-GeV electron/positron storage ring as a dedicated light source, TRISTAN accumulation ring as a parasitic light source and beamlines and experimental stations for exploiting synchrotron radiation in studies involving such research fields as physics, chemistry, biology, medical sciences, pharmacology, earth sciences and lithography. All of the facilities for synchrotron radiation research are open to scientists of universities and research institutes belonging to the government, public organizations, private enterprises and those of foreign countries. The members of institutions affiliated with the Ministry of Education, Science and Culture are given the highest priority among all users. Applications from other organizations are also admitted.

## OVERVIEW OF THE FACILITY

The plan view of the facility is shown in Fig. 1. The 2.5-GeV linac housed in a 450 m long enclosure is used as an injector for both the PF storage ring and the accumulation ring (AR) of TRISTAN main ring. The PF storage ring was already equipped with the flexibility of storing positrons in place of electrons. A part of the AR has been used as a high energy synchrotron radiation source producing radiation from its bending magnet and two insertion devices. One of the insertion devices produces elliptically polarized radiation, and the other highly brilliant radiation in the X-ray region. The AR has been operated for synchrotron radiation users with an energy range from 5.8 to 6.5 GeV.

## ORGANIZATION AND STAFF

The organization of KEK is shown in Fig. 2. The PF is composed of three divisions: Injector Linac, Light Source and Instrumentation. A working group has been organized for the design study of the use of the TRISTAN Main Ring for synchrotron radiation science. The organization of the PF including its personnel is shown in Fig. 3. The Advisory Council for the PF was established to discuss scientific programs and management of the PF. The council consists of twenty one senior scientists including ten non-KEK members (Table 1). The term of membership is two years. The Program Advisory Committee (PAC) consisting of the members listed in Table 2 receives proposals of users and decides priorities for the experiments.

In Table 3 the names of the staff members are listed in alphabetical order to help make direct contact. Also, the numbers of staff members and visiting scientists are summarized in Table 4.

## BUDGET AND OPERATION TIME

The budget of the PF is supplied by the Ministry of Education, Science and Culture. The annual budget after commissioning of the facilities is shown in Table 5. The numbers of beam channels in each year are shown in Table 6.

The machine operation time is divided into three terms per year. Summary and timetable of the machine operation in FY 1992 are shown in Tables 7 and 8, respectively.

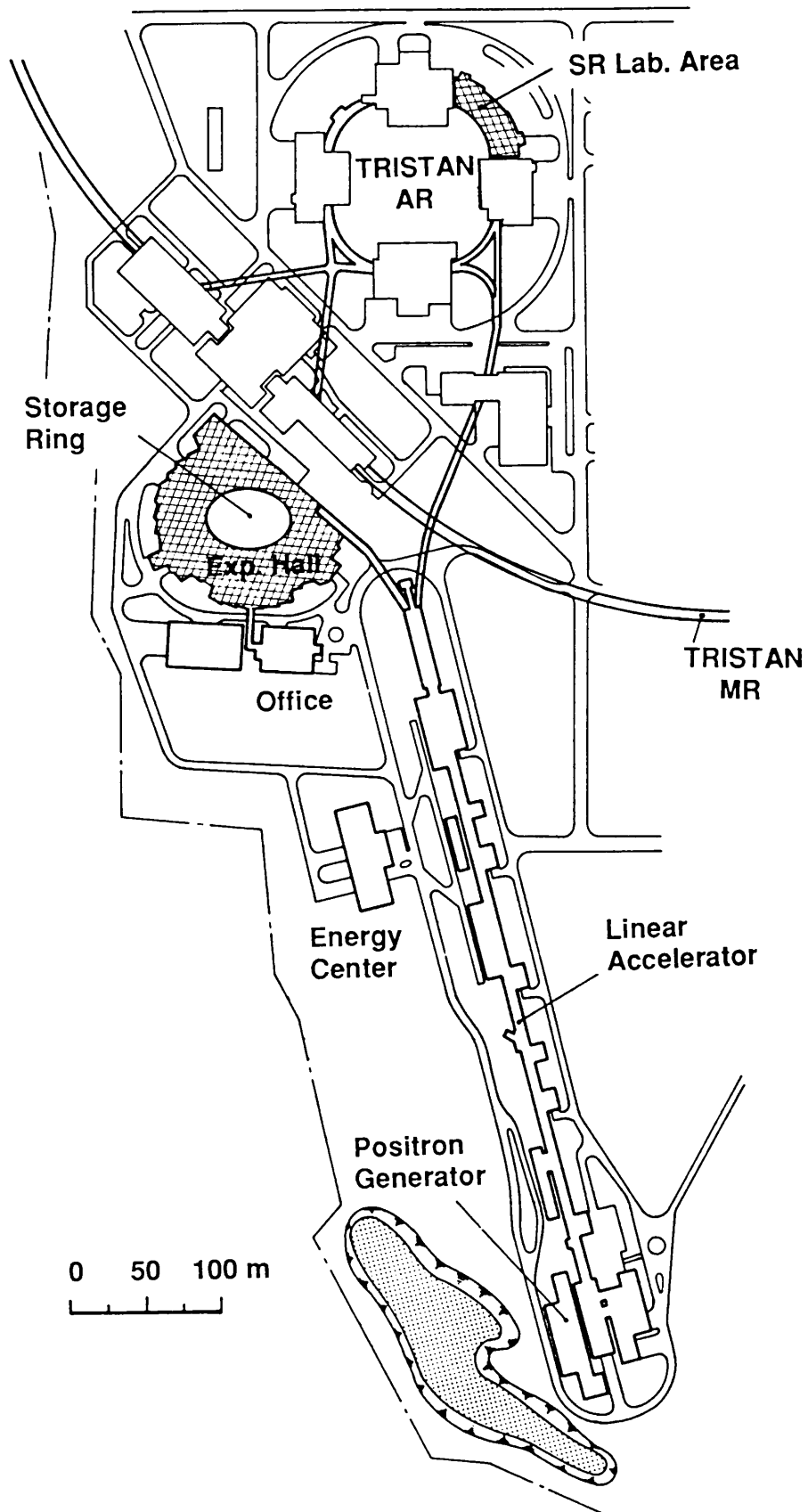


Fig. 1 Plan view of the Photon Factory

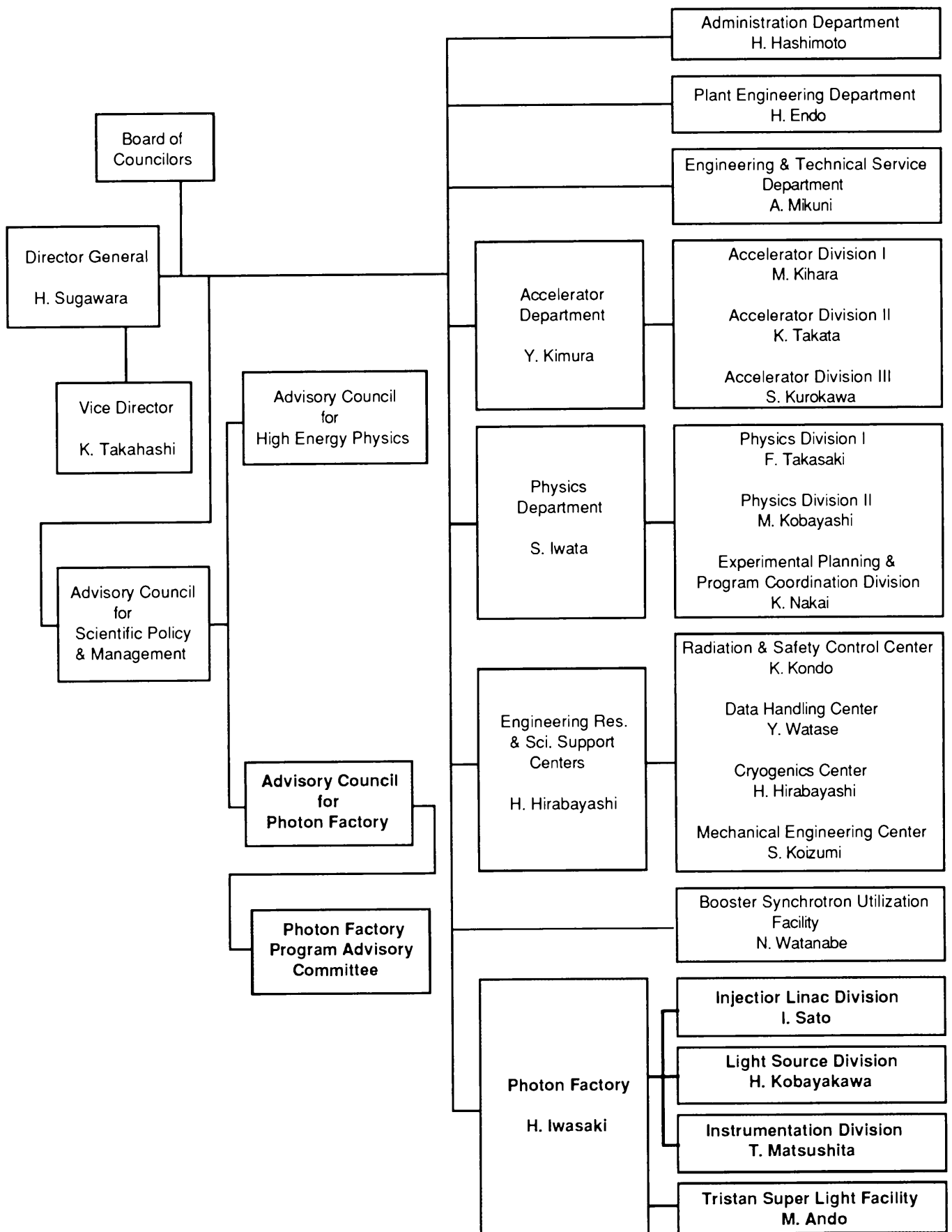


Fig. 2 Organization of KEK



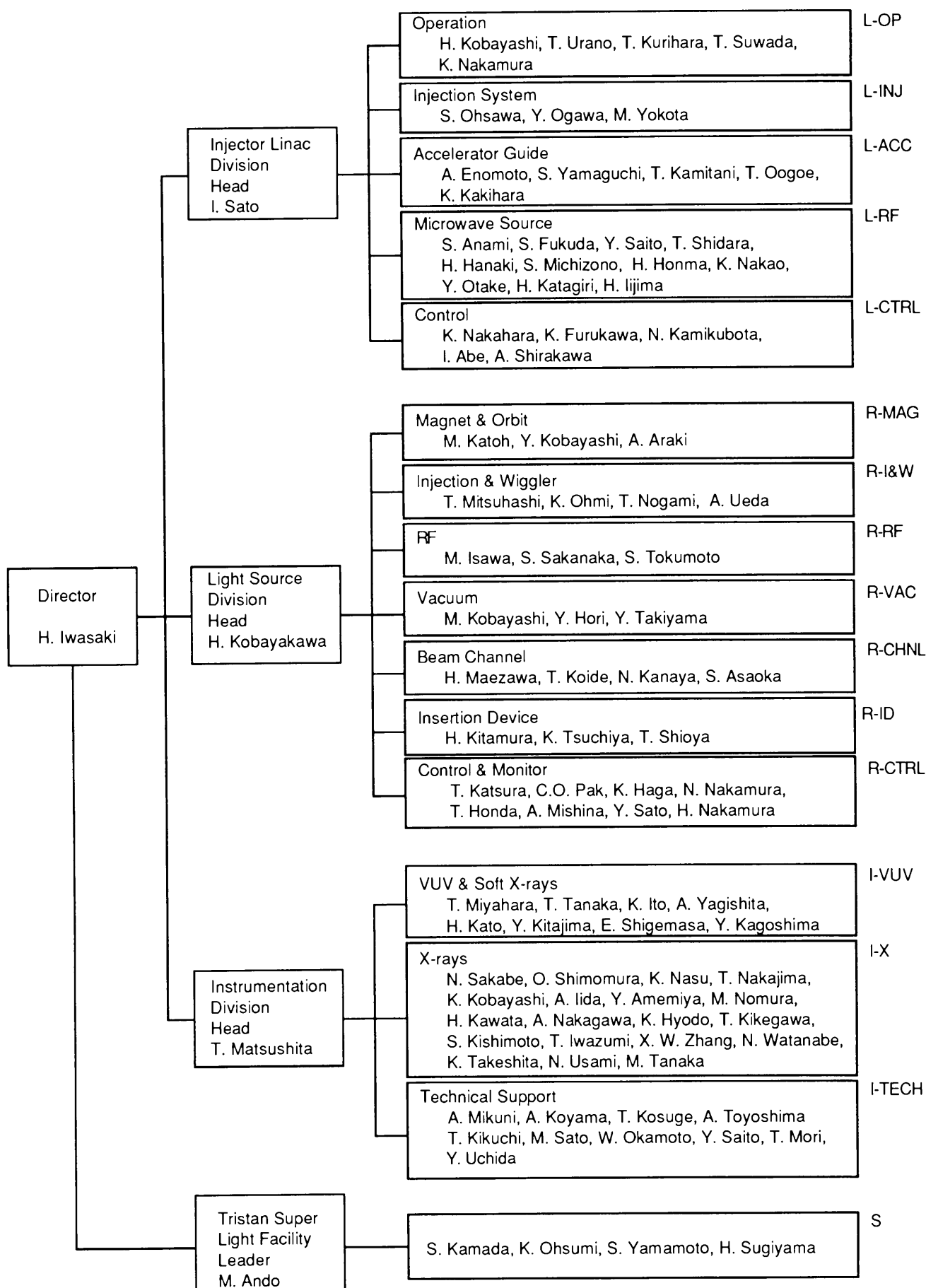


Fig. 3 Organization of the Photon Factory

**Table 1 Members of Advisory Council****\*\* Chairman \* Vice-Chairman**

ANAMI, Shozo	Injector Linac Division, PF, KEK
ANDO, Masami	Instrumentation Division, PF, KEK
FUJII, Yasuhiko	Institute for Solid State Physics, University of Tokyo
HARADA, Jinpei	Faculty of Engineering, Nagoya University
HIEDA, Kotaro	Faculty of Science, Rikkyo University
ISHII, Takehiko*	Institute for Solid State Physics, University of Tokyo
ITO, Kenji	Instrumentation Division, PF, KEK
KATSUBE, Yukiteru	Institute for Protein Research, Osaka University
KIKUTA, Seishi	Faculty of Engineering, University of Tokyo
KOBAYAKAWA, Hisashi	Light Source Division, PF, KEK
KOBAYASHI, Hitoshi	Injector Linac Division, PF KEK
KOBAYASHI, Masanori	Light Source Division, PF, KEK
MAEZAWA, Hideki	Light Source Division, PF, KEK
MATSUSHITA, Tadashi	Instrumentation Division, PF, KEK
NAKAJIMA, Tetsuo	Instrumentation Division, PF, KEK
NITTONO, Osamu	Faculty of Engineering, Tokyo Institute of Technology
OHTA, Toshiaki	Faculty of Science, Hiroshima University
SAKABE, Noriyoshi	Instrumentation Division, PF, KEK
SATO, Isamu**	Injector Linac Division, PF, KEK
SUZUKI, Kenji	Institute for Materials Research, Tohoku University
TOKONAMI, Masayasu	Faculty of Science, University of Tokyo

**Table 2 Members of Program Advisory Committee****\* Chairman**

HASHIZUME, Hiroo	Research Laboratory of Engineering Materials, Tokyo Institute of Technology
KOBAYAKAWA, Hisashi	Light Source Division, PF, KEK
KOTANI, Akio	Institute for Solid State Physics, University of Tokyo
MATSUSHITA, Tadashi*	Instrumentation Division, PF, KEK
MIYAHARA, Tsuneaki	Instrumentation Division, PF, KEK
MURATA, Takatoshi	Department of Physics, Kyoto University of Education
NIHEI, Toshimasa	Institute of Industrial Science, University of Tokyo
OHTA, Toshiaki	Faculty of Science, Hiroshima University
SATO, Isamu	Injector Linac Division, PF, KEK
SATOW, Yoshinori	Faculty of Pharmaceutical Sciences, University of Tokyo
SHIMOMURA, Osamu	National Institute for Research in Inorganic Materials
SUEMATSU, Hiroyoshi	Faculty of Science, University of Tokyo
TOKUNAGA, Fumio	Faculty of Science, Osaka University
YAGISHITA, Akira	Instrumentation Division, PF, KEK
YOSHIDA, Satohiro	Faculty of Engineering, Kyoto University

**Table 3 Staff members of the Photon Factory; Oct. '91 ~ Sept. '92**

Name	Responsibility(*)	e-mail address(**)
<b>Research Staff</b>		
IWASAKI, Hiroshi	Director	
ANAMI, Shozo	L-RF	
ENOMOTO, Atsushi	L-ACC	ENOMOTOA
FUKUDA, Shigeki	L-RF	SFUKUDA
FURUKAWA, Kazuro	L-CTRL	FURUKAWA
HANAKI, Hirofumi	L-RF	HANAKI
KAMIKUBOTA, Norihiko	L-CTRL	KAMI
KAMITANI, Takuya	L-ACC	KAMITANI
KOBAYASHI, Hitoshi	L-OP	HITOSHIK
KURIHARA, Toshikazu	L-OP	TKURIHAR
MICHIZONO, Shin'ichiro	L-RF	MICHIZON
NAKAHARA, Kazuo	L-CTRL	
OGAWA, Yujiro	L-INJ	OGAWAYJ
OHSAWA, Satoshi	L-INJ	OHSAWA
SAITO, Yoshio	L-RF	
SATO, Isamu	L-Head	
SHIDARA, Tetsuo	L-RF	SHIDARA
SUWADA, Tsuyoshi	L-OP	SUWADA
URANO, Takao	L-OP	URANO
YAMAGUCHI, Seiya	L-RF	SYAMA
HAGA, Kaiichi	R-CTRL	HAGA
HONDA, Tohru	R-CTRL	HONDAT
HORI, Yoichiro	R-VAC	HORI
ISAWA, Masaaki	R-RF	ISAWA
KANAYA, Noriichi	R-CHNL	KANAYA
KATOH, Masahiro	R-MAG	KATOHM
KATSURA, Tomotaro	R-CTRL	KATSURA
KITAMURA, Hideo	R-ID	KITAMURA
KOBAYAKAWA, Hisashi	R-Director	KOBAYAKA
KOBAYASHI, Masanori	R-VAC	KOBYASIMR
KOBAYASHI, Yukinori	R-MAG	
KOIDE, Tsuneharu	R-CHNL	
MAEZAWA, Hideki	R-CHNL	MAEZAWAH
MITSUHASHI, Toshiyuki	R-I&W	MITSUHAS
NAKAMURA, Norio	R-CTRL	NORIO
OHMI, Kazuhito	R-I&W	OHMI
PAK, Cheol On	R-CTRL	PAK
SAKANAKA, Shyogo	R-RF	SAKANAKA
TUCHIYA, Kimichika	R-ID	TSUCHIYA
AMEMIYA, Yoshiyuki	I-X	AMEMIYA
HYODO, Kazuyuki	I-X	HYODO
IIDA, Atsuo	I-X	AIIDA
ITO, Kenji	I-VUV	ITO
IWAZUMI, Toshiaki	I-X	IWAZUMI
KAGOSHIMA, Yasushi	I-VUV	KAGOSIMA
KATO, Hiroo	I-VUV	
KAWATA, Hiroshi	I-X	
KIKEGAWA, Takumi	I-X	KIKEGAWA
KISHIMOTO, Syunji	I-X	KISIMOTO
KOBAYASHI, Katsumi	I-X	KOBAYASK
KITAJIMA, Yoshinori	I-VUV	
MATSUSHITA, Tadashi	I-Head	MATSUS

Name	Responsibility(*)	e-mail address(**)
MIYAHARA, Tsuneaki	I-VUV	
NAKAGAWA, Atsushi	I-X	NAKAGAWA
NAKAJIMA, Tetsuo	I-X	
NOMURA, Masaharu	I-X	NOMURAM
SAKABE, Noriyoshi	I-X	SAKABE
SHIGEMASA, Eiji	I-VUV	
TAKESHITA, Kunikazu	I-X	TAKESHIT
TANAKA, Ken'ichiro	I-VUV	
TANAKA, Masahiko	I-X	
USAMI, Noriko.	I-X	USAMI
WATANABE, Nobuhisa	I-X	NOBUHISA
YAGISHITA, Akira	I-VUV	
ZHANG, Xiaowei	I-X	
ANDO, Masami	S-Leader	ANDO
KAMADA, Susumu	S	KAMADA
OHSUMI, Kazumasa	S	
SUGIYAMA, Hiroshi	S	
YAMAMOTO, Shigeru	S	SHIGERU
<b>Supporting Staff</b>		
ABE, Isamu	L-CTRL	ABEI
HONMA, Hiroyuk	L-RF	
IJIMA, Hitoshi	L-RF	
KAKIHARA, Kazuhisa	L-ACC	KAKIHARA
KATAGIRI, Hiroaki	L-RF	
NAKAMURA, Kie	L-OP	KIE
NAKAO, Katsumi.	L-RF	
OOGOE, Takao	L-ACC	OOGOE
OTAKE, Yuji	L-OP	OTAKE
SHIRAKAWA, Akihiro	L-CTRL	SIRAKAWA
YOKOTA, Mitsuhiro	L-INJ	
ARAKI, Akira	R-MAG	
ASAOKA, Seiji	R-CHNL	
MISHINA, Atsushi	R-CTRL	MISHINA
NAKAMURA, Hajime	R-CTRL	
NOGAMI, Takashi	R-I&W	NOGAMI
SATO, Yoshihiro	R-CTRL	YOSHIHIR
SHIOYA, Tatsuro	R-ID	SHIOYA
TAKIYAMA, Youichi	R-VAC	
TOKUMOTO, Shuichi	R-RF	TOKUMOTO
UEDA, Akira	R-I&W	
KIKUCHI, Takashi	I	
KOSUGE, Takashi	I	KOSUGE
KOYAMA, Atsushi	I	
MIKUNI, Akira	I	
MORI, Takeharu	I	
OKAMOTO, Wataru	I	
SAITO, Yuuki	I	YSAITO
SATO, Masato	I	
TOYOSHIMA, Akio	I	
UCHIDA, Yoshinori	I	

(\*) Refer to Fig. 3 for abbreviations.

(\*\*) Use @JPNKEK VX for Bitnet, and @KEKVAX.KEK.JP for Internet.

**Table 4 Annual numbers of staff & visiting scientists**

Position	Department	1982	1983	1984	1985	1986	1987	1988	1989	1990	1991	1992
Chief Director		1	1	1	1	1	1	1	1	1	1	1
Professor	Injector Linac	3	3	3	3	4	4	4	3	3	4	3
	Light Source	4	4	4	3	4	4	4	4	5	5	4
	Instrumentation	1	1	1	2	3	4	5	5	5	6	8
Associate Professor	Injector Linac	2	2	2	2	1	2	3	5	7	6	7
	Light Source	4	3	5	5	3	3	3	5	4	3	3
	Instrumentation	4	5	5	8	7	9	7	10	9	8	10
Research Associate	Injector Linac	7	8	9	10	11	10	10	9	8	9	9
	Light Source	7	7	6	8	9	12	12	9	11	11	12
	Instrumentation	7	10	10	10	13	13	14	11	15	15	15
Technical Staff	Injector Linac	5	5	6	6	7	8	9	10	11	11	11
	Light Source	6	6	6	6	7	7	8	10	10	10	10
	Instrumentation	1	2	4	4	8	9	11	10	9	10	10
Visiting Scientist	Injector Linac	2	2	2	2	2	2	2	2	2	2	2
	Light Source	4	4	4	4	4	4	4	4	4	4	4
	Instrumentation	6	6	6	6	6	6	6	6	6	7	6
Total		64	69	74	80	90	97	103	104	110	112	115

**Table 5 Budget in each fiscal year**

(in million yen)

Item	1982	1983	1984	1985	1986	1987	1988	1989	1990	1991	1992
Salary	402	474	484	510	561	561	642	757	764	859	898
PF Storage Ring (channel, insertion device, etc.)	0	0	0	153	131	647	0	0	196	103	0
PF Experiments	140	153	134	184	190	196	237	341	367	399	375
PF Operation & Maintenance	412	477	552	653	820	907	962	1,078	1,107	1,107	1,042
Computer Rentals	136	135	135	135	136	136	141	145	145	145	145
Positron Source & Electric Plant Operation	0	0	0	41	138	208	258	300	308	300	253
Cooling System & Electric Operation	120	111	124	180	211	214	217	231	235	240	218
Electricity	209	226	257	338	381	331	355	425	423	423	423
PF-Industrial Cooperative Experiments	0	94	84	95	185	166	302	219	171	174	154
AR Construction and Experiments						398	267	387	250	260	148
Miscellaneous	115	134	115	127	162	120	301	243	287	388	564
Total	1,534	1,804	1,885	2,397	2,864	3,884	3,682	4,126	4,253	4,398	4,220

**Table 6 Yearly account of beam channels**

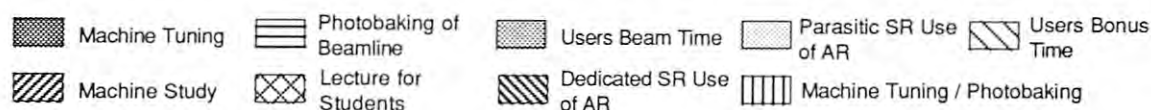
Fiscal	1982	1983	1984	1985	1986	1987	1988	1989	1990	1991	1992
PF	8	8	8	10	12	13	13	15	15	17	20
Institutes	0	0	1	1	1	3	4	4	4	4	3
Industry	0	1	2	4	4	4	4	4	4	4	4
Total	8	9	11	15	17	20	21	23	23	25	27

**Table 7 Summary of operation in FY 1992 (April 1992 - March 1993) (hours)**

Cycle	Linac	PF Ring	Users' time	AR	Dedicated to SR at AR
1	1838	1904	1579	2061	1838
2	1251	1656	1288	1801	1251
3	886	1056	781	1120.5	886
Total	3975	4616	3648	4982.5	3975

Table 8 Timetable of the Machine Operation in FY 1992.

PF : PF ring, AR : Accumulation ring



Cycle	Time	MON	TUE	WED	THU	FRI	SAT	SUN	MON	TUE	WED	THU	FRI	SAT	SUN	MON	TUE	WED	THU	FRI	SAT	SUN
	Date	9/17	9/17	9/17	9/17	9/17	9/17	9/17	9/17	9/17	9/17	9/17	9/17	9/17	9/17	9/17	9/17	9/17	9/17	9/17	9/17	9/17
1-1	Linac																					
	P F																					
	A R																					
1-1 / 1-2	Date	20	21	22	23	24	25	26	27	28	29	30	5/1	2	3	4	5	6	7	8	9	10
	Linac																					
	P F																					
1-2	Date	11	12	13	14	15	16	17	18	19	20	21	22	23	24	25	26	27	28	29	30	31
	Linac																					
	P F																					
1-3	Date	6/1	2	3	4	5	6	7	8	9	10	11	12	13	14	15	16	17	18	19	20	21
	Linac																					
	P F																					
1-4	Date	22	23	24	25	26	27	28	29	30	7/1	2	3	4	5	6	7	8	9	10	11	12
	Linac																					
	P F																					
2-1	Date	9/28	29	30	10/1	2	3	4	5	6	7	8	9	10	11	12	13	14	15	16	17	18
	Linac																					
	P F																					
2-1 / 2-2	Date	19	20	21	22	23	24	25	26	27	28	29	30	31	11/1	2	3	4	5	6	7	8
	Linac																					
	P F																					
2-2 / 2-3	Date	9	10	11	12	13	14	15	16	17	18	19	20	21	22	23	24	25	26	27	28	29
	Linac																					
	P F																					
2-3 / 2-4	Date	30	12/1	2	3	4	5	6	7	8	9	10	11	12	13	14	15	16	17	18	19	20
	Linac																					
	P F																					
2-4	Date	21	22	23	24	25	26	27	28	29	30	31	1/1	2	3	4	5	6	7	8	9	10
	Linac																					
	P F																					
3-1	Date	2/8	9	10	11	12	13	14	15	16	17	18	19	20	21	22	23	24	25	26	27	28
	Linac																					
	P F																					
3-1 / 3-2	Date	3/1	2	3	4	5	6	7	8	9	10	11	12	13	14	15	16	17	18	19	20	21
	Linac																					
	P F																					
3-2	Date	22	23	24	25	26	27	28	29	30	31	4/1	2	3	4	5	6	7	8	9	10	11
	Linac																					
	P F																					

## SEMINARS, MEETINGS AND PUBLICATIONS

Twenty three seminars were given by scientists who visited the PF in 1992. Three users' meetings were held in FY 1992, including the annual PF symposium. The PF publishes its quarterly "PHOTON FACTORY NEWS" in Japanese for communication between users and staff.

### PF seminars

Kortright, J. B. (LBL Center for X-ray Optics) Specular and Off-specular Scattering Measurements of Roughness in X-ray Multilayers	January 20, 1992
Möhling, W. (Zentrallinstitut für Elektronenphysik, Berlin) X-ray Topography – Capacity and Limitations –	January 23, 1992
Yagishita, A. (Photon Factory, KEK) Auger Effects in Near-threshold Inner-shell Photoionization	February 25, 1992
Kodaira, M. (SORTEC Corporation) Present Status of the SORTEC SOR Facility	March 5, 1992
Katoh, M. (Photon Factory, KEK) Design Study on a Low Emittance Configuration of the PF Storage Ring	March 18, 1992
Hedin, L. (Lund University, Sweden) The Role of the Blue Electron in Electron Spectroscopy	April 2, 1992
Mochrie, S. (Department of Physics, Massachusetts Institute of Technology) X-ray Scattering Studies of Surface Phase Transitions: Pt(001) and Si(113)	April 17, 1992
Ban, S. (Radiation & Safety Control Center, KEK) Absolute Measurement of X-ray Intensity in 7-40 keV Region	April 23, 1992
Yamada, H. (Laboratory for Quantum Equipment Technology, Sumitomo Heavy Industries, Ltd.) Photon Storage Ring	April 28, 1992
Wang, Z. J. (Optics and Fine Mechanics, Academia Sinica) Enhancement of the Brightness of X-ray Lasers and X-ray Holography	May 26, 1992
Street, A. (Oxford Instrument) Description of the 6T Wiggler Manufactured for Daresbury Laboratory	May 27, 1992
Hamalainen, K. (NSLS, BNL) High Resolution X-ray Fluorescence Spectroscopy	August 20, 1992
Hitchcock, A. P. (Institute for Materials Research, MacMaster University) Inner-shell Excitation of Clusters of Atoms and Molecules	September 1, 1992
Osterwalder, J. (Institut de Physique, Université de Fribourg) Core and Valence Photoelectron Diffraction from Cu(001) and Cu(111) Surfaces at Low and High Energies	September 16, 1992

Sanche, L. (University of Sherbrooke, Quebec, Canada) Low-energy Electron Interactions with Condensed Atoms and Molecules: Relationship to Surface Photoreactions	September 18, 1992
Lander, G. H. (Institute for Transuranium Elements, Karlsruhe, Germany) Magnetic X-ray Scattering	September 21, 1992
Khmelev, A. V. (Moscow Engineering Physics Institute) Reduction of Oxide Films by Radiation Initiating Electron Transition in Oxide	October 30, 1992
Chidambaran, R. (Bhabha Atomic Research Center, India) Hydrogen Bonding in Biological Molecules	November 2, 1992
Mai, Z. H. (Institute of Physics, Academia Sinica) X-ray Analysis of the Device Structure of Semiconductors Thin Film	December 2, 1992
Mills, D. (Advanced Photon Source ,Argonne National Lab.) Current Status of Advanced Photon Source	December 10, 1992
Lee, W. K. (Advanced Photon Source, Argonne National Lab.) Development of High Heat Load Optics at APS	December 10, 1992
Belyakov, V. A. (All Russian Surface and Vacuum Research Center) Mössbauer Coherent Inelastic Scattering of Synchrotron Radiation	December 16, 1992
Rao, M. R. (Bhabha Atomic Research Center, India) Spectroscopy Beam Lines at Indus-I	December 21, 1992

## Users' Meetings

Users Meeting on Protein Crystal Data Collection System at the Photon Factory	September 5-6, 1992
Users Meeting on Structural Studies under High Pressure using Powder Diffraction	September 17-18, 1992
The 10th Photon Factory Symposium (Annual Users' Meeting)	December 4-5, 1992

## Publications

PHOTON FACTORY NEWS	ISSN 0916-0604	Vol.10, No.1-4
---------------------	----------------	----------------



## GRADUATE UNIVERSITY FOR ADVANCED STUDIES

The National Graduate University was established in 1988. It has the following three schools:

School of Cultural Studies

School of Mathematical and Physical Sciences

School of Life Sciences.

KEK has participated in the University to form the Department of Synchrotron Radiation Science and the Department of Accelerator Science, both of which belong to the School of Mathematical and Physical Sciences.

Students in the Department of Synchrotron Radiation Science are expected to study the basic theory of emission of synchrotron radiation, its characteristics, and interaction of radiation with matter, and then engage in research by using various facilities at the PF. The research field includes the development of radiation sources, optical elements, and instruments for diffraction, scattering, spectroscopy, and irradiation experiments as well as exploration of new areas of applying synchrotron radiation to science and technology.

## PROPOSAL GUIDELINES FOR EXPERIMENTERS AT PHOTON FACTORY

### 1. HOW TO SUBMIT A PROPOSAL

Photon Factory is open to everybody in scientific research. A proposal should be filed using an application form which is available on request from the Research Cooperation Section of the Administration Department of KEK. An applicant should carefully read the guide before filing an application. A spokesperson should get the agreement of the members to join the team.

An overseas applicant is requested to find an appropriate "contact person in Japan (CPJ)", who will mediate between the applicant and KEK\*. Please contact the person in charge of the experimental station you want to use if you do not know any appropriate CPJ. He/she will select a person appropriate for the applicant's research plan. A list of the people in charge of the experimental stations can be found in this report.

All experimental proposals are subject to approval of the Photon Factory Program Advisory Committee (PF-PAC). The CPJ will be informed about the decision.

Note that the procedure has been changed since April 1992. Therefore an applicant should use the new application forms: old one cannot be accepted.

*\* The contact person in Japan will help you translate Japanese and English, assist with visa applications and your experiments. In order to assure his/her agreement the signature or seal imprint of the CPJ is required.*

### 2. CATEGORY OF PROPOSALS

#### 2.1 For University Researchers etc.

There are four categories of application; G(eneral), S(pecial), P(reliminary) and U(rgent). The character, process of approval and terms of validity are different among those categories.

G is the category for general experiments using synchrotron radiation. Deadlines of application and valid terms are as follows:

Deadlines:

July 9, 1993 (a) and January 14, 1994 (b)

Valid terms:

from October, 1993 to September, 1995 for (a)

from April, 1994 to March 1996 for (b).

P is the category for preliminary experiments in order to determine the feasibility of proposals for categories G or S. There are some limitations as listed below.

- 1) The maximum beamtime for one project is less than about 72 hours.
- 2) One spokesperson can have only one project at a time.
- 3) More than three proposals of this category cannot be approved for an experimental station at a PF-PAC.

Deadlines:

July 9, 1993 (a) and January 14, 1994 (b)

Valid terms:

from October, 1993 to September, 1994 for (a)

from April, 1994 to March 1995 for (b).

S is the special category for those experiments that may be difficult to do but may have extremely high scientific value. Those include experiments for the development of a difficult technique or those requiring special operation of the storage ring. Photon Factory supports the projects of this category financially within certain limits; the funds cannot be used for travel expenses or salary. At least one Japanese scientist

should be included in the team. The process of judgement is different from other categories. An applicant has to express his/her plan orally before the PF-PAC. Deadline and valid term are as follows:

Deadline: late September, 1993  
Valid term: from April, 1994 to March, 1997.  
The progress report should be presented at the "Photon Factory Symposium" which takes place every year.

U is the category for urgent proposals which cannot be postponed until the next deadline and which are of extremely high scientific value. Once approved, these projects may exclude already assigned beamtime for other projects. Applicants can apply at any time but the valid terms are limited as follows:

- a project approved between October and March: until end of March
- a project approved between April and September: until end of September.

Results of a project should be reported at the "Photon Factory Symposium."

## 2.2 For Researchers in Private Companies etc.

Photon Factory is also open for scientists working in private corporations within certain limits. However, a fee is charged for beamtime.

## 3. ACCOMMODATION

KEK provides guest houses at low cost for visiting scientists. In the case of domestic experimenters, please contact the person in charge of your experimental station. Overseas experimenters should ask the CPJ to book rooms. KEK supports travel and living expenses for domestic experimenters within certain limits but does not for overseas experimenters.

## 4. OTHERS

- (1) Experimenters must obey the safety rules at PF.
- (2) Further procedure may be requested in order to carry out an experiment.
- (3) If there are question regarding procedures please contact

Research Cooperation Section,  
Administration Department,  
National Laboratory for High Energy Physics,  
Oho, Tsukuba 305, Japan  
FAX: 81-298-64-4602

Table 9    Number of proposals approved by the PAC.

Research Field	1983	1984	1985	1986	1987	1988	1989	1990	1991	1992
(A) EXAFS	42	26	35	40	61	66	57	71	69	67
(B) Biology	18	18	28	28	32	38	57	61	75	89
(C) X-Ray	24	29	75	54	73	65	61	80	92	109
(D) VUV & Soft X-Ray	19	12	27	26	28	28	36	27	45	44
Total	103	85	165	148	194	197	211	239	281	309

区分 category	G型、P型、S型、U型
----------------	-------------

# 高エネルギー物理学研究所放射光実験施設共同利用実験申請書

Application form for synchrotron radiation experiments at Photon Factory (PF)

高エネルギー物理学研究所長殿

申請日 (Date)

実験責任者  
Spokesperson

氏名 (Name)

印 (Signature)

所属、職名  
Affiliation  
Position

連絡先住所  
Mailing  
Address 〒

下記の通り申請します

Tel.

FAX

E-mail

実験課題名 Proposal title	(日本語)					
	(英訳)					
I. 実験 組 織  team	ローマ字 氏 名 Name	所属 Affiliation <sup>1</sup> (大学、学部、学科)	職 名 <sup>2</sup> Position	電話番号 <sup>3</sup> Tel.	PFの利用経験 <sup>4</sup> Experience at PF	分担事項 Role in the team
1. 大学院生は所属大学、研究科、専攻 2. 大学院生は課程、学年 3. 内線を含む 4. ステーション名及び習熟度 (excellent, good, fair, poor, none) 欄が不足する場合は同封別紙に記入の上5枚目に添付						

II. 希望 ビーム タイム  schedule	ステーション Station	希望時期 year/month	希望時間 <sup>5</sup> beam time	III. 希望ステーションとその理由 (Name of stations and why you chose them)  第1希望    第2希望    第3希望
	総 計 total			

5. 時間または日単位で記入 in units of hours or days

For overseas applications, describe the contact person in Japan (Name, mailing address, tel. and FAX)			
氏名	印	Tel.	FAX
所属、職名			
連絡先住所 〒			

Office use

受理年月日	※
受 理 番 号	※

## List of proposals accepted in fiscal 1992

Proposal Number	Spokesperson	Title
92-001	Y. Iwasawa Faculty of Science, Univ. of Tokyo	EXAFS analyses of static and dynamic structures of plane $[\text{HMo}_6\text{O}_{24}]^{8-}$ ensembles attached on $\text{SiO}_2$ , $\text{Al}_2\text{O}_3$ , and $\text{MgO}$
92-002	T. Nasu Faculty of Education, Yamagata Univ.	Structural study of intermetallic compound during solid state amorphization process
92-003	M. Ichikawa Catalysis Research Center, Hokkaido Univ.	Synthesis of novel bimetal clusters under micro gravity and their EXAFS characterization
92-004	M. Ichikawa Catalysis Research Center, Hokkaido Univ.	In-situ EXAFS study of Rh and Rh-Co bimetal carbonyl clusters attached on phosphine modified oxide surface
92-005	K. Kawamura Faculty of Science, Hokkaido Univ.	EXAFS study of molybdenum and tungsten ions in sodium silicate glasses
92-007	N. Takahashi Kitami Institute of Technology	Characterization of Rh-CO species formed on activated carbon by EXAFS
92-008	Y. Iwasawa Faculty of Science, Univ. of Tokyo	EXAFS studies on the structure and dynamic change of RhSn bimetal catalysts for catalytic asymmetric synthesis
92-009	Y. Iwasawa Faculty of Science, Univ. of Tokyo	EXAFS study on new active attached Zr dimer catalysts for methane activation
92-010	I. Nakai Department of Chemistry, Univ. of Tsukuba	Characterization of archaeological objects by X-ray fluorescence EXAFS
92-011	H. Takei Institute for Solid State Physics, Univ. of Tokyo	Study of abnormal valence state of Cu in lithium copper oxides
92-012	T. Hashimoto Research Lab. of Engineering Materials, Tokyo Institute of Technology	Analysis of chemical state of Bi and Pb in $\text{BaPb}_{1-x}\text{Bi}_x\text{O}_{3-d}$ by X-ray absorption spectroscopy
92-014	S. Funahashi Faculty of Science, Nagoya Univ.	Structural study on Co(II), Ni(II), Cu(II), Zn(II), Cd(II) and In(III) complexes in 1, 1, 3, 3-tetramethylurea
92-015	A. Nakamura Faculty of Science, Osaka Univ.	EXAFS studies of W and Mo oxido reductase model complexes
92-017	H. Nasu Faculty of Engineering, Mie Univ.	Relationship between structure and optical nonlinearity in glasses
92-018	Y. Okamoto Faculty of Engineering Science, Osaka Univ.	Structure of molybdenum oxide clusters prepared by photo-oxidation of anchored $\text{Mo}(\text{CO})_6$

Proposal Number	Spokesperson	Title
92-019	Y. Kawamoto Faculty of Science, Kobe Univ.	XAFS analysis of heavy-metal fluoride glasses containing rare earth ions
92-020	I. Nakai Faculty of General Education, Tottori Univ.	The local structure of amorphous $Gd_xY_{67-x}Ni_{33}$
92-021	S. Kashino Faculty of Science, Okayama Univ.	EXAFS studies of the local structure in $C_{60}$ superconductors
92-022	H. Yamazaki Faculty of Science, Okayama Univ.	Anharmonicity in lattice vibrations on oxide superconductors
92-023	K. Oshima Faculty of Science, Okayama Univ.	XAFS measurements in Cu DCNQI salts under pressure
92-024	M. Taniguchi Faculty of Science, Hiroshima Univ.	EXFAS studies on semimagnetic semiconductor $Zn_{1-x}Mn_xTe$
92-025	K. Umeno Faculty of Science, Hiroshima Univ.	Estimation of Ce valence in $Ce_7(Ni_{1-x}Pt_x)_3$ by XANES measurement
92-026	T. Moriga Faculty of Engineering, Tokushima Univ.	Local structure analysis of the pyrochlore-type $Bi_{2-x}Ln_xRu_2O_7$
92-027	S. Saigo Jichi Medical School	Rapid-freeze XAFS studies of reaction intermediates of metalloproteins
92-028	T. Yamamura Faculty of Science, Science Univ. of Tokyo	XAFS study of the ribonucleotide reductase synthetic core
92-029	H. Kasatani Faculty of Science, Kwansei Gakuin Univ.	Polarization EXAFS study of $La_{2-x}Sr_xCuO_4$ single crystal
92-030	H. Wakita Faculty of Science, Fukuoka Univ.	XAFS study on square-planar copper (II) complexes with four-nitrogen atoms
92-031	Q. Wang Univ. of Science and Technology of China	EXAFS study of bimetallic catalysts supported on zeolites
92-032	B. C. Gates Dept. of Chem. Eng., Univ. of Delaware	Characterization of well-defined supported metals on single-crystal supports by X-ray absorption spectroscopy
92-033	A. Nukui National Institute for Research in Inorganic Materials	XAFS study on functional oxide glass

Proposal Number	Spokesperson	Title
92-034	N. Ishizawa Research Lab. of Engineering Materials, Tokyo Institute of Technology	Fluorescent EXAFS of rare-earth tantalum oxides
92-035	Y. Iwasawa Faculty of Science, Univ. of Tokyo	The asymmetric-structure determination of cobalt-oxide layer-growth modes on oxide crystal surface by polarized total reflection fluorescence EXAFS spectroscopy
92-036	T. Ohta Faculty of Science, Univ. of Tokyo	EXAFS study of the local structures of PVA-iodine polarizing films
92-037	M. Wakaki School of Engineering, Tokai Univ.	EXAFS study for the structure parameters of spinel type compounds
92-038	T. Ohta Faculty of Science, Univ. of Tokyo	Study on adsorption behavior of sulfur-containing molecules on nickel single crystals
92-039	H. Kuroda Faculty of Science, Univ. of Tokyo	Study on the step-induced adsorption structures of S and Cl on Ni single crystal
92-040	T. Nakajima Photon Factory, KEK	With the aim of new states and new material phases induced by the photoelectric effect of the high brilliant SR. (I) On a new interpretation of the photoacoustic effect
92-041	I. Tanaka Faculty of Science, Hokkaido Univ.	Crystal structure analysis of DNA binding protein HU
92-042	K. Miki Research Lab. of Resources Utilization, Tokyo Institute of Technology	X-ray crystallographic analysis of chaperonin
92-043	A. Nakagawa Photon Factory, KEK	High resolution data collection of commelinin
92-044	N. Kato School of Medicine, Nagoya Univ.	Analysis of crystals of bacterial lipopolysaccharides
92-045	T. Iwane School of Engineering, Nagoya Univ.	Crystal structure analyses of serine proteases, Bowman-Birk type inhibitors (BBI), and proteases complexed with BBI
92-046	A. Suzuki School of Engineering, Nagoya Univ.	Crystal structure analyses of bacterial $\alpha$ -amylases
92-047	H. Masuda Nagoya Institute of Technology	Structural studies on molecular recognition mechanism for biomacromolecules by synchrotron radiation source
92-048	K. Fukuyama Faculty of Science, Osaka Univ.	X-ray crystallographic analysis of peroxidase

Proposal Number	Spokesperson	Title
92-049	K. Hamada Faculty of Science, Shimane Univ.	Structural study of serratia protease by X-ray diffraction method
92-050	Y. Suzuki Kyoto Prefectural Univ.	X-ray crystal structure analysis of oligo-1, 6-glucosidase
92-051	Y. Mizuno National Institute of Agrobiological Resources	X-ray crystal structure study of rice dwarf virus (RDV)
91-052	Y. Mizuno National Institute of Agrobiological Resources	X-ray structure analysis of recombinant <i>Bacillus subtilis</i> $\alpha$ -amylase
92-053	I. A. Andersson Dept. of Molecular Biology, SW Agricultural Univ.	Understanding catalysis in ribulose-1, 5-bisphosphate carboxylase/oxygenase: High resolution diffraction studies on spinach Rubisco complexed with substrates, substrate analogues, inhibitors and effectors
92-054	J. Hajdu Lab. of Molecular Biophysics, Oxford Univ.	Kinetic X-ray crystallography with a CCD detector: Structural studies on phosphorylase, Rubisco, cytochrome c peroxidase and ribonucleotide reductase
92-055	J. Hajdu Lab. of Molecular Biophysics, Oxford Univ.	Kinetic X-ray crystallography in Weissenberg geometry: Structural studies on Rubisco, cytochrome c peroxidase and ribonucleotide reductase
92-056	A. B. Edmundson Harrington Cancer Center	Three dimensional structure of immunoglobulins
92-057	P. J. Bjorkam California Institute of Technology	Date collection from radiation sensitive Fc receptor and Fc/Fc receptor complex crystals, and characterization of T cell receptor crystals
92-058	D. Wang Institute of Biophysics, Academia Sinica	Crystallographic studies of human insulin mutants from protein engineering
92-059	Q. Huang Peking Univ.	The crystal structures of the complexes formed between the arrowhead trypsin inhibitors and trypsin or chymotrypsin
92-060	B. Wang Crystallography Dept., Univ. of Pittsburgh	Crystallographic studies of T7 RNA polymerase, glutamine binding protein and serum albumin
92-061	R. Pickersgill AFRC, Institute of Food Research	Elucidation of protein structures; glucose oxidase, pectate lyase, CELA & xylanase
92-062	G. Lu Dept. of Biology, Peking Univ.	The collection of diffraction data of autolyzed active products of trypsin, bar-headed goose hemoglobin and antibacterial poly-peptide-LC <sub>1</sub>
92-063	R. L. Williams CABM, Rutgers Univ.	Determination of the structure of nucleoside diphosphate kinase

Proposal Number	Spokesperson	Title
92-064	E. Arnold CABM, Rutgers Univ.	High resolution structure determination of HIV-1 reverse transcriptase complexed with dsDNA primer-template mimics
92-065	N. Tanaka Faculty of Bioscience and Biotechnology, Tokyo Institute of Technology	Structure studies on proteins that containing anomalous scattering atoms
92-066	M. Kataoka Faculty of Science, Osaka Univ.	Diversity of solution structures among complexes between calmodulin and its target peptides
92-067	M. Kataoka Faculty of Science, Osaka Univ.	X-ray solution scattering studies on acid denaturation and refolding of cytochrome c
92-068	F. Tokunaga Faculty of Science, Osaka Univ.	Structure analysis on photolyase
92-069	M. Hirai Faculty of General Studies, Gunma Univ.	Phase diagram of phosphatidylinositoldiphosphate-water system
92-070	K. Matsushige Faculty of Engineering, Kyushu Univ.	Studies on the dynamical mechanism of the gelation process of myofibrillar proteins
92-071	F. Tokunaga Faculty of Science, Osaka Univ.	Structural change of purple membrane during photoreaction cycle
92-072	Y. Tajima Faculty of Science, Tokyo Metropolitan Univ.	Structure studies of actin filaments in a contracting muscle by medium angle X-ray diffraction
92-073	S. Matsuoka Sapporo Medical College	Study of the lipid polymorphism by high-temperature-resolution X-ray diffraction
92-074	H. Sugi School of Medicine, Teikyo Univ.	Effect of anti-myosin S-2 antibody on the X-ray diffraction pattern from contracting muscle
92-075	H. Iwamoto School of Medicine, Teikyo Univ.	X-ray diffraction studies on the "active state" and the calcium-regulation mechanism in skeletal muscles
92-076	H. Kihara School of Nursing, Jichi Medical School	Formation of protein folding intermediates monitored by stopped-flow X-ray scattering method
92-077	Y. Saeki School of Dentistry, Tsurumi Univ.	A time-resolved X-ray diffraction study on myocardial cross-bridge dynamics
92-078	Y. Igarashi School of Medicine, Dokkyo Univ.	Molecular structure and function of giant oxygen carrier proteins by using stopped-flow small-angle X-ray scattering



Proposal Number	Spokesperson	Title
92-079	T. Ikushima Research Reactor Institute, Kyoto Univ.	Single cell gel-electrophoretic analysis of DNA damage induced by ultra-soft X-rays in cultured mammalian cells
92-080	H. Maezawa School of Medicine, Tokai Univ.	Double strand breakage in DNA of cultured mammalian cells by Auger cascades of intracellular phosphorus
92-081	M. Watanabe Faculty of Pharmacology, Nagasaki Univ.	Analysis of <i>in vitro</i> cell transformation by SOR
92-082	S. Komura Faculty of Integrated Arts and Science, Hiroshima Univ.	Time resolved small-angle X-ray scattering study of dynamical structure of lipid bilayer
92-083	M. Sasaki Radiation Biology Center Kyoto Univ.	Energy dependence of RBE of low-energy X-rays
92-084	N. Usami Photon Factory, KEK	Study on the correlation between the cell lethality and the DNA strand breaks induced by inner-shell photoabsorption of phosphorus
92-085	M. Kuwabara Faculty of Veterinary Medicine Hokkaido Univ.	Observation of Auger effects in Br-labeled oligonucleotides and plasmid DNA
92-086	K. Kobayashi Photon Factory, KEK	Study on the sensitization by heavy atom-containing chemicals in the cell lethality of radiation
92-087	K. Osamura Faculty of Engineering, Kyoto Univ.	Structure determination of mesoscopic materials by anomalous small-angle X-ray scattering
92-088	W. G. J. Hol BIOSON, Univ. of Groningen	The structure determination of intact human anti-thrombin III, transglycosylase, the catalytic domain of dihydrolipoyl trans-acetylase and trypanosomal enzymes
92-089	M. James Univ. of Alberta	Protein crystallography data collection of hexosaminidase B, glycogen debranching enzyme, dysentery toxin and RTEM-1/BLIP complex
92-090	C. Uyama National Cardiovascular Center	Fundamental study of monochromatic X-ray computed tomograph system
92-091	H. Takeda Faculty of Science, Univ. of Tokyo	Determination of abundances of trace siderophile and lithophile elements in meteorites and their formation condition
92-092	M. Ishikawa National Institute of Radiological Science	Identification of the elemental migration and the formation mechanisms of tissue in marine organisms
92-093	N. Shimojo Institute of Community Medicine, Univ. of Tsukuba	Nondestructive two dimensional chemical imaging of trace elements on cancerous tissues

Proposal Number	Spokesperson	Title
92-094	A. Iida Photon Factory, KEK	X-ray fluorescence analysis with high spatial resolution
92-095	T. Masujima School of Medicine, Hiroshima Univ.	Fundamental development of X-ray photoacoustic spectroscopy
92-096	J. G. Thompson Research School of Chemistry, ANU	A Re-refinement of commensurately modulated $\alpha$ - $\text{UO}_3$ -related $\text{Ta}_{22}\text{W}_4\text{O}_{67}$
92-097	E. N. Maslen Crystallography Center, Univ. of Western Australia	High precision imaging of the electron density with synchrotron radiation
92-099	K. Ohno National Research Institute for Metals	Precise determination of g-g' lattice constant, their coherency and thermal strain in Ni-base superalloys by SR parallel-beam diffractometry
92-100	K. Tsukimura Geological Survey of Japan	Determination of cation distribution in $(\text{Co}, \text{Ni}, \text{Zn})_2\text{SiO}_4$
92-101	A. Nukui National Institute for Research in Inorganic Materials	Radial distribution function analysis employing anomalous scattering of functional oxide glass
92-102	K. Tsuji Faculty of Science and Technology, Keio Univ.	Phase transitions from crystal to amorphous states in III-V and II-VI compounds under low temperature and high pressure
92-103	Y. Soejima Faculty of Science, Kyushu Univ.	Study of partial Patterson using X-ray anomalous dispersion
92-104	E. Hashimoto Faculty of Science, Hiroshima Univ.	Formation mechanism of crystalline defects
92-105	M. Ushio Faculty of Engineering, Gunma Univ.	Structure analyses of the flux melts and the aqueous solutions for the crystal growth
92-106	K. Tashiro Faculty of Science, Osaka Univ.	Synchrotron X-ray study on crystallization kinetics of polyethylene blends
92-107	T. Yamanaka College of General Education, Osaka Univ.	In situ observation of the pressure-induced amorphization of hydrate-crystals and minerals under high pressure and temperature
92-108	H. Okabayashi Nagoya Institute of Technology	Secondary structure studies of N-acyl glycine and L-glutamic acid oligopeptides in solid states and aqueous solutions
92-109	S. Sasaki Research Lab. of Engineering Materials, Tokyo Institute of Technology	Structure of $\text{C}_{60}$ crystals and the cluster at low temperatures

Proposal Number	Spokesperson	Title
92-110	H. Ohigashi Faculty of Engineering, Yamagata Univ.	Studies of chain motions in the paraelectric phase in ferroelectric polymer crystals
92-111	K. Ishida Faculty of Science and Technology, The Science Univ. of Tokyo	Structure analysis of high-T <sub>c</sub> superconductors using X-ray anomalous dispersion effect
92-113	T. Nakajima Photon Factory, KEK	Study of the phase transitions at the milli-kelvin region by means of SR X-ray diffraction
92-114	K. Sakaue School of Science, Kwansei Gakuin Univ.	Structural study on In <sub>x</sub> Ga <sub>1-x</sub> As/GaAs hetero-interfaces
92-115	J. Yoshimura Faculty of Engineering, Yamanashi Univ.	Study of nonprojectiveness of X-ray Moiré-Fringe patterns
92-116	H. Tsuruta SSRL, Stanford Univ.	Stopped-flow X-ray scattering studies of allosteric transition of aspartate transcarbamylase by means of the imaging plate streak camera
92-117	Y. Masumoto Institute of Physics, Univ. of Tsukuba	Small angle X-ray scattering of CdSSe and CuInS <sub>2</sub> microcrystals
92-118	S. Kondo Faculty of Engineering, Nagasaki Univ.	XSAS study on Cu-Co-X (X=Cr, Fe) alloy
92-119	H. Konishi Japan Atomic Energy Research Institute	Structural aspects and anomalous solid state properties of metallic superlattices
92-120	H. Suematsu Faculty of Science, Univ. of Tokyo	Phase transitions of adsorbed monolayers
92-121	Y. Waseda Institute for Advanced Materials Processing, Tohoku Univ.	Determination of the environmental structure around a specific atom in disordered materials by the anomalous X-ray scattering
92-124	T. Makita Japan Atomic Energy Research Institute	Stress-induced martensitic transformations in AuCuZn <sub>2</sub> and AuZn alloys
92-125	H. Ohno Japan Atomic Energy Research Institute	X-ray diffraction analysis of molten silver halides under high pressure
92-126	K. Tsuji Faculty of Science and Technology, Keio Univ.	Structure of liquid bismuth and liquid tellurium under pressure
92-127	K. Tsuji Faculty of Science and Technology, Keio Univ.	Density of liquid selenium and tellurium under pressure

Proposal Number	Spokesperson	Title
92-128	Y. Fukai Faculty of Science and Technology Chuo Univ.	Phase diagram of V, Ti alloy-H systems
92-129	W. Utsumi Institute for Solid State Physics, Univ. of Tokyo	Phase relation of graphite, hexagonal-diamond, and cubic-diamond under high pressure and high temperature condition
92-130	S. Kishimoto Photon Factory, KEK	Development and performance test of X-ray detectors with subnanosecond time resolution
92-131	K. Kawamura Faculty of Science, Hokkaido Univ.	Pressure induced structure change of potassium silicate liquids
92-132	T. Matsuda Physics Department, KEK	Tests of radiation hardness of double sided silicon detector
92-133	H. Kobayashi Photon Factory, KEK	Generation of synchrotron radiation and slow positron with linac beam
92-134	I. Sato Photon Factory, KEK	Vibration issues on linac beam characteristics
92-135	H. Nozoye National Chemical Laboratory for Industry	Angle-resolved photoemission spectroscopy study on hydrogen adsorbed aluminum surface
92-136	H. Daimon Faculty of Engineering Science, Osaka Univ.	Photoelectron holography
92-137	S. Suga Faculty of Engineering Science, Osaka Univ.	PES and MCD of Cu <sub>2</sub> Sb type TM compounds and RE pnictides
92-138	S. Masude College of Arts and Sciences, Univ. of Tokyo	Photoemission study of the rare earth cobaltates
92-139	M. Yanagihara Research Inst. for Scientific Measurement, Tohoku Univ.	Study of the relaxation of the excited states by measuring polarization of the resonance soft X-ray fluorescence
92-140	Y. Sakisaka Faculty of Science, Hirosaki Univ.	Angle-resolved photoemission from TiO <sub>2</sub> and Cr <sub>2</sub> O <sub>3</sub> single-crystals
92-141	A. Fujimori Faculty of Science, Univ. of Tokyo	X-ray absorption and resonant XPS study of NiS and its substituted compounds
92-142	N. Kosugi Faculty of Science, Kyoto Univ.	Angle distribution of the fragment ions after the inner-shell excitation of triatomic molecules

Proposal Number	Spokesperson	Title
92-143	S. Nakai Faculty of Engineering, Utsunomiya Univ.	Resonant photoemission in 3d transition-metal oxides
92-144	A. Yagishita Photon Factory, KEK	Soft X-ray spectroscopy of free metal atoms
92-145	H. Maezawa Photon Factory, KEK	3d-4f resonance photoemission study of rare earth compounds
92-146	T. Hanyu Faculty of Science, Tokyo Metropolitan Univ.	3d XPS of rare earth superlattices
92-147	N. Kosugi Faculty of Engineering, Kyoto Univ.	Inner-valence ionization and resonance Auger spectra of oxygen-containing linear molecules
92-148	E. Shigemasa Photon Factory, KEK	Angle-resolved photoion spectroscopy of H <sup>+</sup> after the inner-shell excitation of hydrogen halide molecules
92-149	A. Misu Faculty of Science, Science Univ. of Tokyo	Magnetic circular dichroism of rare earth iron garnet
92-150	K. Tanaka Photon Factory, KEK	Ion desorption from simple molecules/Si(100) by core-electron excitation
92-151	H. Fukutani Institute of Physics, Univ. of Tsukuba	Photoabsorption and photoemission of size-selected transition metal cluster
92-152	H. Fukutani Institute of Physics Univ. of Tokyo	Angle resolved photoemission study on the adsorbate induced surface reconstruction of transition metals
92-153	K. Tanaka Photon Factory, KEK	Mass spectrometric study on fundamental process of photochemical etching
92-154	Y. Iguchi Univ. of East Asia	p.A scattering of soft X-ray polycrystalline beryllium
92-155	Y. Sakisaka Faculty of Science, Hirosaki Univ.	Angle-resolved photoemission study of surface states on Cr (100)
92-156	Y. Hatano Faculty of Science, Tokyo Institute of Technology	Florescence measurements from electron-correlation dominated excited states of simple molecules
92-157	Y. Hatano Faculty of Science, Tokyo Institute of Technology	Photodissociation of superexcited hydrogen molecules as studied by using the single-bunched pulse structure of Photon Factory SR

Proposal Number	Spokesperson	Title
92-158	Y. Morioka Institute of Physics, Univ. of Tsukuba	The study of photoelectron spectrum using single bunch photon
92-159	Y. Morioka Institute of Physics Univ. of Tsukuba	The study of photoelectron spectra of molecular clusters
92-160	O. Aita College of Engineering, Univ. of Osaka Prefecture	High resolution photoemission study of $\text{Ba}_{1-x}\text{K}_x\text{BiO}_3$ ( $0 \leq x \leq 0.5$ )
92-161	T. Miyahara Photon Factory, KEK	Studies on magnetic circular dichroism of Dy, Tb and Eu thin films and $\text{Ni}_x\text{Cu}_{1-x}$ and $\text{Ni}_x\text{Pd}_{1-x}$ alloys
92-162	I. Takahashi School of Engineering, Nagoya Univ.	Characterization of MBE grown (Ca, Sr) $\text{F}_2$ on Si(111) surface by CTR scattering
92-163	O. Sakata Research Lab. of Engineering Materials, Tokyo Institute of Technology	Development of grazing-incidence X-ray standing wave method
92-164	H. Hashizume Research Lab. of Engineering Materials, Tokyo Institute of Technology	Structure of insulating fluoride epilayers grown s-treated GaAs substrates
92-165	S. Aibara Research Institute for Food Science, Kyoto Univ.	X-ray crystallography of protein crystals prepared under the microgravity environment
92-G166	K. Kawamura Faculty of Science, Hokkaido Univ.	EXAFS study of chromium ion in alkalisilicate glasses
92-G167	M. Ichikawa Catalysis Research Center, Hokkaido Univ.	EXAFS study of thermal- and photo-activation process of Rh-V clusters in homogeneous and heterogeneous system
92-G168	M. Ichikawa Catalysis Research Center, Hokkaido Univ.	EXAFS characterization of Pt, Rh clusters entrapped in AIP04-5 and 37 zeolite
92-G169	M. Matsuura Miyagi National College of Technology	XAFS studies on the abnormal lattice change of $\text{CeNi}_2$ laves phase due to small Fe addition
92-G170	T. Miyanaga Faculty of Science, Hirosaki Univ.	Local structure and its temperature dependence of lanthanoid (III) complexes by EXAFS
92-G171	M. Sakurai Institute for Materials Research, Tohoku Univ.	EXAFS study about effects of small additives on the ductilization of $\text{Ni}_3\text{Al}$ compound
92-G172	H. Yamaguchi Electrotechnical Laboratory	X-ray absorption study of oxide superconductors

Proposal Number	Spokesperson	Title
92-G173	Y. Abe Faculty of Science and Technology, Science Univ. of Tokyo	Investigation on the structure of polyzirconoxanes in a liquid and solid state
92-G174	Y. Iwasawa Faculty of Science, Univ. of Tokyo	In-situ asymmetric structure determination of metal particles on single crystal surfaces by polarized total-reflection fluorescence EXAFS spectroscopy
92-G175	Y. Iwasawa Faculty of Science, Univ. of Tokyo	Studies of dynamic change of support-surface structure during supported metal catalysis
92-G176	H. Yoshitake Faculty of Engineering, Yokohama National Univ.	Electronic state and structure transformation of fine particle alloy electrodes under electrolysis
92-G177	T. Hashimoto Research Lab. Engineering Materials, Tokyo Institute of Technology	Analysis of chemical state of Bi in ceramics by X-ray absorption
92-G178	T. Hashimoto Research Lab. Engineering Materials, Tokyo Institute of Technology	Study of Electronic Structure and Chemical State of 3d-transition metal oxide by XANES
92-G179	S. Funahashi Faculty of Science, Nagoya Univ.	Solvation structure of first-row transition metal ions in various nitriles
92-G180	M. Yamada Faculty of Engineering, Nagoya Institute of Technology	Structural change of La-Ni-Mg(Al) amorphous alloys by hydrogen absorption
92-G181	T. Murata Department of Physics, Kyoto Univ. of Education	Cl and Br K-XANES in AgCl-AgBr solid solutions
92-G182	I. Watanabe Faculty of Science, Osaka Univ.	Structure analysis of solution surface by photoelectron yield XAFS
92-G183	S. Yoshikawa Institute of Scientific and Industrial Res., Osaka Univ.	XAFS study on infinite-layer superconductor $\text{Sr}_{1-x}\text{La}_x\text{CuO}_2$
92-G184	H. Yamazaki Faculty of Science, Okayama Univ.	XANES study on <i>L</i> -absorption edges in ferromagnetic materials including Pt or rare-earth elements
92-G185	H. Maruyama Okayama Univ.	X-ray magnetic absorption study on spin and electronic states in ferromagnetic Fe oxides
92-G186	H. Maruyama Okayama Univ.	X-ray magnetic absorption study on spin and electronic states in Fe based ferromagnetic disordered alloys
92-G187	T. Yamaguchi Faculty of Science, Fukuoka Univ.	XAFS study of metal complexes formed with biologically active ligands

Proposal Number	Spokesperson	Title
92-G188	T. Yamaguchi Faculty of Science, Fukuoka Univ.	XAFS study of lanthanide aminopolycarboxylates in solution
92-G189	J. Kawai Institute of Physical and Chemical Research	Photoelectron and X-ray absorption spectral measurements under total reflection X-ray conditions
92-G190	Y. Inoue Institute of Physical and Chemical Research	Fluorescence XAFS study on structure and function of the Mn-cluster involved in photosynthetic oxygen evolution
92-G191	T. Iizuka Institute of Physical and Chemical Research	Fluorescence XAFS study on local structure of respiratory metalloproteins
92-G192	M. Tsunoda Dept. of Chemistry, Univ. Fed. Sao Carlos	Investigation of the reversible disulfide bridge rearrangement in $\text{Cp}^*_2\text{Fe}_2(\mu\text{-}\eta^1\text{-S}_2)(\mu\text{-}\eta^2\text{-S}_2)$ by solution-state EXAFS
92-G193	R. Ryoo Dept. of Chemistry, Korea Advanced Inst. of Sci. and Thech.	Catalytic activity of Ru cluster in zeolite supercharge as a function of the cluster size
92-G194	J. S. Lee Dept. of Chemical Engineering, Pohang Institute of Science and Technology	Structure characterization of supported $\text{Mo}_2\text{C-Pt}$ bimetallic catalysts
92-G195	M. Breyse CNRS	XAFS characterization of sulfide catalysts - Comparison between unsupported and supported states of new active phase -
92-G196	J. H. Choy Dept. of Chemistry, Seoul National Univ.	Studies on the average valence states and the short range order for Ce and Nb(Ta) in the perovskite lattice
92-G197	K. Hikichi Faculty of Science, Hokkaido Univ.	X-ray crystal structure analysis of ACC deaminase
92-G198	N. Matsushima Sappori Medical College	X-ray solution scattering study of storage proteins from wheat, barley and maize
92-G199	N. Niimura Faculty of Science, Tohoku Univ.	Interdigital structure and membrane function of phosphatidyl inositol diphosphate
92-G200	N. Niimura Faculty of Science, Tohoku Univ.	Solution scattering study of bacterial histone-like protein HU and DNA complex
92-G201	Y. Izumi Faculty of Engineering, Yamagata Univ.	Solution structure of calmodulin with heavy-atom markers
92-G202	S. Adachi Photon Factory, KEK	Data collection of a high resolution (1.3Å) reference of myoglobin for time-resolved Laue study



Proposal Number	Spokesperson	Title
92-G203	S. Saigusa Photon Factory, KEK	Induction of chromosome aberrations and lethal effects by monochromatic X-rays
92-G204	Y. Sato National Food Research Institute	Structural characterization of oligosaccharide in small-angle X-ray solution scattering
92-G205	Y. Satow Faculty of Pharmaceutical Science, Univ. of Tokyo	Structure studies on affinity maturation of anti-nitrophenol antibody Fab fragments
92-G206	Y. Satow Faculty of Pharmaceutical Science, Univ. of Tokyo	Crystal and solution structures of organic TPEN iron complexes
92-G207	K. Takakura College of Liberal Arts, International Christian Univ.	Strand breaks in DNA induced by inner shell ionization of metals
92-G208	K. Konno Faculty of Science, Ochanomizu Univ.	Structural studies on aminoacyl-transfer RNA synthetases
92-G209	T. Hirai Faculty of Textile Science and Technology Shinshu Univ.	Dynamical Stretching process of electrostrictive polymer gel as artificial muscle
92-G210	I. Hatta School of Engineering, Nagoya Univ.	Electron density of phospholipid bilayers studies by a maximum entropy method
92-G211	Y. Muroga School of Engineering, Nagoya Univ.	The effect of charge density and solvent upon the conformation of helical poly (glutamic acid)
92-G212	Y. Hiragi Institute for Chemical Research, Kyoto Univ.	Mechanism and measurement of formation velocity of a chaperonin of a thermophilic bacterium
92-G213	H. Urakawa Faculty of Engineering and Design, Kyoto Institute of Technology	Lectin/legand agglutination observed by time-resolved SAXS
92-G214	Y. Shirakihara Hyogo Univ. of Education	X-ray crystal analysis of F1-ATPase from a thermophilic bacterium
92-G215	Y. Shirakihara Hyogo Univ. of Education	X-ray crystal analysis of rat DNA polymerase $\beta$ and E. coli phoB protein
92-G216	T. Sano Faculty of Science, Hiroshima Univ.	Kinetic studies on the complex formation of calmodulin by the stopped-flow X-ray scattering method
92-G217	Y. Morimoto Faculty of Engineering, Tokushima Univ.	Evaluation of biological macromolecular crystals obtained in micro gravity
92-G218	Y. Sugawara Institute of Physical and Chemical Research	Crystal structure analysis of <i>Aleuria aurantia</i> lectin

Proposal Number	Spokesperson	Title
92-G219	M. Yamamoto Institute of Physical and Chemical Research	Crystal structure analysis of metalloproteinase
92-G220	J. H. Varghese Biomolecular Research Institute	Three dimensional structure of influenza neuraminidase-antibody complexes
92G-221	M. C. Lawrence Biomolecular Research Institute	Three dimensional structure of sialic acid aldolase antibody complexes
92-G222	J. N. Varghese Biomolecular Research Institute	3-dimensional structure of cytokines leukemia inhibitory factor (LIF) and interleukin-6 (IL-6) cytokines and their receptors
92-G223	G. Y. Lu Department of Biology, Peking Univ.	The collection of diffraction data of autolyzed active products of trypsin, bar-headed goose hemoglobin and antibacterial polypeptide LC <sub>1</sub>
92-G224	A. Mondragon Department of Biochemistry, Northwestern Univ.	Structural studies of E. coli DNA topoisomerase I.
92-G225	Z. Lin Institute of Biophysics, Academia Sinica	Structure analysis of <i>P. versicolor</i> D-glyceraldehyde-3-phosphate dehydrogenase at high resolution
92-G226	Q. Huang Institute of Physical Chemistry, Peking Univ.	X-ray crystallographic studies of ribosome-inactive-proteins
92-G227	M. Guss Department of Inorganic Chemistry, Univ. of Sydney	Protein structure determination: Copper-containing amine oxidase and ATPase complexes
92-G228	D. I. Stuart Univ. of Oxford	Protein crystallography of RAT CD2, HIV RT and AHSV VP7
92-G229	R. J. Read Dept. of Med. Micro and Infect. Diseases, Univ. of Alberta	X-ray data collection on pertussis toxin
92-G230	K. Nagai MRC laboratory of Molecular Biology	Crystallographic studies of the pre-mRNA splicing machinery
92-G231	W. G. J. Hol Dept. of Chemistry, Univ. of Groningen	The crystal structure determination of molluscan hemocyanins, pxruvate dehydrogenase multienzyme complex, trypanosomal enzymes, engineered vaccines, quinoproteins
92-G232	H. K. Schachman Dept. of Molecular & Cell Biology, Univ. of California at Berkeley	Kinetics of subunit assembly and conformational changes of aspartate transcarbamylase (ATCase) by stopped-flow X-ray scattering
92-G233	T. Hondoh Institute of Low Temperature, Hokkaido Univ.	Development of new methods using X-ray scattering for crystallographic analysis of polar ice cores
92-G234	A. Goto Faculty of Engineering, Hokkaido Univ.	Characterization of the surface of ice I <sub>h</sub> by crystal truncation rod technique

Proposal Number	Spokesperson	Title
92-G235	I. Shirotani Faculty of Engineering, Muroran Institute of Technology	Phase transition of ZrRuP at high temperatures and pressures
92-G236	Y. Kudo Faculty of Science, Tohoku Univ.	Effect of pressure on the crystal structure of superhydrous phase B
92-G237	T. Kato Faculty of Science, Tohoku Univ.	Determination of $\alpha$ - $\beta$ transition boundary in divine by high-pressure X-ray diffraction method
92-G238	E. Ohtani Faculty of Science, Tohoku Univ.	Determination of the equation of state and the phase boundaries by using the multianvil press
92-G239	O. Terasaki Faculty of Science, Tohoku Univ.	Structures of low-dimensional alkalimetals and metalsulfides, which are incorporated in the spaces of zeolitics, and the effect of quantum confinement
92-G240	M. Nomura Photon Factory, KEK	Characterization of parallel plate ionization chambers
92-G241	A. Iida Photon Factory, KEK	Characterization of liquid crystal structure using X-ray microprobe
92-G242	H. Kawta Photon Factory, KEK	Magnetic Compton scattering and magnetic XAFS under standing wave field
92-G243	H. Hirayama Radiation & Safety Control Center, KEK	Experiments on energy deposition of X-rays to matter
92-G244	M. Ando Photon Factory, KEK	Development of X-ray optics for a coronary angiography system
92-G245	Y. Itai Institute of Clinical Medicine, Univ. of Tsukuba	Coronary arteriography with synchrotron radiation
92-G246	Y. Masumoto Institute of Physics, Univ. of Tsukuba	Small angle X-ray scattering of CuCl and CuBr microcrystals
92-G247	M. Wakatsuki Institute of Materials Science, Univ. of Tsukuba	Analysis of impurity distribution in diamond by X-ray fluorescence methods
92-G248	T. Takeda Institute of Clinical Medicine, Univ. of Tsukuba	Synchrotron radiation computed tomography to detect the tracer material for biomedical purpose
92-G249	O. Shimomura National Institute for Research in Inorganic Materials	EXAFS study of amorphous Ge under pressure

Proposal Number	Spokesperson	Title
92-G250	K. Yaoita National Institute for Research in Inorganic Materials	Abrupt structural changes of liquids under pressure
92-G251	H. Horiuchi Faculty of Science, Univ. of Tokyo	Studies on crystal structures of REAlO <sub>3</sub> (RE=La, Ce, Pr and Nd)
92-G252	A. Koma Faculty of Science, Univ. of Tokyo	Structure analysis of van der Waals hetero interfaces by surface X-ray diffraction
92-G253	S. Orito Faculty of Science, Univ. of Tokyo	Search for weakly-interacting neutral bosons
92-G254	S. Nanao Institute of Industrial Science, Univ. of Tokyo	Spin-dependent absorption in Re-Tm amorphous thin films
92-G255	T. Takahashi Institute for Solid State Physics, Univ. of Tokyo	Characterization of interfaces of epitaxially grown Si/Ge system by X-ray CTR scattering
92-G256	S. Hayakawa Faculty of Engineering, Univ. of Tokyo	Trace element quantification in a small area using X-ray fluorescence analysis
92-G257	N. Hamaya Faculty of Science, Ochanomizu Univ.	Ultra-small-angle X-ray scattering study of colloidal crystals
92-G259	N. Hamaya Faculty of Science, Ochanomizu Univ.	Crystal structure of rare-earth metal under pressure : La, Pr, Nd
92-G260	O. Nittono Faculty of Engineering, Tokyo Institute of Technology	Crystallinity and light emission of PS layers studied by means of X-ray multi-crystal diffractometry using plane waves
92-G261	H. Hashizume Research Lab. of Engineering Materials, Tokyo Institute of Technology	Characterization of microstructure in CaSrF <sub>2</sub> and HgCdTe epilayers by high-resolution X-ray diffraction and spectroscopy
92-G262	S. Sasaki Research Lab. of Engineering Materials, Tokyo Institute of Technology	Development of the high-resolution powder diffraction method by using a collimating X-ray mirror
92-G263	S. Sasaki Research Lab. of Engineering Materials, Tokyo Institute of Technology	Structure of a noncubic garnet Ca <sub>3</sub> (Cr, Fe) <sub>2</sub> Si <sub>3</sub> O <sub>12</sub>
92-G264	H. Suzuki Tokyo Engineering Univ.	Observations on phase separation and lattice defects in solid mixtures <sup>3</sup> He- <sup>4</sup> He
92-G265	T. Mizoguchi Faculty of Science, Gakushuin Univ.	Structure relaxation of non equilibrium magnetic alloys prepared by mechanical alloying

Proposal Number	Spokesperson	Title
92-G266	K. Hasegawa College of Engineering, Hosei Univ.	Test of integrating type 1D position-sensitive detectors
92-G267	M. Takahashi Faculty of Textile Science and Technology, Shinshu Univ.	Crystallization of low molecular weigh PEO in melts and blends
92-G268	F. Itoh Faculty of Engineering, Gunma Univ.	X-ray magnetic absorption and magnetic compton scattering on some actinede compounds
92-G269	F. Itoh Faculty of Engineering, Gunma Univ.	Magnetic absorption and magnetic Compton scattering on metallic artificial multilayers
92-G270	I. Hatta School of Engineering, Nagoya Univ.	Study on phosholipid monolayer-ion systems by grazing-incidence X-ray diffraction
92-G271	M. Yamada Faculty of Engineering, Nagoya Institute of Technology	X-ray structure analysis of Nb-Ni-Al and Zr-Ni-Al amorphous alloys
92-G272	S. Ito Radioisotope Research Center, Kyoto Univ.	Electron-avalanche mechanism of the PSPC for high-energy X-rays studied in the region of the limited proportionality
92-G273	K. Kajiwara Faculty of Engineering and Design, Kyoto Institute of Technology	Dynamic observation of the internal structure of microgels during its formation
92-G274	T. Yamanaka College of General Education Osaka Univ.	The influence of $^{13}\text{C}$ isotope on the structure of diamond
92-G275	S. Endo Research Center for Extreme Materials, Osaka Univ.	Determination of the phase boundaries of $\text{SnO}_2$ and $\text{HfO}_2$ under high pressure and temperature
92-G276	H. Kawamura Faculty of Engineering, Himeji Institute of Technology	Orientational ordering in Solid $\text{C}_{70}$ under high pressure
92-G277	N. Sakai Faculty of Science, Himeji Institute of Technology	Study on magnetic materials with magnetic Compton profiles
92-G278	A. Koizumi Faculty of Engineering, Himeji Institute of Technology	Application of pulsed high magnetic field to X-ray magnetic scattering absorption
92-G279	T. Kato National Institute of Radiological Science	Diagnosis of pancreatic cancer by synchrotron radiation imaging
92-G280	H. Konishi Japan Atomic Energy Research Institute	Crystal structure analysis of uranium oxides under high pressure

Proposal Number	Spokesperson	Title
92-G281	H. Ohno Japan Atomic Energy Research Institute	EXAFS of amorphous uranium oxides
92-G282	H. Macta Japan Atomic Energy Research Institute	Diffuse scattering study on growth of vacancy clusters in quenched copper
92-G283	Y. Tanaka Institute of Physical and Chemical Research	Magnetic Compton scattering experiment using high energy X-ray (> 130 keV)
92-G284	S. Shimomura Institute of Physical and Chemical Research	Pressure induced phase transition in orthorhombic C <sub>60</sub>
92-G285	Z. H. Mai Institute of Physics, Chinese Academy of Science	Study on the structural perfection of III-V compound semiconductor superlattices
92-G286	H. S. Kim Dept. of Mat. Sci. and Met. Eng., Sunchen National Univ.	X-ray topographic studies of dislocation free zone and dislocation motions in the crack tips of Si and Mo
92-G287	T. J. White RCAMMP, Univ. of Western Australia	Determination of rare earth element partitioning in synthetic zirconite
92-G289	A. P. Jones Department of Geological Sci., Univ. College London	Carbonate melt viscosity at high pressure and temperature
92-G290	A. van Rissen Dept. of Applied Physics, Curtin Univ.	Depth profiling of zirconia-toughened alumina using multi-wavelength X-ray diffraction data
92-G291	D. P. Siddons NSLS, BNL	Mossbauer studies of amorphous magnetic system using polarization-suppression of non-resonant photons
92-G292	S. Kono Res. Inst. for Scientific Measurement, Tohoku Univ.	Core-level-photoemission of clean and Na-adsorbed single-domain Si (001) surfaces at low temperatures
92-G293	N. Miyamoto Res. Inst. of Electrical Communication, Tohoku Univ.	Growth kinetics of Si epitaxial film using synchrotron-radiation assisted CVD
92-G294	S. Nakai Faculty of Engineering, Utsunomiya Univ.	The experimental study of satellite structure in rare-earth 3d XPS spectra
92-G295	Y. Kitajima Photon Factory, KEK	Characterization of YB <sub>66</sub> single crystal as a monochromator for 1-2 keV
92-G297	Y. Takata Photon Factory, KEK	Adsorption of thiophene and thiophenol molecules on Ni (100) studied by C K-edge XANES and XPS
92-G298	S. Kikuta Faculty of Engineering, Univ. of Tokyo	Analysis of metal-silicon surface and interface by X-ray diffraction

Proposal Number	Spokesperson	Title
92-G299	H. Namba Research Center for Spectrochemistry, Univ. of Tokyo	Photodecomposition of semiconductor-alkyls on Si single crystal
92-G300	Y. Tezuka Institute for Solid State Physics, Univ. of Tokyo	Angle resolved photoemission spectroscopy of rutile (TiO <sub>2</sub> )
92-G301	E. Miyazaki Faculty of Science, Tokyo Institute of Technology	Angle-resolved photoemission study of the electronic structure of TaC (111) single crystal surface
92-G302	T. Koizumi College of Science, Rikkyo Univ.	Photoionization of Ba <sup>+</sup> ions due to photoexcitation of 4d-shell electron
92-G303	H. Daimon Faculty of Engineering Science, Osaka Univ.	Angle-resolved photoelectron spectroscopy on Si (111) 3x1-Na
92-G304	K. Nakagawa Kobe Univ.	Color center formation quantum yield in anthracene crystal as a function of incident photon energy
92-G305	J. Kawai Institute of Physical and Chemical Research	Threshold excitation resonance X-ray emission spectroscopy of boron, carbon and nitrogen compounds
92-G306	S. J. Oh Dept. of Physics, Seoul National Univ.	High resolution and resonance photoemission study of rare-earth metal overlayers on compound semiconductors.
92-G307	C. Y. Park Dept. of Physics, Sung-Kyun-Kwan Univ.	Angle resolved photoelectron spectroscopy for Mg-adsorbed Si (111) surface
92-G308	S. J. Oh Dept. of Physics, Seoul National Univ.	Photoelectron diffraction study of oxygen chemisorption on compound semiconductor surfaces
92-G309	H. Tagawa Nihon Univ.	Dynamical SR-SAXS investigations on micro-phase segregated structures of segmented polyurethanes
92-G310	H. Tagawa Nihon Univ.	Conformational analysis of polyaminoacid block copolymers
92-G311	T. Kikegawa Photon Factory, KEK	Search for post simple cubic high pressure phase of arsenic
92-G312	T. Kikegawa Photon Factory, KEK	EXAFS study of Na <sub>2</sub> O-Ga <sub>2</sub> O <sub>3</sub> -SiO <sub>2</sub> glass under high pressure
92-G313	T. Kikegawa Photon Factory, KEK	Crystal structure analysis of high pressure phase of bismuth
92-G314	S. H. Kim Univ. of California	X-ray crystallographic studies on mutants of the aspartate receptor protein

Proposal Number	Spokesperson	Title
92-P001	A. Morikawa Faculty of Engineering, Tokyo Institute of Technology	Investigation of photo-induced structure change of Rh(I) complex supported on porous vycor glass
92-P002	T. Matsui School of Engineering, Nagoya Univ.	EXAFS study on local structure of CaF <sub>2</sub> -type compounds
92-P003	T. Okano Univ. of Tokyo	Crystal structure analysis of native polysaccharide crystals
92-P005	N. Yamada Univ. of Electro-Communications	Oxygen K absorption spectroscopy of Y <sub>1-x</sub> Pr <sub>x</sub> Ba <sub>2</sub> Cu <sub>4</sub> O <sub>8</sub>
92-Y001	T. Kobayashi Central Research Institute, Mitsui Toatsu Chemicals, Inc.	XAFS studies of Cds microcrystallites-doped polymers
92-Y002	Y. Goto Fundamental Research Lab., NEC Corp.	X-ray optics, X-ray lithography and photo-chemical reaction experiments
92-Y003	Y. Ishii Interdisciplinary Research Laboratory, NTT	Materials analysis, lithography and photo-reaction using SR
92-Y004	M. Ohtsuki Fujitsu Laboratories Ltd.	Exposure tests by synchrotron radiation in BL-17A, BL-17B, and BL-17C
92-Y005	K. Yoshida Central Research Lab., Mitsubishi Chemical Industries Ltd.	The structural analysis of Co-Ru catalysts by XAFS
92-Y006	M. Miyao Center Research Laboratory, Hitachi Ltd.	BL-8A; Soft X-ray diffractometry, XPS. B; Silicon EXAFS experiments, total reflection measurement. C; Digital radiography, lithography, microprobe experiments, CT, and micro X-ray diffractometry
92-Y007	T. Yamamoto Central Research Lab., Idemitsu Kosan Co., Ltd.	EXAFS studies on catalyst for olefin polymerization
92-Y008	T. Yamamoto Central Research Lab., Idemitsu Kosan Co., Ltd.	EXAFS studies of supported platinum catalysts
92-Y009	T. Kobayashi Center research Institute, Mitsui Toatsu Chemicals Inc.	XAFS analysis of modified metallic copper catalysts (2)
92-Y010	M. Aoki Fuji Photo Film Co., Ltd.	XAFS study on structure of Cu complexes in solution and solid
92-Y011	M. Miyao Center Research Laboratory, Hitachi Ltd.	BL-8A; Soft X-ray diffractometry, XPS. B; Silicon EXAFS experiments, total reflection measurement. C; Digital radiography, lithography, microprobe experiments, CT, and micro X-ray diffractometry



Proposal Number	Spokesperson	Title
92-Y012	Y. Goto Fundamental Research Lab., NEC Corp.	X-ray optics, X-ray lithography and photo-chemical reaction experiments
92-Y013	M. Ohtsuki Fujitsu Laboratories Ltd.	Exposure tests by synchrotron radiation in BL-17A, BL-17B, and BL-17C
92-Y014	T. Onoda Central Research Lab., Mitsubishi Chemical Industries Ltd.	The structural analysis of Co-Ru catalysts by XAFS
92-Y015	S. Oda Fuji Photo Film Co., Ltd.	XAFS study on structure of metal complexes in solution
92-Y016	S. Sasaki Japan Tobacco Inc.	X-ray crystallographic studies on leukotriene producing enzymes
92-C001	K. Akimoto Fundamental Research Lab., NEC Corp.	Characterization of semiconductor materials by high precision X-ray goniometer system
92-C002	Y. Ohishi Tsukuba Research Laboratory, Sumitomo Chemical Co., Ltd.	Small angle X-ray scattering study for dynamical structural change of polymers
92-C003	S. Suzuki Tsukuba Research Center, Sanyo Electric Co., Ltd.	Microfabrication technique using synchrotron radiation
92-C004	Y. Takagi Nippon Steel Corp.	Dynamic observation of materials processing using synchrotron radiation
92-C005	S. Kawado Research Center, Sony Corp.	Characterization of Si crystals and process-related materials
92-C006	K. Hayashi Nippon Steel Corp.	Quantitative materials evaluation by monochromatic X-ray CT using synchrotron radiation
92-C007	T. Arikado ULSI Research Center, Toshiba Corp.	Metal film deposition by SOR light irradiation
92-C008	A. Aoki Technical research Center, NKK Corp.	Structure analysis of materials bombarded with particle beams
92-C009	H. Nagata Nikon Corp.	Reflectivity measurement of Mo/Si multilayers
92-C010	Y. Yoshinaga Technical Research Center, NKK Corp.	Design study on the advanced SR beamline
92-C011	S. Nakagawa Sumitomo Heavy Industries Ltd.	Developments of in-vacuum damping wigglers

Proposal Number	Spokesperson	Title
92-C012	H. Hoshino Development Center, Konika Corp.	Study on structure of photographic silver halide microcrystals using high resolution X-ray powder diffraction
92-C013	Y. Himeno Power Reactor and Nuclear, Fel Development Corp.	The basic study of the development for high intensity CW electron liner accelerator
92-C014	Y. Fukuda Cannon Inc.	Reflectivity measurements of Mo-Si multilayer mirrors
92-C015	N. Ishikawa Petroleum Energy Center	EXAFS study on hydrodesulfurization catalysts for ultra low sulfur distillate
92-C016	S. Suzuki Nuclear Power Division, Shimizu Corp.	Study on the effect of the building distortion to the beam orbit
92-C017	H. Yamada Sumitomo Heavy Industries Ltd.	Study for the development of ultra high brightness insertion device
92-C018	H. Hashimoto Toray Research Center	Study of REFAXFS using a dispersive X-ray absorption spectrometer
92-C019	M. Matsumoto Mechanical Research Lab., Hitachi Ltd.	Reduction of photodesorption with surface conditions of Practical materials
92-C020	M. Jinno Shimazu Corp.	Characterization of high spatial resolution soft X-ray recording material and its application by using radiation

G : General

P : Preliminary

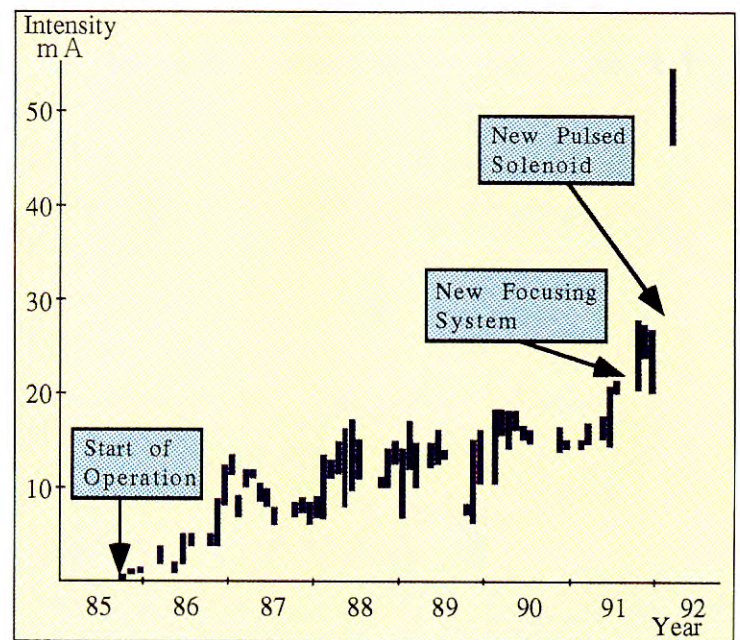
Y : Approved for charged beam time.

C : Collaborations between the Photon Factory and institutes of private companies.

# Injector Linac



*New pulsed solenoid*



*Positron-beam intensity vs. year*

*Improvements in the focusing system of the positron generator were started in 1990 and were completed this year. The positron beam was increased as expected.*

You can jump to the article by clicking its title.

## CONTENTS

	Page
<b>A. INTRODUCTION</b>	L – 1
<b>B. OPERATION</b>	L – 1
<b>C. PROGRESS AND IMPROVEMENTS</b>	
1. POSITRON BEAM IMPROVEMENTS DUE TO THE USE OF A NEW PULSED SOLENOID	L – 2
2. CONTROL SYSTEM REJUVENATION	L – 4
3. OPERATOR'S CONSOLE SYSTEM	L – 4
<b>D. RESEARCH</b>	
1. TEST LINAC	L – 5
2. SLOW-POSITRON SOURCE	L – 6
<b>E. R&amp;D REGARDING B-FACTORY</b>	
1. NEW HIGH-CURRENT PRE-INJECTOR	L – 7
Outline of the New Pre-injector	
Beam Dynamics	
Focusing System	
Electron Gun	
Pulse Power Supply	
Prebuncher and Buncher	
RF System	
Vacuum System	
500-MeV Energy-Analyzing System	
Monitor	
Commissioning	
2. ENERGY UPGRADE	L – 17
High-Gradient Acceleration Test	
Modulator Upgrade	
High-peak Power Microwave	
3. BEAM POSITION MONITOR	L – 20

A. INTRODUCTION

Operation of the PF 2.5-GeV linac was satisfactorily performed during this period. Following the previous year, additional improvements have continued: (1) Improvements in the pulsed solenoid just downstream from the positron target as a final step in a positron reinforcement project started in 1990. (2) Preparation for the replacement of the control system which has been used for more than 10 years. (3) Improvements in the operator's console system using NetWare system. In addition to these improvements, research concerning (1) high-brightness beam generation at the test linac, and (2) production of slow positron beams using the PF 2.5-GeV linac, has also been performed.

Research and development for the KEK B-factory (a positron-electron collider with asymmetric rings), which is presently under consideration as a future project, have been carried out. The injection system (pre-injector) of the PF 2.5-GeV linac was extensively upgraded during the summer of 1992 so that intense beam acceleration can be investigated. This represents the first step toward upgrading the linac in order to meet the requirements of the KEK B-factory. It requires intense beams in order to achieve a practically short injection time. It is therefore important to understand how high-intensity electron beams, which will be used for positron production, can be accelerated up to several GeV in the linac. Studies concerning high-current beam acceleration as well as the instabilities of the beams will be performed using the upgraded linac.

Reinforcement of the electron-beam energy from 2.5 to 8.0 GeV is also an important factor of this project. If this large increase in the energy is possible, both 8-GeV electrons and 3.5-GeV positrons can be injected directly to asymmetric rings. High-power microwave sources, power-multiplying techniques, such as a traveling-wave resonant ring or a SLED (SLAC energy doubler), and high-gradient endurance of the accelerating structures presently used are key issues for the above-mentioned increased energy, and are being investigated.

Accurate beam tuning is important for high-current beam acceleration in order to avoid any

beam instability due to wakefields, and precise beam-position monitors which are indispensable for this purpose are under development. The results of these studies concerning the B-Factory during this period are described.

B. OPERATION

During the period from October, 1991, to September, 1992, the PF 2.5-GeV linac has been stably operated with a total operation time of 5,053 hours and an operation rate of 98.4%. The operation statistics for this period are given in Table 1. There were no severe failures which would take a comparatively long recovering time during this period.

In the Accumulator Ring(AR) of TRISTAN, only one bucket is filled with electrons; those accumulated in the other buckets become noise for experiments concerning the Mössbauer effect. The electron gun of the PF 2.5-GeV linac was replaced from the oxide type to the barium impregnated(BI) type (expecting a long lifetime) during the scheduled maintenance in November, 1991. Several weeks later, the signal-to-noise(S/N) ratio in the AR, which had been around of  $10^7$ , became worse by several orders of magnitude. The higher operation temperature at 1100°C for the BI cathode, compared with 850°C for the oxide cathode, may have been the cause of grid emission which would have caused the large noise. The electron gun was immediately replaced by the oxide cathode. In connection with an improvement of the injector, the electron gun with the BI cathode was again tried; the details are described later.

Table 1. Operation and failure time during this period.

	date	operation time (hrs)	failure time (hrs)	rate (%)
FY 1991	Sep. 30–Nov. 6	876	9.6	98.9
	Nov. 12–Dec. 25	1013	23.9	97.6
	Feb. 10–Mar. 26	1040	25.7	97.5
FY 1992	Apr. 2–May 2	716	10.6	98.5
	May 6–May 27	496	7.0	98.6
	June 2–July 10	912	3.3	99.6
total		5053	80.1	98.4

Table 2. Cumulative usage hours of klystrons during the past years.

Period	Total	Unused	Failed		Living		MTBF
	No.of tubes	No.of tubes	No.of tubes	Mean age (hours)	No.of tubes	Av.op.time (hours)	
up to 1985/7	79	2	28	3,600	49	6,200	13,400
up to 1986/7	91	3	39	4,400	49	7,400	13,100
up to 1987/7	106	4	52	4,400	50	9,600	13,600
up to 1988/7	120	2	67	4,500	51	11,400	13,500
up to 1989/7	140	5	82	6,400	53	12,400	14,400
up to 1990/7	158	6	98	8,500	54	11,200	14,700
up to 1991/7	176	14	107	10,100	55	11,100	15,800
up to 1992/7	191	24	113	10,800	54	13,400	17,100

Table 3. Averaged fault rate and averaged applied voltage to klystrons.

Period	Fault rate (/day.tube)	Applied voltage (kV)	Total operation (tube.days)
1985/8–1986/7	1.0	238	5,600
1986/8–1987/7	1.0	239	7,740
1987/8–1988/7	1.0	240	9,990
1988/8–1989/7	0.6	241	10,510
1989/8–1990/7	0.3	244	10,690
1990/8–1991/7	0.2	246	10,750
1991/8–1992/7	0.1	248	10,140

The operational data of klystrons are as follows: The cumulative usage hours and the averaged fault rate at the averaged applied anode voltage during the past years are given in Tables 2 and 3, respectively. The cumulative status of the klystrons (divided according to the cathode materials) is given in

Table 4. Due to higher averaged anode voltage, four standing-by klystrons have become available under 2.5-GeV operation. Klystrons with BI cathodes have been introduced into the PF 2.5-GeV linac since 1987, and replacement was completed by the end of July, 1991. A very low fault rate of the BI tubes at a comparatively higher anode voltage was also obtained.

## C. PROGRESS AND IMPROVEMENTS

### 1. Positron Beam Improvements due to the use of a New Pulsed Solenoid

The focusing system of the KEK positron generator linac was recently reconstructed in two steps. In the second stage the pulsed solenoid, located just downstream from the positron-production target,

Table 4. Cumulative status of klystrons up to July 1992 corresponding to the year of production. Unused tubes are those which have never been used in the klystron gallery. STB (standby) tubes are those which have been used in the gallery and can be used there again.

Year of production	Cathode	Total		Living			Failed			Cumulative operation (tube-hours)	MTBF (hours)
		No.of tubes	Unused tubes	No.of tubes	(STB $e^-$ )	(Working $e^+$ )	Av.op.time (hours)	No.of tubes	Causes (arcing window others)	Mean age (hours)	
1979	oxide	4	0	0	(0 0 0)	—	4	(2 1 1)	3,902	15,608	3,902
1980	oxide	20	0	1	(1 0 0)	3,657	19	(13 5 1)	9,050	175,606	9,242
1981	oxide	20	0	1	(1 0 0)	11,277	19	(11 2 6)	15,965	314,611	16,588
1982	oxide	9	0	1	(1 0 0)	2,120	8	(5 2 1)	10,054	82,549	10,317
1983	oxide	13	0	1	(1 0 0)	14,170	12	(6 2 4)	18,753	239,205	19,934
1984	oxide	13	1	0	(0 0 0)	—	12	(10 0 2)	9,950	119,401	9,950
1985	oxide	12	1	0	(0 0 0)	—	11	(7 0 4)	13,409	147,494	13,409
1986	oxide	15	0	1	(1 0 0)	11,568	14	(13 0 1)	3,524	60,910	4,351
1987	oxide	7	0	0	(0 0 0)	—	7	(5 1 1)	4,342	30,393	4,342
total		113	2	5	(5 0 0)	8,558	106	(72 13 21)	10,783	1,185,777	11,187
1987	BI	7	0	6	(0 6 0)	22,745	1	(0 1 0)	10,219	146,690	146,690
1988	BI	20	1	15	(2 10 3)	16,237	4	(0 3 1)	12,814	294,811	73,703
1989	BI	18	1	15	(0 13 2)	13,539	2	(0 1 1)	5,185	213,454	106,720
1990	BI	18	6	12	(0 10 2)	7,684	0	(0 0 0)	—	92,210	—
1991	BI	15	14	1	(0 1 0)	3,273	0	(0 0 0)	—	3,273	—
total		78	22	49	(2 40 7)	13,849	7	(0 5 2)	10,263	750,438	107,205
total		191	24	54	(7 40 7)	13,359	113	(72 18 23)	10,751	1,936,215	17,135

Table 5. Parameter changes of the pulsed solenoid.

	previous		present
Effective length $L$ (mm)	76	→	45
Field strength $B_i$ (T)	1.2	→	2.3
Inductance ( $\mu\text{H}$ )	10	→	4
Number of turns	16	→	8
Peak current (kA)	5	→	10
Peak Voltage (kV)	1	→	2

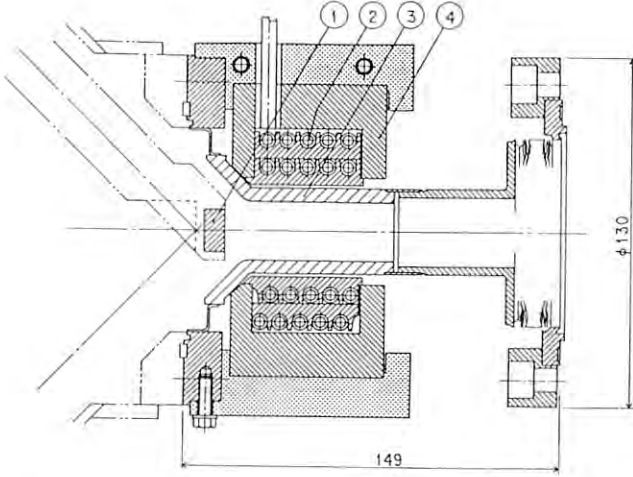


Fig. 1 New pulsed solenoid for strong positron-focusing: (1) a positron production target, (2) a pulsed solenoid, (3) a ceramic tube and (4) a ferrite yoke.

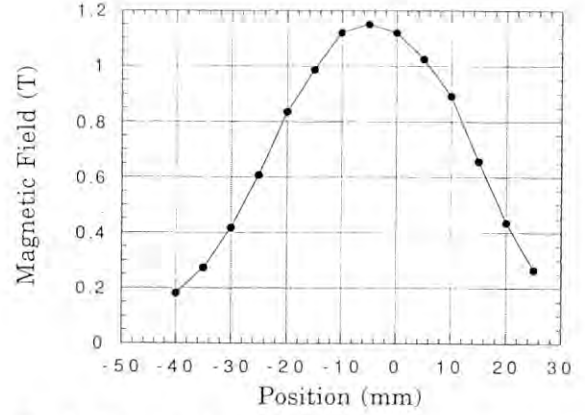


Fig. 2 Magnetic field distribution of the new pulsed solenoid.

Table 6. QWT parameters change due to the pulsed solenoid improvements.

	previous	present
Acceptance $U$ ( $\pi\text{MeV/c cm}$ )	0.15	→ 0.3
Matched beam on the radiator		
radius $x$ (cm)	0.12	→ 0.12
momentum $P$ (MeV/c)	8.7	→ 9.9
transverse momentum $p$ (MeV/c)	1.25	→ 2.4
Positron yield (relative value)		
solid angle $\delta\Omega$	1	→ 2.9
momentum acceptance $\delta P$	1	→ 0.59
Angular dependence $G(\theta_1)$	1	→ 0.84
specific yield $n/E$	1	→ 1.44

was improved. It is a quarter-wave-transformer (QWT)-type focusing solenoid. After the improvements, the positron beam was increased by a factor of 1.5, as was expected based on a general consideration.

Both the pulsed focusing solenoid and its power supply were renewed. The new power supply was installed in the summer of 1991; the pulsed solenoid was then replaced with a newly designed one in January, 1992. In order to avoid any problems, such as water leaking into the vacuum, the pulsed solenoid was required to be outside of the vacuum. Moreover, it was designed to make the field length shorter, since a general consideration suggested that a shorter range field is expected to make the solid angle wider and, as a result, to increase the positron yield.

The parameters of the pulsed solenoid were changed, as listed in Table 5. We decreased the number of windings by half in order to make the

pulsed solenoid shorter. This required an increase in the current.

Fig. 1 shows the structure of the new pulsed solenoid. It has 8 winding turns and a return-yoke made of ferrite. The maximum applied current was increased from 5 to 10 kA. The field has been greatly improved from 1.2 T  $\times$  76 mm to 2.3 T  $\times$  45 mm. The field distribution is shown in Fig. 2.

Table 6 shows the parameter change produced due to the pulsed solenoid improvements. The features of the new positron focusing system are as follows: (1) The shorter pulsed solenoid made the spatial acceptance larger; (2) though the pulsed solenoid became shorter, the stronger field keeps the acceptable positron momentum ( $P \propto B_i \times L$ ) higher, while suppressing any debunching effects due to their velocity/orbit difference; (3) the stronger DC-coil field ( $B_f$ ), which is applied just after the pulsed field, keeps the positron momentum acceptance ( $\delta P \propto P(B_f/B_i) \propto B_f L$ ) wide. Approximate improvement factors regarding the spatial ac-



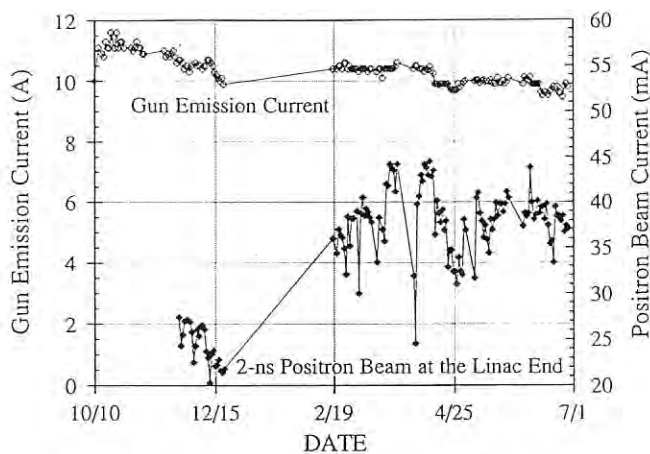


Fig. 3 2-ns beam current during one half-year under the normal operation. The positron beam current was increased by a factor of 1.5 after the new pulsed solenoid was installed.

ceptance, momentum acceptance and yield are also listed in Table 6. The factor for the positron yield was evaluated while taking into account the angular dependence of the positron production cross section.

The new pulsed solenoid was installed in January, 1992. As can be seen in Fig. 3 the 2-ns positron beam injected into the TRISTAN ring was increased by about 50% after the improvements in the pulsed solenoid. The 40-ns positron beam for the Photon Factory was also increased by more than 50%.

*S. Ohsawa and A. Enomoto*

## 2. Control System Rejuvenation

An upgrade of the main part of the control system is now under way. Since the system resources have become inadequate and the computer company no longer supports our mini-computers, we will replace the mini-computers as well as the main computer network.

Unix-based workstations, VME-bus computers and the standard communication network will be employed in the new system. A group of Unix-based workstations will serve as an interface to the operator's console system, and will manage the data bases and communications between other control components. The VME-bus computers will control the accelerator equipment and communicate with the workstations. A TCP/IP protocol suite will be utilized on the new network system. Most of the control

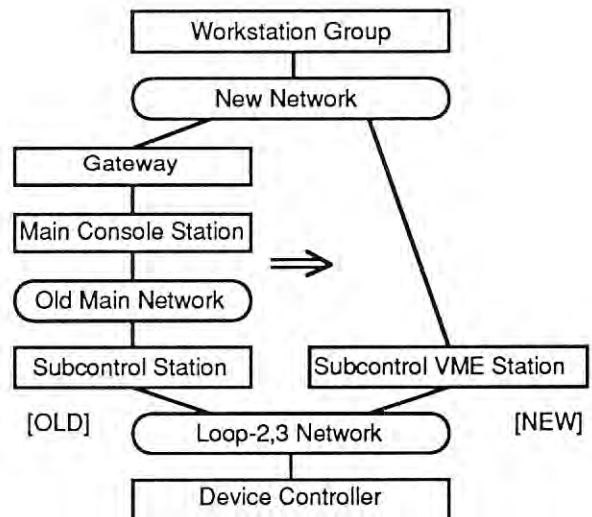


Fig. 4 Transition of the system connection and the control message flow.

communication software will be based on the TCP protocol for scalability, since it is widely available.

Since the main part of the control system is being replaced, the control software will also be upgraded. The system software has been developed so as to support both the old and new control schemes. Since we invested much in the operator's console system using old-formatted control messages, we will continue to support it. A new control scheme is also being developed on the basis of an object orientation concept. It includes a new control message format with device or class names, commands and realistic parameters instead of binary numbers. It will make the development of application programs easier.

At the time of the upgrade, we must be careful to carry out a smooth transition from the old to the new systems. We have developed a gateway system between the old and new systems for this purpose. It will hide most of the complexity at the transition time. The transition is expected to take place during the summer shutdown of 1993.

*K. Furukawa*

## 3. Operator's Console System

The operator's Console Network (NetWare system) has been installed in order to replace the DSLINK system, which has been used for a human interface in the PF 2.5-GeV linac control system.



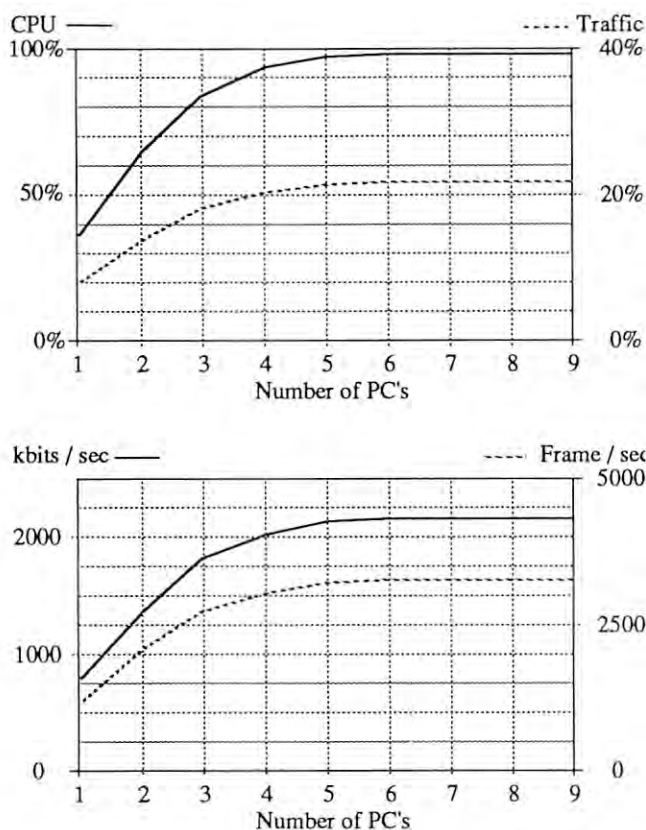


Fig. 5 Network performance.

The performance of the NetWare segment has been measured using an FMR70 (FUJITSU Co.) and IBM PCs; the results are given in Fig. 5.

Most of the application programs written for the DSLINK are completely upward compatible on the new NetWare network system.

Macintosh and IBM PCs were installed on the same segment, which had been running only with FMR personal computers. The system has become a multi-vendor network.

The reliability of the network file server has been improved in the new system. Although we used to experience many unexplainable faults (troubles) under the DSLINK, there has been no problems experienced with the new system during the past 4 months.

A new concept of OOP (object-oriented programming) is also introduced in the PC network environment.

## D. RESEARCH

### 1. Test Linac

In the test linac, emittance measurements of electron guns with three different types of cathodes (a barium-impregnated cathode, a single-crystal  $\text{LaB}_6$  and polycrystal  $\text{LaB}_6$ ) have been carried out. Details concerning the emittance-measurement system, in which a pepper-pot mask with many pinholes is used, have been reported elsewhere.<sup>1)</sup> In an electron gun, a space between the high-temperature cathode and the Wehnelt electrode is necessary for thermal insulation. At the beginning of the gun design, we tried to make the space as small as possible, thus adopting 0.1 mm, which was neglected in the calculation with the EGUN code by Herrmannsfeldt. The cathode is heated in a so-called Vogel-type cathode-holder (Fig. 6(a)). We noticed from the experimental results that this small space had greatly distorted an equipotential contour near to the cathode edge. Two pinhole images appeared through one pinhole (Fig. 7(a)), showing a non-laminar flow of the electron beams. We have developed a new Vogel-type cathode-holder in which the cathode is surrounded by a carbon heater. The space for the thermal insulation is set between the carbon heater and the Wehnelt electrode (Fig. 6(b)). The beam trajectories in the new gun agree well with our calculations; thus the laminar flow of electron beams has been realized (Fig. 7(b)).

It is pointed out that the roughness of the cathode surface is one of the crucial parameters which determine the brightness; however, few experiments, as far as we know, have been carried out concerning this problem. The surface of barium-impregnated cathodes, which have been extensively used, shows craters several microns in diameter among tungsten grains. The surface of the polycrystal of  $\text{LaB}_6$  is similar to that of the barium-impregnated one. One of these three kinds of cathodes, single-crystal  $\text{LaB}_6$ , has an extremely flat surface, and has been compared with the other two types of cathodes. The shape of the pepper-pot image, which directly expresses the transverse momentum of the electron beams, shows particular properties: pepper-pot images for the polycrystal  $\text{LaB}_6$  are almost two-times larger than that of the single-crystal type in size; those of the BI cathode are almost the same as those

I. Abe

<sup>1)</sup> Y. Yamazaki et al. *Nucl. Instrum. Meth.*, A322 (1992) 139.

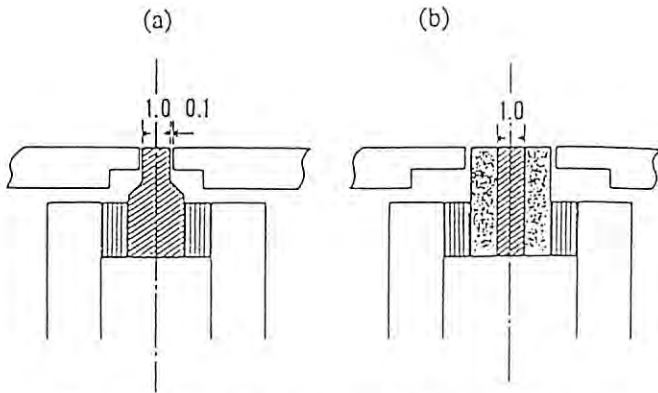


Fig. 6 Cathode holder without (a) and with (b) the surrounding carbon.

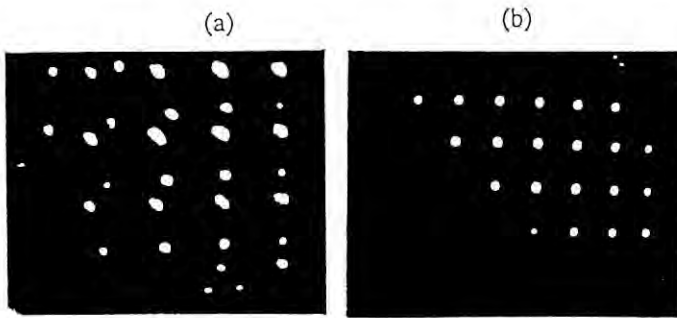


Fig. 7 Typical example of images at beam edge without (a) and with (b) the surrounding carbon.

of the single-crystal type in size, but are oval or distorted in shape, in contrast to very circular images for the single-crystal. Further studies are being carried out.

*H. Kobayashi*

## 2. Slow-Positron Source

After the summer shutdown in 1991, the first machine study of the slow-positron source project was conducted on 19 November. By that time, since the switchyard line to the slow-positron source chamber had been completed, we obtained each parameter for a 18-degree bending magnet, a Q magnet and so on to transport a 2.5-GeV electron beam (a pulse width of 2 ns) to the target chamber of the slow-positron source. During the winter shutdown, beam monitors for slow-positrons were installed in the beamline. As detectors, five channel-electron multipliers were used for beam monitors within the 30-m length beamline. Together with the 20 sets

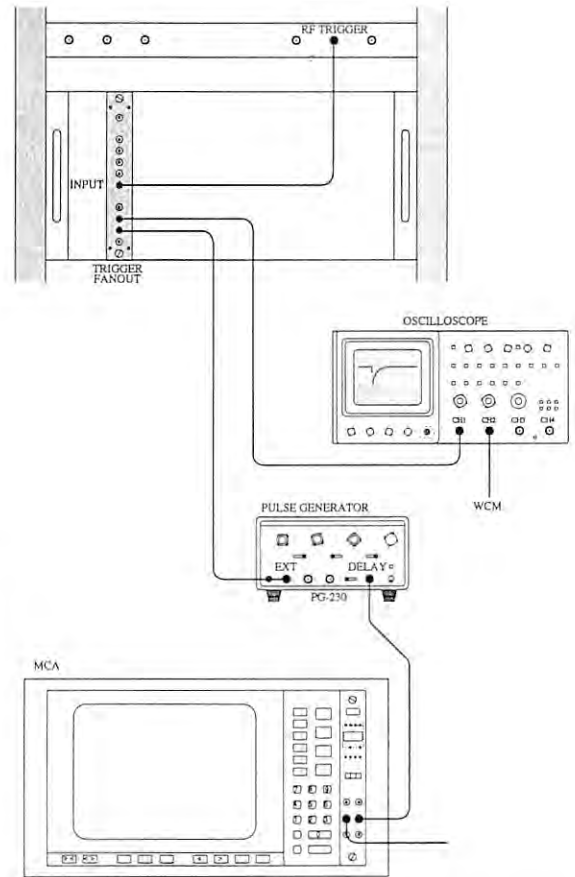


Fig. 8 Diagram of the experimental set up to counts annihilation gamma rays at the end of the slow-positron beam line gated with an RF Trigger.

of steering coils, the slow positron beam would be adjusted to the proper trajectory.

From 25 February, 1992, an experiment to irradiate Ta targets by the 2.5-GeV electron beam was started. The experimental area is situated just at the north end of the klystron gallery; since the klystron (No. 8 of 5 sector) is closer to the detector, the noise level is about 50 mV (p-p). We decided to stand by all klystrons of 5 sector in order to reduce electro-magnetic noise induced by these klystron modulators.

Transported positrons were detected at the end of the beamline by a photomultiplier tube (HAMAMATSU H2611) with a BGO scintillator. The experimental setup is shown in Fig. 8.

The first result to obtain annihilation gamma rays was obtained on 10 June. The estimated number of slow positrons which were transported from the target to the beam end was  $1 \times 10^3/\text{kW}$ . The

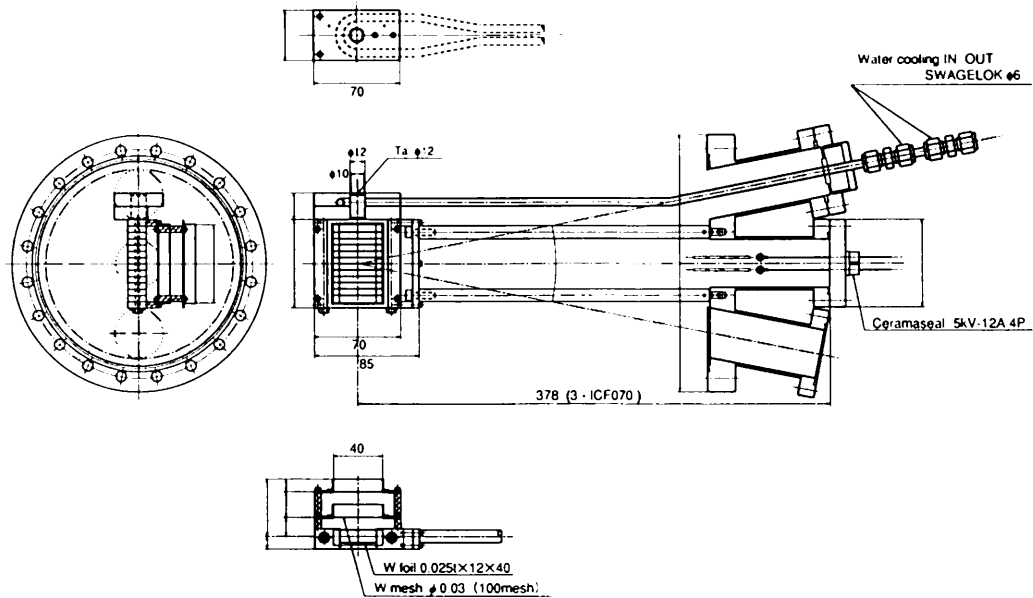


Fig. 9 Water-cooled tantalum target with a multi-layered tungsten moderator. It contains 2 grids.

beam parameters at that machine study time were as follows. The electron beam had an energy of 2.0 GeV, a pulse width of 2 ns and a repetition rate of 25 pulse per sec. During irradiation of the 2.0-GeV electron beam, the target is easy to heat, unless the power of the irradiated beam is only about a few watts. During the summer shutdown in 1992, we modified the target moderator structure by cooling the new target assembly (see Fig. 9). Due to the cooling system, the target chamber now maintains its vacuum condition at about  $10^{-6}$  Pa. The estimated number of slow positrons detected at the end of the beam line is  $1 \times 10^5/\text{kW}$ .

*T. Kurihara and A. Shirakawa*

## E. R&D REGARDING B-FACTORY

### 1. New High-Current Pre-injector

#### 1.1 Outline of the New Pre-injector

The upgrade of the pre-injector (injection system) was completed with the hearty cooperation of many interested persons. The layout of the new pre-injector is shown in Fig. 10. The improved items extend over a wide area. The main items are the following: (1) The electron gun was newly designed. The gun voltage was increased up to 200 kV in order not only to increase the beam current, but also

to reduce any space-charge effects at the low- $\beta$  region. Moreover, increasing the voltage is effective to decrease the gun voltage change due to beam loading, which is not negligible at high current. (2) Because of the gun voltage change, it became necessary to design a new bunching system that matches 200 keV beams. A double prebuncher and a high-field buncher were adopted in order to obtain short bunches with a high bunching efficiency. They are all of the traveling-wave type. (3) As the prebuncher became double, one more unit of the rf phase-shifter and power-adjuster was added. The new system was also capable of independently adjusting the phase and power level. The system was rearranged so as to easily adjust the beam phase with respect to the rf in the accelerator sections following the bunching system. (4) The focusing system was reinforced. Solenoids were extended to the buncher end. A Q-triplet was added. (5) The beam monitors were enriched: they are fluorescent-screen-type monitors using chromium-doped ceramics, current monitors, and an optical transition radiation (OTR) monitor. The OTR monitor comprises a polished stainless-steel plate emitting transition light, an optical transport system and a streak camera which analyzes the time structure. (6) Since the beam energy increases due to the new buncher, the momentum analyzer was replaced with a new one which can analyze beams up to 60 MeV. It deflects beams by  $90^\circ$ . It

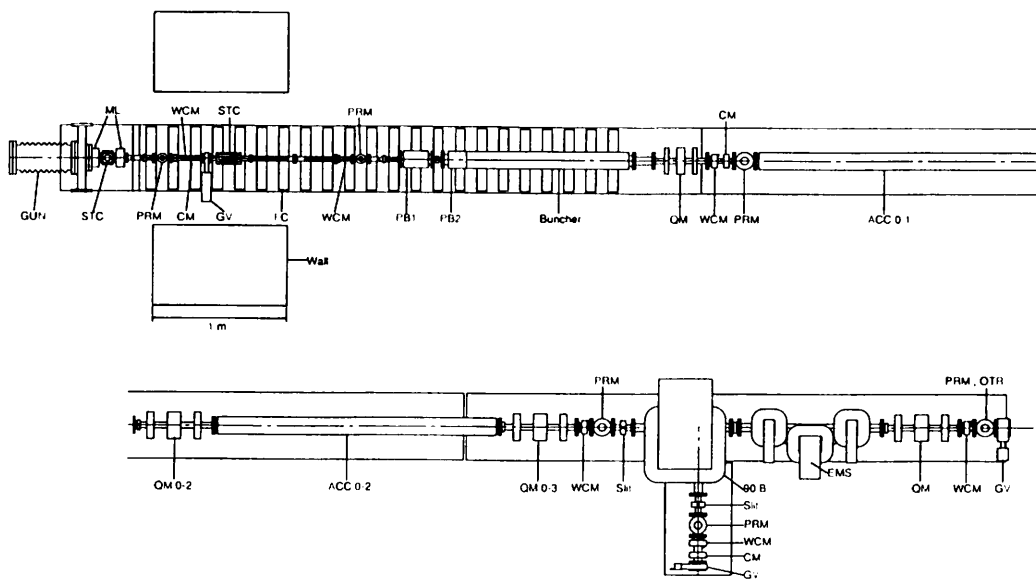


Fig. 10 Layout of the new injection system of the PF 2.5-GeV linac. GUN is an electron gun; STC, steering coils; ML, a magnetic lens; PRM, a profile monitor; WCM, a wall current monitor; CM, a core monitor; GV, a gate valve; FC, a focusing coil; PB1, first prebuncher; PB2, second prebuncher; Buncher, a buncher with accelerating cavities; QM, quadrupole magnets; ACC, accelerating cavities; 90-B, a bending magnet; EMS, an energy monochromatic system; and OTR, an optical transition radiation monitor.

became compact compared with the previous one, which deflected beams by  $45^\circ$  two times. (7) An energy monochromatic system was installed near to the exit of the injection system. It also functions as a bunch compressor, which will be useful to further reduce the bunch length. (8) Many softwares of the control system were modified or added according to the hardware changes. (9) The iron girders supporting the entire pre-injector were changed to ones made of aluminum.

*S. Ohsawa*

## 1.2 Beam Dynamics

In designing the bunching system we performed a simulation study on the beam dynamics in a search for the optimum parameters to make the bunch length short, while keeping its emittance small. The dependence on the following factors was mainly studied: (1) the rf input powers and relative phases in the pre-bunchers and in the buncher and (2) the distribution of the focusing magnetic field by the coils. The PARMELA code was used for the simulation. The distribution of the particles in the beam was represented by several hundreds of macro particles in the six-dimensional phase space. The code

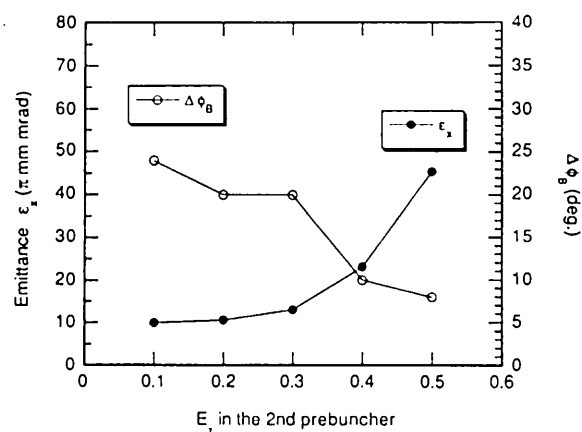


Fig. 11 Dependence of the transverse emittance and the bunch length of the beam on the rf power in the second prebuncher. (Simulation)

takes into account not only the forces by the electromagnetic fields in the cavity and the focusing magnetic field, but also the space-charge force between the particles. Fig. 11 shows the dependence of the bunch length and the transverse emittance of the beam on the rf power in the second prebuncher. The change in the transverse emittance of the beam in the bunching system is shown in Fig. 12. The magnetic field distribution for the smallest emittance

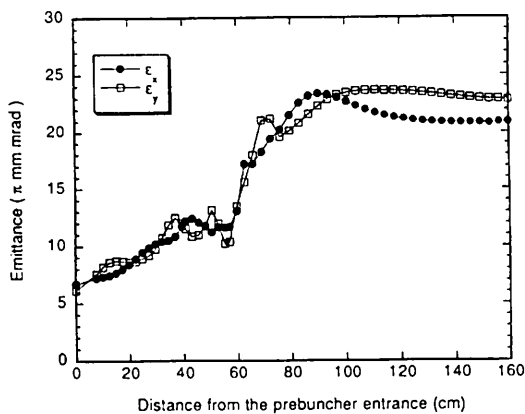


Fig. 12 Emittance growth in the prebunchers and buncher. (Simulation)

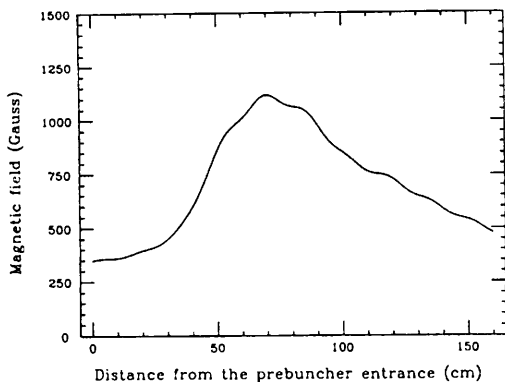


Fig. 13 Idealistic focus field distribution. (Simulation)

was calculated (Fig. 13).

In order to check the validity of the simulation, the results should be compared with the measurements. We are preparing systems which can be used to measure the transverse emittance and the bunch length. The emittances can be measured by observing the variation of the dimensions of the beam profiles on the fluorescent screen with the strength of the quadrupole. The beam profiles are observed by a CCD camera with a time gate synchronized with the beam-trigger signal. The video signals are processed with an image analyzer in order to obtain the transverse dimensions of the beam. The bunch lengths are measured with the optical transition radiation emitted from a polished stainless-steel plate inserted in the beam line. The light is guided to a streak camera in order to analyze its time structure. These experimental studies with an actual beam will

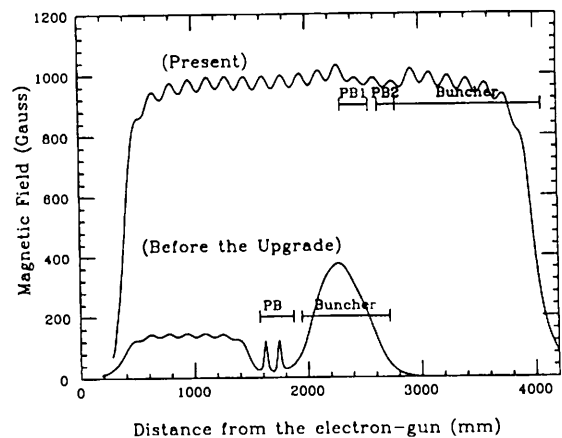


Fig. 14 Solenoidal field distribution before/after the upgrade.

start soon.

*T. Kamitani*

### 1.3 Focusing System

In the upgrade of the pre-injector system we have improved the beam transport system regarding (1) the solenoidal magnetic field, (2) the quadrupole focusing system and (3) the energy monochromatic system (bunch compression system).

(1) The new solenoidal focusing system comprises twenty-two Helmholtz coils of almost the same size with thirteen power supplies. The coils were designed so as to be capable of generating a magnetic field of up to 1.4 kG, since a strong magnetic field is required to focus a high-current beam. The number of power supplies was increased so as to be almost three times as large as the previous one in order to make a field distribution close to the ideal form estimated by the simulation. The calculated field distributions are shown in Fig. 14.

(2) One quadrupole triplet was added for the larger acceptance and the better beam optical matching to the regular section. Fig. 15 shows the calculated result of the beam size in the improved system; the calculation was carried out using the TRANSPORT code. Two of the power supplies of the quadrupole magnets were changed from unipolar to bipolar. It is required for measurements of the emittance at both polarities. (3) A set of bending magnets was placed as energy monochromatic system (EMS) by magnetic bunch compression, as shown in Fig. 16. Electrons from the buncher have

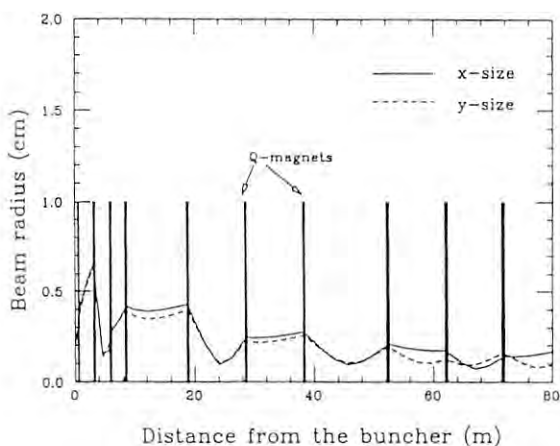


Fig. 15 Change in the beam size with the TRANSPORT code.

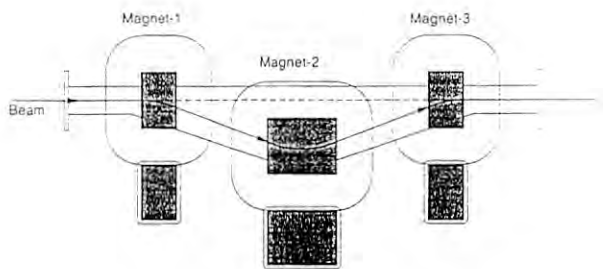


Fig. 16 Layout of the energy monochromatic system.

such an energy distribution in the bunch that the electrons at the bunch head have a lower energy than do those at the tail. In the EMS, since electrons with lower energies make longer detours, the bunch length becomes shorter after passing through the EMS. For high-current beams, it is not easy to make its bunch length shorter only with the prebunchers and the buncher, since the space-charge force between electrons is strong at the low- $\beta$  ( $=v/c$ ) region. The co-operation of medium bunching in the buncher with additional bunching in the EMS is expected to improve the performance.

*T. Kamitani and T. Oogoe*

#### 1.4 Electron Gun

The gun voltage and the maximum current were increased from 100 to 200 kV and from 3.8 to 10 A, respectively, in order to investigate the high-current

beam-loading effect in the PF 2.5-GeV linac. Several types of guns have been designed using the EGUN code developed by Herrmannsfeldt of SLAC. The design current is 10 A at maximum. For the beam injection to TRISTAN, about 1 A is required, and is obtainable by adjusting the grid voltage. The specific performance requested by the Accumulator Ring (AR) of TRISTAN (where experiments concerning the Mössbauer effect have been being carried out) is a single-bunch beam with a very good signal-to-noise (S/N) ratio of  $10^7$ . The pulse width of the gun voltage is 3  $\mu$ s; a 2-ns pulse is applied to the grid of the gun for beam injection to the AR. The electron emission from the cathode should be sharply cut off due to the grid bias. A very small grid emission and/or insufficient cutoff by the grid bias will deteriorate the S/N ratio in the AR. The barium-impregnated (BI) cathodes are usually operated at 1100°C, and the oxide cathodes at 850°C. The oxide cathode operated at low temperature is desirable from the viewpoint of grid emission, and the BI cathode is advantageous from the viewpoint of the lifetime. We did not know which of these cathodes was the most suitable for our purpose. Therefore, three types of cathodes operated at different temperatures and with different diameters (Y-796(BI,16mm $\phi$ ), 646E(BI,10mm $\phi$ ) and 646(oxide,10mm $\phi$ ), supplied by EIMAC) were prepared. The electron gun comprising Y-796 was attached first, setting a comparatively low operation temperature as the BI cathode, and has so far been successfully used. Others are used on a standby basis. Thus, the high S/N ratio has always been monitored in the AR during experiments employing a single-photon counting method.

*H. Kobayashi and M. Yokota*

#### 1.5 Pulse Power Supply

The gun pulser was modified so as to increase the maximum voltage up to 200 kV. The changed elements are a thyatron, a pulse forming network (PFN) and a pulse transformer with some other elements. They are listed in Table 7 along with their associated parameters. In addition, a heat exchanger was introduced outside of the insulating oil tank.

(1) Since at the maximum voltage operation the thyatron anode voltage exceeds the maximum level of 33 kV, which is permitted for the thyatron of ITT 8789/F-105, we exchanged it with an ITT F-



Table 7. Gun pulser parameter changes.

	previous	present
Maximum voltage	160 kV →	200 kV
Pulse duration	3 $\mu$ s →	3 $\mu$ s
Thyratron	ITT 8789 →	F-175
Pulse-forming network		
capacitor	18 nF →	14.6 nF
section number	3 × 4 →	3 × 5
coil (No. of turns)	12 →	10
Pulse transformer		
step-up ratio	1 : 9.56 →	1 : 12
secondary impedance	1.14 k $\Omega$ →	1.8 k $\Omega$
Load resistance (k $\Omega$ )	9.2 / 9 →	8.2 × 2/9

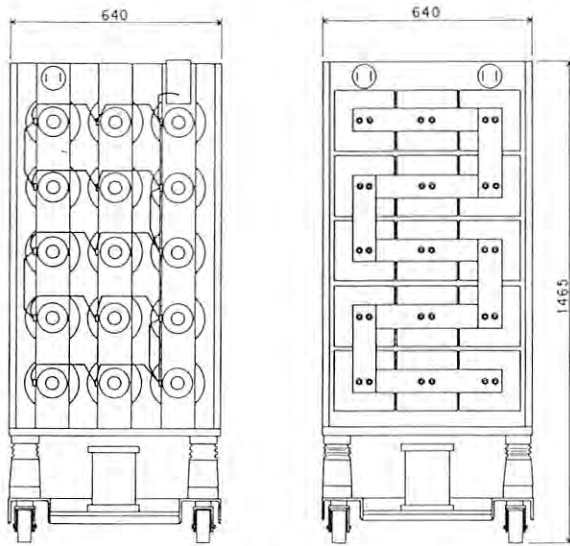


Fig. 17 New pulse-forming network.

175, which has a higher permitted anode voltage (50 kV).

(2) The capacitor of the gun pulser PFN was that which had been used in the klystron modulator at the beginning. In order to increase the gun pulser voltage, we decided to change the capacitors with new ones which are being used in the klystron modulator, because they are reliable and long-lived. For keeping the output impedance of the gun pulser unchanged, the turn number of the coil and the section number were changed (Table 7). The new PFN is shown in Fig. 17.

(3) In order not to change the fundamental design of the gun pulser, itself, we increased the step-up ratio of the pulse transformer. As a result, the load resistance increased to 1.8 k $\Omega$ . The new load comprises two parts connected in serial, each of

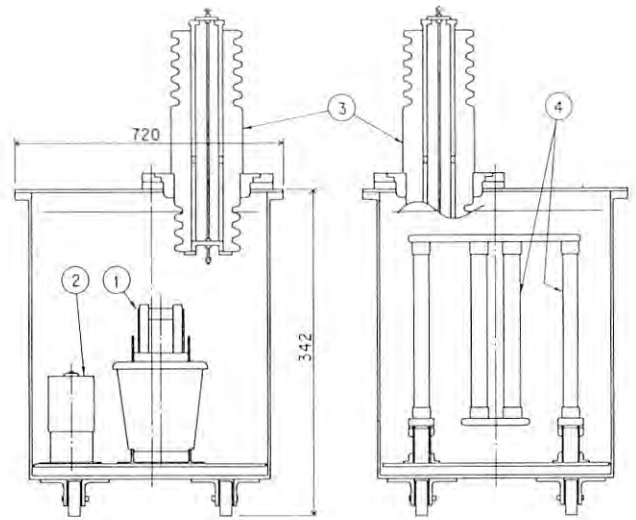


Fig. 18 Arrangement of the new pulse transformer and associated elements. (1) pulse transformer (2) capacitive divider (3) bushing (4) load resistance

which is made of 9 resistors connected in parallel. In addition, the bushing made of ceramics became large. The arrangement of these elements is shown in Fig. 18.

(4) Since the power dissipation in the load resistors increased, it became necessary to use a heat exchanger which circulated the insulating oil with a motor pump. Previously, heat was exchanged by a coiled copper pipe around the load resistors. The new heat exchanger is external to the oil tank in order to make the oil tank smaller. It has the ability to suppress the temperature rise to less than 10°C under full operation.

*M. Yokota and S. Ohsawa*

## 1.6 Prebunchers and Buncher

The role of the bunching system is to make the bunches as short as possible with a high bunching efficiency, while keeping the beam emittance small. As the beam intensity increases, it becomes difficult to obtain short bunches, due to the space charge. We adopted a multi-bunching system comprising double prebunchers and a high field buncher. Our new system has some other features: (1) The distance between the second prebuncher and the buncher was made short (almost the limit). They are connected

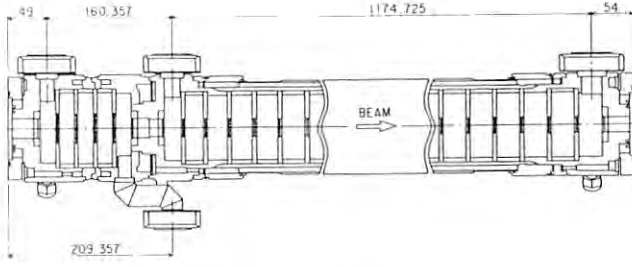


Fig. 19 Structure of the second prebuncher and buncher, which are connected mechanically, but separated electrically.

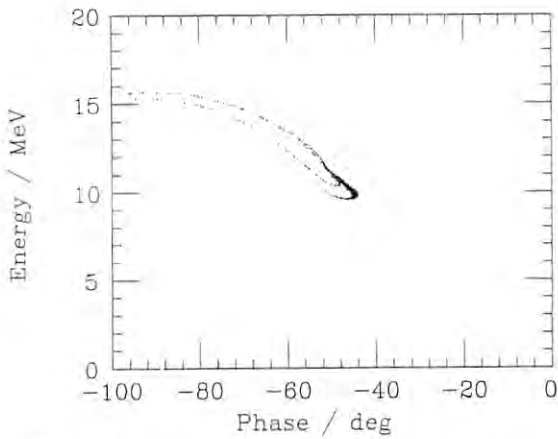


Fig. 20 Simulation example of the energy distribution versus the buncher rf phase.

mechanically, can be seen in Fig. 19. It is important to make the distance short, especially for intense beams in order to obtain short bunches. (2) The prebunchers were designed so as to have a very low shunt impedance and large group velocities. The aim was to reduce the wakefield effects caused by intense beams. (3) The buncher comprises two sections: The beginning part is the bunching section, which has 6 cavities, including an input coupler. Each cavity has a different phase velocity, which gradually varies from  $0.77c$  to  $0.99c$ . A normal section with a phase velocity of  $c$  follows the bunching section without any gap. (4) All of the prebunchers and buncher are of the traveling-wave type.

According to our beam simulations, double prebunchers are useful for obtaining short bunches with a high bunching efficiency. In the second prebuncher, electrons loosely bunched by the first prebuncher will be accelerated at different phases, so that they will be even more bunched due to the en-

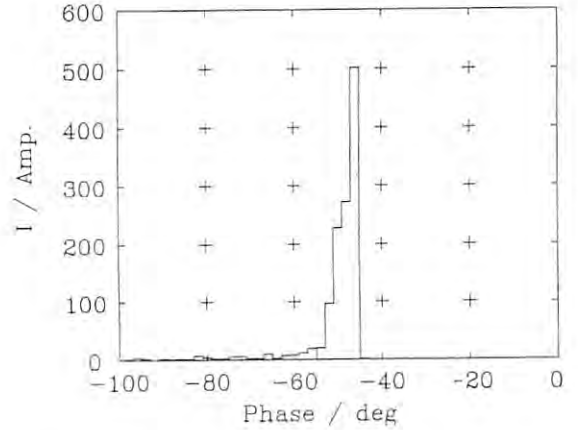


Fig. 21 Current density versus the rf phase in the same case.

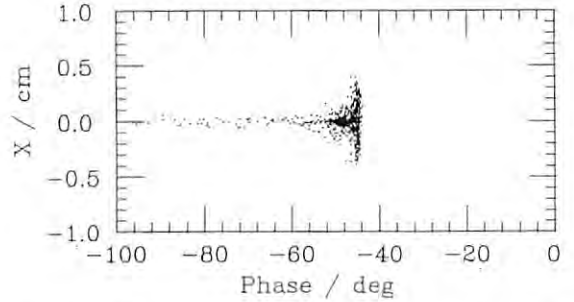


Fig. 22 Horizontal position  $x$  versus the rf phase. It exhibits a beam distribution in real space.

ergy differences obtained in the second prebuncher. The role of the second prebuncher will become more important as the beam intensity becomes higher. The electrons are finally bunched by a buncher with a high field. They are then rapidly accelerated in order to prevent debunching.

The field strengths and phase velocities of the bunching system were determined by simulations performed using PARMELA. Some examples are shown in Figs. 20 to 22. The simulation predicts a  $8^\circ$  bunch length at the buncher exit for a beam of 200 keV and 8 A from the gun. The electrons plotted in these figures reach just 90% of the input ones.

In the design of the coupler cavities, a method based on an equivalent-circuit technique was used with the help of MAFIA to determine the resonant frequencies of the system. The field asymmetry of the coupler cavities was also investigated by



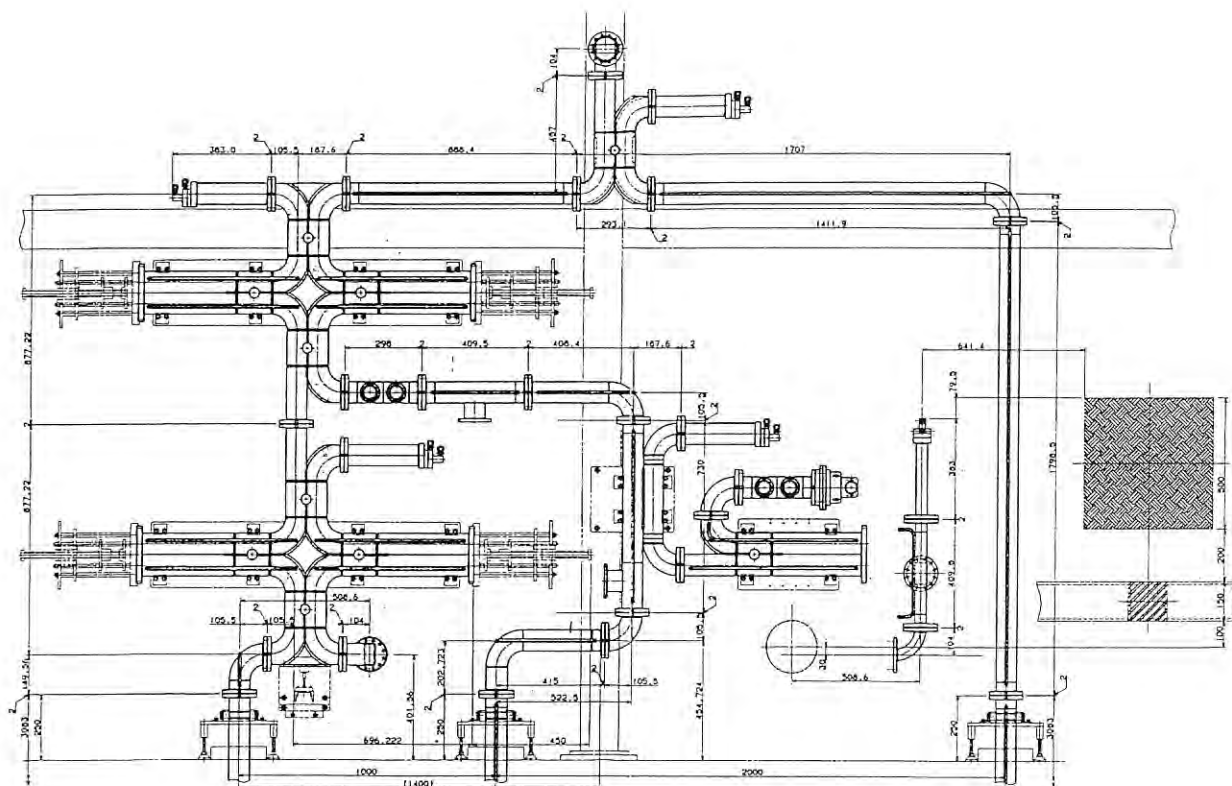


Fig. 23 Arrangement of the new rf adjusting system.

the method. The asymmetry was compensated for by offsetting the coupler cylinder instead of making a counter slot on the cylinder wall just facing the waveguide slot. We adopted this method in order to simplify the coupler structure for avoiding electric breakdown, since in many of our accelerator sections, a dark-colored area is seen near to the corner in the counter slot.

S. Ohsawa and H. Hanaki

## 1.7 RF System

Since a double prebuncher system was adopted, one more unit of the attenuator and phase shifter became necessary for adjusting the rf. In our system the rf power level and the phase can be changed independently. This is useful for simplifying rf optimization in the bunching section.

This time, the rf adjusting system was rearranged while adding one more unit. The new rf system is shown in Figs. 23, 24. It has the following additional features: (1) The power-divide ratio for the second prebuncher and buncher, which is controlled by the first unit, can be continuously

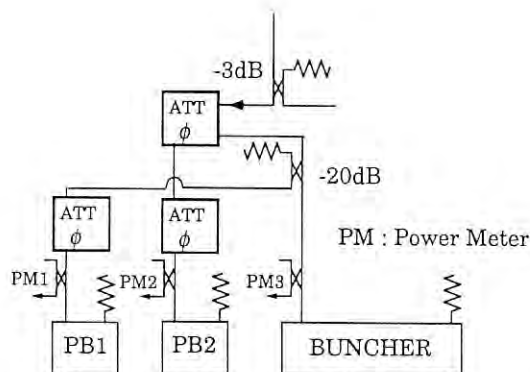


Fig. 24 Schematic diagram of the new rf adjusting system.

changed without any phase shift. (2) When the same unit is driven as a phase shifter, all of the rf phases in the bunching system are simultaneously shifted with the same value. This property is very useful for adjusting the beam bunch phase with respect to the fixed microwaves in the following accelerator sections, since the phase adjustment between these two does not affect the beam bunches.

The rf power levels and phases are optimized using a beam in the following processes: (1) The

Table 8. Bunching system design values.

Prebuncher 1			
maximum field	0.4	MV/m	
shunt impedance	15.96	M $\Omega$ /m	
group velocity/c	0.0459		
attenuation coefficient	0.0643	neper/m	
available input power	100	kW	
cavity number	7		
cavity size D	24.318	mm	
2a	35.74	mm	
2b	89.418	mm	
Drift space	158.71	mm	
Prebuncher 2			
maximum field	1.0	MV/m	
shunt impedance	14.97	M $\Omega$ /m	
group velocity/c	0.0494		
attenuation coefficient	0.0597	neper/m	
available input power	1	MW	
cavity number	5		
cavity size D	24.318	mm	
2a	36.89	mm	
2b	90.075	mm	
Drift space	42.27	mm	
Buncher			
field strength	~15	MV/m	
available input power	13	MW	
cavity number			
bunching section		6	
normal section		29	
cavity size D	27.01~34.99	mm	
2a	22.44~19.32	mm	
2b	83.057~81.735	mm	

power-divide ratio of the second prebuncher to the buncher is set (at first) according to the computer simulation. This is performed by the first rf adjusting unit. (2) Next, only the buncher is fed rf power. The power to the prebunchers is completely attenuated. The beam is bunched and accelerated only by the buncher. (3) The buncher rf phase is optimized with respect to the rf phase in the following accelerator sections, so that the beam energy becomes maximum at the 90°-analyzer in the injection system. (4) Then rf power is fed into the second prebuncher. The power level and phase are optimized so that the beam current increases. The same process is performed for the first prebuncher. (5) Finally, every parameter is again adjusted by making slight changes.

The rf power levels and phases are roughly optimized according to the above-mentioned processes. For fine tuning, the bunch monitor will be used to minimize the bunch length, which is presently being tested.

*S. Ohsawa and M. Yokota*

Table 9. Specifications of the beam ducts and other vacuum ducts.

	material	pipe diameter (mm)	type of flange
Beam duct			
gun to PB	SUS316L	34	knife edge
others	SUS304	34, 42.7, 60.5	metal o-ring
Vacuum duct	SUS304	42.7, 139.8	metal o-ring

## 1.8 Vacuum System

In connection with the pre-injector upgrade, the vacuum system was also considerably modified: Almost all of the beam ducts and vacuum ducts were newly manufactured, since main elements and their locations have been completely changed. Ion pumps distributed along the beam line in order to differentially evacuate the gun were removed this time due to a lack of space. This eliminates any possibility of disturbing the focusing magnetic field. In order to save beamline space, a gate valve installed between the buncher and the first accelerator section was removed. The gate valve has been useless since the rf adjusting system was improved from a pressurized SF<sub>6</sub> type to the vacuum type, in which both sides of the gate valve are connected through the waveguides. The separated two vacuum ducts were then unified. Furthermore, the locations of the vacuum ports were changed from the beam ducts to the waveguides.

In order not to increase radioactive material, the old vacuum ducts were reused for the new system as much as possible. In this work, both cutting and welding were carried out inside our laboratory. For the same reason, all of the ion pumps are arranged external to the accelerator tunnel (as before).

The entire new system of the vacuum is shown in Fig. 25. The length of the beam line from the gun to the prebuncher 1 is 2.3 m. 316L stainless steel was used for the welded parts so that they would not become ferromagnetic. The specifications of each duct are listed in Table 9.

*K. Kakiyama*

## 1.9 500-MeV Energy-Analyzing System

One of the main purposes of the upgrade of the pre-injector system is to improve the bunching sys-

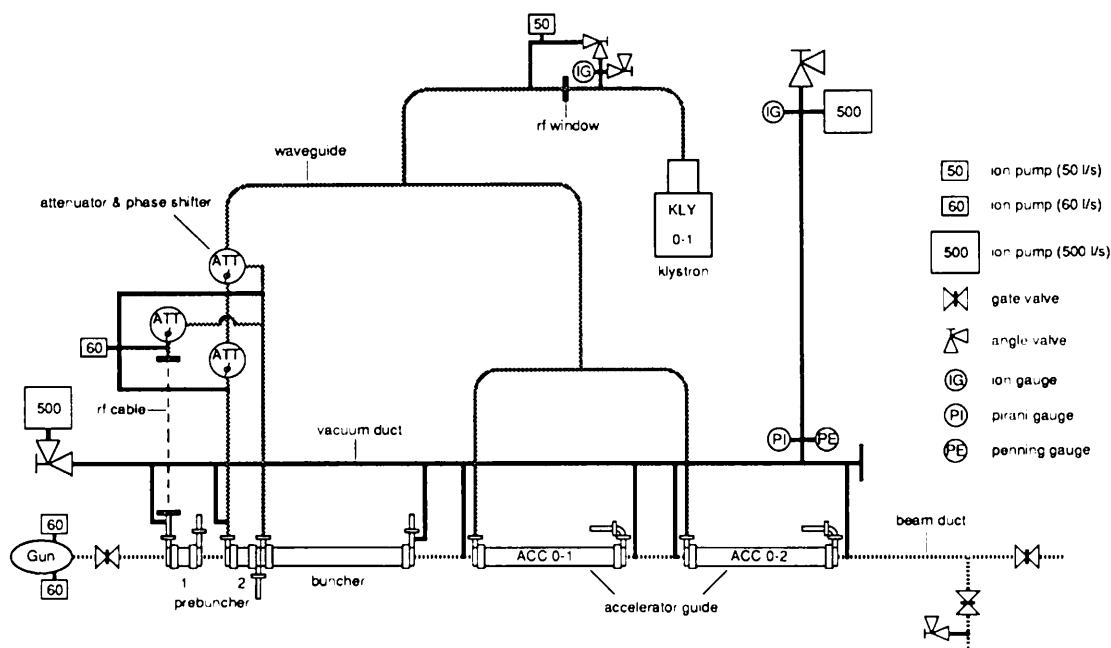


Fig. 25 The new vacuum system of the injection system.

tem for the acceleration of high-current beams in order to study any instabilities due to wakefields. An energy-analyzing system is necessary in order to measure the beam-energy spectrum and to observe any transverse deviation of the bunches from the axis of the accelerator; the deviation may be caused by the wakes. In the PF 2.5-GeV linac, we already have two energy analyzers: one at the pre-injector section (at 35 MeV) and the other at the end of the linac (at 2.5 GeV). Nevertheless, they are not suitable for the study, since the beam is not yet affected by the wakefield at the pre-injector, and is already lost far before the end of the linac. Another analyzer should be placed at the site of medium energy where the beam is affected by the wakefields, but it is not yet lost.

We have constructed an energy-analyzing system in the beam switch yard at the end of the Sector-1, where the beam energy is about 500 MeV. It is also used as an achromatic and energy-defining beam transport system to deliver the beam into the switch yard line for future experiments, like a free-electron laser. The layout of the system is shown in Fig. 26. An energy-analyzing bending magnet, a quadrupole singlet and a bending magnet forms an achromatic system. Two horizontal energy-defining slits and a vertical slit are placed in the beam line. The collimators are used to eliminate any off-momentum

particles emerging from the slit. The energy spectrum can be measured using the wall-current monitor behind the energy-defining slit by changing the bending magnetic field. The energy-analyzed profile of the beam can be observed on the screen monitor.

*T. Kamitani*

### 1.10 Monitor

A new beam-monitor system was installed in the new pre-injector of the PF 2.5-GeV linac. Four wall-current monitors (WCMs), five profile monitors (PRMs) and a bunch monitor (OTR monitor) were newly installed (see Fig. 10), especially for monitoring the high-intensity beam characteristics. The beam currents and profiles are precisely measured at the following positions: (1) at the exit of the electron gun, (2) at the entrance of the prebuncher, (3) at the exit of the buncher, and (4) at the exit of the first regular accelerator section. The beam currents are measured with the WCMs to a precision of about 10% at the main control room. These monitors make possible more reliable and easier operation of the beam-transport system. A 35-MeV energy-analyzer was replaced by a new energy-analyzing system (EAS) with a compact 90° bending magnet which allows better energy resolution. A bunch monitor which utilizes an optical transition radia-

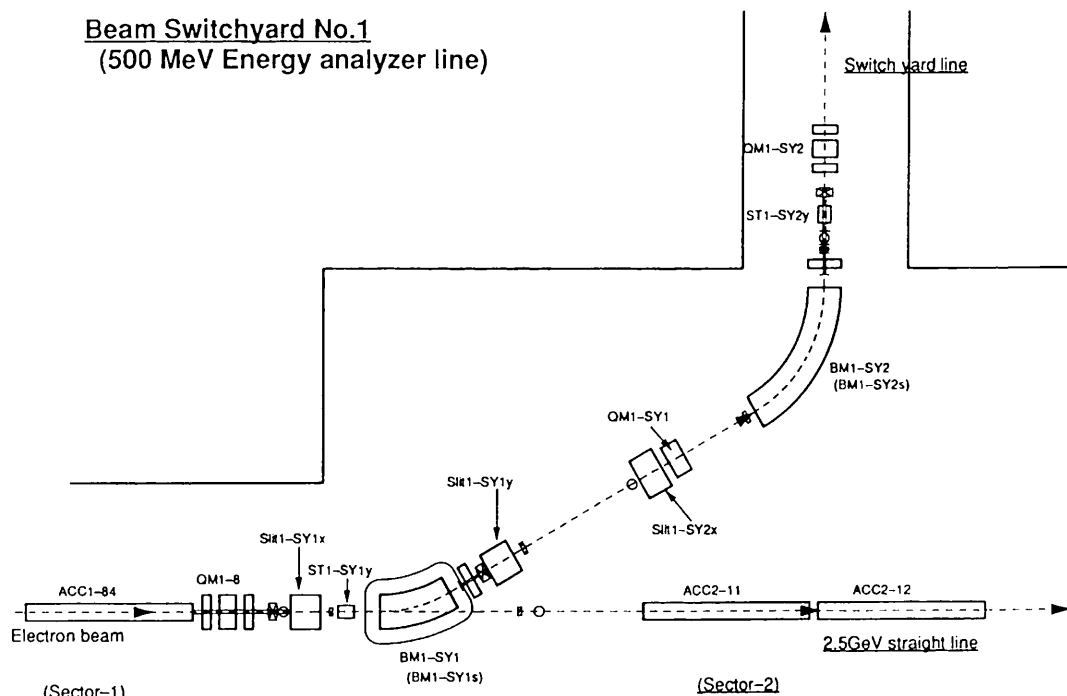


Fig. 26 Layout of the 500-MeV energy-analyzing system.

tion (OTR) is now under development. This monitor is installed after the energy monochromatic system (EMS) and measures the bunch structure of the beam after 35-MeV acceleration. A schematic view of the OTR monitoring system is shown in Fig. 27. A well-polished thin metal foil (SUS304) is placed as a radiator at the position of PRM0-40. The OTR, which is generated with a narrow opening angle by colliding with the metal tilted at  $45^\circ$  to the beam axis, is ejected from a viewing port to the OTR transport line. The OTR is divided into two parts by using a half mirror; a part of the OTR enters a CCD camera by which the light intensity is measured; the other part is transported to a streak camera in the klystron gallery by using the optical system shown in Fig. 27. The fine time structure of an intense beam can be observed by the streak camera with a time precision of less than 2 ps. Especially, the effect of a longitudinal wakefield of a high-intensity beam can be precisely studied by this monitor.

*T. Suwada and Y. Ogawa*

### 1.11 Commissioning

The new injection system was installed during the summer maintenance period from 11 July to 27

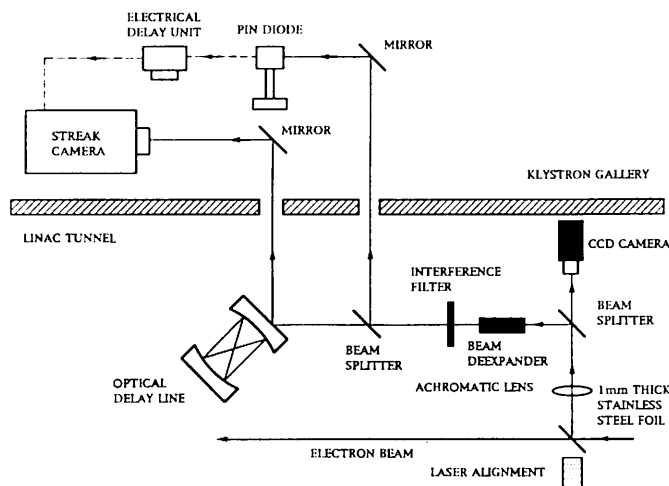


Fig. 27 Setup of OTR measurement.

September, 1992. At first, almost the entire previous system in the tunnel was completely removed. All of the devices, including the supporting girder, were replaced with new ones, except for two quadrupole magnets and two accelerating sections. Test operations with beams were performed on 24 to 25 September, as scheduled. Everything was completed within this period, except some small items. Normal

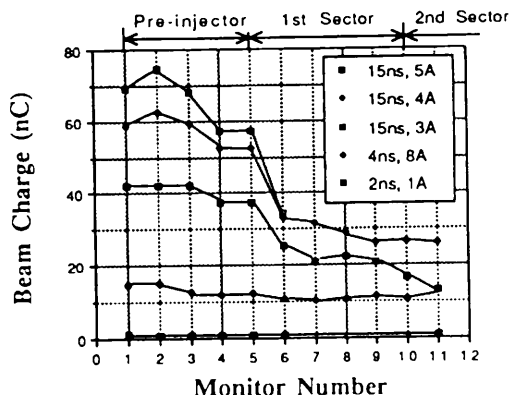


Fig. 28 Very preliminary results of beam acceleration using the new injection system.

operation started on 28 September, as was prearranged.

A very preliminary result is given in Fig. 28. Wall-current monitor No. 1 is located at the exit of the electron gun; No. 5 is located at the end of the injection system, where the beam energy is about 50 MeV; No. 11 is located at the center of the second sector, where the beam energy would be 800 MeV. After the upgrade, the beam currents increased as well as the transmission rate, as was expected. The 2-ns doubly increased beam is being satisfactorily injected into the AR of TRISTAN. The 4-ns and 15-ns beams are used only in machine studies. Operation was just started. In the acceleration of very high charge beams, some instabilities have been observed. Hereafter, many investigations of intense beam acceleration will be performed in the PF 2.5-GeV linac for the B-factory.

*S. Ohsawa*

## 2. Energy Upgrade

### 2.1 High-Gradient Acceleration Test

A high-gradient acceleration test has been carried out in order to prepare for a future energy-upgrade plan of the PF 2.5-GeV linac. In the B-factory project, the linac energy will be increased from 2.5 GeV to 8 GeV (Table 10); this is a factor of 3.2 in energy and by roughly an order in power. The energy upgrade will be performed mainly by increasing the peak rf power fed to an accelerator section (see also the following sections 2.2 and 2.3): the linac length will slightly be extended, since the effective upgrade of the rf source is limited due to practical reasons, such as the modulator cost and the available high-power klystrons.

Regarding the upgrade of the fed rf power, one of the most important problems is electric breakdown, such as in the rf windows and in the accelerator sections. In the present acceleration unit, one 2856-MHz klystron feeds rf pulses of 30 MW (maximum peak power), 3.5  $\mu$ s (width) and 25 pps (repetition) into four 2-m accelerator sections. In order to check the running performance under a higher rf power, the total power from one klystron was fed into one accelerator section by changing the rf-guide system (Fig. 29). This test was carried out at the PF 2.5-GeV linac (No. 4–8) acceleration unit, which can usually be standby for acceleration under 2.5-GeV operation. After rf processing, this unit was able to run at the maximum peak power at a pulse repetition rate of 50 pps without any significant problems in rf breakdown or the vacuum. The results concerning the test are summarized in Table 11. The acceleration energy ( $37 \pm 2$  MeV) was obtained from the difference between the maximum and minimum

Table 10. Expected parameter change of the linac beam from the present (PF: for Photon Factory, TR: for TRISTAN) to the KEK B-Facility Plan (BF).

		Present		8-GeV	Upgrade
	$e^+$ (PF)	$e^+$ (TR)	$e^-$ (TR)	$e^+$ (BF)	$e^-$ (BF)
Energy (GeV)	2.5	2.5	2.5	3.5	8
Pulse Width (ns)	40	2	2	Single Bunch	
Particles/Pulse ( $\times 10^9$ )	1.6	.44	>2.5	1~4	
(Charge (pC))	(250)	(70)	(>400)	(160~640)	
Repetition (pps)	25	25	25	50	
Energy Width ( $1\sigma$ ) (%)	0.35	0.22	0.2	0.25	
Emittance ( $\times 10^{-6}$ m-rad)	1.0		0.3	<1.0	

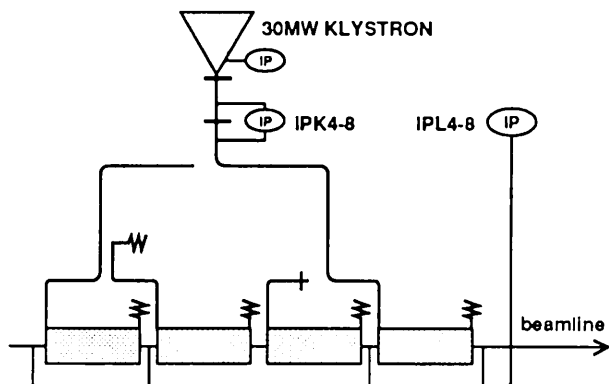


Fig. 29 High-gradient acceleration test at the PF 2.5-GeV linac No.4-8 unit by changing the waveguide system.

Table 11. Results of a high-power running test at the PF 2.5-GeV linac No.4-8 acceleration unit.

Acceleration energy	$37 \pm 2$ MeV
Acceleration field 1	$9.6 \pm 1$ MeV/m
Fed rf power	$24 \pm 2.5$ MW
Vacuum degradation	from $8 \times 10^{-7}$ to $9.5 \times 10^{-7}$ Pa

beam energies measured at a 2.5-GeV energy analyzing station by changing the rf phase of the 4-8 unit. The klystron output power was estimated to be about 24 MW based on the shunt-impedance of this accelerator section.

In the first stage of the high-gradient acceleration test, we confirmed the reliability for high-gradient acceleration at a level of around 20 MeV/m; however, it is still not sufficient for the future plan. From the autumn of 1992, the next stage will start in two different ways using a traveling-wave resonant ring accelerator section and a SLED-type rf pulse compressor.

A. Enomoto

## 2.2 Modulator Upgrade

The energy upgrade of the PF 2.5-GeV linac necessitates the replacement of the existing 30-MW klystrons with new units together with a certain microwave power multiplying scheme. Although the details concerning this energy upgrade have not yet been decided, we have started to modify one of the existing modulators at the klystron gallery (No. 4-

6) in order to confirm the feasibility and long-term stability of this modification.

There are two limitations concerning our modulator upgrade: the maximum available space at the klystron gallery and the budget for the modulator. Taking these limitations into account, the average power of the upgraded modulator was so designed as to be twice that of the existing modulator. This amount of reinforcement is the limit for us to utilize those components of the existing modulator as much as possible. The specifications of the original and two types of modified modulators (SLED and traveling-wave resonant ring, respectively) are shown in Table 12. The rectifier transformer and charging transformer assemblies are water cooled in order to maintain the present volume. The inductance of the charging transformer was reduced to half the original modulator in order to realize the same charging time (10 msec). A new pulse-forming-network (PFN) which reuses the existing capacitors is being fabricated with two identical networks in parallel. This scheme lessens the effect of any residual inductance of the PFN capacitors, since the characteristic impedance of each network is twice that of the modulator.

The No. 4-6 klystron modulator was reinforced in order to confirm the above-mentioned modifications (see Fig. 30). Preparations of more practical tests utilizing SLED-type cavity are presently underway.

T. Shidara and H. Honma

## 2.3 High-peak Power Microwave

We have investigated a SLED-type of microwave-pulse compressor as a candidate for the upgrade, and started a test of the SLED network developed by the JLC group at KEK.

The SLED network comprises two rf cylindrical cavities attached to a 3-dB coupler, as shown in Fig. 31. The cavities are tuned so as to resonate at the operating frequency, and are over-coupled to the coupler.

After the input rf pulse is turned on, the fields in the cavities build up exponentially. At one accelerator filling time before the end of the rf pulse, the phase of the rf pulse is switched to the 180°-opposite phase. The cavities then radiate stored microwaves and the coupler combines them so as to add forward waves and to cancel backward waves. Fig. 31

Table 12. Comparison of the original and modified modulator specifications.

	Original	Modified (SLED)	Modified (recirculation)
Maximum peak power (MW)	84	117	153
Maximum average power (kW)	14.7	30	30
Transformer step-up ratio	1:12	1:13.5	1:15
Output pulse voltage (kV)	23.5	23.5	23.5
Output pulse current (A)	3600	5000	6530
PFN impedance ( $\Omega$ )	6.0	4.7	3.6
PFN total capacitance (mF)	0.3	0.6	0.6
Pulse width ( $\mu$ s)	3.5	5.6	4.3
Rise time ( $\mu$ s)	0.7	0.8	0.8
Fall time ( $\mu$ s)	1.2	1.3	1.5
Pulse repetition rate (pps)	50	50	50
Maximum pulse height deviation from flatness (%)	0.3 (peak to peak)	0.3	0.3
Maximum pulse amplitude drift (%/hour)	0.3	0.3	0.3
Thyatron anode voltage (kV)	47	47	47

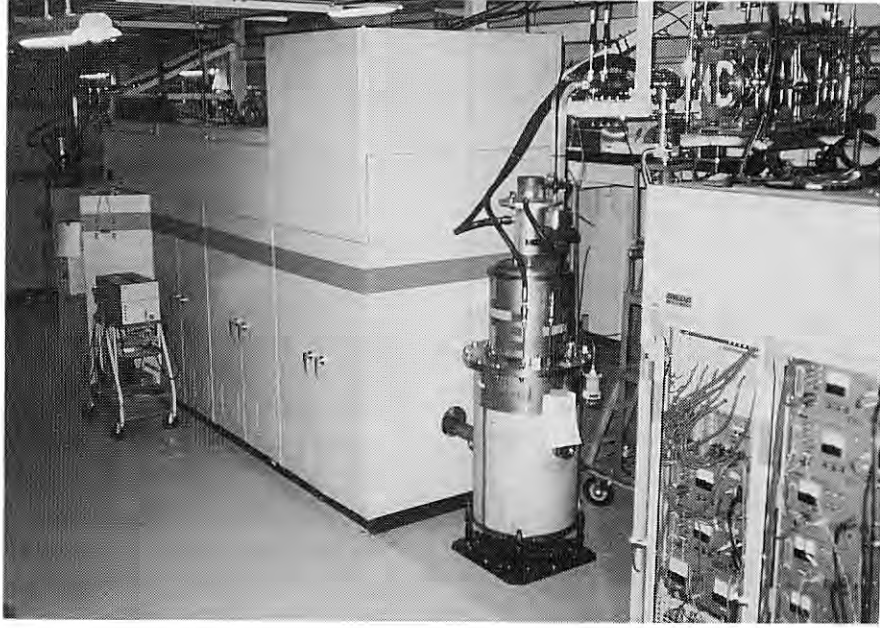


Fig. 30 Modified klystron modulator in the klystron gallery.

also illustrates a typical waveform of the amplified rf pulse. The total beam-energy gain by applying SLED (energy multiplication factor) depends on the rf pulse width and the cavity Q value, as given in Fig. 32.

The SLED enables a reduction in the maximum power of the rf-power source. This advantage obviously contributes to the avoidance of any serious problems which may occur in development of a high-power klystron.

We used the SLED network which was developed by the JLC group to investigate the high-power rf source and to test high-gradient acceleration. The SLED cavity was designed so as to resonate at the *TE015* mode, which has a Q value of  $1 \times 10^5$ . The rf pulse length should be as long as possible. However, it may not be allowed to extend a pulse-forming network so as to generate a flat rf pulse longer than  $4 \mu$ s, since minimizing the cost for a modification of the present klystron modulator is absolutely required. Therefore,  $4\text{-}\mu$ s pulse width is assumed in



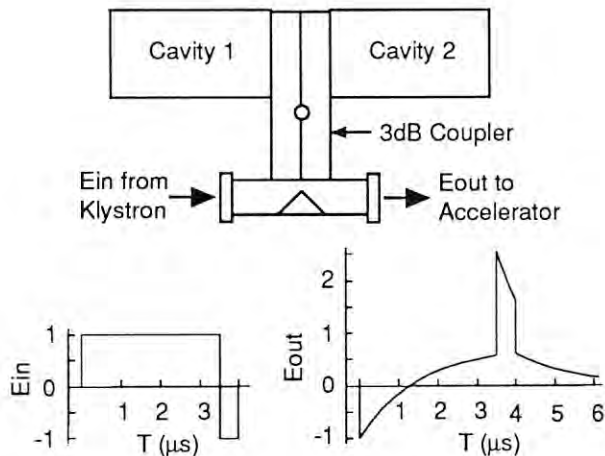


Fig. 31 SLED and rf waveforms.

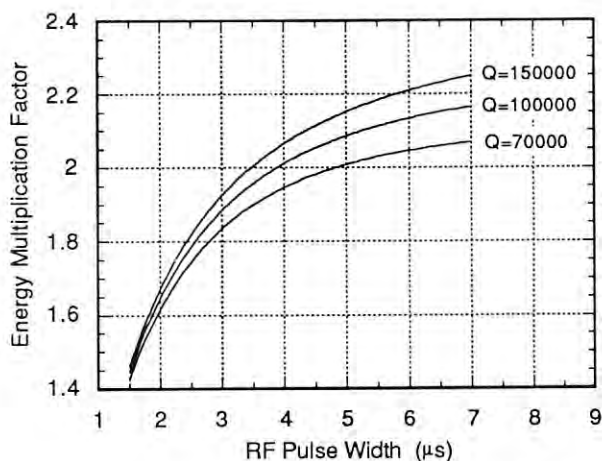


Fig. 32 Energy multiplication factor vs. rf pulse width.

the following discussion. Fig. 32 indicates that the choice of a higher  $Q$  value doesn't give any remarkable benefit at around this pulse width.

In the case of our C-type accelerator section (2 m long,  $0.5 \mu\text{s}$  filling time), an ideal calculation shows that the peak output power of the SLED is 6.59-times the input power, and that the energy multiplication factor is 2.01. A more practical estimation can be made by taking into account the finite rise time of a phase switch. For example, when the peak power loses 16% at a 120-ns phase switching time, the energy multiplication factor remains at 97% of the ideal value.

The low-power performance of a prototype SLED was examined very recently. A result, the waveform of the output power from the SLED, is

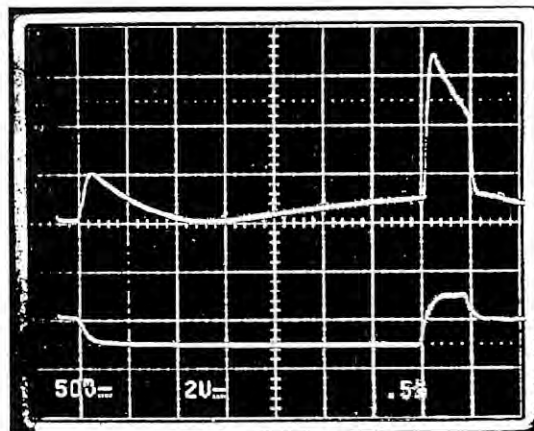


Fig. 33 Output power from the SLED (upper).

given in Fig. 33. The measured peak power was 5.90-times the input microwave. A high power test will be carried out from January, 1993.

*H. Hanaki*

### 3. Beam Position Monitor

A beam-position monitor (BPM) using wireline pickups is under development at the PF 2.5-GeV linac. This linac is now being operated in the following accelerating modes: a short-pulse mode (2 ns) and a long-pulse mode ( $1 \mu\text{s}$ ) for electron beams, and a short-pulse mode (2 ns) and a semi-long pulse mode (40 ns) for positron beams. Especially, in the future B-factory project a high-current mode (a few amperes) will be added. Under these operation modes, the beam current will be several hundred mA to a few amperes for the electron beams; this is a few mA to a few hundred mA for the positron beams; the beam pulse width is 1 ns to  $1 \mu\text{s}$  for the electron beams and is 1 ns to 40 ns for the positron beams. Therefore, the BPM needs to be developed based on the following constraints: a nearly  $10^3$  dynamic range for both the beam current and the beam pulse width. Especially, a high-current mode in the B-factory operated by a single-bunch beam predicts a beam blowup as well as a variation in the beam energies due to both transverse and longitudinal wake-fields in the accelerating units, respectively. The accuracy of the beam displacement from the central orbit needs to be determined to less than 0.1 mm in order to make possible more reliable and easier operation of the beam-transport system and, especially,



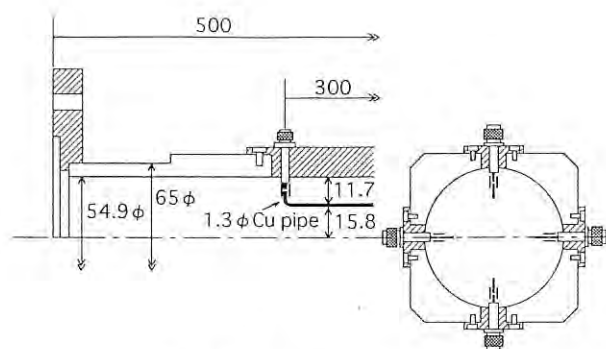


Fig. 34 Prototype wireline BPM

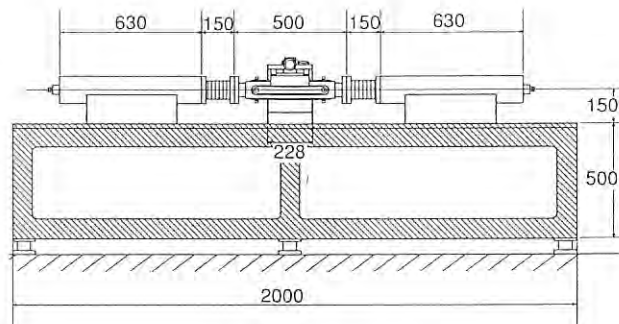


Fig. 36 Test bench.

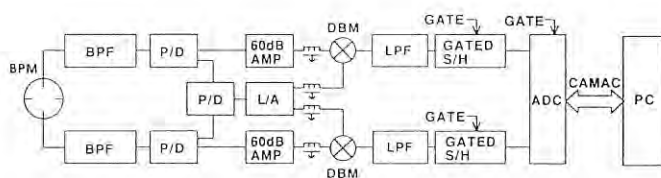


Fig. 35 Block diagram of the beam position-detection equipment.

to suppress any wakefields in the high-current beam for the B-factory.

### Wireline Pickup

A prototype BPM using wireline pickups, which has a relatively good sensitivity and a wide dynamic range, was tested by a test bench. The horizontal and longitudinal cross sections of the BPM are shown in Fig. 34. Two pairs of pickups are set so as to face each other at a distance of 15.8 mm from the beam center in the horizontal and vertical directions. The horizontal (vertical) beam position can be measured by using the opposite pickups set to the horizontal (vertical) direction. The pickups are made from a 1.3 mm $\phi$  Cu cylindrical pipe, 30 cm in length. The beam tube is made of an aluminum pipe (54.9 mm in inner diameter and 50 cm in length). The beam position is proportional to the difference in signals A and B from the opposite pickups of the BPM. For the linear BPM, the beam position ( $y$ ) is calculated as follows:  $y = a(A - B)/(A + B) = a\Delta/\Sigma$ , where  $a$  is the aperture factor of the monitor.

### Electric Circuit

The four signals of the BPM are transmitted to the electric circuit from 50 ohm SMA feedthroughs connected with the pickups by coaxial cables. Fig. 35 shows the electric circuit. The main parts of this

circuit comprise bandpass filters (BPFs) of 250 MHz in center frequency, 25 MHz in band width, 60-dB amplifiers, and synchronous RF-receivers. The RF signals from the pickups first pass matched bandpass filters (250 $\pm$ 12.5 MHz), which respond to a single-bunch signal by a 250 MHz RF-burst that is about 40 ns wide. The RF-burst signals are transmitted to the 60-dB amplifier and are detected by the synchronous RF-receivers. On the other hand, the pickup signals divided by power dividers (P/D) are transmitted to a hard limiter (L/A) comprising 5 cascaded RF limiter-amplifier integrated circuits. The 250-MHz signals can be demodulated by a homodyne mixer (DBM), which provides an amplitude-envelope of the 250 MHz signal at the output of the low-pass filter (LPF). Then the signals drives to the sample-hold (S/H) module, which detects the gated peak of a pulse. The output signals of the S/H-modules are fed directly to the CAMAC ADC module, which digitizes the peak voltage and are read out in real time by a personal computer which calculates the beam position.

### Bench Test

Fig. 36 shows a schematic view of the test bench. The BPM is set at the center of the bench connected to the precision micro-adjustable stage. The broad matching transformers are connected to both sides of the BPM. These matching sections need to match the cable impedance to the characteristic impedance of the beam tube. The conventional technique (employing a thin current-carrying wire (2.3 mm $\phi$ ) stretched through the center of the monitor to simulate the beam) was used. The position of the wire relative to the monitor was changed by fixing both the wire and the matching sections and moving the monitor with the precision micro-adjustable stage. Fig. 37 shows the sensitivity curve for the out-

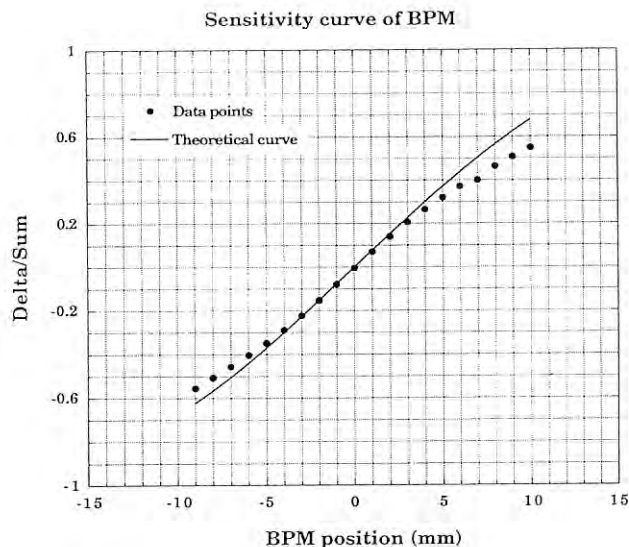


Fig. 37  $\Delta/\Sigma$  versus position measurements along with horizontal direction.

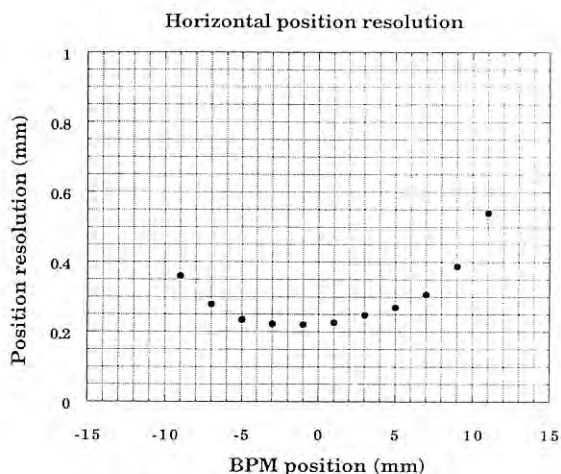


Fig. 38 Position resolution versus position measurements along with horizontal direction.

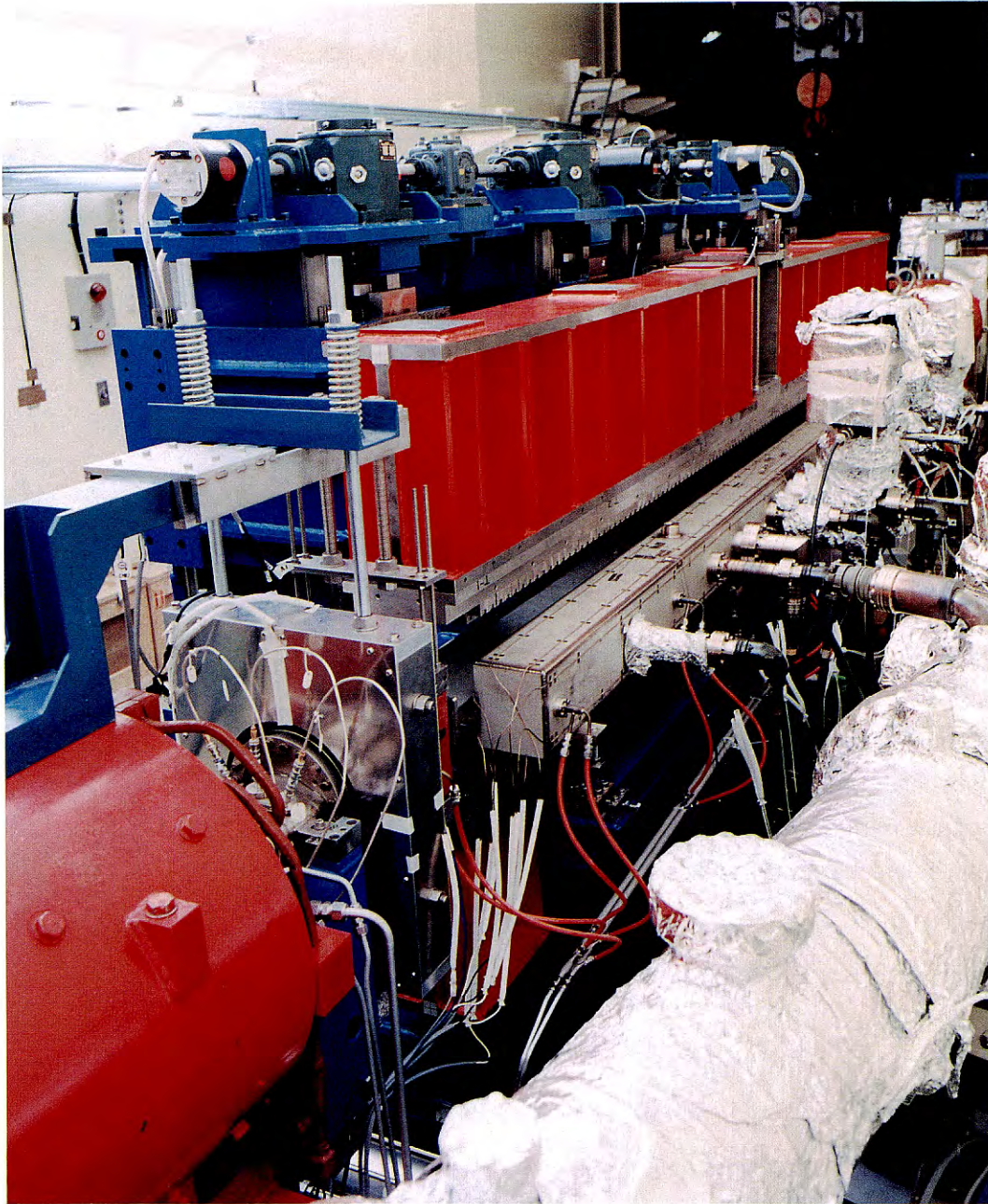
As mentioned above, the BPM using wireline pickups was developed so as to improve the beam operation of the electron/positron beams at the PF 2.5-GeV linac. Especially, in the beam injection into the B-factory, the BPM needs to be used due to the wakefield effects caused by any beam displacement from the central orbit. In this bench test the accuracy of the BPM was about 0.25 mm by one-standard deviation over a  $\pm 5$  mm region from the center position. This accuracy is mainly attributed to the instability and to the noise level of the hard limiter in the electric circuit. Upgrades of the electronics and further study are continuing.

*T. Suwada and T. Urano*

puts of the pickups measured by moving the monitor along to the horizontal direction. These experimental data points nearly coincide with the theoretical curve in the central region after correcting for the pedestals of the ADC modules as well as the gain variations of the amplifiers to the pulse height. Fig. 38 shows the difference between the data and the values calculated by using the least-square fit of a straight line over a  $\pm 5$  mm region. As the results show, an accuracy of about 0.25 mm was yielded over a  $\pm 5$  mm region from the wire center.



# ***Light Source***



*Optical klystron installed in the 5-m straight section of the storage ring (see 5.1)*

You can jump to the article by clicking its title.

# CONTENTS

	Page
<b>A. INTRODUCTION</b>	R – 1
<b>B. SINGLE-BUNCH OPEARTION</b>	
1. NEW BEAM PURIFICATION METHOD	R – 3
<b>C. IMPROVEMENTS AND DEVELOPMENTS</b>	
1. INJECTION	R – 5
Replacement of a Ceramic Duct of the Injection Kicker Magnet	
2. RF	R – 5
Development of a Longitudinal Feedback System	
3. VACUUM	R – 6
Water-Leakage Accident in a Vacuum Duct	
Installation a Copper Duct	
Construction of a Test Beam-Port in the Ring Tunnel	
4. MAGNET	R – 9
Reinforcement of the Sextupole Magnet Power Supplies	
5. INSERTION DEVICES	R – 9
FEL Oscillator at the PF Ring	
Control System for the Superconducting Wiggler	
6. MONITOR	R – 12
Installation of an Additional Beam Position Monitor	
Test of Fast-Digital Beamline Feedback System	
Installation of a New DC Current Monitor	
Horizontal Distortion of the Storage Ring	
Upgrade of the Photon Counting System	
Installation of a Fast Beam Position Detector	
7. CONTROL	R – 16
Replacement of the Main Console Switch Panel System	
8. BEAM CHANNEL	R – 16
Operation of a Fast-Closing Valve System	
Heat-Load Experiments Using Multipole Wiggler Radiation	
<b>D. LIGHT SOURCE SPECIFICATIONS</b>	R – 22

## A. INTRODUCTION

A big vacuum accident occurred on December 16, 1991. A water-cooled SR-absorber just downstream of the wiggler melted due to high-power radiation at a beam current of 290 mA during a test operation of the superconducting wiggler (BL-14) with 5T, 5-pole. A large amount of water flowed into the ring duct. Although the interlock system completely closed and all of the isolation valves in the storage ring immediately operated within one second, 2/3 of the ring circumference was contaminated by water vapor. The broken absorber was made of stainless steel. It was an old mistake which had occurred in the early days of the Photon Factory; the absorber had been believed to be made of copper. It was 8-days before a long scheduled shutdown. The remainder of the user time was therefore canceled, and recovery work started immediately. It was lucky that the accident took place during the time for accelerator-physics studies, and all of the isolation valves for beamlines had been closed. Therefore, no downstream beamline suffered due to this serious problems. After two months of hard recovery work, we started storage ring operation again from February 12, 1992.

During the scheduled summer shutdown from July 11 to September 30, 1992, large modifications related to the vacuum system were carried out. It was a large-scale venting of the storage-ring ducts; more than 2/3 of the vacuum ducts were vented. The following work was carried out during the summer shutdown:

1. An optical klystron was installed in the straight section between B01 and B02 in exchange for the 120-pole undulator.
2. In straight section B04-05, three components were installed for the following accelerator-physics studies; (i) a fast kicker magnet for precise measurements of the dynamic aperture, (ii) an rf-cavity for feedback to suppress any longitudinal beam instabilities under low energy operation, (iii) a pick-up electrode system for a beam-position monitor to test bunch-to-bunch transverse feedback.
3. Installation of a copper-made straight chamber downstream of VW#14 for testing outgassing under high-power synchrotron radiation.
4. The ceramic duct of injection kicker K3 was replaced by a new one. The old kicker duct had a heating problem under single-bunch operation in excess of a beam current of 100 mA.
5. MPW#16 at BL-16 was removed from the storage ring, since the permanent-magnet arrays of this wiggler were first made of Neomacs-permanent magnets, and had a problem in that the magnet pieces sometime fell off during users' runs. We therefore closed BL-16 during the autumn-run, and replaced then with a new magnet array. New types of Neomacs and redesigned holders were developed. We finished the trimming work of the magnetic-field strength in November. This wiggler was reinstalled in January, 1993.
6. A new beam-current monitor (DCCT) was installed downstream of the optical klystron/undulator.
7. The photon-beam position monitors of BL-21 and other beamlines were repaired and reconditioned.
8. The old and bad-conditioned components of beam channels were replaced.
9. The insulation oil of the high-voltage klystron-power supplies was checked and exchanged with new oil.

The FEL-project at the PF storage ring is underway. This project involves FEL research for developing a shorter wavelength region. A gain measurement at 177-nm is our present goal. High-quality beams under 0.75-GeV operation were essential for this project. For this project, we use BL-2 where, at present, the 120-pole undulator is operating as the most popular insertion device at the Photon Factory. This undulator was replaced by an optical klystron during the summer shutdown. The optical klystron has a special structure in that the magnet configuration can be switched back to that of the undulator. During users' runs, it can be operated completely under the undulator mode, including independent-gap tuning. The time for the FEL-study is prepared between users' runs by taking extra runs of typically several days. On December 7, 1992, a spectrum of spontaneous radiation from the optical klystron was observed at a beam energy of 0.75 GeV.

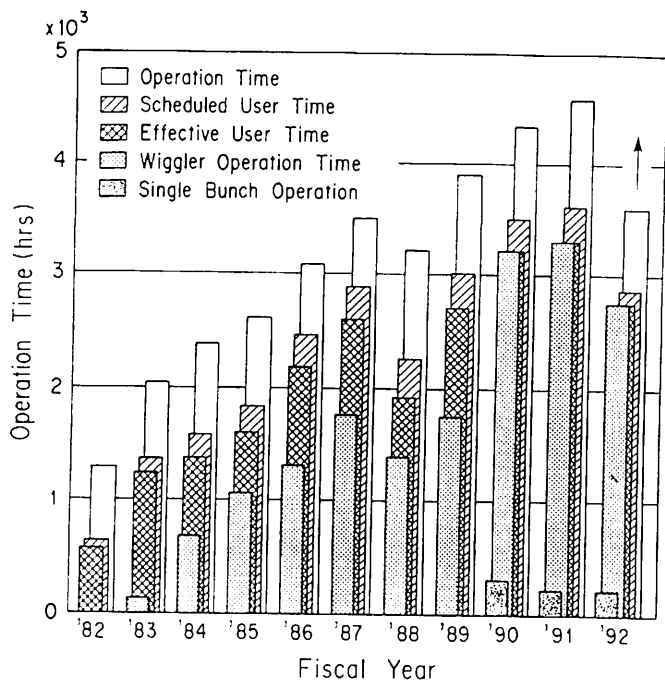


Fig. 1 Operation times of the storage ring.

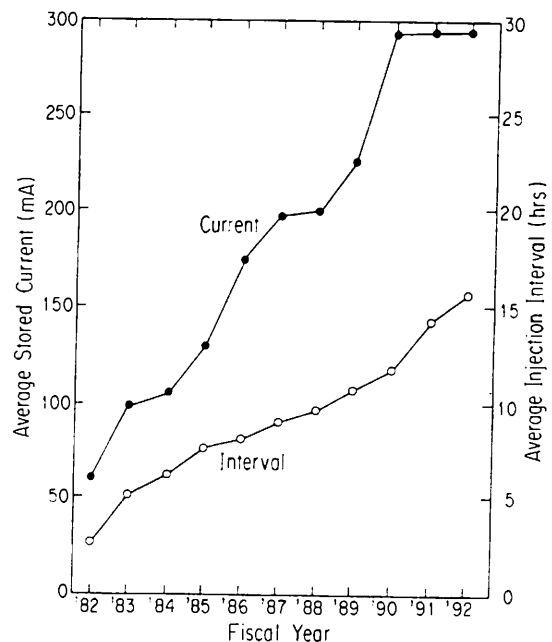


Fig. 2 Average stored currents and injection intervals.

It was more than ten years ago, March of 1982 when the PF storage ring stored its first electron beam. Since the lifetime was only 4 minutes at 6 mA, it was only 0.024 Amp-min. On March 13, 1992, we held a small 10-year celebration party. "Old soldiers" met at the conference room of the PF research building and talked about old heroic episodes. On December 3 and 4, 1992, we held a symposium to look back at this decade of the Photon Factory, and to consider the next ten years.

We are planing to upgrade the storage ring; the present horizontal emittance of the beam is 130 nm-rad. The new plan is to reduce the emittance by a factor of 5 by changing the lattice and increasing the brilliance by 10 times. Under this plan we must add new quadrupole and sextupole magnets, each of which will have a small-bore radius of 40 mm (the present bore radius is 55 mm); their side-yokes are open for the beamline ports. Since the bending magnets will not be changed, the source points and lines of the synchrotron light will also not be changed.

Almost all of the vacuum system must be significantly changed: the bending magnet ducts, beam channel ports, straight ducts and beam-position monitors and so on. The rf-cavities should be replaced by improved ones in order to suppress any higher-order-mode resonances.

## SUMMARY OF STORAGE RING OPERATION

A summary of the operation times of the storage ring is given in Fig. 1. Table 1(a) shows the operation statistics for the fiscal year 1991, and (b) those of between April 4 and December 21, 1992. The injection intervals and average currents are given in Fig. 2. The initial stored current is 350–360 mA for a user-run and the beam lifetime is more than 60 hours at 300 mA. The average stored current is about 300 mA during 24-hours of operation. During fiscal year 1991, 208.1 hours were provided for single-bunch users. In fiscal year 1992, the single-bunch time was 216.5 hours, as listed in Table 1(b). The beam lifetime at 50 mA is 10–20 hours, and is limited mainly by the Touschek effect. Cleaning of the beams in the neighboring buckets routinely takes place every beam injection. The ratio of the satellite bunch to the main one is becomes less than  $10^{-5}$  by using the rf knock-out and vertical scrapers at B04-B05.

Figure 3 is a plot of  $I\tau$  (beam current  $\times$  lifetime), which is a good standard of the storage-ring performance. The value of 1400 Amp-min in 1991 was very large; it is presently being kept at around 1000 Amp-min now.

Table 1(a). Statistics of the storage ring operation during fiscal year 1991.

	Multi-bunch	Single-bunch	Total
Ring Operation Time (hours)	—	—	4557.5
Scheduled user time (hours)	3284.0	344.0	3628.0
Net user time T (hours)	3062.7	208.1	3270.8
Time used for injection (hours)	99.0	12.6	111.6
Integrated current in T (Ahours)	888.1	7.1	895.2
Average current in T (mA)	290.0	34.1	—
Number of injections	224	25	249
Interval between injections (hours)	13.7	8.3	—

Table 1(b). Statistics between April 4 and December 21, 1992.

	Multi-bunch	Single-bunch	Total
Ring Operation Time (hours)	—	—	3560.0
Scheduled user time (hours)	2635.0	232	2867.0
Net user time T (hours)	2527.4	216.5	2743.9
Time used for injection (hours)	59.7	11.8	75.1
Integrated current in T (Ahours)	736.2	10.1	746.3
Average current in T (mA)	291.2	46.5	—
Number of injections	162	22	184
Interval between injections (hours)	15.6	9.8	—

## B. SINGLE-BUNCH OPERATION

### 1. New beam purification method

During single-bunch operation, any undesired satellite bunch which follows a main bunch can be eliminated by a purification method<sup>1)</sup> just after the beam injection. However, after that, the current of a satellite bunch gradually increases since positrons in the main bunch are scattered out by the Touschek effect, and are then captured by the satellite bunch with a certain probability. The impurity is defined by the ratio of the satellite-bunch current to the main-bunch current ( $I_s/I_m$ ) and should be less than  $\sim 10^{-5}$  for good synchrotron radiation experiments using a single bunch beam.

Assuming that there are only two bunches (a main bunch and a neighboring satellite bunch), the relation between the current of the main bunch and the satellite bunch can be expressed by following equations:

$$\frac{dI_s}{dt} = P \left( -\frac{dI_m}{dt} \right) - \frac{I_s^2}{(I \cdot \tau)_s}, \quad (1)$$

and

$$\frac{dI_m}{dt} = -\frac{I_m^2}{(I \cdot \tau)_m}. \quad (2)$$

where  $P$  is the capture probability,  $I$  the beam current (equivalent to the number of positrons), and  $\tau$  the beam lifetime.  $I_m$  and  $I_s$  denote the current of the main bunch and that of satellite bunch, respectively. The product  $I\tau$  is a constant for each bunch under the same operational conditions, since the probability of scattering is proportional to the positron density in a bunch. Other effects, such as bunch lengthening are ignored. For the initial conditions  $I_m(0) = I_0$  and  $I_s(0) = 0$ , the solution is approximately given by

$$I_s(t) = P(I_0 - I_m(t)) \quad \text{for } P \ll 1/4. \quad (3)$$

The same solution can be obtained when the decay of the satellite bunch (the second term in Eq. (1)) is neglected. From Eq. (3), the growth rate of the impurity is given by

$$\frac{d}{dt} \left( \frac{I_s}{I_m} \right) = \frac{P \cdot I_0}{I \cdot \tau} = \text{const.} \quad (4)$$

which indicates that the growth rate is constant in terms of time.

Using a photon-counting system,<sup>2)</sup> the relative number of positrons in a main bunch and a satellite bunch were measured (Figs. 4 and 6), as well as the impurity ( $I_s/I_m$ ) as a function of time (Fig. 5). The



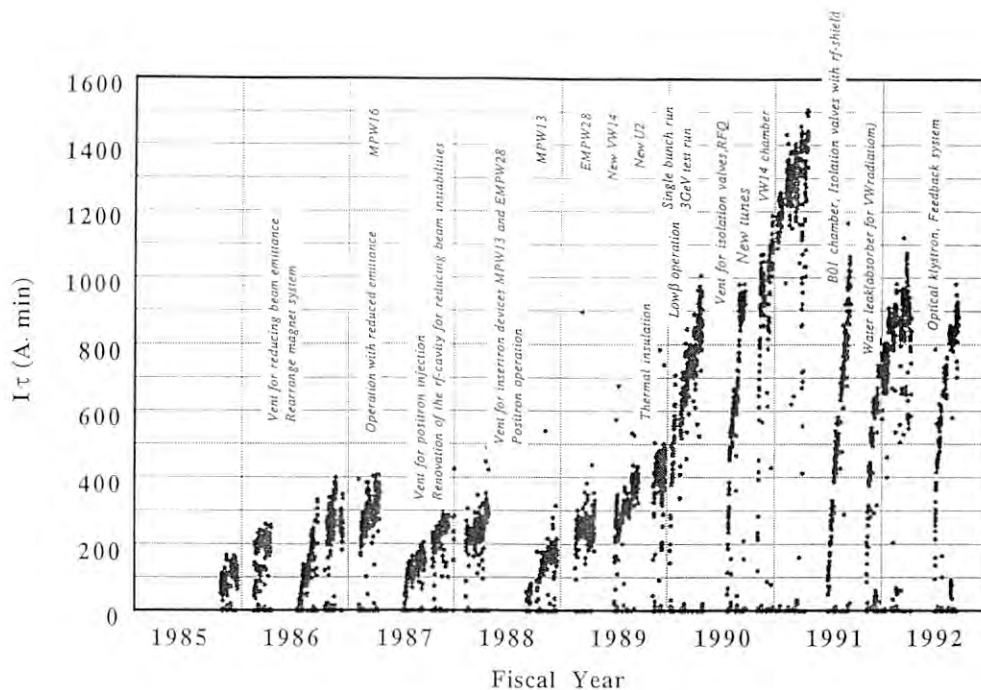


Fig. 3 Plot of  $I\tau$

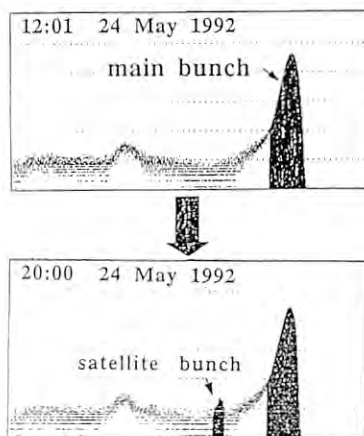


Fig. 4 Change in the bunch population under single-bunch operation observed by a photon counting system without continuous purification.

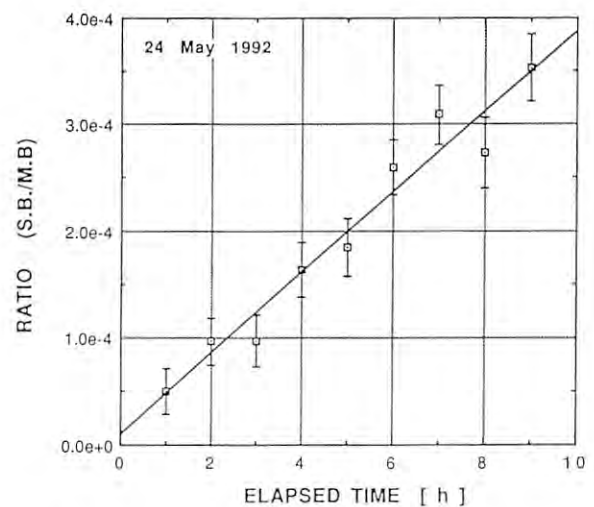


Fig. 5 Impurity ( $I_s/I_m$ ) as a function of time.

beam current decayed from 60 mA to 40 mA and the impurity ( $I_s/I_m$ ) increased to  $3.5 \times 10^{-4}$  during nine hours' of operation (Fig. 4). By inspecting Fig. 5, the growth rate of the impurity was estimated to be  $6.3 \times 10^{-7}/\text{min.}$ , and a probability  $P$  of  $3.5 \times 10^{-4}$  was derived.

To keep the impurity less than  $\sim 10^{-5}$ , a continuous purification method was employed. Although the principle is similar to that of the purification

method,<sup>1)</sup> no scraper is necessary with this method: the betatron oscillation is excited by continuously sweeping rf knock-out signals. As described in Ref. 1, the tune is first measured at low ( $\leq 1$  mA) and high ( $\geq 40$  mA) beam currents. Then, the center frequency, the scanning width and the amplitude of the rf signals are determined so as not to affect the main bunch, even when the current of the main



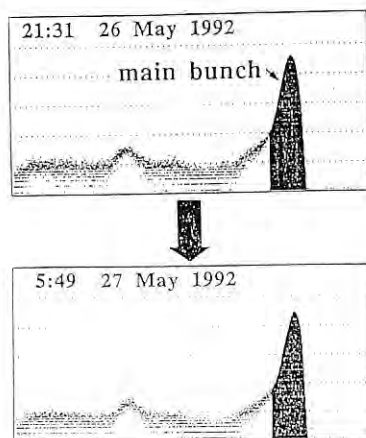


Fig. 6 Change of the bunch population in single-bunch operation observed by photon counting system<sup>2)</sup> with the continuous purification.

bunch decays and its tune come close to the exciting rf frequency.

The growth of a satellite bunch was measured again after 8 hours (Fig. 6). No satellite bunch was detected and, thus, the impurity ( $I_s/I_m$ ) was kept below the maximum sensitivity of this measurement ( $\sim 10^{-5}$ ) during the run. This fact shows that this purification method is effective for suppressing any impurity.

## References

- 1) Photon Factory Activity Report 1990.
- 2) Photon Factory Activity Report 1991.

## C. IMPROVEMENTS AND DEVELOPMENT

### 1. INJECTION

#### 1.1 Replacement of a Ceramic Duct of the Injection Kicker Magnet

One of the ceramics ducts of the injection kicker magnet (K3) was replaced with a new one since the temperature rise at that ceramic duct had abnormally reached approximately 44 °C during single-bunch operation (Fig. 7). Since the ceramic ducts are cooled by air, the temperature rise had been normally kept below 36 °C, even at a beam current of 100 mA under single-bunch operation, as well as 350 mA under multi-bunch operation.

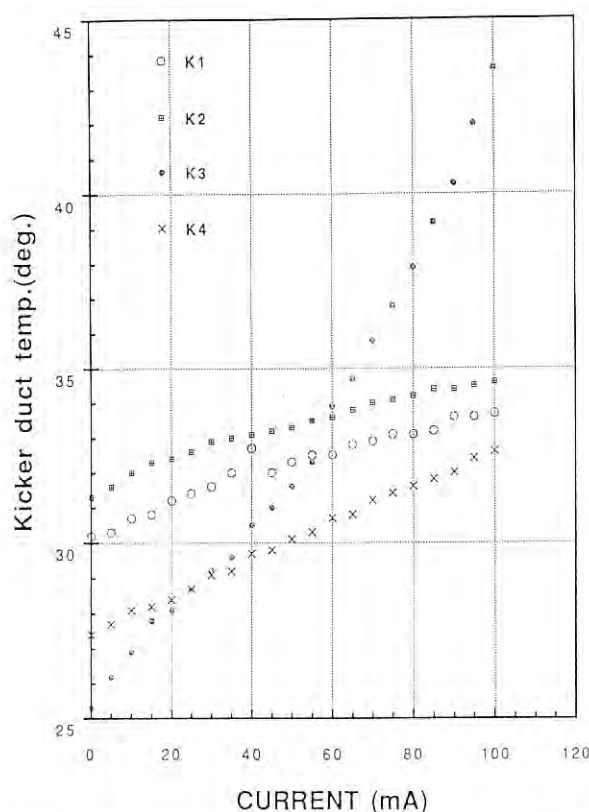


Fig. 7 Measured temperature rise of the vacuum duct.

The ceramic ducts are coated over the inner surface with a Titanium membrane of 6–10  $\mu\text{m}$  thick. However, the duct in question had a trace amount of discharge, such as “ladder of stockings”, from the nearby Kovar collar to the inside of the duct. This was probably due to a discharge which first began at a small crack in the membrane near to the Kovar collar, and was gradually grew during every injection.

After replacing the duct, kicker magnet K3 was operated without any problem.

### 2. RF

#### 2.1 Development of a longitudinal feedback system

Under low-energy (0.75 GeV) operation for FEL experiments, the longitudinal coupled-bunch instability is one of the most severe problems that limit the maximum beam currents and beam quality. The longitudinal coupled-bunch instability has been suppressed by applying Robinson damping<sup>1)</sup> during test operation. Since this method is effective only for

Table 2. Specification of the feedback cavity.

Resonant frequency	$f_{\text{res}}$	500.1 MHz
Unloaded-Q	$Q_0$	630
Loaded-Q	$Q_L$	80
Filling time	$T_f$	51 ns
Shunt impedance	$R_{\text{sh}}$	110 k $\Omega$
Maximum gap voltage	$V_c$	750 V



Fig. 8 Installing the feedback cavity.

single-bunch operation, a longitudinal feedback system is under development in order to realize 4-bunch operation for FEL experiments.

For our feedback system, a bunch-by-bunch feedback scheme<sup>2,3)</sup> was employed. Phase oscillation of each bunch is detected with a button-type electrode signal. The oscillation signals are amplified and their phases are shifted by 90° to obtain energy-oscillation signals. With these signals, a correction voltage is applied to each bunch with a feedback cavity, thus damping longitudinal oscillations.

The feedback cavity is a ceramic-loaded rectangular cavity. The cavity body, made of stainless steel, is located in the air, and a ceramic gap inside the cavity breaks the ring vacuum from the air. A maximum gap voltage of 750 V is obtained at an input power of ~22 W. The feedback cavity was designed using the computer code MAFIA. The principal parameters are shown in Table 2. The cavity was fabricated and installed during the last summer shutdown. Figure 8 shows a scene during the installation of the cavity. Feedback circuits were also fabricated and being tested.

## References

- 1) Photon Factory Activity Report #8 (1990) p. R-6.
- 2) T. Kasuga, M. Hasumoto, T. Kinoshita and H. Yonehara, Jpn. J. Appl. Phys., 27, (1988) p. 100.
- 3) M.A. Allen, M. Cornacchia and A. Millich, IEEE Trans. on Nucl. Sci. NS-26 (1979) p. 3287.

## 3. VACUUM

### 3.1 Water-leakage accident in a vacuum duct

An accident occurred on December 16, 1991, during a machine-study concerning the 5-pole-operation of VW#14 (superconducting vertical wiggler) at a beam current of 290 mA.

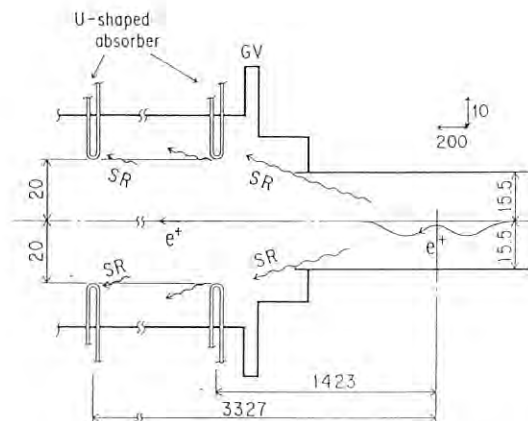
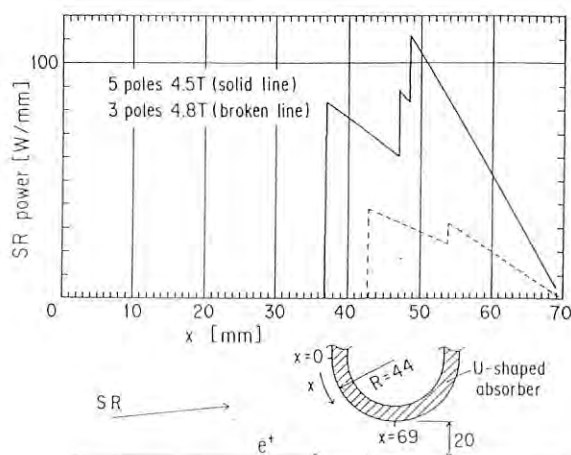
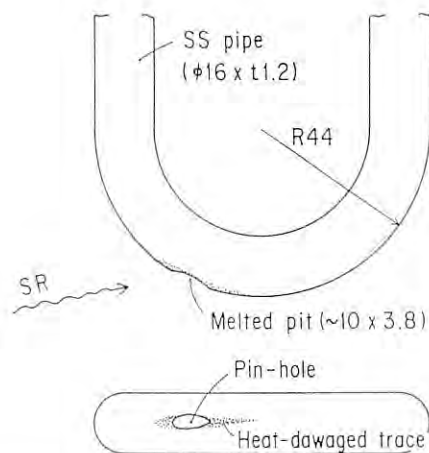
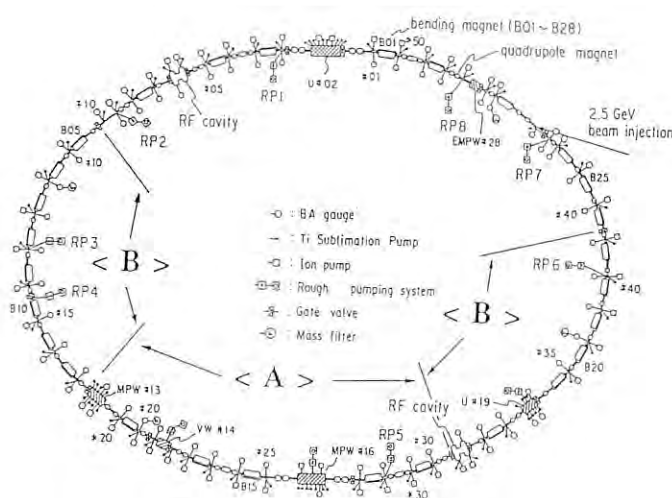
The pressure downstream of the VW#14 increased abruptly; the stored beam was dumped. The vacuum interlock system, triggered by failure signals of two neighboring SIPs (sputter ion pumps), immediately closed all of the sector valves in the ring, and turned off all B-A gauges. The pressure in section <A> (Fig. 9) was so high that the SIPs could not be re-started.

A water leak from the photon absorber was at first suspected. We drained the water from all four absorbers for VW#14; an air-leak through one of the absorbers was soon detected. We decided to vent section <A> and to check these absorbers. When one of the flanges at the bottom pits of the duct was dismantled, a bucket of water came out.

We found that two absorbers just downstream of VW#14 were unexpectedly made of stainless steel, and two others slightly distant downstream were made of copper.

A melting trace and a pinhole were found on the leaking absorber, as illustrated in Fig. 10. We removed and cleaned all of the duct components contaminated by liquid water. Fortunately, no "liquid" water was found in any other ducts. Since the pressure in section <B> of Fig. 9 did not recover as before, due to the high partial pressure of H<sub>2</sub>O, we baked out sections <A> as well as <B>. The front-ends of the beam lines connecting the sections were also damaged and needed baking. The vacuum in other sections was protected by the interlock. The ring was shut down and the schedule for users' runs for eight days were canceled.

Water leakage from the absorber was caused by the following reasons: Four U-shaped cooling water



pipes used as photon absorbers were situated downstream of VW#14 in order to shield the pumping ports and electrodes of BPM (beam position monitor) from the irradiation of synchrotron radiation generated by VW#14. The leaking absorber located at the upper part near the VW#14 was exposed to the most intense synchrotron radiation (Fig. 11). Figure 12 shows the calculated input power distributions on the absorber for 5-pole-operation (290 mA) during a machine study, and 3-pole-operation (350 mA) during the usual users' runs.

The stainless-steel absorbers were replaced by copper absorbers. The restoration work went smoothly. Operation of the ring started again from February 12, as scheduled. The changes in the average ring pressure ( $p/I$ ) normalized by the beam current, and the product of the beam lifetime and beam current ( $I\tau$ ) after the restorations are shown in Fig. 13. For a comparison, plots made after the summer shut down in 1991 are also shown in the figure. The ring vacuum and the beam lifetime recovered very quickly. It can be explained by the following facts: 1) almost all of the ducts had not been exposed to the atmosphere for a long time, except for the wetted duct; 2) the contamination by water and/or water vapor might be within top surface of the duct wall, and thus it was easily eliminated by SR irradiation.

### 3.2 Installation of a copper duct

During the summer shut-down in 1992, we installed a copper duct in exchange for the Al duct downstream of VW#14, where a water-leak accident occurred in the end of 1991, as described in the pre-

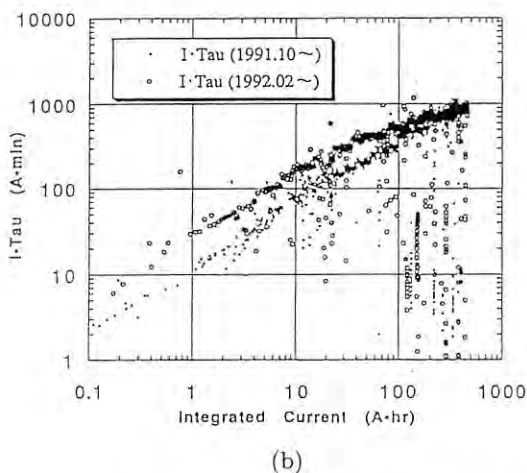
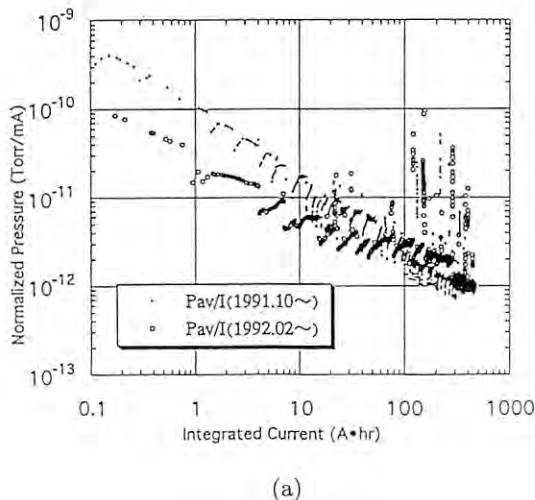


Fig. 13 a) Changes in the normalized pressure ( $p/I$ ) as a function of the integrated beam current. b) Changes in the beam lifetime ( $I\tau$ ) as a function of the integrated beam current.

vious section. The installation of the new duct was a scheduled task, and its purposes were: 1) to manufacture and test a copper duct of which the inner surface is machined in order to reduce a PSD (photon stimulated desorption) yield; 2) to reduce any radiation damage caused by irradiation (critical energy = 20 keV) from VW#14 which can easily penetrate the beam duct wall made of aluminum alloy; and 3) to allow it to work as a photon absorber with a water-cooling channel.

Figure 14 shows drawings of the copper duct. It comprises of a straight copper duct 1.7 m long, two pumping ports, a BPM (beam position monitor) section and two bellows. As shown in Fig. 14, the

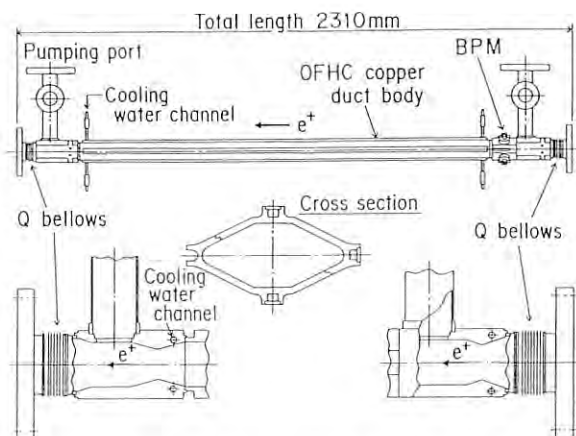


Fig. 14 Drawing of the copper duct.

copper duct has water-cooling channels to absorb any vertically radiated photons from VW#14.

The bellows, conflat flanges and pumping ports are made of stainless steel. The duct was assembled not by brazing, but by welding and EBW (electron beam welding). Inconel was used as an intermediate material for welding.

The BPM section of copper was constructed very precisely in one block, and then BPM electrodes with Kovar collars were welded onto it. The inner surface of the duct was machined using an NC miller, since the experimental results<sup>1)</sup> at BL21 showed that machining the inner surface is most effective to reduce the PSD yield ( $\eta$ : molecules/photon). Since photons from the upstream bending magnet cannot reach the copper duct because of the narrow VW duct, only VW#14 can be considered to be a SR source. By assuming the copper duct to be a closed chamber, the  $\eta$  for the duct can be estimated based on the pumping speed and the number of incident photons. The incident photons can also be estimated by calculating the power distribution of synchrotron radiation over the duct (Fig. 15). The estimated  $\eta$  as a function of the integrated photon dose is shown in Fig. 16, where  $\eta$  is the nitrogen equivalent  $\eta$ . For comparison, the result obtained in our study<sup>1)</sup> is also shown in the figure. Though  $\eta$  was large at the beginning of the ring operation, it became smaller quickly.

## Reference

- 1) S. Ueda, M. Matsumoto, T. Kobari, T. Ikeguchi, M. Kobayashi and Y. Hori; Vacuum, 41 (1990) 1928.



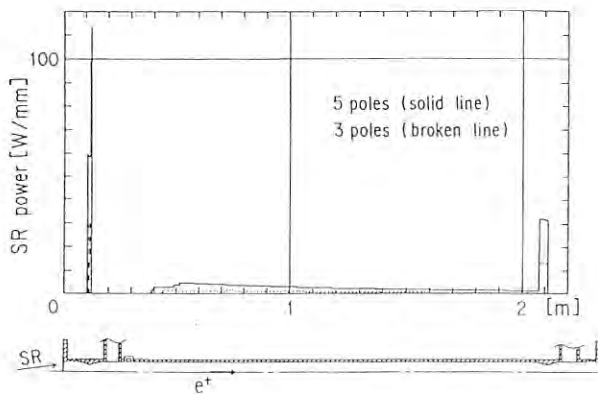


Fig. 15 SR power distribution on the upper side of the copper duct.

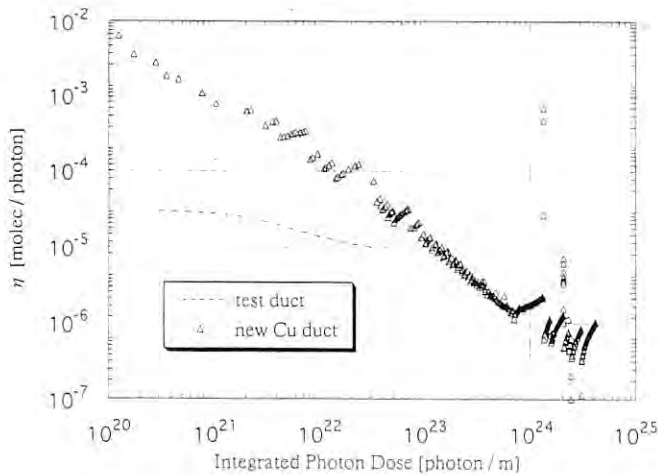


Fig. 16 Estimated  $\eta$  of the copper duct after installation.

### 3.3 Construction of a test beam-port in the ring tunnel

A test beam-port from bending section B24 was constructed. It is used for experiments concerning machine development, such as SR irradiation tests of materials.

The test beam-port is schematically shown in Fig. 17. A vacuum interlock system is equipped in order to immediately close an absorber (SR beam stopper) and a gate valve when an upstream B-A gauge detects a pressure higher than the predetermined set point. There are two branch lines downstream of the test beam-port, through which a 12 mrad and a 3 mrad of SR in the horizontal plane are extracted to the experiments. The 3-mrad line has been in operation since November, 1992. The

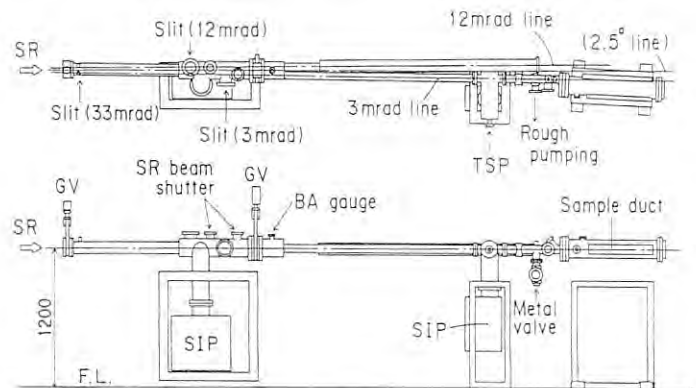


Fig. 17 Schematic view of the beam line.

outgassing characteristics of a material under SR irradiation were examined at this test beam-port with the collaboration of NKK Co.

## 4. MAGNET

### 4.1 Reinforcement of the Sextupole Magnet Power Supplies

The power supplies of the sextupole magnets (SX) were additionally installed in order to obtain large positive chromaticities and/or to suppress any non-linear effects of the sextupole fields on the beam.

The new power supplies can excite these magnets to be 1.5-times higher than the old ones. Figure 18 shows the excitation curve of the SXs. Although the magnetic field does not saturate up to a maximum current of 7 A, it is necessary to cool the magnets for currents exceeding 5 A. Since eleven pairs of SXs are independently excited by eleven new power supplies, we are able to adjust eleven kinds of sextupole strengths. During user's run, a normal chromaticity correction (two family corrections) is made using two types of sextupole strengths: focusing (SF) and defocusing (SD). The sextupole excitation currents are shown in Fig. 19 as a function of the chromaticities. As shown in Fig. 19, we can operate the ring with a large positive chromaticity.

## 5. INSERTION DEVICES

### 5.1 FEL Oscillator at the PF Ring

An optical klystron (TOK) with a period length of 9 cm was constructed and installed into the 5-m long straight section (B01-B02) in October (Fig.

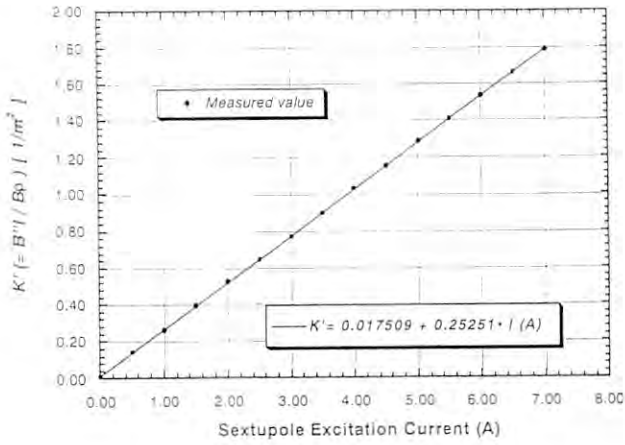


Fig. 18 Excitation curve of SXs.

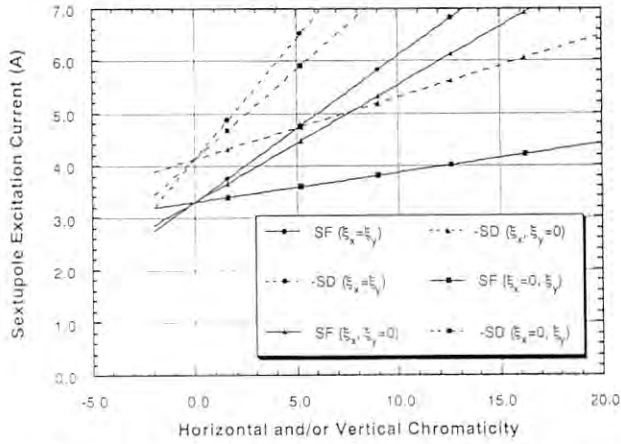


Fig. 19 Sextupole excitation currents as a function of chromaticities.

20). This TOK will be used as (1) a component of an FEL oscillator in the VUV region, and (2) an insertion device (U#02) with a period length of 6 cm for soft x-ray (SX) experiments at BL-2. For compatibility between FEL and SX experiments, the TOK was designed so that any exchange of magnet arrays for FEL ( $\lambda_u = 9$  cm) or SX ( $\lambda_u = 6$  cm) can be made quickly.

The design parameters for FEL operation are shown in section D. The choice of the beam energy (0.75 GeV) was made for the following reason. Although the natural emittance is decreased by lowering the beam energy, the emittance growth by intra-beam scattering becomes remarkable. The minimum emittance of the ring is expected to be obtained as 15 nm-rad at 0.75 GeV, higher than the natural one

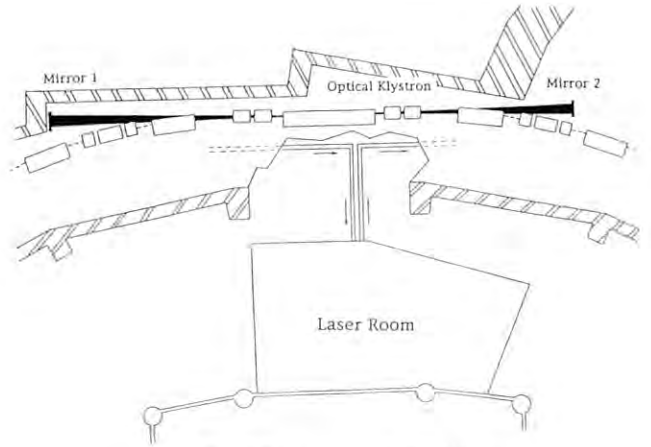


Fig. 20 FEL system at the PF ring.

by a factor of 1.5.

Considering the gain measurement, the target wavelength for FEL (1770Å) has been chosen as described below. We have chosen the parameters of TOK, such as the periodic length, number of periods, deflection parameter and  $N_d$  (the ratio of the distance between the two wavepackets to the laser wavelength), so that a maximum gain of 0.6%/Amp can be obtained. Figure 21 is a schematic drawing of the TOK.

Since the maximum peak current of a bunch is expected to be 30A, so that the maximum gain should be 18%. However, the net gain should be 6% since the cavity loss is estimated to be at least 12%. As shown in Fig. 20, the cavity comprises two mirrors (M1 and M2) placed at a distant of 23.4m. Although  $\text{MgF}_2$  dielectric multilayer mirrors have a maximum reflectivity of 96% in the wavelength region around 1770Å, degradation of reflectivity is caused by the irradiation of soft x-rays. Mirror M1 will be directly irradiated by spontaneous emission containing a large number of soft x-rays. Therefore, we have chosen an ultra-high-vacuum (UHV) Al mirror for M1 and a  $\text{MgF}_2$  mirror for M2. A maximum reflectivity of 92% has been reported for a UHV Al mirror.

We have been preparing a gain measurement system employing a coherent radiation scheme using a laser. Instead of a CW laser system, which is not available for the VUV region, we have employed a mode-lock Nd-YAG laser system in combination with a regenerative Nd-YAG amplifier. Figure 22 shows a schematic diagram of the gain-measurement system. Coherent radiation of 1770Å can be ob-

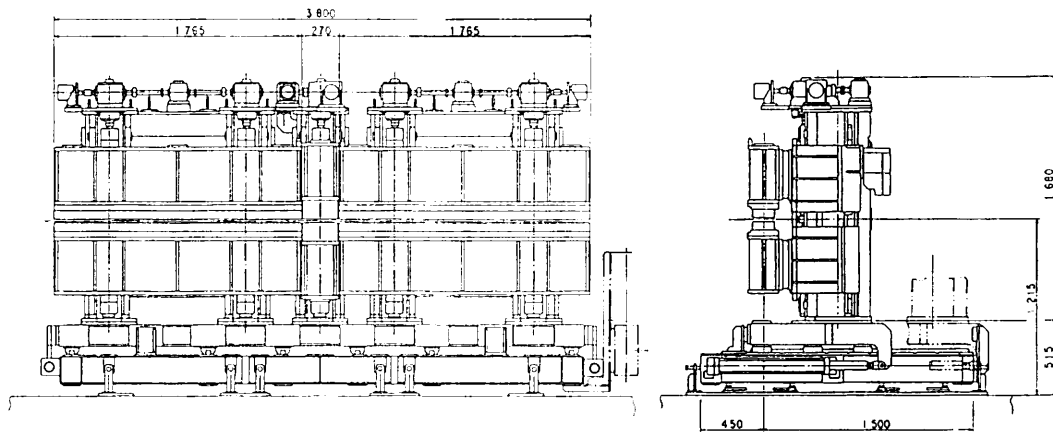


Fig. 21 Schematic drawing of the TOK.

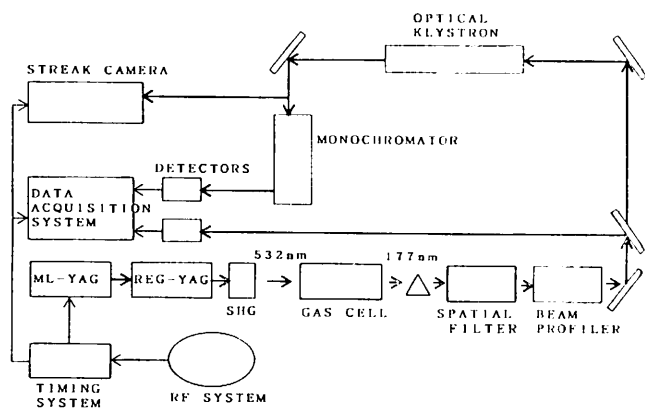


Fig. 22 Schematic diagram of the gain-measurement system.

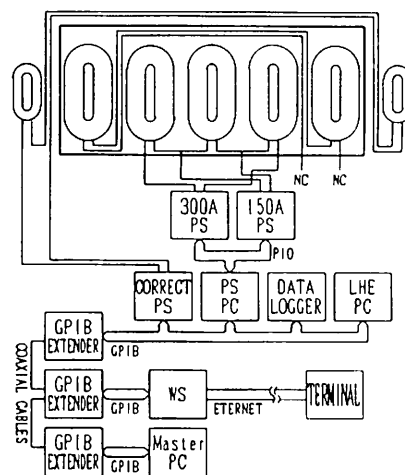


Fig. 23 Control system of the superconducting vertical wiggler.

tained by third-harmonic generation using Xe gas or Cd vapor as a harmonic material with an input laser power of 200 MW at 5320Å. The maximum pulse power at 1770Å is expected to be 1 kW. An experiment concerning the gain measurement will be carried out at the end of FY1992. After that, the oscillator experiment will be continued.

## 5.2 Control System for the Vertical Wiggler

A control system for the 5-pole superconducting vertical-wiggler (4.8 Tesla) has been built according to a master-slave configuration. The control system comprises three PC-9801 personal computers (PC) connected to each other through a GPIB interface (Fig. 23).

One of the computers is used as a master computer and an operator console display, which is placed in the control room of the storage ring. The

master accepts any GPIB service requests from two slave computers (PS-PC and LHe-PC). By communicating between these slave computers, the master can (1) display the operational status of the wiggler, (2) indicate any alarm or a warning message on the console when the wiggler is in abnormal condition, and (3) send a command string (solicited by an operator) to any one of the slave computers in order to set the operational parameters to a component of the wiggler. In addition, the operator can set the correction current to an orbit-corrector through the console display. The orbit-corrector then compensates any closed-orbit errors by controlling the power supply of two steering magnets installed at both sides of the wiggler.

One of the slave computers (PS-PC) is used

to control two power supplies (5V-300A and 5V-150A) for the wiggler magnets. Corresponding to a command string from the master, PS-PC executes preprogrammed sequences; for example, it increases/decreases the currents in the magnets, turns on/off a superconducting circuit switch, and manages a safety interlock.

The remaining slave computer (LHe-PC) monitors the operational status of a liquid-He (LHe) refrigerator, a LHe reservoir tank and a water-cooling system for a photon absorber. It periodically sends such status information to the master. LHe-PC also monitors the surface level of the LHe in the reservoir, and keeps the level within an operational range by turning on/off a pressure-valve in order to supply LHe from the tank to the reservoir when the LHe is consumed during operation of the Wiggler. It also monitors the operational status of the He-cryostat.

A data-logger is used to acquire the following types of data: the temperature of the cryostat, the pressure in a thermally-insulated vacuum chamber of the cryostat and the magnetic field strength of the Wiggler. It then periodically sends such status information to the master.

Since a workstation is also connected to the GPIB bus, the operational status information can be displayed on a terminal display on Ethernet.

## 6. MONITOR

### 6.1 Installation of an additional Beam Position Monitor

For beam-orbit measurements, electrostatic beam position monitors (BPM) are distributed along the storage ring. A BPM unit comprises six button-type electrodes welded onto the vacuum chamber near to the quadrupole magnet.

An additional beam-position monitor (PM47) was installed at the downstream end of B04 (Fig. D-6) having a mechanical precision less than 100  $\mu\text{m}$  in order to measure the beam position at the steering magnet at beamline BL-4. Before installation, the BPM unit was calibrated using a probe antenna to obtain the position sensitivity and displacement of the electrical center from the mechanical center. The electrode signals were switched with a coaxial switch, and fed to a data-processing computer through one of the 8 substations that handle a set of six position monitors. The number of BPMs is now 46 in total.

### 6.2 Test of Fast-Digital Beamline Feedback System

A fast-digital feedback system for stabilizing the photon beam position at beamline BL-4 was tested. This system comprises a fast-digital controller, an existing beam-position monitor and steering magnets. The controller has a 32-bit floating-point DSP (digital signal processor) and a TMS320C30 having a higher performance regarding the signal-processing speed than ordinary microprocessors. The DSP is connected to 16-bit ADCs and 14-bit DACs through a local bus of DSP; it is connected to the bus of a personal computer (PC-9801).

The DSP system takes signals from the photon beam-position monitor at a sampling rate of 10 kHz, and sets the output currents of the power supplies for the steering magnets through the ADCs. The steering magnets make a closed-orbit bump in order to cancel the beam movement at the beamline. The program of the feedback control was coded in C-language and compiled/linked with PC-9801; it was then downloaded to DSP. While DSP is running, the PC-9801 numerically and graphically displays the feedback parameters, such as the photon beam position and the setting currents of the magnet power supplies.

The feedback system was tested at beamline BL-4. Three vertical steering magnets located near to bending magnet BM4 and a photon beam-position monitor at branch beamline BL-4C were used. After the transfer function of the feedback system was measured, the gain/phase characteristics of the feedback system were compensated by adding a compensation part of the control program in order to improve the feedback performance. As a result, the feedback system stabilized the beam position (less than a few Hz) within a few microns (Fig. 24). Figure 25 shows that the feedback system suppressed the beam oscillation up to 100 Hz. For example, beam oscillation with a 14.5 Hz peak, caused by an air-conditioner, was reduced from 22  $\mu\text{m}$  to 1.4  $\mu\text{m}$ . In order to use this system for actual operation at some beamlines, further development (such as an interlock monitoring system and automatic feedback on/off system) is required.



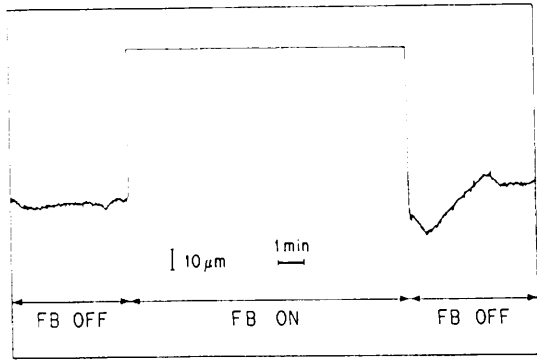


Fig. 24 A typical chart recording of the position monitor signal at BL4.

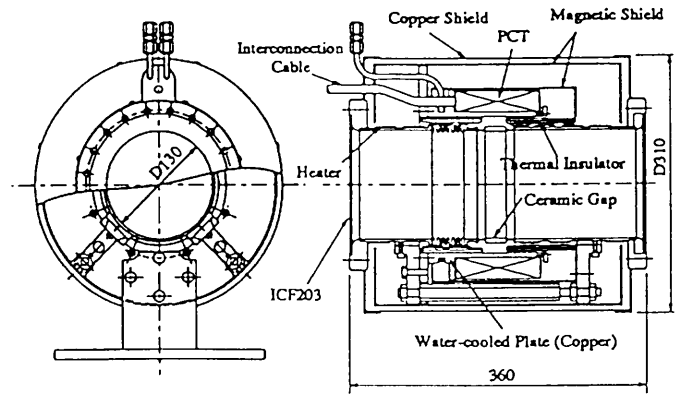


Fig. 26 Mechanical design of the DC current transformer.

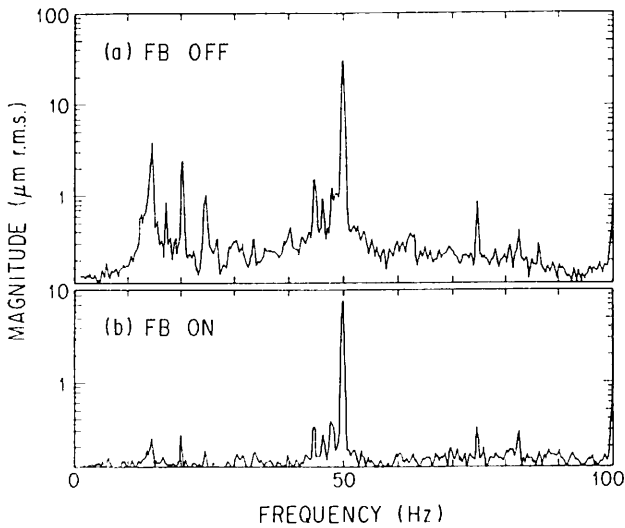


Fig. 25 Frequency spectra of the beam position noise (a) without and (b) with feedback.

### 6.3 Installation of a New DC Current Transformer

A new DC current transformer was installed at the end of a straight section between B01 and B02. The transformer unit comprises a parametric current transformer (PCT)<sup>1)</sup> manufactured by BERGOZ Co., France. The measurement principle of the PCT is the well-known second harmonic detection method using magnetic modulation. The PCT also has an active current transformer in a common feedback loop with a magnetic modulator. Its frequency response ranges from DC to 30 kHz.

A cross-sectional view of the vacuum chamber is shown in Fig. 26. The vacuum pipe has a ceramic insulator (25 mm in length) and a bellows to

minimize any mechanical stress on the ceramic ring. Tape heaters and thermal insulators were placed between the chamber wall and a water-cooled copper cylinder. The temperature of the transformer was held under 45 °C, while the vacuum chamber was baked out at about 180 °C.

Magnetic shields using two concentric cylinders were applied in order to reduce any interference due to environmental magnetic fields caused by B- and Q-magnets of the ring, which generate the largest background field in the ring tunnel. Such magnetic fields reached several tens of Gauss at the PCT assembly. The outer cylinder was made of a permalloy which has a high-saturation flux density ( $B_s \sim 1.5 \times 10^4$  G,  $\mu \sim 10^4$  and 1.2 mm thick) in order to avoid breaking the shielding due to magnetic saturation. The inner cylinder was made of a typical shielding material similar to Mu-metal ( $B_s \sim 0.7 \times 10^4$  G,  $\mu \sim 10^5$  and 2 mm thick). The offset drift of the PCT was successfully suppressed to within  $\pm 12 \mu\text{A}$ , even at maximum exciting currents of B- and Q-magnets.

Figure 27 shows the measured beam currents during injection for the multi-bunch operation. The PCT signal was fed to a lowpass filter (cutoff frequency 1 kHz); its output signal was then measured with a digital voltmeter at a sampling time of 4 ms. This PCT is sufficiently sensitive to observe any change in the beam current (about 20  $\mu\text{A}$ ) at an injection rate of 25 Hz.

### Reference

- 1) K.B. Unser, CERN SL/91-42 (BI).

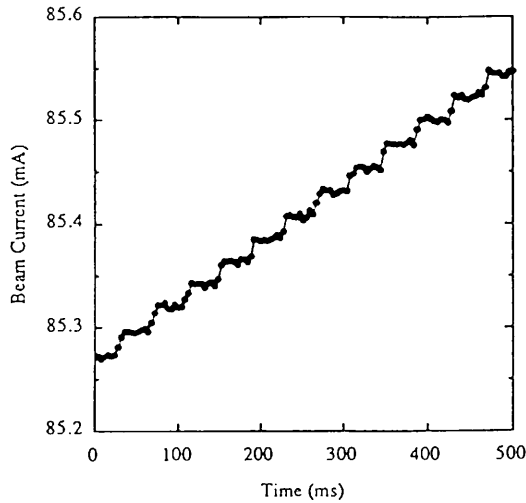


Fig. 27 Beam stacking process during injection under multi-bunch operation.

#### 6.4 Horizontal Distortion of the Storage Ring

Building distortion, caused by thermal stress due to solar irradiation, has been conceivably worsening the beam position stability. It has already been reported that the cause of the vertical distortion was solar irradiation.<sup>1,2,3)</sup>

In order to estimate the horizontal distortion of the storage ring, the major axis length of the ring ( $L$ ) and the ring circumference ( $C$ ) were measured. The major axis length variation was measured by using a laser interferometer system. The measuring system comprised a laser, a reflector, an interferometer and a vacuum pipe about 55 m long. The vacuum pipe was evacuated in order to reduce the measurement error due to any air-temperature variation.

The ring circumference variation has been calculated using the relation  $\Delta C = -C \cdot \Delta f_{rf} / f_{rf}$ , where  $\Delta f_{rf}$  is the deviation of the RF frequency, which was adjusted by a feedback system<sup>4)</sup> to compensate the horizontal COD (closed-orbit-distortion).

Figure 28 shows the measured major axis length, circumference and atmospheric temperature as a function of time during a day. There was a close correlation between the atmospheric temperature variation and the other variations. Measured results were also compared with those obtained from a computer simulation<sup>5)</sup> of the building distortion. Figure 29 shows both measured and simulated variations of the major axis length, which were qualitatively in good agreement from the point of diurnal variation.

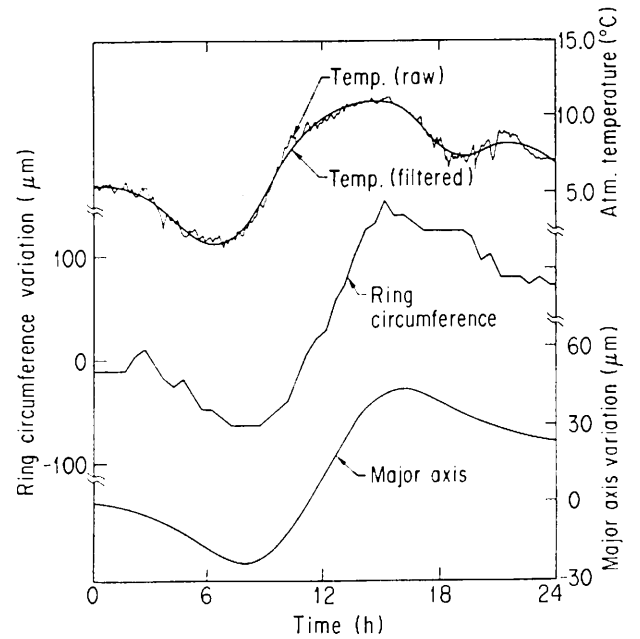


Fig. 28 Measured major axis length, ring circumference and atmospheric temperature as a function of the time during a day (Dec. 7, 1991). A smoother curve of the temperature is attached in order to show its slowly varying components of data.

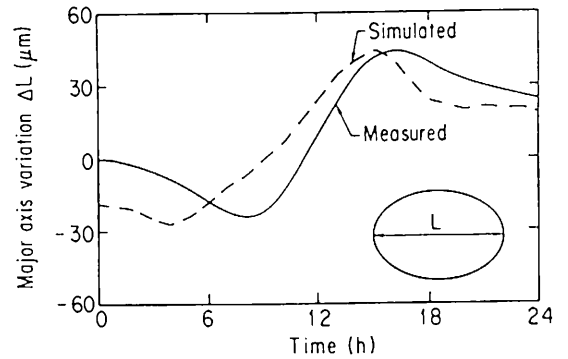


Fig. 29 Variation of the major axis length (measured with a laser interferometer and simulated from a computer model).

In conclusion, the horizontal distortion was also caused by solar irradiation. The relation between the major axis and the circumference is being investigated in order to estimate the shape of the ring distortion.

## References

- 1) Collaboration with Shimizu Corporation.
- 2) T.Katsura, et al., Third European Particle Acc. Conf., March 1992, p. 1631
- 3) PF Activity Report 1990, R-15.
- 4) PF Activity Report 1989, R-19.
- 5) PF Activity Report 1988, R-12.

## 6.5 Upgrade of the Photon Counting system

The photon counting system<sup>1)</sup> installed in BL-21 is used to measure the single-bunch impurity during single-bunch operation (see section B). The large dynamic range of the system enables us to quantitatively measure the impurity to at least  $10^{-5}$ . An improvement was made in the time resolution of the photon counting system. It was found that the constant fraction discriminator (CFD) was limiting the time resolution of the old system. The time resolution was greatly improved by employing a high-speed CFD.<sup>2)</sup> The time response of the system was determined by the transit time spread (TTS) of the photomultiplier (PMT). The TTS of the PMT was measured by using an ultra-short pulse laser,<sup>3)</sup> of which pulse width and wavelength were about 7 ps in FWHM and 800 nm, respectively. The TTS was about 24 ps in FWHM, consistent with another report.<sup>4)</sup> The current dependence of the bunch time structure was measured with the improved system, and is shown in the lower frame of Fig. 30. The asymmetry of the bunch shape increases with the current, as shown in the upper frame of Fig. 30. The degree of asymmetry is measured in terms of  $\tau$ , which is a parameter used to convolute the time structure with Gaussian function times ( $\tau^{-1} \exp(-h/\tau)$ ). Detailed analyses are in progress.

## References

- 1) In collaboration with Hiroshima University.
- 2) Model TC454, Tennelec/Nucleus Inc., USA.
- 3) The pico second pulse laser system, Faculty of Integrated Arts and Science, Hiroshima University.
- 4) H. Kume, K. Kinoshita, N. Tamai and I. Yamazaki, Bunko Kenkyu Vol. 38 (1989) 391

## 6.6 Installation of a Fast Beam Position Detector

A new beam position monitor<sup>1)</sup> with multiple pick-up electrodes has been developed for a bunch-

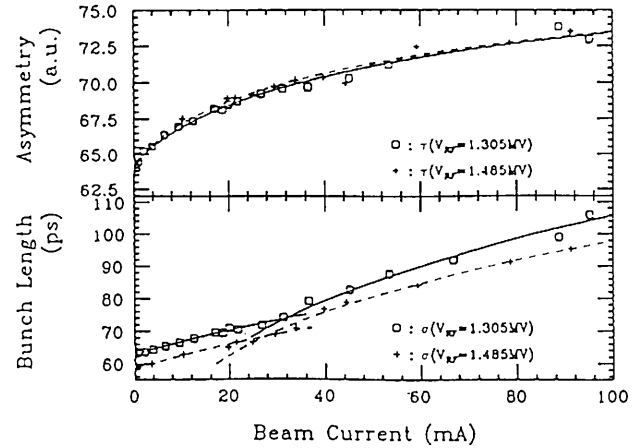


Fig. 30 Bunch length and bunch asymmetry vs beam current.

by-bunch feedback system to be used for high-current rings, e.g. the B-Factory ring. Storing a high current in many bunches with a minimum spacing of down to 2 ns will cause strong coupled bunch instabilities. Any transverse oscillation of individual bunches is to be detected by using the high-frequency components of the beam spectrum. To obtain clean signals in the high frequency region, the electrode structure and cabling are optimized so as to reduce any ringing of a signal caused by an impedance mismatch.

The position monitor was installed in the straight section between bending magnets B04 and B05. The monitor comprises two sets of six button-type pickup electrodes, one set in the horizontal plane and the other in the vertical. A block diagram of the detection system is shown in Fig. 31. The signals from consecutive electrodes are delayed with a spacing of  $\lambda/2$ , which is shorter than the bunch spacing. By mixing them with a local signal of frequency  $c/\lambda$ , a train of pulses with alternating polarity is derived for each bunch, and is fed to a lowpass filter in order to obtain a beam-position signal as an average of the pulses. Detailed beam tests of the entire system are in progress.

## Reference

- 1) This work was carried out in collaboration with the B-Factory Task Force and Hiroshima University.

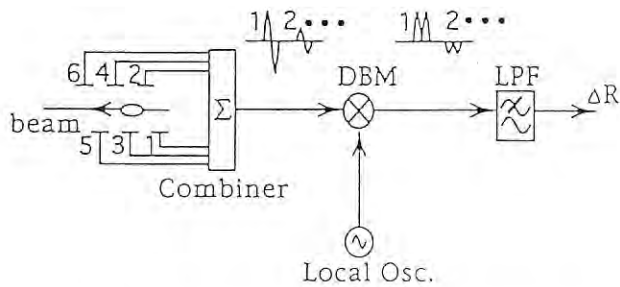


Fig. 31 New position monitor for detecting any transverse bunch oscillation. 1,2,...,6: electrodes,  $\Sigma$ : combiner, DBM: double balanced mixer, LPF: low pass filter,  $\Delta R$ : signal proportional to beam position. Cables between electrodes and combiner have the same length.

## 7. CONTROL

### 7.1 Replacement of the Main Console Switch Panel System

We replaced the Main Console Switch Panel (MCSP) system, which is a man-machine interface with which an operator can specify the operational mode of the storage ring. The old MCSP comprised mechanical switches, LED indicators and hard-wired TTL logic.<sup>1)</sup> This system has been in use for over 10 years, and some hardware failures have occurred. MCSP was thus replaced with a new system.

The new system was designed to be sufficiently flexible to allow future modifications by using a programmable touch-panel (model GP-510T of Digital Co. Ltd.) and a programmable controller (Fig. 32). The touch-panel comprises  $16 \times 10$  transparent touch-buttons and a color graphic display ( $640 \times 400$  pixels, TFT (thin-film-transistor) and LCD (liquid-crystal-display)). The programmable controller (PC) interfaces between signals from the touch-panel and interlock signals from equipment of the storage ring via some matrix circuits. Upon request by the operator, the operation mode of the storage ring is determined in accordance with the diagram, as shown in Fig. 33. The operation mode of the storage ring is enabled by the MCSP only if all of the equipment of the ring satisfy the safety conditions.

## Reference

1) "Photon Factory Activity Report 1983/1984", pp. IV30-33.

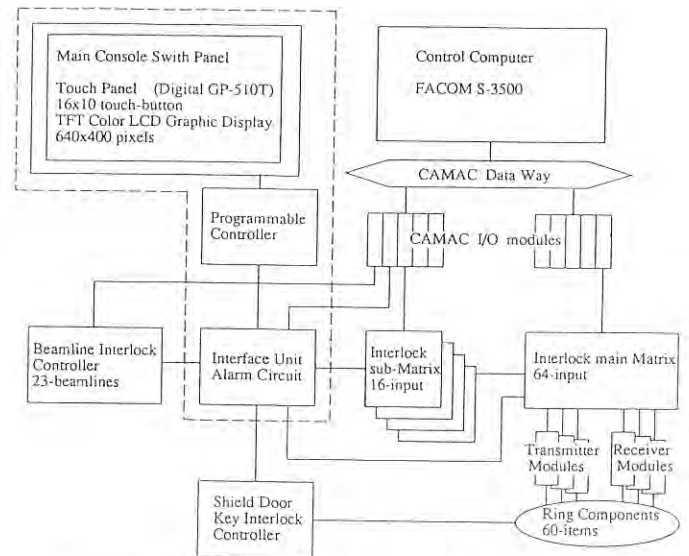


Fig. 32 Main Console Switch Panel (MCSP) system.

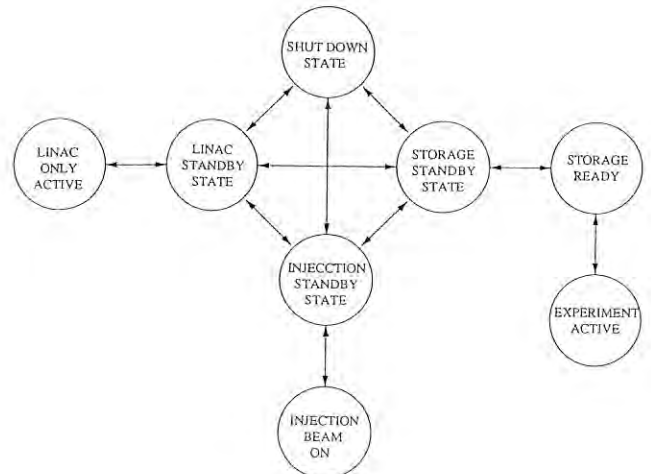


Fig. 33 Operation mode of the storage ring.

## 8. BEAM CHANNEL

### 8.1 Operation of a fast-closing valve system

On November 8, 1992, there was an instantaneous vacuum failure at experimental branch beamline BL-1A, the downstream end of front-end beamline BL-1.

Upon detecting the vacuum failure, the Fast-Closing Valve system,<sup>1)</sup> which is installed in the front-end beamline, automatically closed its blade in order to intercept intruding gas from the branch beamline (the closing time of the blade is  $\sim 0.01$  sec).

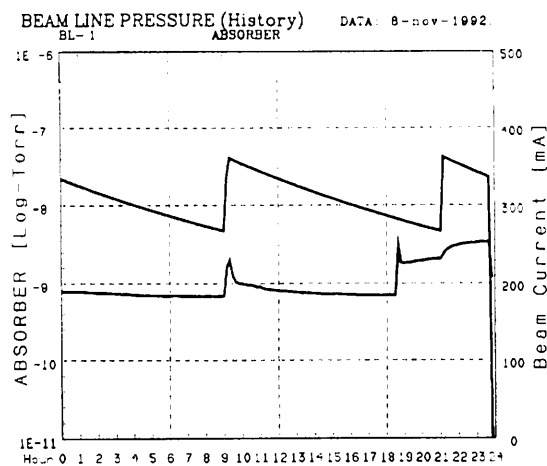


Fig. 34 Pressure rise near to the absorber of the beamline and the beam current at the upstream end of the beamline.

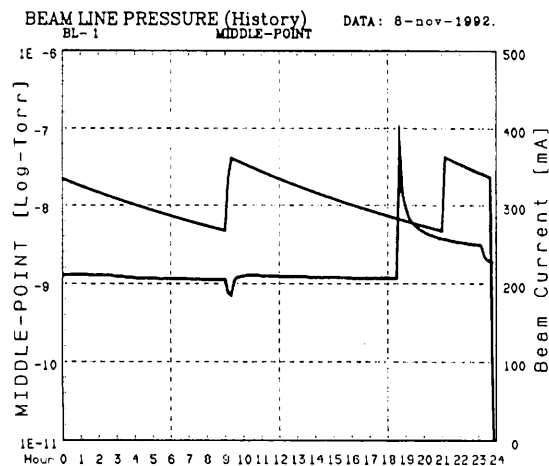


Fig. 35 Pressure rise and the beam current at the center of the beamline.

onds). The computer of the beamline control system simultaneously caused all vacuum-valves/shutter to close. All valves/shutter of the beamline completely closed the aperture of the beamline within 3 seconds. As a result, the ultra-high-vacuum of the storage ring could be successfully protected from the instantaneous vacuum failure. This failure was caused by a malfunction of a turbo-molecular pump at an experimental vacuum chamber at BL-1A.

Figure 34 shows the pressure rise near to the absorber of the beamline at the upstream end of the beamline and the beam current. Note that the pressure rose only from  $8 \times 10^{-10}$  to  $5 \times 10^{-9}$  Torr, and did not affect the beam; the vacuum leakage at the branch beamline therefore did not interfere with the rest of the synchrotron-radiation experiments when the vacuum failure occurred.

Figure 35 shows the pressure rise at the center of the beamline and the beam current. Although the figure shows that the pressure rise reached  $1 \times 10^{-6}$  Torr, the worst pressure rise, however, was roughly estimated to be over  $5 \times 10^{-4}$  Torr since the set-point of the FCV was  $5 \times 10^{-4}$  Torr. This is because pressure data were logged at intervals of 10 minutes by the computer of the beamline-control system.

## Reference

- 1) N. Kanaya, et al, IEEE Trans. Nucl. Sci., 36 (4), 1989, p. 1391.

## 8.2 Heat-load experiments using multipole wiggler radiation

Heat-load experiments were made on some beamline elements using a test apparatus which had been facilitated during Oct. 1990–Aug. 1992 at a straight-through port of a multipole wiggler beamline BL-28. Some of the experiments were made in order to review and check our criteria used to design the beryllium windows<sup>1)</sup> and carbon foil filters.<sup>2)</sup> Other experiments were performed to develop heat-load-resistant multilayer mirrors<sup>3)</sup> and a new type of silicon carbide (SiC) based grating.<sup>4)</sup> Prior to these experiments, the total power and angular power distribution of the wiggler radiation were measured using a calorimetric device<sup>5)</sup> to provide a quantitative basis for these experiments. These studies were partly supported by the Director's R & D program for future accelerator projects at KEK. The following is a summary of these experiments.

### 8.2.1 Calorimetric measurements of the power distribution in the multipole wiggler radiation

The power density of the multipole wiggler radiation was measured with a funnel-shaped copper absorber by vertically shifting a small aperture of 0.8 mm by 1.6 mm. Figure 36 shows a schematic diagram of the measurement on beamline BL-28. The cross section of the photo absorber and a water-cooled heat sink is also shown in Fig. 36.

When we assume no thermal radiation loss, the incident power ( $Q$ ) in a thermally steady state is

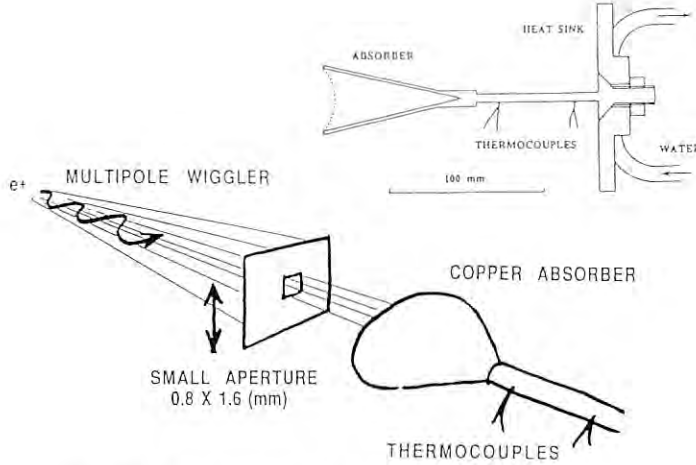


Fig. 36 Cross section of the photo absorber and the heat sink (top) as well as a schematic layout of the measurement (bottom).

given by

$$Q = \kappa a \frac{\Delta T}{l}, \quad (1)$$

where  $\kappa$ ,  $a$ , and  $(\Delta T/l)$  are the thermal conductivity of copper, the cross section of the copper rod, and the temperature gradient produced over a distance of  $l$  along the rod, respectively. The temperatures at two fixed points on the rod ( $T_1$  and  $T_2$ ) ( $\Delta T = T_1 - T_2$ ) were measured with alumel-chromel thermocouples.

Figure 37 shows the power-density distribution for deflection parameters ( $K$ ) of 14.66 and 7.66. The circles show the measured points and the solid curves the calculation using Kim's formula for an infinitesimal emittance; both are normalized to a ring current of 300 mA. The measured density is lower by  $\sim 20\%$  than the calculated one at the peak, and in FWHM of the density distribution the measured value is larger by  $\sim 10\%$ .

Although the one-electron scheme might possibly be responsible for the discrepancy, a calculation including the effect of finite emittance gives only a small decrement of at most 3% at the peak. Therefore, the remaining discrepancy might be ascribed to other reasons, such as an imperfection of the wiggler magnet array as well as radiation loss due to Cu-K x-rays from the calorimetric device. Nevertheless, Kim's formula for the radiation power was reliable in the heat-load experiments using the existing wiggler within an accuracy of less than 20%.

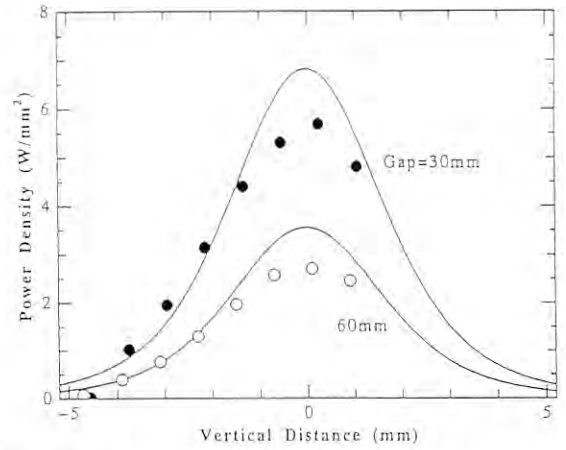


Fig. 37 Power-density distribution of radiation from the BL-28 multipole wiggler measured at a distance of 14.1 m for the deflection parameter of 14.66 and 7.66. The circles and curves show the measured data as well as that calculated using Kim's formula; both are normalized to a ring current of 300 mA.

### 8.2.2 Limit of the thermal breakdown of a beryllium window and a carbon foil filter

The temperature difference between the center and periphery of a window or a foil filter having a rectangular shape under irradiation by a multipole wiggler is expressed simply by

$$\begin{aligned} \Delta T &= T_c - T_p \\ &= \frac{e_0}{3\epsilon_0} \left( \frac{w}{L} - \frac{8}{21\gamma} \right) \left( \frac{1}{\kappa t} \right) \left( \frac{N K I \gamma^3}{\lambda_0} \right) R, \quad (2) \end{aligned}$$

where  $T_c$  is the temperature at the window center,  $T_p$  the temperature at the periphery of the window (which is in contact with a cooled frame),  $2w$  the vertical width of the window,  $L$  the distance from middle point of the source,  $\kappa$  the thermal conductivity of the window or filter material,  $t$  the foil thickness,  $e_0$  the unit charge,  $\epsilon_0$  the dielectric constant in vacuum and  $R$  the ratio of the radiation power absorbed by the foil to that incident to the foil expressed as

$$R = \frac{\int_0^\infty G_1(\omega) [1 - \exp\{-\mu(\omega)t\}] d\omega}{\int_0^\infty G_1(\omega) d\omega}. \quad (3)$$

Here  $\mu(\omega)$  is the linear absorption coefficient of the foil material, and  $G_1(\omega)$  is the spectral power distribution function.

We confirmed the above expression on a beryllium window using the irradiation test facility, and experimentally derived the limit of the thermomechanical failure of the window to be  $\Delta T \approx 300^\circ\text{C}$ ; this was in good agreement with a simple theory of fracture due to the maximum shearing stress. We must keep the temperature rise  $\Delta T \ll 300^\circ\text{C}$ , far below the melting point of beryllium.

In order to reduce the temperature rise in the beryllium windows, carbon foil filters are used in the multipole wiggler beamlines. We have found, however, that a 1.3-mm thick carbon filter at BL-16 (the most powerful wiggler beamline) was sublimated and became partially transparent. The temperature at the central portion of the filter must have been overheated to  $\approx 3000^\circ\text{C}$ ; this was based on a calculation using Eq. (2) for a beam energy of 2.5 GeV, a beam current of 400 mA, and a deflection parameter of 16.8. To reduce the temperature rise, the filter was replaced with a thicker one (4.2 mm). However  $\Delta T$  decreased to only  $\approx 2000^\circ\text{C}$  for the same condition. Since the filter is still in critical condition, we are now searching for a foil of graphite with a higher thermal conductivity; and further in contemplation to adopt another type of filter assembly.

### 8.2.3 Stability of soft x-ray multilayers under exposure to multipole wiggler radiation

The stability of soft x-ray (SXR) multilayers of Mo/BN, Mo/B<sub>4</sub>C, W/BN, and W/B<sub>4</sub>C was examined upon exposure to white radiation from the multipole wiggler.

Mo/BN, Mo/B<sub>4</sub>C, W/BN, and W/B<sub>4</sub>C multilayers were prepared onto superpolished CVD-SiC substrates by magnetron sputtering. Each multilayer comprises 51 layers with a d-spacing of about 84 Å, such that the structure yields a peak in reflectance at around 105 eV for an incidence angle of 45°. Molybdenum and tungsten were dc sputtered at an input power of 100 W, while BN and B<sub>4</sub>C were rf sputtered at an input power of 400 W. The argon gas pressure was tuned to 2.0 mTorr during all deposition processes. The reflectance of the prepared samples was evaluated using a reflectometer equipped with a laser-produced plasma source.

The ultrahigh-vacuum test chamber for irradiation tests was installed 16.5 m from the middle point of the source. The incident power was measured

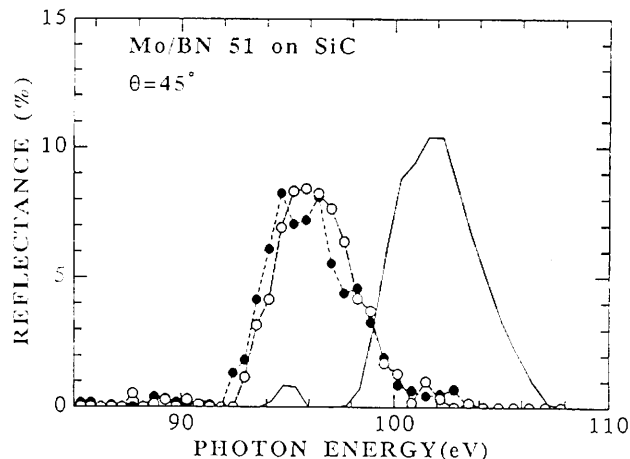


Fig. 38 Reflection peaks of the Mo/BN multilayer measured prior to exposure (solid line), after exposure to the radiation with a power density of 2.3-W/mm<sup>2</sup> (dotted line with solid circles) and after exposure to radiation with a power density of 0.9-W/mm<sup>2</sup> (broken line with open circles), respectively.

using the photocalorimetric device. Four samples placed adjacent to each other were attached tightly to a water-cooled copper heat sink with aluminum foil acting as a thermal conductor. The wiggler radiation passing through an aperture of 8 mm by 9 mm was incident normal to the sample surface. The lower half of each sample was first irradiated for 45 minutes with a deflection parameter of 3.15 and a ring current of 315 mA, providing an average power density of roughly 0.9 W/mm<sup>2</sup> at the center of the irradiated area. The upper half of each sample was then irradiated for 10 min with a K parameter of 7.66 and a ring current of 345 mA, delivering a power density of 2.3 W/mm<sup>2</sup> on the average.

The effect of the irradiation was evaluated by comparing the specular reflectance at an incidence angle of 45°. Figure 38 shows the measured reflection peaks for the Mo/BN sample. The solid curves show the reflectance for as-prepared samples; the broken lines with open circles show the reflectance after exposure to the radiation having a power density of 0.9 W/mm<sup>2</sup>. The dotted lines with solid circles show the reflectance after exposure to radiation having a power density of 2.3 W/mm<sup>2</sup>. The sample underwent a  $\sim 20\%$  reduction in the peak reflectance, and the peak shifted from 102 eV to 96 eV, probably due to increase in volume of the BN layer. However there was no observable difference between the irradiated areas under different expo-

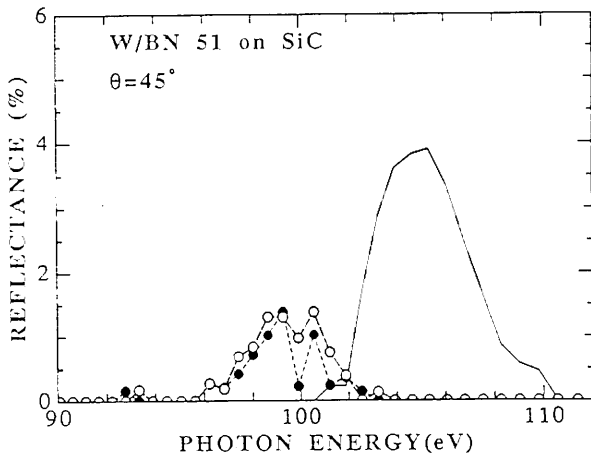


Fig. 39 Reflection peaks of the W/BN multilayer presented in the same manner as in Fig. 3.

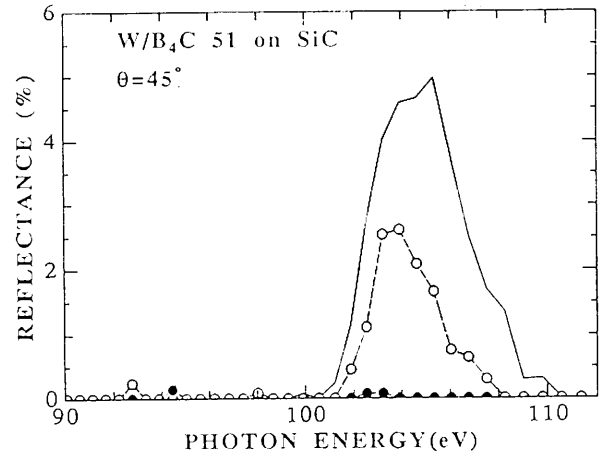


Fig. 41 Reflection peaks of the W/B<sub>4</sub>C multilayer.

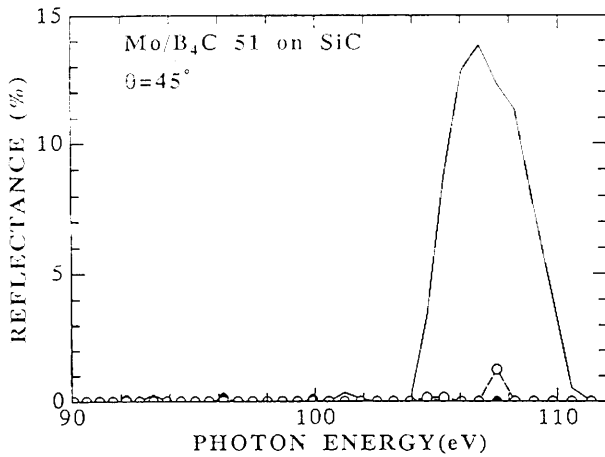


Fig. 40 Reflection peaks of the Mo/B<sub>4</sub>C multilayer.

sure conditions. Figure 39 shows the result on the W/BN multilayer, which showed a similar effect on the Mo/BN sample. However there was a reduction in the peak reflectance to  $\sim 65\%$ . Figure 40 shows the result on the Mo/B<sub>4</sub>C multilayer, which was almost destroyed physically in such that the damage was visibly observable. Figure 41 shows the result on the W/B<sub>4</sub>C multilayer. In this sample, degradation in reflectance was  $\sim 50\%$  upon  $0.9\text{-W/mm}^2$  irradiation, while more than  $\sim 98\%$  upon  $2.3\text{-W/mm}^2$  irradiation.

The above results are characterized mainly by the spacing materials (BN and B<sub>4</sub>C), and not by the metals. The Mo/BN and W/BN samples withstood  $2.3\text{-W/mm}^2$  irradiation, while the reflectance peak shifted towards the longer wavelength. On the

other hand, the Mo/B<sub>4</sub>C and W/B<sub>4</sub>C samples were not able to withstand  $2.3\text{-W/mm}^2$  irradiation, while the peak position was remained unchanged under irradiation with a power density of at least less than  $0.9\text{-W/mm}^2$ .

#### 8.2.4 Heat-load test of silicon-carbide-based holographic laminar gratings

A heat-load experiment was carried out on two pieces of a silicon-carbide-based holographic laminar grating, which were developed in one of the R & D programs for the SPring-8 project.<sup>4)</sup> A non-coated grating and a gold-coated grating were chosen as the test pieces. The diffraction efficiency of the pieces before and after irradiation was measured in the VUV and soft x-ray regions from 40 to 700 eV using beamlines at UVSOR, IMS, Okazaki.

The experiment was performed at 2.5 GeV, 300 mA, and  $K = 14.67$ . The gratings were placed at 16.67 m from the middle point of the wiggler with their surfaces normal inclined to the incident beam by  $52.5^\circ$ . The results of the experiment were as follows:

- 1) For the non-coated grating, no degradation in the diffraction efficiency was observed after exposure, with no deformation in the laminar grooves.
- 2) As for the gold-coated one, no substantial degradation in the diffraction efficiency was observed within the measured wavelength range, due to well-preserved grooves beneath the coated gold layer, which was fatally destroyed.

The temperature difference between the front and rear surfaces of a plate-type element is roughly



given by

$$\Delta T = \frac{7e_0}{16\epsilon_0} \left( \frac{NKI\gamma^4}{\lambda_0} \right) \frac{t \cdot \cos \Theta}{\kappa L^2}, \quad (4)$$

when the front surface is exposed to multipole wiggler radiation and the rear surface is in contact with a cooled heat sink. Here,  $t$  is the thickness of the plate and  $\Theta$  is the incidence angle of the beam measured from the surface normal. Substitution of 150 W/m-deg into  $\kappa$  and 0.01 m into  $t$  leads to  $\Delta T = 200^\circ$ , which is far below the melting point of gold. The fatal degradation of the gold coating layer was, therefore, due not to thermal damage, but to radiation-stimulated damage. Although the coating material is still a problem, the holographically fabricated SiC-based grating is the most promising candidate for a future high heat load-resistant dispersive element in the VUV and soft x-ray regions.

## References

- 1) S. Asaoka, H. Maezawa, Y. Kamiya, and M. Yanagihara, Rev. Sci. Instrum., 63 (1992) 473–476.
- 2) H. Maezawa, S. Asaoka, M. Yanagihara, and Y. Kamiya, SPIE Proceedings, Vol. 1739 (1992).
- 3) M. Yanagihara, K. Mayama, S. Asaoka, and H. Maezawa, SPIE Proceedings, Vol. 1739 (1992).
- 4) E. Ishiguro, H. Maezawa, M. Sakurai, M. Yanagihara, M. Watanabe, M. Koeda, T. Nagano, K. Sano, Y. Akune, and K. Tanino, SPIE Proceedings, Vol. 1739 (1992).
- 5) M. Yanagihara, Y. Goto, S. Asaoka, H. Maezawa, and H. Sugawara, SPIE Proceedings, Vol. 1739 (1992).

## D. 2.5 GeV LIGHT SOURCE SPECIFICATIONS

This section contains major specifications of the 2.5 GeV PF ring to provide quick and handy information for users and machine physicists.

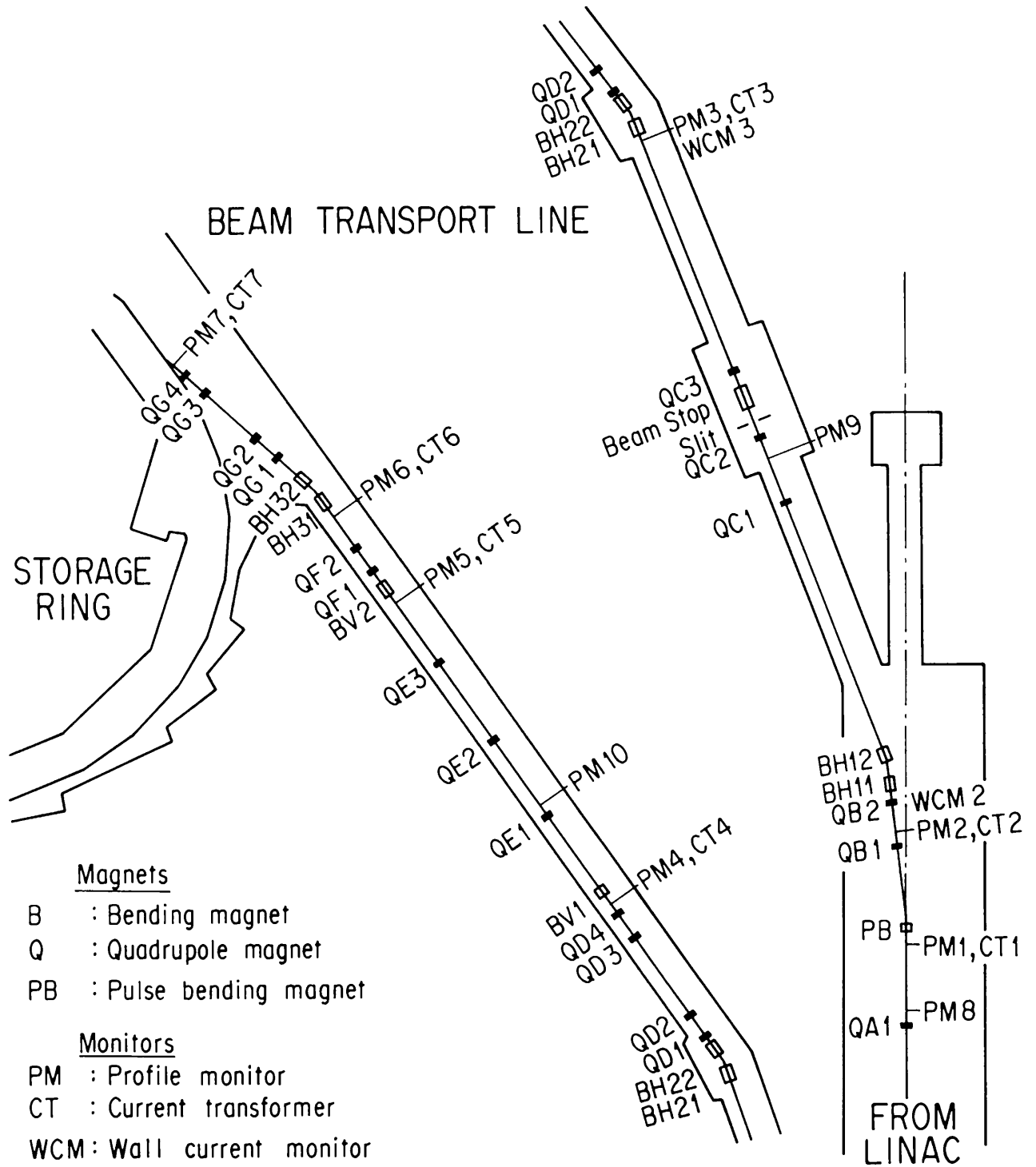


Fig. D-1. Beam transport line.

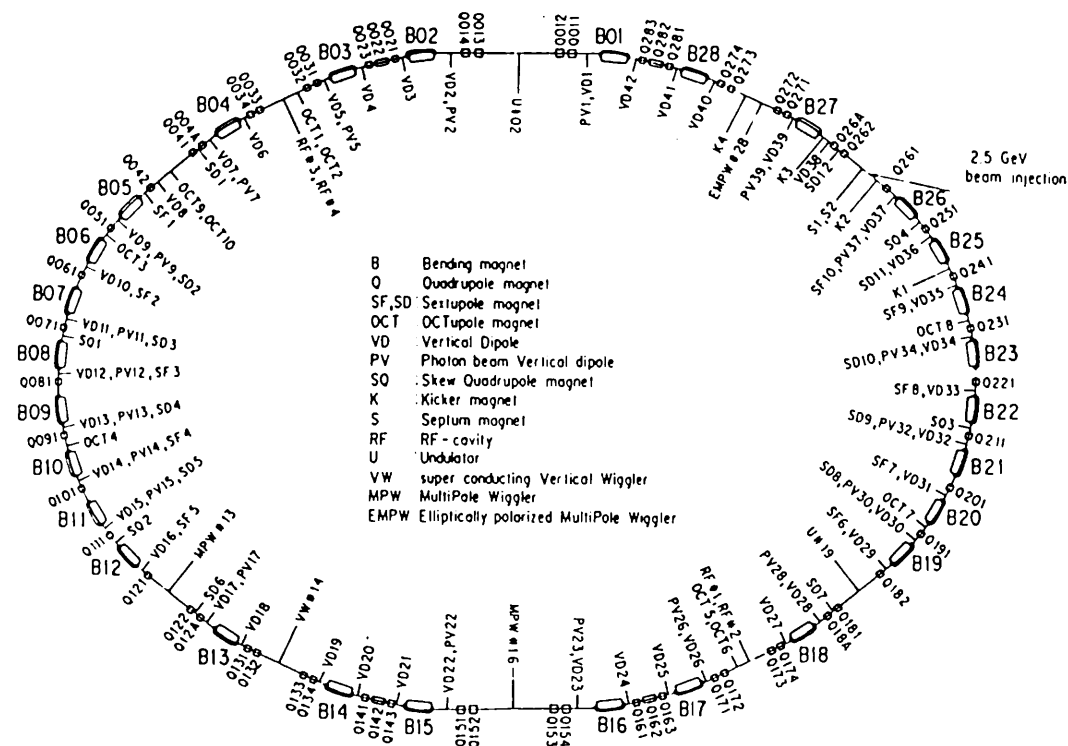


Fig. D-2. Ring lattice components.

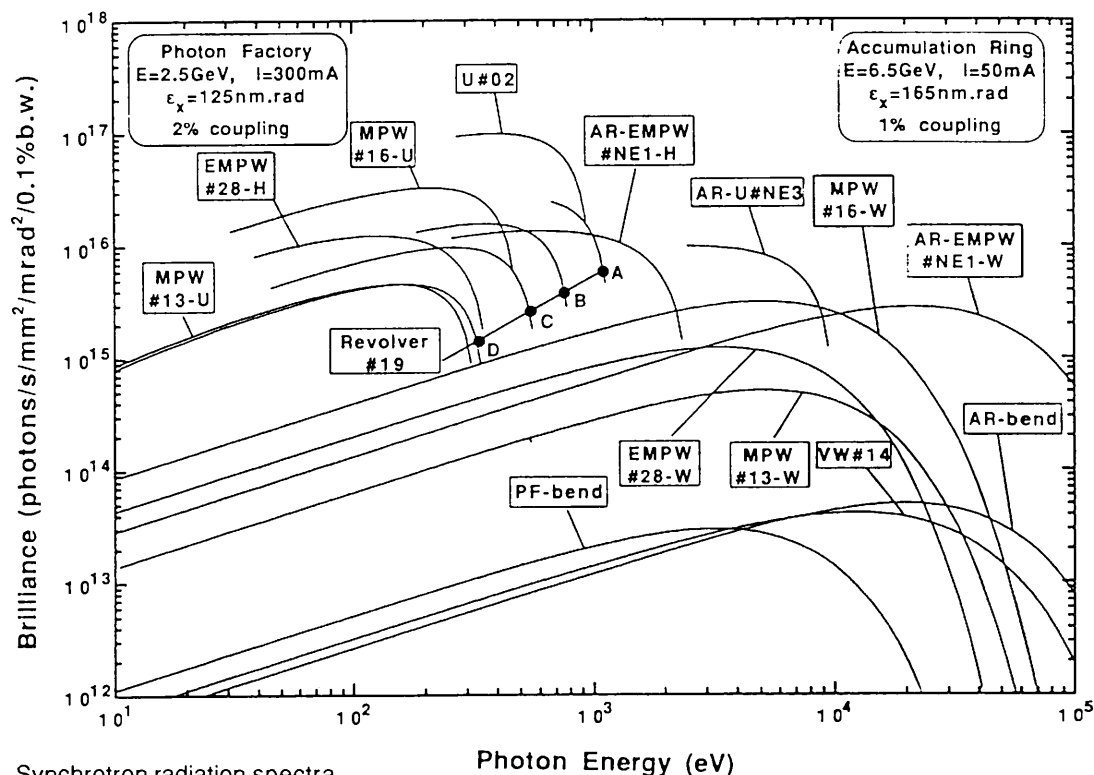


Fig. D-3. Synchrotron radiation spectra. Brilliance of radiation vs. photon energy for the insertion devices (U#02, MPW#13, VW#14, MPW#16, Revolver#19 and EMPW#28) and the bending magnet (Bend) of the PF, and for the insertion device (EMPW#NE1) of the AR. The name of each source is assigned in Table D-4. Several insertion devices have both undulator and wiggler modes, which are denoted by U or W, respectively. The spectral curve of each undulator (or undulator mode of multipole wiggler) is a locus if the peak of the first harmonic within the allowable range of K-parameter. Spectra of Revolver#19 are shown for four kinds of period lengths.

Table D-4 Insertion devices

Calculated spectral performances of the bend source and 6 insertion devices at the Photon Factory. E/I: beam energy and current,  $\lambda_u$ : period length, N: number of periods, L: length of undulator or wiggler,  $G_v(G_x)$ : minimum vertical (horizontal) gap height,  $B_v(B_x)$ : maximum vertical (horizontal) magnetic field, P: pure configuration, H: hybrid configuration, S.C.: superconducting magnet,  $\sigma_{x,v}$ : horizontal or vertical beam size,  $\sigma_{x',v'}$ : horizontal or vertical beam divergence,  $K_h(K_v)$ : horizontal(vertical) deflection parameter,  $\epsilon_1/\epsilon_c$ : photon energy of the first harmonic(critical energy in the case of bend source or wiggler),  $\Delta\epsilon/\epsilon$ : relative bandwidth, Pc: degree of circular polarization,  $\mathcal{D}$ : photon flux in unit solid angle (photons/s  $\cdot$  mrad<sup>2</sup>  $\cdot$  0.1%b.w.),  $\mathcal{B}$ : brilliance (photons/s  $\cdot$  mm<sup>2</sup>  $\cdot$  mrad<sup>2</sup>  $\cdot$  0.1%b.w.),  $P_T$ : total radiated power, dP/d $\Omega$ : power in unit solid angle. Different operating modes of undulator and wiggler are denoted by -U and -W, respectively.

Name	E/I GeV/μA	$\lambda_u$ cm	N	L m	$G_v(G_x)$ cm	$B_v(B_x)$ T	Type of magnet	$\sigma_x$ mm	$\sigma_y$ mm	$\sigma_{x'}$ mrad	$\sigma_{y'}$ mrad	$K_h(K_v)$	$\epsilon_1/\epsilon_c$ keV	$\Delta \epsilon / \epsilon$	$\mathcal{D}$	$\mathcal{B}$	$P_T$ kW	dP/dΩ kW/mrad <sup>2</sup>
Bend	2.5/300							0.74	0.26	0.38	0.037		4.0		3.5E13	2.9E13		0.060
U#02		6.0	60	3.6	2.8	0.4	H(NdFeB)	0.78	0.11	0.16	0.022	2.25	0.28	0.029	5.2E16	9.7E16	0.68	2.7
MPW#13-W -U		18.0	13	2.5	2.7	1.5	H(NdFeB)	1.66	0.17	0.15	0.019	25.0 2.0	6.2 0.108	0.086	9.7E14 5.7E15	4.9E14 3.2E15	6.7 .042	2.6 0.19
VW#14					5.0	5.0	S.C.	1.05	.096	0.16	0.025		20.8		2.2E13	3.4E13		0.18
MPW#16-W -U		12.0	26	3.1	1.9	1.5	H(NdFeB)	0.78	0.11	0.16	0.022	16.8 2.0	6.2 0.162	0.050	1.8E15 1.6E16	3.1E15 2.8E16	8.3 0.12	4.9 0.52
Revolver #19		5.0	46	2.3	3.0	0.28	H(NdFeB)	1.66	0.17	0.15	0.019	1.3	0.637	0.021	4.1E16	2.3E16	0.21	1.27
		7.2	32			0.41	H(NdFeB)					2.7	0.176	0.039	2.1E16	1.2E16	0.44	1.54
	10.0	23			0.53	H(NdFeB)					5.0	0.0436	0.047	6.9E15	3.8E15	0.78	1.53	
	16.4	14			0.62	P(NdFeB)					9.5	0.0078	0.066	1.2E15	6.3E14	1.05	1.09	
EMPW#28 -W -U	16.0	12	1.9	3(11)	1(0.2)	P(NdFeB)	1.05	.096	0.16	0.025	15(1) 1(1)	4.2(Pc=89%) .18(Pc=99%)	0.11	2.5E14 6.3E15	3.4E14 9.8E15	2.3 0.02	0.38 0.058	

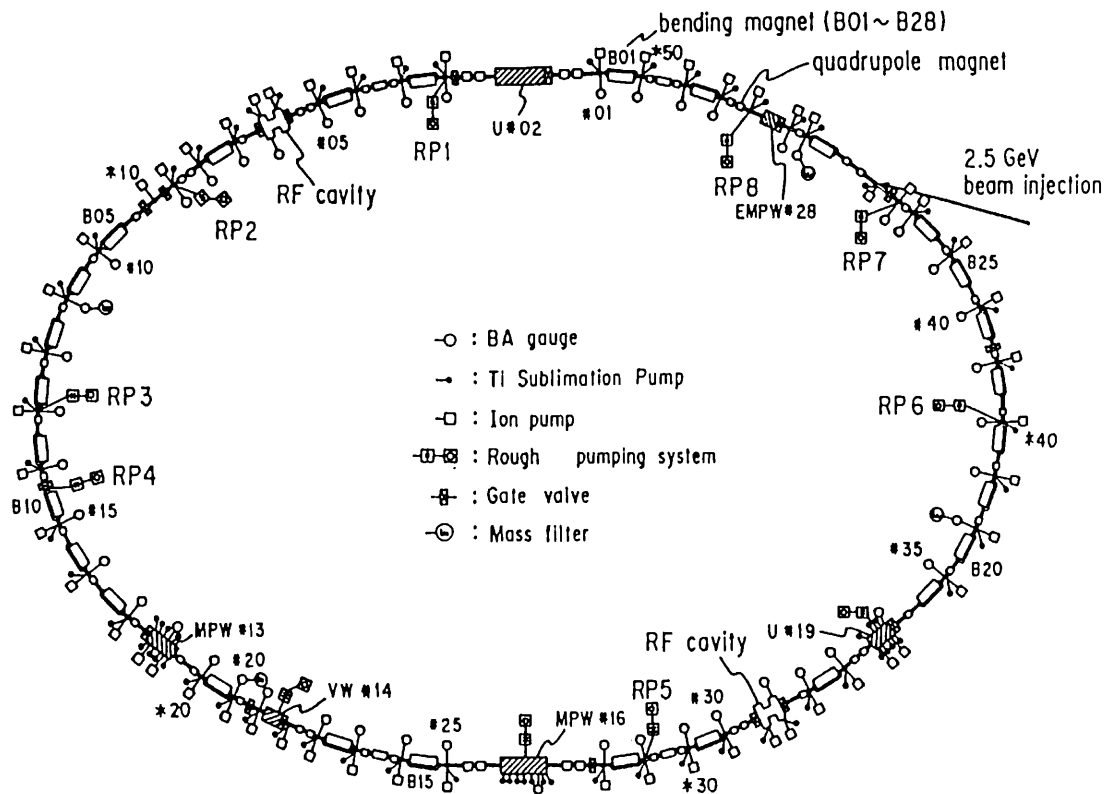


Fig. D-5. Vacuum system components.

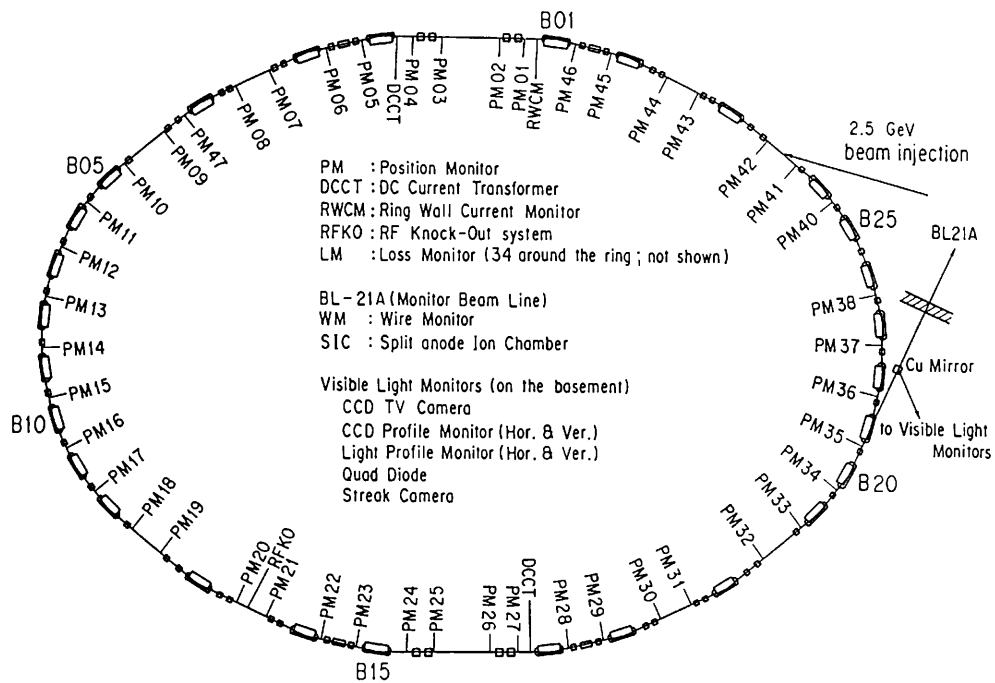


Fig. D-6. Beam monitors.

Table D-7. General parameters of the storage ring.

Energy	2.5 GeV	(0.75 GeV to 3 GeV)
Initial stored current (multi-bunch)	350 mA	(max 500 mA)
(single bunch)	60 mA	(max 104 mA)
Emittance	130nm·rad(horizontal) ~2nm·rad(vertical)	
Circumference	187m	(bending radius=8.66m)
RF frequency	500MHz	(harmonic number=312)
Injection	2.5GeV Linac	(positron/electron)
Beam lifetime	60 h (at 300 mA)	$I \cdot \tau \geq 18 \text{ A} \cdot \text{h}$ (at ~250 mA ~ 350 mA)
Vacuum pressure	$\geq 3 \times 10^{-10}$ Torr (at 300mA) $P/I \sim 8 \times 10^{-10}$ Torr/A (at ~250 mA ~ 350 mA) $\sim 3 \times 10^{-11}$ Torr (at 0 mA)	
Insertion devices	Superconducting vertical wiggler 5T 60 period undulator $K=1.78 \sim 0.1$ 26 period multipole wiggler/undulator 1.5T~0.04T Four way revolver type undulator 14 period multipole wiggler Elliptically polarized multipole wiggler	
SR channels	SR experiment 22 Beam diagnosis 3	

Table D-8. Beam parameters.

Horizontal tune $\nu_x$	8.45
Vertical tune $\nu_y$	3.30
Compaction factor $\alpha$	0.015
Natural chromaticity $\xi_x$	-15.8
$\xi_y$	-8.6
Bunch length $\sigma_z$	1.5cm
Transverse damping time	7.8msec
Longitudinal damping time	3.9msec
Energy spread	$7.3 \times 10^{-4}$
Radiation loss (without insertion devices)	400keV

Table D-9. Principal parameters of the accelerator system.

**Magnet system**

	number of magnets	number of power supplies
Bending	28	1
Quadrupole	58	12
Sextupole	22	2
Octupole	11	10
Skew quadrupole	4	4
Dodecapole	6	6
Vertical steering	42	42
Photon beam steering	20	20
Others		
Backleg winding of bending magnet	28	
Electric shunt for tune compensation	12	

## RF system

Number of RF stations	4
Number of klystrons	4 (180kW/klystron)
Number of RF cavities	4 (single cell cavity)
Shunt impedance	32M $\Omega$ (four cavities)
Unloaded Q	39000
Total power dissipated in cavity wall	89kW
Total cavity gap voltage	1.7MV
Synchrotron frequency	37kHz

## Vacuum system

main pumping system		
pump	pumping speed	number
SIP (Sputter Ion Pump)	128 l/sec	54
DIP (Distributed Ion Pump)	150 l/sec	26
Ti sublimation	-----	71
NEG (Non-Evaporable Getter)	-----	2
total effective pumping speed = $2 \times 10^4$ l/sec (for CO)		
Rough pumping system		
	pumping speed	number
TMP (Turbo Molecular Pump)	300 l/sec	12
Measurement		
	number	
B-A gauge	48	
mass filter	4	
cold cathode gauge	16 (for baking)	
Sector gate valve		
	number	
all metal with RF shield	5	
all metal without RF shield	1	
Viton seal with RF shield	10	

## Injection system

Septum magnet		
name	Septum I (S1)	Septum II (S2)
core material	laminated silicon steel (passive type)	
length [mm]	1500	1000
maximum current [A]	6000	6000
deflection angle [degree]	7.0	5.0
pulse width [msec]	88	60
Kicker magnet		
name	K1, K2, K3, K4	
core material	ferrite (window frame type)	
core length [mm]	300	
maximum current [A]	3500	
maximum deflection angle [mrad]	4.4	
pulse width [msec]	5	

## Superconducting vertical wiggler

Maximum field strength on the beam orbit	5 Tesla
Magnet gap	66 mm
Magnet pole size (widthxheight)	40 mm × 260 mm
Number of magnetic poles	5 poles arranged every 200 mm
Rated exciting current	220 A at 5 Tesla
Superconducting wire	NbTi : Cu 1 : 1 size 1.70 × 0.85 mm <sup>2</sup>
Cross section of coils	65 mm × 70 mm
Number of turn	2520
Liquid helium consumption in the permanent current mode	0.1 L/h
Damping rate of the permanent current	$1.4 \times 10^{-5}/h$
Inductance	1.31 H/coil

## FEL oscillator

1. General	
target wavelength	177 nm
FEL gain	18 %
cavity loss	12 %
net FEL gain	6 %
2. Storage ring	
beam energy	0.75 GeV
number of bunches	4
bunch length(2s)	60 psec
peak current	30 A
beam emittance	15 nm · rad
energy spread	$3.5 \times 10^{-4}$
accelerating frequency( $f_{rf}$ )	500.1 MHz
3. Optical klystron	
periodic length	9 cm
number of periods	19+19
max. magnetic field	0.7 tesla
max. deflection parameter	5.9
optimum $N_d$	210
FEL gain	0.6 %/amp
4. Optical cavity	
type	Fabry Perot
cavity length	23.38 m
mirror 1(UHV Al)	R=92%
mirror 2(MgF <sub>2</sub> multilayer)	R=96%
cavity loss at 1770 Å	12 %
5. Laser system	
mode-lock YAG laser	
mode-lock frequency	83.35 MHz (= $f_{rf}/6$ )
regenerative YAG amplifier	
repetition rate	50 Hz
pulse energy at 5320 Å	15 mJ
pulse duration	80 psec
Harmonic generation	
harmonic material	Xe or Cd vapor
max. pulse power	1 kW



## Monitor system

### I. Orbiting Beam Monitors

PM(Position Monitor)	46
DCCT(Direct Current Current Transformer)	2
RFKO(Radio Frequency Knock-Out system)	1
WCM(Wall Current Monitor)	1
Visible Light Monitor	
CCD TV camera	1
CCD Profile Monitor (H & V)	1
Light Profile Monitor (H & V)	1
Quad Diode	1

### II Photon beam position monitors installed in beamlines of PF ring

Beamline	Source	Upstream	Downstream	Ver./Hor.
BL 2	U	DSPM	DSPM	V, H
BL 3A	B	SPM		V
BL 3C	B	SPM	SPM	V
BL 4C	B	SPM	SPM	V
BL 6B	B	SLIT		V
BL 6C	B	SLIT		V
BL 6C	B	SPM	SPM	V
BL 7C	B	SLIT	SPM	V
BL 10A	B	SIC		V
BL 10B	B	SLIT		V
BL 12A	B	WM	WM	V
BL 14C	SVW	SPM	SPM	H
BL 15A	B	SPM		V
BL 16	MPW	DSPM		V, H
BL 21	B	WM		V
BL 27	B	SPM		
BL 28	EMPW	Under constr.		

Note:    SPM : Split photoemission monitor                      B:      Bending magnet  
             SIC : Split ion chamber                                      U:      Undulator  
             WM: Wire monitor    SVW: Superconducting vertical wiggler  
             DSPM: Dual SPM for insertion device line                MPW: Multipole wiggler  
    EMPW: Elliptical MPW

## Control system

		number	memory
Control computers	FACOM S-3500	4	16 Mbyte
Library computer	FACOM M-780/10R	1	32 Mbyte
Computer network (type : optical token ring)			
number of nodes = 5 (max. 256)			

Table D-10. Beam size and divergence at source point.

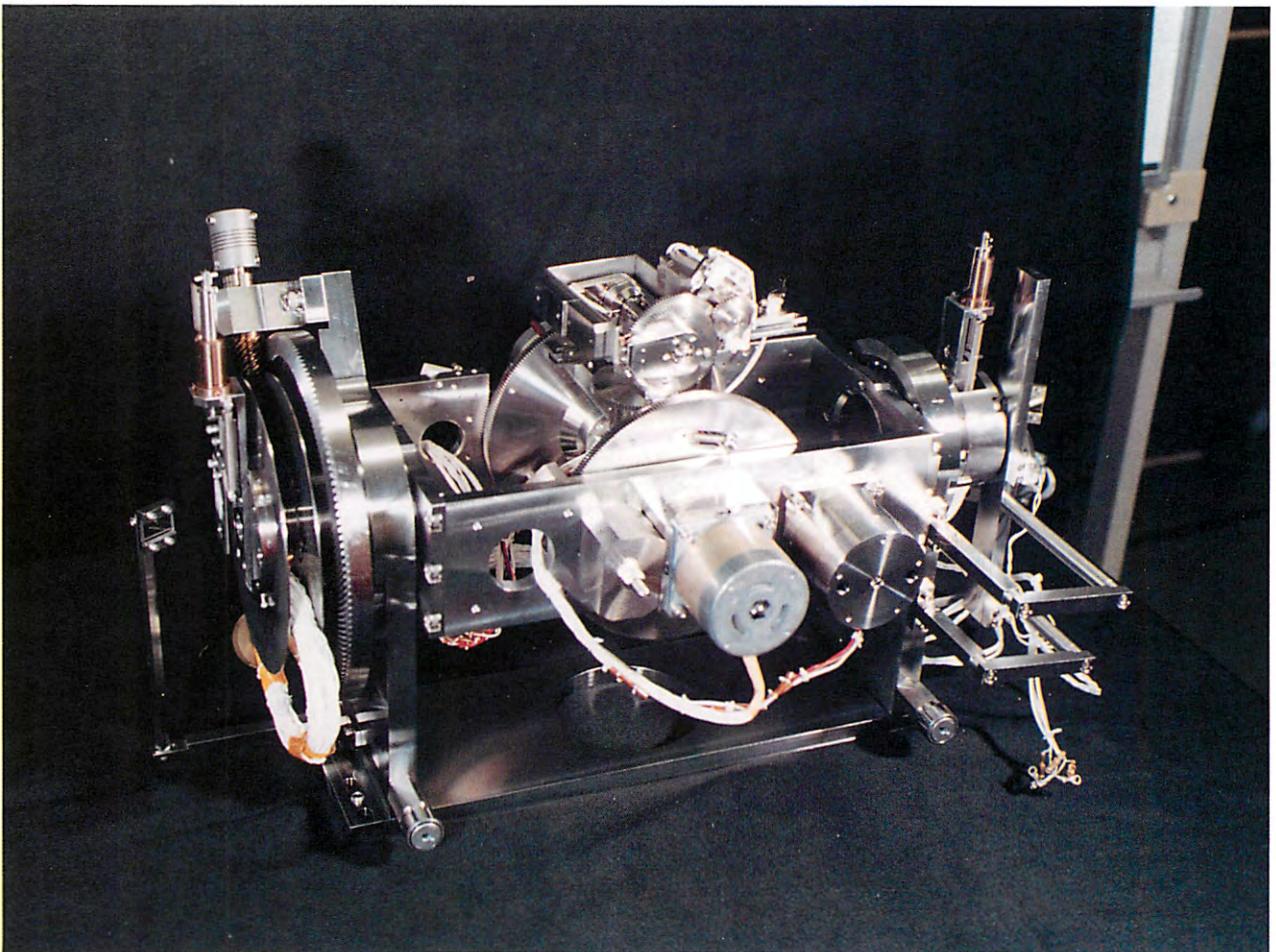
location	$\sigma_x$ [mm]	$\sigma_y$ [mm]	$\sigma'_x$ [mrad]	$\sigma'_y$ [mrad]
B15&B01	0.34	0.16	0.41	0.033
B02&B16	0.60	0.13	0.38	0.033
B03&B17	0.43	0.22	0.32	0.018
B04&B18	0.52	0.18	0.29	0.045
B05&B19	1.26	0.21	0.39	0.037
B06&B20	0.85	0.25	0.38	0.037
B07&B21	1.26	0.21	0.39	0.037
B08&B22	0.85	0.25	0.38	0.037
B09&B23	1.26	0.21	0.39	0.037
B10&B24	0.85	0.25	0.38	0.037
B11&B25	1.26	0.21	0.39	0.037
B12&B26	0.85	0.25	0.38	0.037
B13&B27	0.44	0.23	0.31	0.045
B14&B28	0.50	0.20	0.30	0.018

Table D-11 Summary of Beamline (front-ends) in FY 1992.

Beamline	Affiliation	Source	Spectral range	Status
BL-1	NTT	bending magnet (B1)	VUV and soft X-ray	in operation
BL-2	KEK-PF	60-period permanent magnet undulator	Soft-X-ray	in operation
BL-3	KEK-PF	bending magnet (B2 & B3)	VUV and X-ray	in operation
BL-4	KEK-PF	bending magnet (B2)	X-ray	in operation
BL-5	KEK-PF	permanent magnet wiggler/undulator (under design)	-	under installation
BL-6	KEK-PF	bending magnet (B6)	X-ray	in operation
BL-7	University of Tokyo	bending magnet (B7)	VUV and X-ray	in operation
BL-8	Hitachi Ltd.	bending magnet (B8)	VUV and X-ray	in operation
BL-9	Nippon Electrical Co. (NEC)	bending magnet (B9)	VUV and X-ray	in operation
BL-10	KEK-PF	bending magnet (B10)	X-ray	in operation
BL-11	KEK-PF	bending magnet (B11)	VUV and soft X-ray	in operation
BL-12	KEK-PF	bending magnet (B12)	VUV	in operation
BL-13	KEK-PF	27-pole wiggler	Soft and hard X-ray	in operation
BL-14	KEK-PF	superconducting vertical wiggler	Hard X-ray	in operation
BL-15	KEK-PF	bending magnet (B15)	X-ray	in operation
BL-16	KEK-PF	53-pole permanent magnet wiggler/undulator	Soft and hard X-ray	in operation
BL-17	Fujitsu Ltd.	bending magnet (B16 & B17)	VUV and X-ray	in operation
BL-18	ISSP and KEK-PF	bending magnet (B18)	VUV	in operation
BL-19	ISSP and KEK-PF	permanent magnet multi-undulator	VUV	in operation
BL-20	KEK-PF	bending magnet (B20)	VUV and X-ray	in operation
BL-21	KEK-PF	bending magnet (B21)	White, visible, and X-ray	in operation
BL-27	KEK-PF	bending magnet (B27)	Soft X-ray and X-ray	in operation
BL-28	KEK-PF	25-pole permanent magnet wiggler/undulator	Circularly polarized VUV and soft X-ray	in operation



# ***Beamlines and Instrumentation***



*A beam ellipsometer "ELLI" (see article on page I-11).*

## CONTENTS

	Page
<b>A. INTRODUCTION</b>	I – 1
<b>B. BEAMLINES</b>	
<b>1. NEW BEAMLINES IN OPERATION</b>	I – 1
BL-13C   Soft X-ray Undulator Beamline	
BL-27    Beamline for Radioactive Materials Studies	
<b>2. BEAMLINES UNDER CONSTRUCTION</b>	I – 2
BL-12A   2m Grazing-Incidence Monochromator Beamline	
BL-18B   Branch Beamline for Macromolecular Crystallography	
BL-20B   Australian National Beamline	
<b>3. IMPROVEMENT OF BEAMLINES</b>	I – 4
BL-3B    24-m Spherical Grating Monochromator	
<b>C. NEW INSTRUMENTATION</b>	
Tunable X-ray Polarimeter	I – 5
Apparatus for Radiation Biology Studies	I – 6
<b>D. SELECTED EXPERIMENTS</b>	
Amorphization from a Quenched High-Pressure Phase in Tetrahedrally Bonded Materials	I – 6
Direct Observation of Ge and Si Ordering at the Interface by Anomalous X-ray Diffraction	I – 7
Exciting Advances in Collagen Fibre Diffraction	I – 8
X-ray Microprobe Analysis of Thin Film and Multilayer using Grazing-Exit Condition	I – 9
Degradation of Cystathionine Irradiated with Monochromatic Soft X-rays at the K-shell Resonance Absorption of Sulfur	I – 9
Polarization Measurement of SR with the Use of Multilayers in the Soft X-ray Region	I – 11
Symmetry-Resolved K-Shell Photoabsorption Spectra for Free Diatomic Molecules	I – 11
<b>E. SUMMARY OF EXPERIMENTAL STATIONS     AND BEAMLINE OPTICS</b>	I – 12

## A. INTRODUCTION

Continuing efforts to build new beamlines and improving existing beamlines have been made in 1992. Three branch beamlines, BL-13C, BL-27A and BL-27B became operational. BL-13C is a soft X-ray undulator beamline, covering the energy range of 200 -1000 eV. BL-27A and B covers the energy ranges of 1.5 - 6 keV and 4 - 15 keV, respectively. Both of these two branch beamlines are designed for the use of radioactive samples.

The 1m Seya-Namioka monochromator on BL-12A was abandoned and has been replaced by a 2m grazing incidence monochromator. This decision had been made because the BL-20A station completed in 1991 and equipped with a new normal incidence monochromator can accept most of users' experiments performed on BL-12A.

The construction of the new protein crystallography station BL-18B went smoothly. This branch beamline was constructed to satisfy increasing demands of the protein crystallography users. About 100 experimental proposals are active now, to which beam time should be assigned at the existing Weissenberg camera station on BL-6B. The first beam had already been observed on BL-18B and we expect to assign beam time to users on the new station from April, 1993.

It should also be noted that the first white beam was observed in October 1992 on BL-20B which is being constructed under a collaborative program between the Australian National Beamline Consortium and the Photon Factory. We expect to extract the first monochromatic X-rays into the hutch in early 1993. This station will offer more chances for many Australian scientists to have more frequent access to synchrotron radiation experiments.

Among a number of new developments performed in 1992, the ellipsometer using soft X-ray multilayers is worth mentioning. With this new instrument, we can determine the polarization state of synchrotron radiation around 100eV to a few hundred eV.

As is reported in the section of Light Source, the new low emittance lattice for the 2.5 GeV ring is being proposed. A study for reexamining the matching between the optics of the existing beamlines and the new source parameters is under way.

Several examples of typical experiments are also given in this section.

## B. BEAMLINES

### 1. NEW BEAMLINES IN OPERATION

#### BL-13C Soft X-ray Undulator Beamline

A soft X-ray monochromator has been installed at BL-13 with a 13-period multipole wiggler/undulator. The monochromator was designed to achieve both a high resolution and high flux at the same time for the undulator radiation. The design is based on a cylindrical element monochromator (CEM) concept proposed by Chen<sup>1)</sup>. The photon energy range of the monochromator is 200-1000 eV, which covers the core level excitation energy of carbon, nitrogen and oxygen. The optical arrangement of the BL13C<sup>2)</sup> is described in the Users' Reports (proposal No. 91-030).

Figure 1 shows the spectrum of the undulator radiation (ring current = 300 mA) with a field parameter of  $K=1.18$  (Gap = 180 mm), obtained by the monochromator using a copper mesh (80% transmission) photocathode.

Adjustment of the optical elements has almost been completed, except for part of the function of movable exit slit and refocussing mirrors. The energy resolution at the C K-edge was estimated to be below 0.1 eV at the present stage. Fine adjustment for higher resolution is now progressing.

*N. Matsubayashi (Nat. Inst. Mat. Chem. Res.)*

- 1) C. T. Chen, Nucl. Instr. and Meth. **A256** (1987) 595.

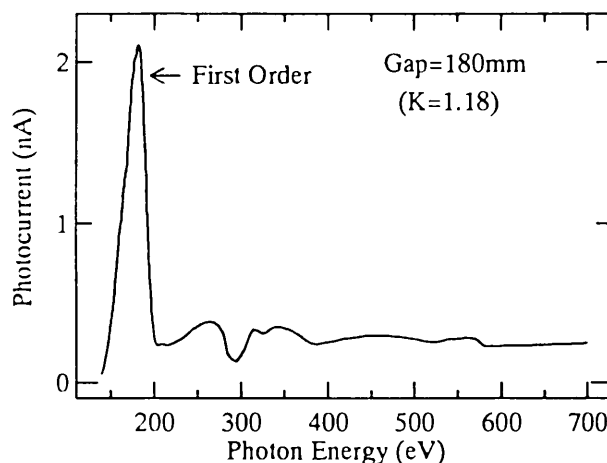


Fig. 1 Undulator radiation spectrum (ring current = 300 mA) under typical MPW/U operation with a field parameter of  $K=1.18$  (gap = 180 mm) measured with a copper-mesh (80% transmission) photocathode.



- 2) N. Matsubayashi, H. Shimada, K. Tanaka, T. Sato, Y. Yoshimura, and A. Nishijima, *Rev. Sci. Instrum.*, **60** (1989) 2533.

### BL-27 Beamline for Radioactive Materials studies

The construction of BL-27 has been completed in cooperation with outside user groups; characterization of monochromatized beams was carried out in the Spring of 1992. The purpose of the beamline is to study samples containing radioactive materials. It comprises two branch beamlines: one covering the photon energy range of 1.5 to 6 keV (BL-27A line), the other, 4 to 15 keV (BL-27B line).

In the BL-27A which is equipped with an InSb double-crystal monochromator, an irradiation apparatus for radiation biology studies and an XPS apparatus have been installed. A monochromatized beam has been focused at the sample position in the XPS chamber using a bent cylindrical mirror made of SiC. At the sample position in the irradiation chamber for biology, the beam size is about  $2 \times 20$  mm<sup>2</sup> and the photon flux is  $3.9 \times 10^9$  /sec/mm<sup>2</sup> (400 kR/min) at 2.1 keV, which means  $1.5 \times 10^{11}$  photons/sec at the XPS sample position(focal point).

In the BL-27B, which is equipped with a Si double-crystal monochromator, equipment for XAFS and the irradiation of biological samples has been installed. A diffractometer for studying diffuse scattering will be installed in the Spring of 1993. The obtained beam size and photon flux were  $3 \times 40$  mm<sup>2</sup> and  $1.7 \times 10^9$  photons/sec/mm<sup>2</sup> (14 kR/min) at 8 keV when a flat crystal was used as the second crystal in the monochromator. A sagittal focusing mechanism was installed in the monochromator; about  $2 \times 10^{11}$  photons/sec in total can be expected at the sample position of the diffractometer when focused.

K. Kobayashi

## 2. BEAMLINES UNDER CONSTRUCTION

### BL-12A 2m Grazing-Incidence Monochromator Beamline

On beamline 12A, a 1m Seya-Namioka monochromator(1-m<sub>u</sub>NIM) was installed and is used mainly for gas-phase spectroscopic studies over an energy range of 10-40 eV. Recently, a high-flux 3m normal-incidence monochromator was constructed and installed on BL-20A; most of the experiments usually carried out on BL-12A were moved to BL-20A.

In May, 1991, it was decided to introduce a Vodar-type 2m grazing-incidence monochromator (2m-GIM) on BL-12A as a post 1-m<sub>u</sub>NIM monochromator. The 2m-GIM monochromator was specially designed in order to study and test optical elements and to cover a photon energy range of 30-1000 eV with a high photon flux, moderate resolution and little contamination of higher order light.

Figure 2 is a schematic optical layout of the new BL-12A beamline. A Pt-coated SiC cylindrical bent mirror (M0) installed in a prefocusing mirror chamber (15.5 m from the source) accepts a 2.20 mrad horizontal divergent SR beam, reflects it by 5° and then focuses it onto the sample position (28.5 m from the source) in the horizontal direction. The 2m-GIM monochromator is located at about 25.5 m from the source, and comprises several optical components, as shown in Fig. 2. Operation of this Rowland mounting-type monochromator is based on a coordinated motion of the prefocusing mirror (ME), a plane mirror (MP), the entrance slit (S1) and the grating (G). Specifically, mirrors ME and MP translate parallel to the incoming beam. Mirror MP, the entrance slit and the grating are linked to each other. The coordinated motion of mirror MP and the grating corresponds to a rotation of the Rowland circle around the fixed exit slit (S2). The prefocusing

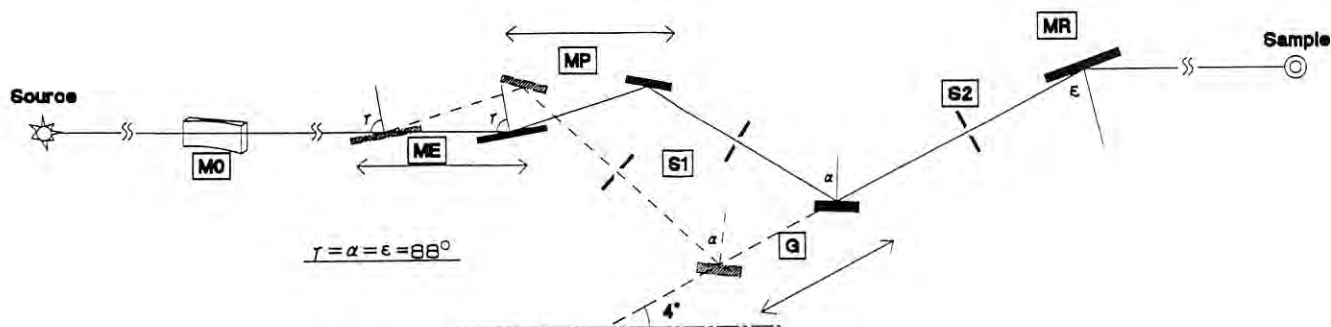


Fig. 2 Schematic layout of BL-12A



ellipsoidal mirror (ME) accepts a 0.34 mrad vertical divergent SR beam and then focuses it onto the entrance slit. The postfocusing ellipsoidal bent mirror (MR) focuses the output beam onto the sample position in the vertical direction. When a 1200 grooves/mm grating and a 10  $\mu$ m slit are used, we expect an output photon flux of  $10^{10}$ - $10^{11}$  photons/s and a resolving power of  $10^3$  at 300 eV.

Removing the 1-muNIM monochromator and installing a prefocusing mirror chamber and 2m-GIM monochromator were completed during the summer shutdown in 1992. Precise adjustments of the optical components and further improvements are now in progress.

*K. Tanaka*

### BL-18B Branch Beamline for Macromolecular Crystallography

The layout of the beamline is shown in Fig. 3. The beamline is equipped with a 1m long Pt-coated bent cylindrical mirror of fused quartz, and a double-crystal monochromator using silicon (111), (220) or germanium (111) crystals. The installation of the mirror and the monochromator was completed during the summer shutdown. Performance tests are now in progress. The mirror can focus an X-ray beam to a size of  $\sim 0.4$  mm (vertical)  $\times$   $\sim 1.2$  mm (horizontal). Photon flux at the sample position was estimated using an ionization chamber, and summarized in Table 1. The beamline will be opened for general

users in April, 1993, and a data collection for macromolecular crystallography will be carried out using the Weissenberg camera (type-II) until a type-IV camera is installed. The beamline will also be usable as a white X-ray station for the time-resolved Laue method.

*N. Watanabe*

Table 1. Intensity of monochromatic beam at the sample position at 2.5 GeV, 300 mA. The acceptance angle of the first slit was about 0.2 mrad (vertical) and 2.0 mrad (horizontal). The beam size was about 0.4 mm (vertical) and 1.2 mm (horizontal).

Crystal	Wavelength ( $\text{\AA}$ )	Flux (photons/sec)
Si(111)	1.00	$1.1 \times 10^{10}$
Si(111)	1.38	$9.6 \times 10^9$
Ge(111)	1.00	$1.5 \times 10^{10}$
Ge(111)	1.38	$2.3 \times 10^{10}$

### BL-20B Australian National Beamline

The construction of a multi-purpose X-ray experimental station at BL-20B was commenced during the summer shut-down in 1992. During this first phase of construction, a white-beam beamline was installed from the front-end to the experimental hutch; an experimental station was constructed on an optical table inside the hutch.

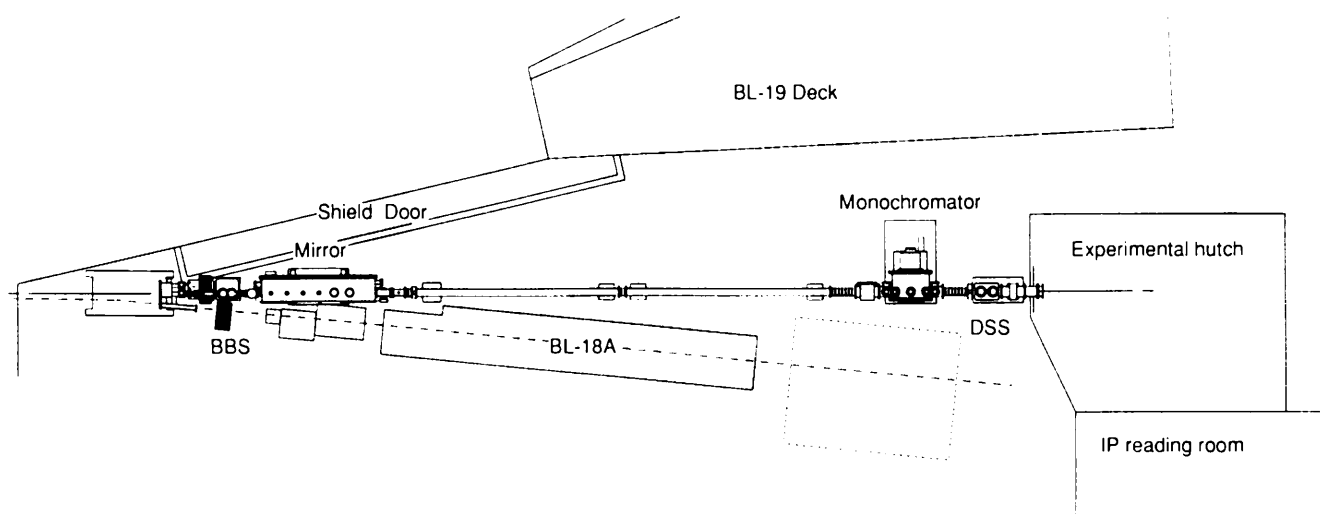


Fig. 3 Layout of BL-18B.

The first beam was accepted into the hutch in October; since that time, white X-ray experiments have been carried out. In its current con uration, the beamline is suitable for a variety of white-beam experiments, such as X-ray topography, fluorescence and Laue diffraction. Several groups of users from Australia have already visited PF to make use of the experimental station at BL-20B. The experiments carried out include Laue and topographic studies of phase transitions in a Martensite AuCuZn alloy, the topography of several optoelectronic materials, and a study of the behavior of an aluminosilicate perovskite under compression using a diamond anvil pressure cell and a solid state energy dispersive detector.

The second phase of beamline construction will begin in January, 1993, when the first monochromator will be installed. This Si(111) channel-cut monochromator was constructed in Australia at University College, University of New South Wales, in Canberra. The channel-cut crystal was manufactured by M. Hart of Manchester University. A fixed-exit height sagittal focusing double-crystal monochromator is also under construction.

The main experimental instrument, which comprises a multi-configuration diffractometer, is under construction at the CSIRO-DMST laboratory in Melbourne, and will arrive in Japan in the Spring of 1993. This instrument combines a two-circle goniometer with a large radius (0.57 m) imaging plate cassette covering an angle of approximately 270° around the sample. The two-circle goniometer incorporates angle encoders, with a sub-arc-second

resolution on each axis. The goniometer has been extensively tested, particularly to investigate the effect of mounting it with the rotation axis horizontal (see Figure 4).

The diffractometer has been optimized for a number of different experimental techniques, including: protein crystallography (Wiessenberg geometry), high-resolution powder diffraction, and small-angle scattering.

*G. Foran, D. Cookson, and R. Garrett  
(Australian National Beamline)*

### 3. IMPROVEMENT OF BEAMLINES

#### BL-3B 24-m Spherical Grating Monochromator

Recently, high-resolution spectroscopy in the VUV and soft X-ray range has been a topic of much interest along with both conceptual and technological improvements of monochromators. A 24-m spherical grating monochromator (24-m SGM) at BL-3B was designed in order to provide a high photon flux with relatively high-resolution. A 200 l/mm grating was installed in February 1992 to cover the photon energy region between 10 and 300 eV. With three in-situ interchangeable gratings (200, 600, and 1800 l/mm) the 24-m SGM covers the spectral range from 10 to 300 eV. The theoretical resolving power of the 24-m SGM is 2000-6000 with 50  $\mu$ m slit openings. It turned out, through a performance test of the 24-m SGM in 1991, that the resolving power is close to the theoretical value over the entire photon energy region when the gratings are shadowed horizontally, providing a total illuminated area of about 20 %.

In order to improve such circumstances, a realignment of the optical elements was carried out this year. As a result, it was found that the main reason why the theoretically predicted resolution could not be realized without any restriction on the illuminated area of the gratings, was due to a misalignment of the exit slit. After a realignment, it was confirmed that almost the same resolving power as in the previous case could be achieved without any restriction regarding the illuminated area of the gratings. Under this condition, the photon intensity at the sample position increased by more than three times of the previous one, as expected. The total-ion yield spectra for the rare-gases measured with three gratings are shown in figures 5-7 in order to demonstrate the resolving power of the 24-m SGM. The estimated resolving power is indicated in each figure.

*E. Shigemasa*

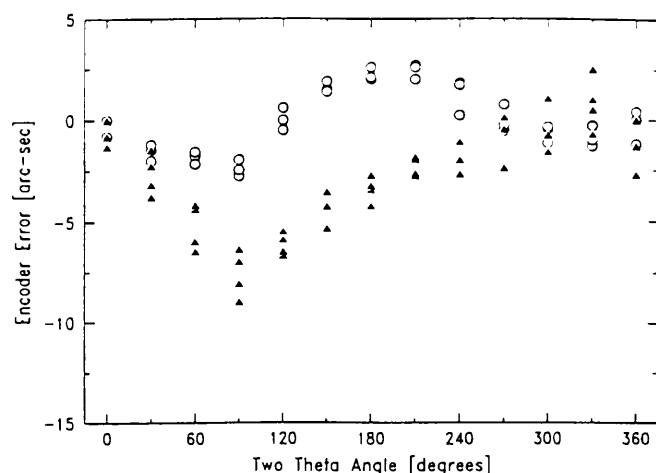


Fig. 4 Goniometer encoder angle errors measured with an auto-collimator and standard prism. The open circles are those measured with the rotation axis vertical; the filled triangles represent those measured with the goniometer mounted on its side i.e. with the rotation axis horizontal.

## C. NEW INSTRUMENTATION

### Tunable X-ray Polarimeter

A tunable X-ray polarimeter has been constructed to measure the optical activity and Faraday rotation in the energy range of 4 ~15 keV. The apparatus is basically the same as that developed by P. Siddons et. al.<sup>1)</sup> and employs a high-performance Bragg reflection polarizer for X-rays which is able to operate over a certain spectral range. The polarimeter comprises two such devices as the polarizer and analyzer in an arrangement similar to that used in visible-light optics, i.e. crossed Polaroid. When the Si 422 crystals are used, its extinction ratio of  $\pi$  component to  $\sigma$  should be about  $10^6$  near the cobalt K edge and exceeds  $10^4$  through the energy range from 7.0 ~9.2 keV, which allows measurements to be made near a large number of absorption edges in the transition metals and rare earth. A different choice of Bragg reflection in the polarimeter would provide a different operating range.

The polarimeter and analyzer are similar crystals. Each is a monolithic channel-cut crystals providing four consecutive Bragg reflections, two on each side of the channel. The special polarizing arise because the angle between the two sides of the channel may be offset by a small amount by using a controlled elastic deformation of the monolith. The offset is smaller than the angular width of the perfect-crystal Bragg reflection for the  $\sigma$  polarization but larger than that for  $\pi$  polarization. Thus, consecutive reflections across the channel are imperfectly aligned and the  $\pi$  polarized radiation is selectively suppressed at each reflection. The effect is enhanced by multiple reflections.

The first of two such devices, the polarizer, receives the white synchrotron radiation beam, and diffracts a monochromatic component in the vertical plane. The diffraction plane of the polarizer can be rotated (by  $\pm 3^\circ$ ) about the incident beam direction, if required. Since the synchrotron beam is already partially polarized in the horizontal plane, the output beam from this element is extremely well polarized. Its spectral purity is also high because this same offsetting technique also dramatically reduces harmonic contamination. The second crystal device, the analyzer, is arranged with its diffraction plane horizontal, i.e., orthogonal to that of the first crystal. This plane can be rotated (by  $\pm 3^\circ$ ) about the incident-beam direction. The rotation axis of the diffraction plane has to exactly coincides with the incident-beam direction so that the angular position

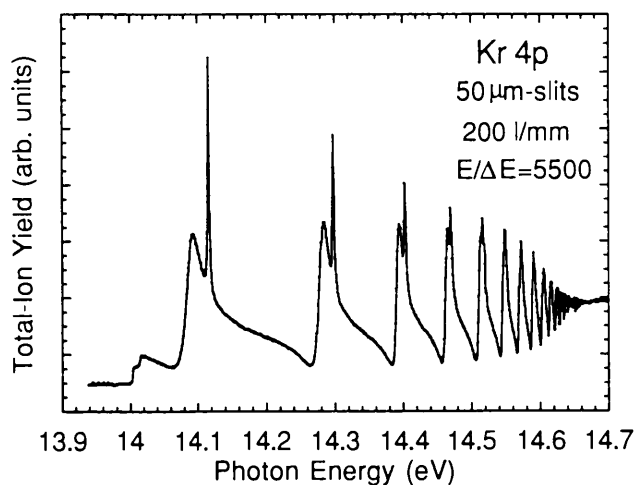


Fig. 5 Kr 4p photoabsorption spectrum.

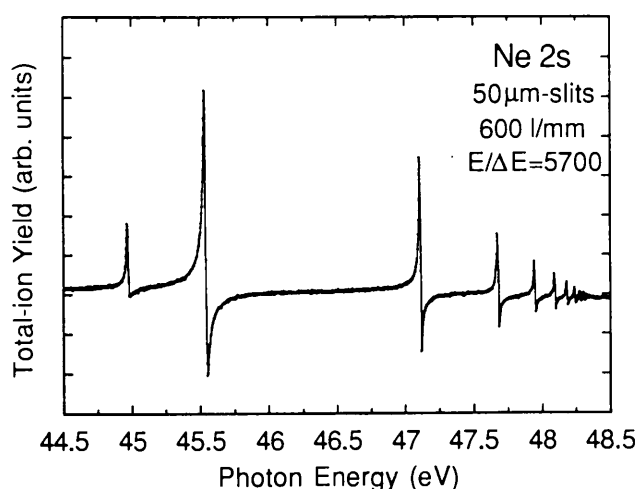


Fig. 6 Ne 2s photoabsorption spectrum.

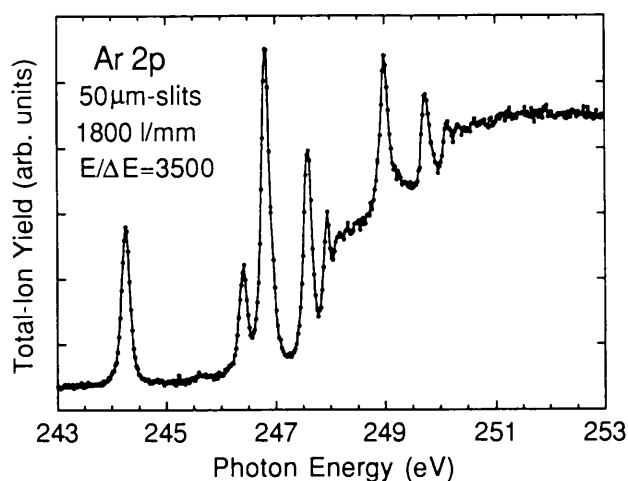


Fig. 7 Ar 2p photoabsorption spectrum.

and depth of the intensity minimum can be precisely located. A measurement of the minimum intensity and its angular position constitutes a measurement of the polarization state of the beam transmitted by the sample. The sample is placed between the polarizer and analyzer, with transmission ionization chambers before and after it to provide conventional absorption data. A useful reduction in background is achieved by the use of an intrinsic germanium solid-state detector after the analyzer. The performance of the polarimeter is now being measured.

*T. Oguchi & Y. Amemiya*

- 1) D.P.Siddons, M.Hart, Y.Amemiya & J.B. Hasting; Phys.Rev.Let., 64 (1990) 1967-1970.

### Apparatus for Radiation Biology Studies

A new apparatus for irradiation in radiation biology studies was installed at beamline BL-27A, where radioactive tracers can be used. It comprises two vacuum chambers. An upstream chamber contains a shutter, a slit system, an intensity monitor and a removable fluorescent screen, which is used to observe the beam profile. At both ends of the chamber, small apertures are attached in order to reduce the vacuum conductance, and to act as a differential pumping section. A downstream chamber is a sample irradiation chamber. It is equipped with a computer-controlled linear manipulator (stroke, 150 mm), which enables the successive irradiation of at most 15 samples. A sample holder attached at the end of the manipulator was designed to hold four sample plates, on which biological samples are placed. Therefore, 60 samples can be irradiated without breaking the vacuum of the chamber. At the downstream end of the chamber, two thin films (25  $\mu$ m Kapton and 5  $\mu$ m Mylar) are attached to 10 mm-diameter apertures in order to extract the soft X-ray beam into the air for irradiating wet biological samples.

To protect the vacuum of the beamline, the vacuum of the irradiation chamber is always monitored; in the case of a vacuum accident, a pneumatic valve between the two chambers automatically closes within 0.1 second.

*K. Kobayashi*

## D. SELECTED EXPERIMENTS

### Amorphization from a Quenched High-Pressure Phase in Tetrahedrally Bonded Materials

Amorphization from a quenched high-pressure phase has been studied for tetrahedrally bonded materials.<sup>1)-4)</sup> X-ray diffraction measurements at low temperatures and high pressures were carried out by an energy-dispersive method using synchrotron radiation from a bending magnet (BL-6C1). A diamond anvil cell which was driven by He gas through bellows allowed us to control the pressure continuously, even at low temperatures.<sup>5)</sup>

The high-pressure phases with the  $\beta$ -Sn structure for Si and Ge were quenched at low temperature to a much lower pressure; they transformed to amorphous phases when the temperature was elevated. The high-pressure phase of GaSb with the  $\beta$ -Sn structure was quenched at 100°K by reducing the pressure to 0.5 GPa. The quenched high-pressure phase showed amorphization when the temperature was elevated at 0.5 GPa and 1.0 GPa. At 2.5 GPa, however, it returned to the ZnS structure at 280°K, instead of forming an amorphous phase. Similar amorphization from the quenched high-pressure phase was observed when the pressure was reduced at 250 and 270°K. On the other hand, at 300°K the high-pressure phase returned to the ZnS structure. The results are summarized in Fig. 8. Thus, the behavior of the phase transitions strongly depends on the paths in the pressure-temperature diagram. For AlSb, amorphization from the  $\beta$ -Sn phase was observed when the pressure was reduced at 2.5 GPa and when the temperature was elevated to 300°K. In the case of CdTe, at 100°K the high-pressure phase of CdTe with the  $\beta$ -Sn structure returned to the NaCl phase at 9-6 GPa; the NaCl phase was quenched by reducing the pressure to 2.5 GPa, which was the lowest pressure at which the measurements were made. The quenched high-pressure phase with the NaCl structure began to return to the ZnS phase at 140°K, and the transition was completed at 250°K. No amorphization was observed in CdTe.

These results were analyzed using a configuration-coordinate model.<sup>1)-4)</sup> The height of the potential barrier ( $\Delta U$ ) between the two phases before and after the phase transitions was estimated from the temperature dependence of the diffraction-peak intensities. The pressure dependence of  $\Delta U$  was considered in connection with above-mentioned phase transitions.

For covalently bonded materials, the force

between atoms is anisotropic. For example, the Keating force constant includes the bond bending force constant in addition to the bond stretching force constant. In the  $\beta$ -Sn structure, the bond angle between atoms deviates from that for diamond or the ZnS structure. This anisotropic interaction should be the origin of the large height of the potential barrier. The ionic character of III-V or II-VI compound with the ZnS structure should lower the height of the potential barrier between the  $\beta$ -Sn phase and another phase. Thus, a strongly ionic character of the bonding nature prohibits amorphization.

K. Tsuji (Keio Univ.)

- 1) M. Imai, T. Mitamura, K. Yaoita and K. Tsuji, Proc. 4th Intern. Conf. High Pressure in Semiconductor Physics, (Porto Carras, Greece, 1990) p. 188.
- 2) M. Imai, K. Yaoita, Y. Katayama, J.-Q. Chen and K. Tsuji, J. Non-Cryst. Solids. 150 (1992) 49.
- 3) K. Tsuji, Y. Katayama, N. Koyama and M. Imai, Jpn. J. Appl. Phys. 32 (1993) Suppl. 32-1, 185.
- 4) K. Tsuji, Y. Katayama, N. Koyama, Y. Yamamoto, J.-Q. Chen and M. Imai, J. Non-Cryst. Solids (1993) in press.
- 5) K. Tsuji, Solid State Physics under Pressure, (KTK, Tokyo, 1985) p. 375.

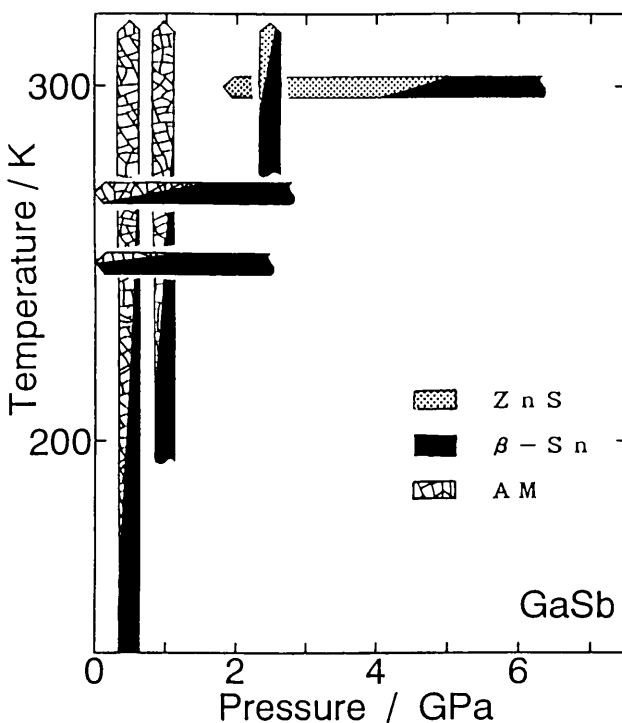


Fig. 8 Phase diagram for phase transitions from the quenched high-pressure phase along various paths for GaSb.

## Direct Observation of Ge and Si Ordering at the Interface by Anomalous X-ray Diffraction

We have modified a multiple-wavelength anomalous dispersion (MAD), a powerful direct method of structure analysis, and applied it for the first time to an interface.<sup>1)</sup>

Recently, we have observed many reconstructed structures at interfaces,<sup>2)</sup> instead of at surfaces, and considered the relation between the electronic properties and the structures. Many kinds of atomic elements are involved at these interfaces. In order to obtain real space structures, it is necessary to distinguish the atomic elements. For that purpose, we modified MAD for structural studies of interfaces.

At the Si/GeSi(111) interface, a boron-induced  $\sqrt{3} \times \sqrt{3}R30^\circ$  reconstructed structure has been found. This is expected to be a useful material since it exhibits delta-doping, in which boron-produced holes are trapped at the interface. The experiment involved using grazing-incidence diffraction techniques to obtain the integrated intensities of ten  $\sqrt{3}$  reflections. These were measured as a function of the X-ray energy across the Ge K-shell absorption edge. By separating anomalous parts, the structure factor for the boron and Si atoms and the structure factor for the normal part of the Ge atoms could be independently obtained through fitting to the experimental data.

From the resulting set of fitted structure factors, we generated separate partial Patterson functions for boron and Si, Fig. 9a and for Ge, Fig. 9b. The Patterson maps are quite different, providing direct, model-independent evidence that Ge and Si occupy different sites. These results quickly lead to a structural model. We found that the boron is in a Si substitutional site surrounded by four Si nearest-neighbor atoms, with the other sites dominated by Ge. Due to size considerations, one might expect that

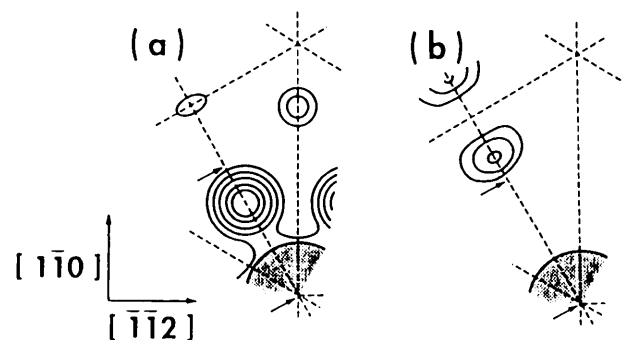


Fig. 9 Partial Patterson maps for (a) boron and Si and for (b) Ge.

boron should be surrounded by Ge, not Si. However, the binding-energy effects combined with a kinetic, surface-strain mechanism may explain this structure.

*K. Akimoto & D. J. Tweet (NEC)*

- 1) D. J. Tweet, K. Akimoto, T. Tatsumi, I. Hirose, J. Mizuki, and J. Matsui: *Phys. Rev. Lett.* 69 (1992) 2236.
- 2) K. Akimoto, J. Mizuki, I. Hirose, and J. Matsui: *Appl. Surf. Sci.* 41/42 (1989) 317.

## Exciting Advances in Collagen Fibre Diffraction

Collagen has been studied extensively by both high and low-angle X-ray diffraction over the last few decades but, because of the paucity of the data obtained, the structures have not yet been fully resolved for all types and hybrids of this heterogeneous collection of proteins. The high intensity of the beam at BL15A, coupled with the extremely high resolution obtainable from the Imaging Plates, has allowed us to expand the available data for this fibre, providing not only additional reflections in the regular arrays but also improved resolution of the known peaks and, in addition, new reflection data sets. Since collagen is the most abundant protein in mammals, providing the structural support for almost every tissue of the body by virtue of its unique molecular structure, the study of collagen is not only important in itself but vital for the complete understanding of most connective tissue disorders. We have studied the changes in collagen related to diabetes, myxomatous heart valves and carcinoma of the breast, together with in-vitro studies to determine the nature of the changes and the efficacy of proposed inhibitors.

The accepted standard X-ray diffraction pattern for collagen contains two mutually perpendicular sets of reflections, the equatorial and the meridional. The meridional pattern, in the direction of the sample, has a regular spacing of  $670\text{\AA}$ , this being the repeat distance of the gap-overlap pattern formed by the staggered layer formation of the collagen fibres under stretch conditions. The equatorial patterns for human collagen contained only one very diffuse reflection, at approximately  $15\text{\AA}$ . This distance can be related to the interfibrillar spacing of the collagen pseudo-hexagonal packing.

Two further series of reflections, both in the equatorial direction, have been added by our results from a number of two dimensional collagenous tissues, all hybrids of Types I and III. The first of

these series gives spacings over a range of  $40\text{\AA}$  to  $170\text{\AA}$ . These values provide new information about the fibril diameters for the individual tissue samples. The second series of reflections has been obtained giving identical spacings for all samples regardless of tissue, that is,  $3525\text{\AA}$ . Whilst the first relates to the fibril width, this second set possibly relates to the length of the collagen molecule itself. Up to 44 orders have been indexed for this series of reflections.

Perhaps the most spectacular of our results in this area are those observed for human myxomatous heart valves where a 2D crystalline pattern has been obtained. This is utterly unique in collagen studies. No other cases of such crystallinity have been reported. The valves examined here came from regular heart-valve replacement surgery. These crystalline patterns were evidenced in all myxomatous heart valves examined but not in the patterns from normal hearts.

Figure 10 shows (a) the accepted collagen pattern and (b) the crystalline pattern obtained from myxomatous heart valves. There are 14 sharp

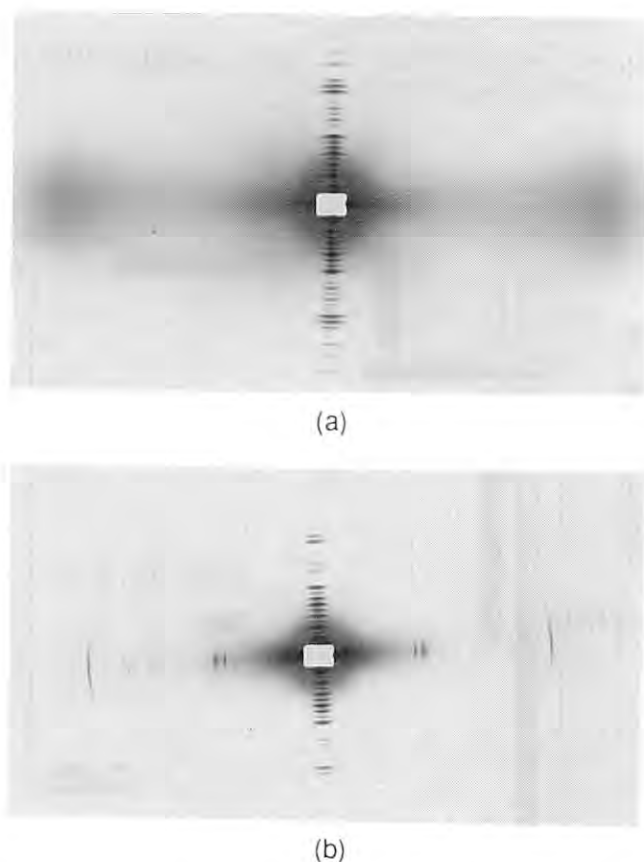


Fig. 10 (a) Accepted collagen diffraction pattern (b) X-ray diffraction pattern of a diseased heart valve showing a gap-overlap spacing and equatorial spacing of  $659\text{\AA}$ .

reflections in the equatorial direction, the spacings of which index onto 659Å, identical to that of the meridional spacing. The individual reflections present coupled with the large intensity of the reflections would be consistent with extensive cross-linking in the gap-overlap region involving the terminal poly-peptides. In some cases the patterns appeared almost colloidal and might relate to such an arrangement of cross-linked molecules. The patterns also indicate an increase in the tilt-angle of the helices of up to 10%. Such a change in the tilt angle is consistent with the known gradual change in d-spacing with age.<sup>1)</sup> These very exciting results will increase greatly the potential of collagen low angle X-ray diffraction studies of the future .

V. James (Univ. New South Wales)

- 1) James V.J. McConnell J.F. and Capel M. Biophys Biochem Acta (1991),1078,1,19-21

### X-ray Microprobe Analysis of Thin Film and Multilayer using Grazing-Exit Condition

The development of a characterization technique that is sensitive to the material surface with a high lateral spatial resolution is vital due to recent advances in both science and technology. Though the grazing-incidence (GI) condition has been widely used in various X-ray research fields to study the surface and a thin film, it is difficult to achieve sufficient lateral spatial resolution. According to the optical reciprocity theorem, information obtained through the GI experiment is the same as that with the grazing exit (GE) experiment, in which emitted fluorescent X-rays are measured at the grazing exit-angle. A combination of the GE condition and a newly developed X-ray microprobe at BL-4A has realized both a surface sensitivity and a lateral resolution of about 5 µm.

A characterization of a layered thin film was made for a patterned electrode (Cr [50 nm] / Ni [100 nm] / SiO<sub>2</sub> [substrate]). Both a scanning mode (the sample is scanned with a fixed exit-angle) and a point mode (the exit-angle is changed at a fixed sample position) were used. The lateral elemental distribution, including depth information, was obtained in the scanning mode, while the fluorescent intensity curve, which showed a strong interference effect in films, was used for detailed characterizations of thin films in the point mode (see detail in user's reports).

A synthetic multilayer (W/Si,  $d=30.6$  Å) was also

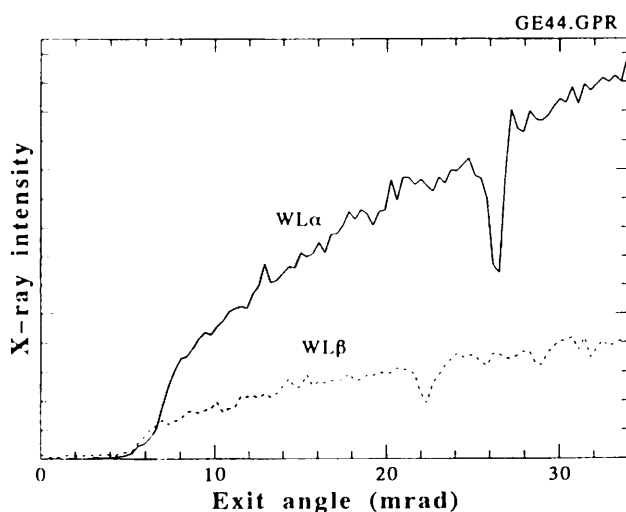


Fig. 11 W L $\alpha$  and L $\beta$  fluorescence intensities as a function of the exit-angle from a synthetic multilayer (W/Si). The incident X-ray energy was 12.5 keV.

characterized. Fig. 11 shows the W L $\alpha_{1,2}$  and L $\beta_2$  fluorescent intensities as a function of the exit-angle. The dips correspond to the X-ray intensity modulation at the Bragg condition and is due to the standing wave of fluorescent X-rays, themselves, generated in the multilayer (reciprocity X-ray standing wave). The relative angular position of the dips in the W L $\alpha$  and L $\beta$  fluorescent curves gives the absolute  $d$ -spacing, and the dip profile, itself, reflects the perfection of the layered structure. The  $d$ -spacing variation over a small region was observed.

These results show that a GE experiment using the X-ray microprobe allows the 3-dimensional characterization of a material.

A. Iida

### Degradation of Cystathionine Irradiated with Monochromatic Soft X-rays at the K-Shell Resonance Absorption of Sulfur

We found that monochromatic soft X-rays which are efficiently absorbed by phosphorus K-shell showed higher efficiencies of lethality or of the induction of genetic changes on the basis of exposure(incident photon fluence) than X-rays of less energy, which cannot be absorbed by phosphorus atoms. Inner-shell ionization/excitation, followed by the Auger effect, is considered to produce some specific damage of DNA which is hardly repaired by the cellular repair ability. To investigate the molecular damage produced specifically by inner-



shell photoexcitation, cystathionine, an amino acid, having a sulfur atom at the center of its mainchain (Fig. 12), was irradiated with monochromatic soft X-rays with the energy of the K-shell resonance absorption peak of sulfur (2472 eV) as well as with the energy just below the peak (2466 eV) using synchrotron radiation as the light source. Most of the expectable degradation products from cystathionine

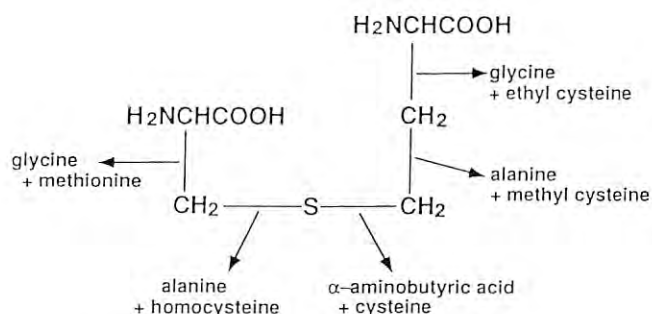


Fig. 12 Molecular structure of cystathionine

would be amino acids and can be easily analyzed by high-performance liquid chromatography.

Among the products observed,  $\alpha$ -aminobutyric acid, a product due to the cleavage of the S-C bond in the cystathionine molecule, was produced three fold upon irradiation with 2472 eV X-rays, compared to irradiation at 2466 eV, on the basis of exposure (incident flux). On the other hand, almost the same amount of glycine, a product due to C-C bond cleavage, was produced at the two irradiation energies. The yields of the two products were analyzed on the basis of the photons absorbed by either the sulfur K-shell electrons or by all of the electrons in cystathionine, except for the sulfur K-shell electrons. The analysis revealed that glycine was hardly produced through the inner-shell ionization of sulfur. Multiple ionization of sulfur as the result of an Auger cascade is suspected to be the cause of the observed change in the degradation pattern.

*K. Kobayashi*

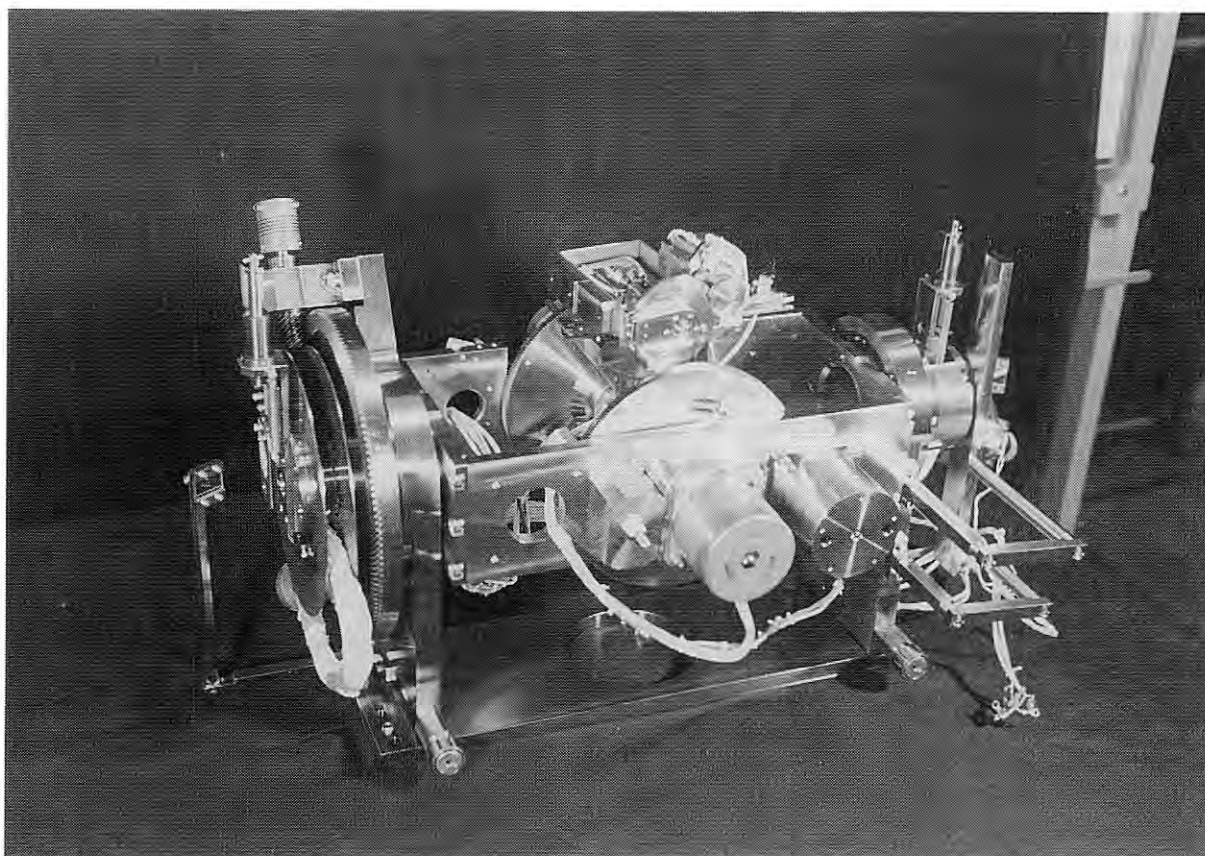


Fig. 13 A photograph of the inside mechanism of ELLI.



## Polarization Measurement of SR with the Use of Multilayers in the Soft X-ray Region

We have constructed a beamline ellipsometer, called "ELLI", which includes two polarization elements of a soft X-ray multilayer mirror (Fig. 1)). One works as a phase shifter, and the other as an analyzer. Using ELLI, RAE(Rotating-Analyzer Ellipsometry) and RAEP(Rotating-Analyzer Ellipsometry with Phase shifter) can be performed. From the phase information and the ratio of the maximum and minimum intensities, we find by RAE the azimuth of the major axis of the polarization ellipse ( $\delta$ ) as well as the degree of linear polarization ( $P_L$ ). We can also find by RAEP  $\delta$  the degree of polarization ( $V$ ), the ellipticity angle( $\epsilon$ ) for the light, and retardation, the ratio of the amplitude reflectance for the s- and p-components ( $\alpha$ ), for the phase shifter.

We determined the polarization states of light with a 12.7-nm wavelength emitted from a bending magnet (BL-18A) and a linear undulator (BL-28A) through the above-mentioned measurement. The parameters of the polarization states are listed in Table 2.

At BL-28A we detected the vertical component of the light emitted from the bending magnets sandwiching the undulator, which does not depend on the undulator gap. At BL-18A we found the dependence of  $\delta$  of monochromatized light on the vertical observation angle( $\Theta$ ) of SR. Since we confirmed a constant  $\delta$  with direct SR without using a monochromator at SOR-RING, we concluded that the inclination of  $\delta$  is caused by the effect of the beamline optical elements. Noticing this, the inclination can be well explained quantitatively (Fig. 14). The same type phenomena have been found for right- and left-handed circularly polarized light at a helical undulator beamline (BL-28A).

The polarization state of light is changed by utilizing the beamline optics. It is difficult to predict the polarization state of light emerging from the monochromator by only a theoretical prediction.

The multilayers used in this study (Mo/Si 3.19 nm/6.03 nm 101L) were qualified as an analyzer.  $\alpha^2$  of the multilayer was 700 at the above-mentioned wavelength; it was over 100 in the wavelength region from 10 to 20 nm. However, the multilayers were not sufficiently good as a phase shifter. We need to develop a good phase shifter for this wavelength region.

*H. Kimura and T. Miyahara*

Table 1-2 The parameters of the polarization state of the light.

	V	$\epsilon$ (deg)	$\delta$ (deg)
Linear undulator	0.980 $\pm$ 0.003	0.8 $\pm$ 0.8	-0.6 $\pm$ 0.1
Peak of 1st harmonics			
Bending Magnet on-axis	0.980 $\pm$ 0.008	0.2 $\pm$ 0.3	0.4 $\pm$ 0.1
Bending magnet off-axis(-1/ $\gamma$ )	0.775 $\pm$ 0.02	6.2 $\pm$ 0.9	-10.8 $\pm$ 0.3

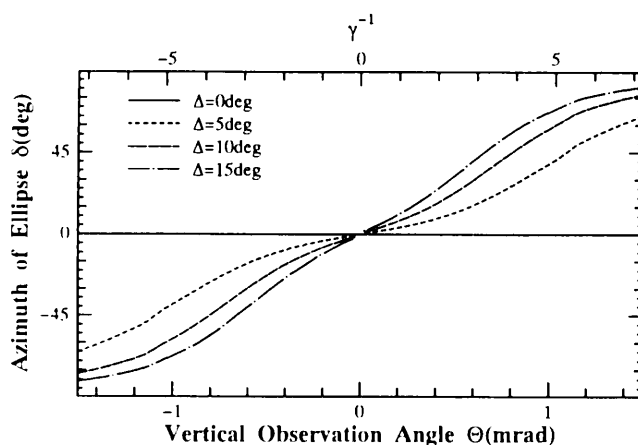


Fig. 14 Calculated  $\delta$  as a function of  $\Theta$  for several retardations  $\Delta$  of the beamline elements.

## Symmetry-Resolved K-Shell Photoabsorption Spectra for Free Diatomic Molecules

In electric-dipole transitions for molecules induced by linearly polarized light, the transition probabilities are related to the molecular orientations relative to the polarization direction. There are two types of dipole-allowed transitions for the K-shell excitations of diatomic molecules:  $\sigma \rightarrow \sigma$  ( $\Delta\Lambda=0$ ) and  $\sigma \rightarrow \pi$  ( $\Delta\Lambda=1$ ) transitions. For the  $\sigma \rightarrow \sigma$  transitions the molecules oriented parallel to the polarization direction are selectively excited, while for  $\sigma \rightarrow \pi$  transitions the molecules oriented perpendicular to the direction are preferentially excited from a random ensemble of free molecules. Such a molecular orientation is directly reflected in the angular distribution of fragment photoions emitted immediately from a repulsive potential of molecular ions, which is reached by a fast Auger decay of the K-shell vacancy, compared to the molecular rotation periods. The photoion angular distribution would be  $\cos^2\theta$  for pure  $\sigma \rightarrow \sigma$  transitions and  $\sin^2\theta$  for pure  $\sigma \rightarrow \pi$  transitions, below the K-shell ionization threshold, where  $\theta$  is the angle between the electric vector and the molecular axis. Above the ionization threshold, since the  $\Delta\Lambda=0$  and  $\Delta\Lambda=1$  ionization channels are

degenerate, the angular distribution would be  $A\cos^2\theta + B\sin^2\theta$ . The angle-resolved photoion spectroscopy, combined with linearly polarized light, offers a valuable opportunity to decompose the degenerate ionization channels.

The soft X-ray undulator beamline (BL-2B), equipped with a 10-m grazing incidence monochromator, was used, since intense, highly polarized photons were needed for the angle-resolved photoion measurements. Two identical parallel-plate analyzers with position-sensitive detectors were used to detect any energetic photoions emitted at  $0^\circ$  and  $90^\circ$  with respect to the electric vector of the incident light. The  $\sigma \rightarrow \sigma$  ( $\Delta\Lambda=0$ ) component spectrum ( $\sigma_0$ ) was obtained by counting the signals from the  $0^\circ$  positioned analyzer as a function of the photon energy. The  $\sigma \rightarrow \pi$  ( $\Delta\Lambda=1$ ) component spectrum ( $\sigma_1$ ) was obtained by the same procedure using the  $90^\circ$  positioned analyzer.

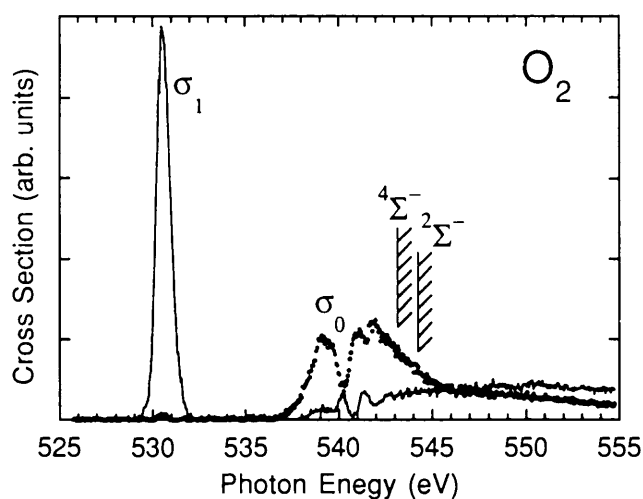


Fig. 15  $\sigma_0$  and  $\sigma_1$  symmetry-resolved K-shell photoabsorption spectra of  $O_2$ .

As an example of our work, the symmetry-resolved oxygen K-edge photoabsorption spectra of  $O_2$  are shown in Fig. 15, which were measured with a monochromator bandpass of 0.5 eV. As can be clearly seen from Fig. 1), the  $\sigma_0$  and  $\sigma_1$  spectra nicely demonstrate the symmetry decomposition of the conventional K-shell photoabsorption spectrum. The  $\sigma_0$  spectrum comprises two broad enhancements due to the  $1s\sigma \rightarrow 2p\sigma^*$  bound-state resonances, and weak peaks on the upper  $2p\sigma^*$  resonance due to the Rydberg states with  $\sigma$  symmetries. The  $\sigma_1$  spectrum comprises a strong peak corresponding to the  $1s\sigma \rightarrow 2p\pi^*$  resonance, and weak peaks for the Rydberg states with  $\pi$  symmetries.

The present technique provides a significant new approach to molecular photoabsorption: a direct method for determining the symmetries by the decomposition of the photoabsorption spectra. As a result, it has become possible to directly determine the molecular symmetries of the K-shell excited states, and to decompose degenerate states in the continuum for diatomic molecules. Symmetry-resolved K-shell photoabsorption spectroscopy with high-resolution will be performed in the near future.

*E. Shigemasa*

## E. SUMMARY OF EXPERIMENTAL STATIONS AND BEAMLINE OPTICS

Fig. 16 is the latest plan view of the SR laboratory area of the PF experimental hall schematically showing the arrangement of the experimental stations now in operation or under construction. Table 3 summarizes the experimental stations in operation with the names of contact persons. The basic characters of X-ray beamlines are listed in Table 4. And the types of monochromators for VUV and soft X-ray beamlines are listed in Table 5.

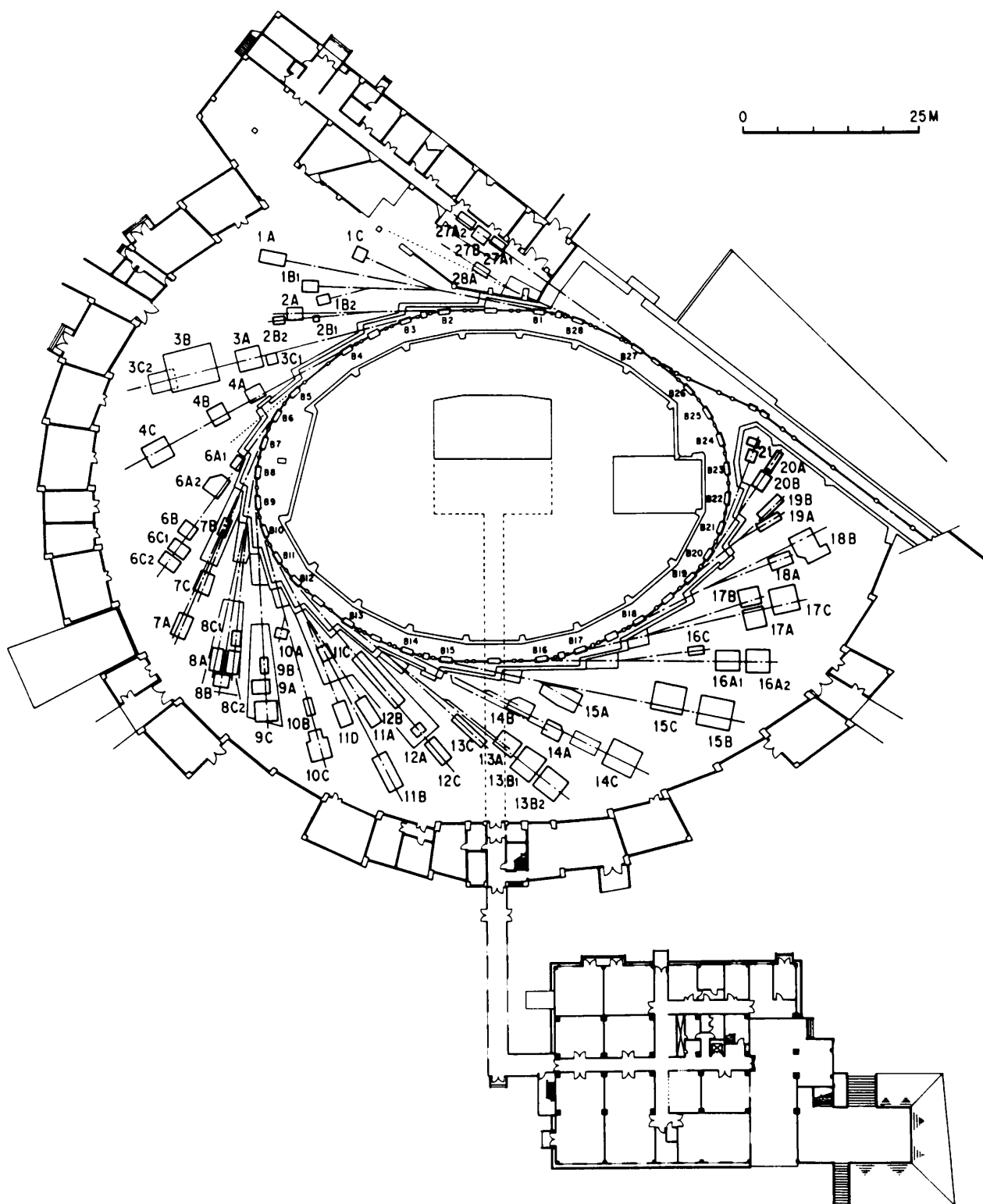


Fig. 16 Map of the experimental hall at the PF 2.5 GeV storage ring.

**Table 3. List of Experimental Stations**

Experimental Station	Contact person
BL-1 [NTT]	
A Solid surface analysis	M. Oshima
B X-ray lithography	H. Kinoshita
C Photochemical reaction	Y. Utsumi
BL-2 (Undulator)	
A Soft X-ray spectroscopy	Y. Kitajima
B1 Soft X-ray microscopy	A. Yagishita
B2 Soft X-ray spectroscopy	"
BL-3	
A X-ray diffraction and scattering	T. Matsushita
B VUV and soft X-ray spectroscopy	E. Shigemasa
C1 X-ray diffraction	T. Matsushita
C2 X-ray topography in milli-Kelvin region (for solid helium)	T. Nakajima
BL-4	
A Trace element analysis	A. Iida
B Liquid/melt structure analysis, powder diffraction, micro-crystal structure analysis	K. Ohsumi
C X-ray diffuse scattering, fluorescent EXAFS	S. Kishimoto
BL-6	
A1 Ultra small-angle X-ray scattering	M. Ando
A2 Macromolecular crystallography by Weissenberg camera	N. Sakabe
B X-ray spectroscopy and diffraction	M. Nomura
C1 X-ray diffraction at low temperatures	T. Nakajima
C2 Accurate lattice spacing measurement	M. Ando
BL-7 [The Research Center for Spectrochemistry, The Univ. of Tokyo]	
A Soft X-ray photoelectron spectroscopy	H. Namba
B Surface photochemical reaction and angle resolved photoelectron spectroscopy	"
[PF]	
C X-ray spectroscopy and diffraction	M. Nomura
BL-8 [Hitachi]	
A Soft X-ray spectroscopy	Y. Hirai
B EXAFS	A. Nakano
C1 X-ray lithography	M. Itou
C2 X-ray tomography and digital radiography	K. Usami
BL-9 [NEC]	
A X-ray lithography	K. Suzuki
B Photochemical reaction	I. Nishiyama
C EXAFS and X-ray topography/diffraction	J. Mizuki
BL-10	
A X-ray diffraction/scattering, crystal structure analysis	M. Tanaka
B XAFS	N. Usami
C Small-angle X-ray scattering of enzymes, surface diffraction	K. Kobayashi
BL-11	
A Soft X-ray spectroscopy	A. Yagishita
B Surface EXAFS, soft X-ray spectroscopy	Y. Kitajima
C VUV spectroscopy (solid state)	H. Kato
D Angle-resolved photoelectron spectroscopy	"

Experimental Station	Contact person
BL-12	
A Soft X-ray spectroscopy (under construction)	K. Tanaka
B VUV high-resolution spectroscopy	K. Ito
C Photochemical reaction	K. Tanaka
BL-13 (Multipole wiggler/Undulator) [Research team for advanced materials*]	
A Accurate lattice parameter measurement	K. Nakayama
B1 Surface-sensitive XAFS, X-ray diffraction	H. Oyanagi
B2 High pressure & high temperature X-ray diffraction	O. Shimomura
C Soft X-ray photoemission spectroscopy and XAFS	N. Matsubayashi
BL-14 (Vertical wiggler)	
A Crystal structure analysis, EXAFS	S. Kishimoto
B High-precision X-ray optics	X. Zhang
C General purpose (X-rays)	N. Watanabe
BL-15	
A Small-angle X-ray scattering of muscle and alloys	Y. Amemiya
B X-ray topography and interferometry	H. Kawata
C High-resolution X-ray diffraction	X. Zhang
BL-16 (Multipole wiggler/Undulator)	
A General purpose (X-rays)	K. Takeshita
U Soft X-ray spectroscopy	H. Kato
BL-17 [Fujitsu]	
A Characterization of crystals	S. Komiya
B Photochemical vapor deposition	"
C X-ray lithography	"
BL-18 [The Institute for Solid State Physics, The Univ. of Tokyo]	
A Angle-resolved photoelectron spectroscopy of surfaces and interfaces	A. Kakizaki
B Macromolecular crystallography (Weissenberg and Laue)	N. Watanabe
BL-19 (Revolver undulator) [The Institute for Solid State Physics, The Univ. of Tokyo]	
A Spin-polarized photoelectron spectroscopy	A. Kakizaki
B Photoelectron spectroscopy at various temperatures	"
BL-20 [PF]	
A VUV spectroscopy	K. Ito
[Australia]	
B White and monochromatic beam general purpose X-ray station	G. Foran
BL-21 [Light Source Division]	
Beam position monitoring	T. Katsura
BL-27 (Beamline for experiments using radioisotopes, under construction)	
A Radiation biology, Soft X-ray photoelectron spectroscopy	K. Kobayashi
B Radiation biology, X-ray diffuse scattering	K. Kobayashi
BL-28 (Multipole wiggler/Undulator)	
U VUV and soft X-ray spectroscopy with circularly polarized undulator radiation	T. Miyahara

\* National Laboratory of Metrology, National Institute of Researches in Inorganic Materials, Electrotechnical Laboratory, National Chemical Laboratory, The Institute of Physics and Chemical Research

**Table 4. X-Ray Beamline Optics**

Branch Beam Line	Acceptance Horis. (mrad)	Beam Size (H × W) (Hmm × Vmm)	Photon Flux at Sample Position	Type of Monochromator	Energy Resolution ( $\Delta E/E$ ) $\times 10^{-4}$	Photon Energy (keV)	Mirror
BL-3A	4	100 × 5 4 × 0.1		Double Crystal Si(111) Sagittal Focusing	~ 2	4 ~ 25	Collimating and Focusing Mirrors (Fused Quartz)
BL-3C1/C2	2	20 × 4		None		4 ~ 30	None
BL-4A	6	50 × 4 4 × 1		Double Crystal Sagittal Focusing	~ 2	4 ~ 20	None
BL-4B	4.5	50 × 5		Double Crystal Si(111)	~ 2	4 ~ 35	None
BL-4C	4	4 × 1		Double Crystal Si(111) Sagittal Focusing	~ 2	4 ~ 20	None
BL-6A1	0.1	10 × 3		Plane(111)	7.5	8 ~ 17	
BL-6A2	4	2.5 × 1		Bent Si(111) ( $\alpha = 0, 6.0^\circ, 7.8^\circ, 9.5^\circ, 11.4^\circ, 13.7^\circ, 16.5^\circ$ )		5 ~ 25	Bent Plane Fused Quartz
BL-6B	4	8 × 1		Double Crystal Si(220), Si(111), Si(311) Sagittal Focusing with Si(111)	~ 2	4 ~ 25 (4 ~ 13)	None
BL-6C1	0.5	10 × 5		None		8 ~ 30	
BL-6C2	0.5	5 × 5		Channel-Cut Si (111)	7.5	8 ~ 12	None
BL-7C	4	8 × 1	$1 \times 10^{10}/6\text{mm}^2$ (8 keV, 300 mA) ( $1 \times 10^{11}$ when focused)	Double Crystal Si (111) Sagittal Focusing	~ 2	4 ~ 20 (4 ~ 13)	Double Mirror Fused Quartz Focusing
BL-8C1/C2	5	50 × 5	$2 \times 10^6/\text{mA}\cdot\text{mm}^2$ at 10 keV with Si (111)	Channel-Cut Si(220), Si(111), Si(400)	~ 2	5 ~ 40	None
BL-9A	5	25 × 25				1.2 ~ 3.1	SiC
BL-9C	5	150 × 5		Double Crystal Si(111) Sagittal Focusing	~ 2	5 ~ 25	None
BL-10A	1	10 × 3		Si(111), Si(220) Ge(111), InSb(111) Quartz(100), PG(002) Curved Si(111) ( $\alpha \sim 4^\circ, 8^\circ$ )	50 ~ 5	5 ~ 25	None
BL-10B	2	8 × 1	$1 \times 10^9/7\text{mm}^2$ (10 keV, 300 mA)	Channel-Cut Si(311)	1	6 ~ 30	None

Branch Beam Line	Acceptance Horis. (mrad)	Beam Size (H × W) (Hmm × Vmm)	Photon Flux at Sample Position	Type of Monochromator	Energy Resolution (ΔE/E)×10 <sup>-4</sup>	Photon Energy (keV)	Mirror
BL-10C	4	6 × 1.5	~ 10 <sup>10</sup> /9mm <sup>2</sup> (8 keV, 100 mA)	Double Crystal Si(111)	2	4 ~ 10	Bent Cylinder
BL-13A	1			Double Crystal Si(220)	~ 0.1	4 ~ 30	None
BL-13B1/B2	4	4 × 1		Double Crystal Si(111), Si(220) Sagittal Focusing	~ 2	4 ~ 30	Bent plane Fused Quartz
BL-14A	1.28 (Vertical)	5 × 38		Double Crystal Si (111) Si (422) Si (553)	2	5.1 ~ 19.1 14.4 ~ 51.7 22.7 ~ 84.5	Bent Cylinder for Vertical Focusing, Pt-coated Fused Quartz
BL-14B	2.2	5 × 30		Double Crystal Si(111), Si(220), Si(311)	2	5.2 ~ 57	None
BL-14C	1.3	10 × 40		Double Crystal Si(111), Si(220)	2	5.5 ~ 69	None
BL-15A	2	0.7 × 0.8 at focus	9 × 10 <sup>10</sup> /6mm <sup>2</sup> (8.0 keV, 150 mA)	Curved Crystal Ge(111) (α = 8.0°)	~ 10	5.6 ~ 12.4	Cylinder, Fused Quartz
BL-15B	0.14	5 × 5		None		3.5 ~ 34	None
BL-15C	2	60 × 6		Double Crystal Si(111)		4 ~ 30	None
BL-16A	4	4 × 1		Double Crystal Si(111) Sagittal Focusing	~ 2	4 ~ 35	Commissioning
BL-17A	4	100 × 10		Double Crystal Si(111)	~ 2	5 ~ 13	None
BL-17C	1	20 × 5		None		2	Quartz (plane)
BL-18B	2 (Vertical)	1.2 × 0.4	1.1 × 10 <sup>10</sup> (12.4 keV, 300 mA) Si(111)	Double Crystal Si (111) Si (220) Ge (111) Ge (220)	~ 2	6 ~ 30	Bent Cylinder Fused Quartz, Pt-coated
BL-20	2	26 × 3		Channel Cut Si (111)	~ 2	4 ~ 25	None
BL-27B	4	100 × 10		Double Crystal Si (111)	~ 2	4 ~ 20	None

**Table 5. VUV and Soft X-ray Monochromators**

Branch Beamline	Acceptance Horiz./Vert. (mrad)	Type of Monochromator	Grating Groove density (l/mm)	Photon Energy (eV)	Beam Size (mm)	Typical Resolution ( $\lambda/\Delta\lambda$ )	Reference
BL-7B (RCS)	6     4	1m Seya-Namioka	1200 2400	5 ~ 50	1 × 1	1000	1
BL-11C	4.8   3	1m Seya-Namioka	1200	4 ~ 35	~1 $\phi$	1000	2
BL-12B	5     3.6	6.65 m Off-Plane Eagle	1200 4800	5 ~ 30	-----	$2.5 \times 10^5$	4, 5
BL-20A	28     5	3m Normal Incidence	1200 2400	5 ~ 40	2 × 1	$30 \times 10^4$	-----
BL-1A (NTT)	4     0.5	Grating/Crystal	1200 2400	50 ~ 900	4 × 1	500	6
BL-1B' (NTT)	1.2   4	Plane Grating	600 1200 2400	10 ~ 500	5 × 1	200	-----
BL-1C' (NTT)	2     4	Plane Grating	600 1200	15 ~ 300	-----	100	-----
BL-2B2 Undulator	K = 0.55 ~ 2.2 $\lambda_u = 6$ cm	10 m Grazing Incidence $\alpha = 89^\circ$	1200 2400	250 ~ 1600	< 0.2 $\phi$	500 ~ 5000	7, 8
BL-3B	10     2	Grazing Incidence R = 24 m $\alpha+\beta = 165^\circ$	200 600 1800	10 ~ 280	< 2 $\phi$	200 ~ 3000	9
BL-7A (RCS)	6     1	Plane Grating	1200 2400	10 ~ 1000	2 × 1	500	10
BL-8A (Hitachi)	0.5   1	Varied-space Plane Grating	800 2400	40 ~ 1800	5 × 1	1000	11
BL-11A	1     0.5	2 m Grazing Incidence $\alpha = 88^\circ$ Grasshopper Mark VII	600 1200 2400	40 ~ 1000	< 1 $\phi$	200 ~ 2000	12
BL-11D	1.5   2	Grazing Incidence R = 2 m $\alpha+\beta = 154^\circ$	600 1200 2400	20 ~ 150	1.5 $\phi$	100 ~ 1500	13
BL-12C'	5     1	Plane Grating	1200	50 ~ 800	1 × 1	100	-----
BL-13C Undulator	K = 0.3 ~ 4.2 $\lambda_u = 18$ cm	Grazing Incidence R = 50 m $\alpha+\beta = 173.2^\circ$	750	140 ~ 1000	5 × 1	~ 3000	
BL-16U Undulator	K = 0.5 ~ 5.75 $\lambda_u = 12$ cm	2 m Grazing Incidence $\alpha = 87^\circ$	1200 2400	40 ~ 600	-----	1400 ~ 2500	14
BL-18A (ISSP)	2     2	Grazing Incidence R = 3 m $\alpha+\beta = 160^\circ$ R = 6.65 m $\alpha+\beta = 167.5^\circ$	300 600 1200 500	7 ~ 150	< 1 $\phi$	1000 ~ 2000	15

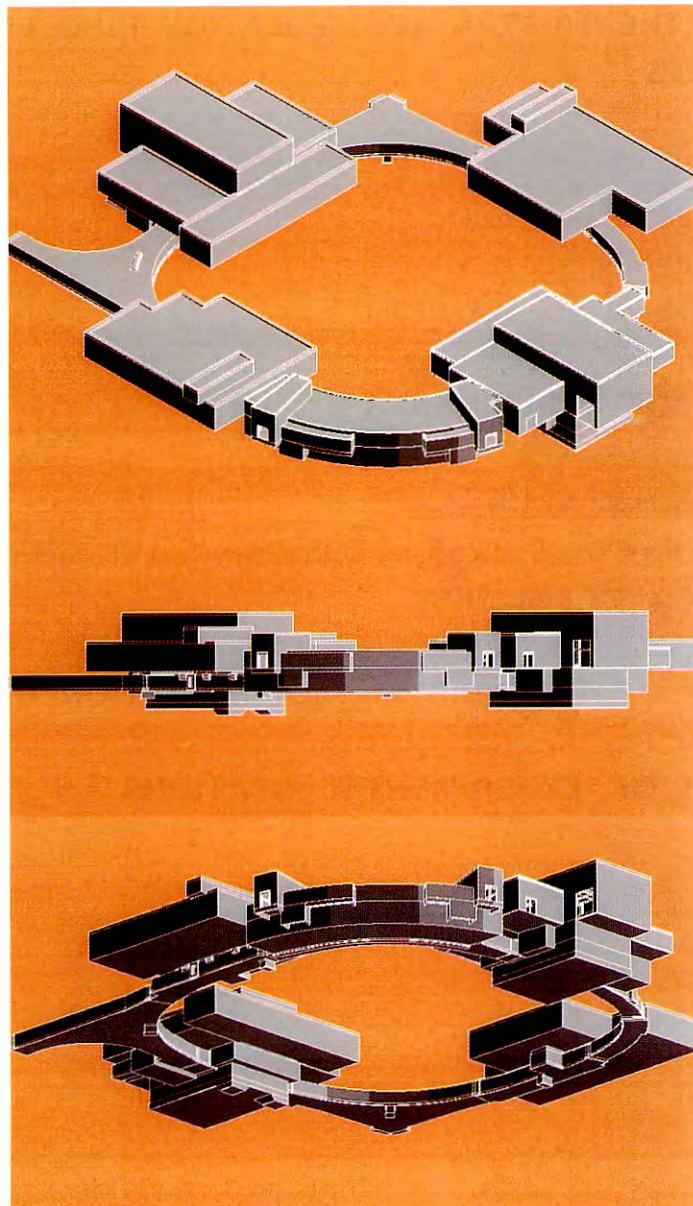


Branch Beamline	Acceptance Horiz./Vert. (mrad)	Type of Monochromator	Grating Groove density (l/mm)	Photon Energy (eV)	Beam Size (mm)	Typical Resolution ( $\lambda/\Delta\lambda$ )	Reference
BL-19A Revolver Undulator (ISSP)	$K = 1.0 \sim 9.0$ $\lambda_u = 16.4$ cm	Grazing Incidence $R = 2$ m $\alpha+\beta = 160^\circ$ $R = 4$ m $\alpha+\beta = 170^\circ$	600 1200 600 1200	12 ~ 250	$< 0.7 \phi$	1000	16
BL-19B Revolver Undulator (ISSP)	$K = 0.5 \sim 1.25$ $\lambda_u = 5$ cm $K = 0.5 \sim 2.5$ $\lambda_u = 7.2$ cm $K = 1.0 \sim 5.0$ $\lambda_u = 10$ cm	Varied-space Plane Grating	800 2400	10 ~ 1200	$< 0.5 \phi$	1500	16
BL-28U Undulator	$K_x \approx 0.5 \sim 3$ $K_y \approx 0.5 \sim 0.75$ $\lambda_u = 16$ cm	Grazing Incidence $R = 2$ m $\alpha+\beta = 160^\circ$ $R = 4$ m $\alpha+\beta = 170^\circ$	600 1200 600 1200	15 ~ 280	$< 0.5 \phi$	1000	----
BL-1A (NTT)	4      0.5	Grating/Crystal InSb (111)   Si (111)	----	1800 ~ 4000	$4 \times 1$	2000	6
BL-2A Undulator	$K = 0.5 \sim 2.2$ $\lambda_u = 6$ cm	Double Crystal InSb (111)   Si (111)	----	1760 ~ 6000	$< 0.5 \phi$	5000	8
BL-8B (Hitachi)	3      0.5	Double Crystal InSb (111)   Si (311)	----	1700 ~ 14000	$1.9 \times 0.5$	5000	----
BL-11B	4      0.6	Double Crystal InSb (111)	----	1760 ~ 3650	$8 \times 1$	2000	17, 18
BL-27A	5      0.5	Double Crystal InSb (111)	----	1800 ~ 6000		2000	----
BL-1B (NTT)	1.2    4	Plane Mirror	----	----	$5 \times 1$	----	----
BL-1C (NTT)	2      4	Toroidal Mirror	----	----	$3 \times 5$	----	19
BL-2B1	$K = 0.5 \sim 2.2$ $\lambda_u = 6$ cm	Zone Plate	----	400 ~ 830	$\sim 0.01\phi$	50	20, 21
BL-9A (NEC)	5      0.3	Oscillating Mirror	----	----	----	----	22
BL-9B (NEC)	10	Plane + Toroidal Mirrors	----	----	$15 \times 20$	----	22
BL-12C	3.8    1	Toroidal + Multilayer Mirrors	Rh - Si 21 Layers Rh - C 21 Layers	80 ~ 103 89 ~ 124	$2 \times 1$	12 15	23
BL-17B (Fujitsu)	8      1	Toroidal Mirror	----	----	$10 \times 1$	----	----

## References

1. H. Namba et al., Rev. Sci. Instrum. **60**, 1917 (1989).
2. Photon Factory Activity Report 1982/1983, V-15 (1984).
3. Photon Factory Activity Report 1982/1983, V-17 (1984).
4. K. Ito et al., Appl. Opt. **25**, 837 (1986).
5. K. Ito et al., Appl. Opt. **28**, 1813 (1989).
6. T. Kawamura et al., Rev. Sci. Instrum. **60**, 1928 (1989).
7. H. Maezawa et al., Nucl. Instrum. and Meth. **A246**, 310 (1986).
8. H. Maezawa et al., Rev. Sci. Instrum. **60**, 1889 (1989).
9. A. Yagishita et al., KEK Preprint 90-132 (1990).
10. H. Namba et al., Rev. Sci. Instrum. **60**, 1909 (1989).
11. M. Itou et al., Appl. Opt. **28**, 146 (1989).
12. M. Yanagihara et al., KEK Report 84-17 (1984).
13. T. Miyahara et al., Jpn. J. Appl. Phys. **24**, 293 (1985).
14. Y. Muramatsu and H. Maezawa, Rev. Sci. Instrum. **60**, 2078 (1989).
15. S. Suzuki et al., Activity Report of SRL-ISSP **60** (1989).
16. A. Kakizaki et al., Rev. Sci. Instrum. **60**, 1893 (1989).
17. T. Ohta et al., Nucl. Instrum. and Meth. **A246**, 373 (1986).
18. M. Funabashi et al., Rev. Sci. Instrum. **60**, 1983 (1989).
19. T. Urisu et al., Rev. Sci. Instrum. **60**, 2157 (1989).
20. Y. Kagoshima et al., Jpn. J. Appl. Phys. **29**, L 172 (1989).
21. Y. Kagoshima et al., Rev. Sci. Instrum. **60**, 2448 (1989).
22. Photon Factory Activity Report 1988 # 6, I-13 (1989).
23. Photon Factory Activity Report 1988 # 6, I-11 (1989).

# ***The TRISTAN Synchrotron Radiation Facility at the Accumulation Ring***



*A computer sketch of the AR tunnel, an arc-shaped experimental hall for utilization of SR, two big square shaped north and south buildings having deep underground parts and two other buildings having only ground levels for power stations. The top, the middle and the bottom picture corresponds to a bird's-eye view, a horizontal one and that seen from the underground.*

You can jump to the article by clicking its title.

## CONTENTS

	Page
<b>A. INTRODUCTION</b>	A - 1
<b>B. OPERATION OF THE TRISTAN ACCUMULATION RING FOR SR EXPERIMENTS</b>	A - 2
<b>C. BEAMLINES</b>	A - 2
Present Status of the AR Beamlines	A - 2
Construction of BL-NE9	A - 3
New Monochromator System at BL-NE3	A - 5
<b>D. NEW RESULTS OF EXPERIMENTS</b>	A - 6
Site Specific Magnetic XANES	A - 6
MCD Measurement at BL-NE1B	A - 7
Development of a Six-Circle Surface X-ray Diffractometer at BL-NE3A2	A - 8
Monochromatic X-ray CT at BL-NE5A	A - 10
<b>E. SPECIFICATIONS OF THE TRISTAN ACCUMULATION RING</b>	A - 11
<b>F. SPECIFICATIONS OF EXPERIMENTAL STATIONS</b>	A - 13

## A. INTRODUCTION

TRISTAN Accumulation Ring (AR) has been used successfully as a high energy photon source. We describe briefly in what follows a history of the use of the AR including research activities.

In 1982 we were invited to become involved in the design of an experimental hall attached to the AR and its future use as a synchrotron radiation activities center. At that time the Photon Factory (PF) was still in a commissioning phase, which means none of us was close to what we see now, like the number of beamlines and the number of registered users, and proprietary involvement of utilizing the synchrotron radiation, all of which are based on superb machine features. The architecture department of the KEK has agreed that a crescent-moon-shaped space around 1000m<sup>2</sup> will be built, which can accommodate 5 beamlines in the north east part of the AR. The shape of the radiation shield was just arc-shaped, so that one could be ready to receive SR from either electrons or positrons, or even both, in which one could do photon-photon collision experiments if desired.

The critical photon energy of the AR machine can tell its fascination and possible capability to those who want to use so-called hard x-rays. In the Photon Factory area a superconducting wiggler which provides hard x-rays was planned from the beginning. That device was designed so that one could use vertical polarization. Soon after that device was put into normal operation for users, not only previously scheduled scientific subjects, such as protein crystallography, very high-precision x-ray diffraction and dynamic x-ray topography but also angiography and high pressure and high temperature diffraction, have been performed in experiments at that wiggler beamline. So the Photon Factory has realized that only one such device could not meet the requirements fully for the hard x-ray activities. In particular, the group for the study of materials of all types subjected to high pressure and high temperature, which has many proposals, covering from geology to synthesis and phase diagram determination of many chemical and geological materials and another newly formed group for the angiography needed a hard x-ray larger beam size.

Nevertheless the machine staff had problems and worked to learn operation points of the superconducting wiggler such that everyone would have been happy and satisfied with such an insertion device. Not only machine people but

most users have thought that one could not have longer beam life time due to that particular device. As to considering multiplication of any insertion devices in the available straight sections, none have seemed to welcome such installation.

In order to encourage and to promote x-ray studies using high energy photons and to obtain experience as well as know-how in using SR emitted from a high energy machine for a future SR accelerator, it is of great importance to use, the AR, a high energy machine. Particular points such as operation of the machine and beamlines, shielding against the gamma rays, and so on were of great importance. The expected situation we would have been in a use was a parasitic one, which might have been comparatively a problem for anyone familiar with a completely dedicated run of the machine. One could not have expected a very comfortable situation with the AR.

Having started with only one test beamline in 1984 to accommodate two experimental stations, one for angiography and the other for the MAX 80, with which one could do a high pressure and high temperature experiments, very luckily a budget for a three-year plan, 1987-1989, and successively a two-year plan, 1990-1991, has been approved in order to accommodate two types of insertion devices and their associated beamlines and one more bend source beamline.

One of the characteristic features in utilizing the AR is tunable acceleration energy between 2.5 GeV and 6.5 GeV. Due to the relatively large bending radius of the orbit the critical photon energy at the AR, if it is operated at 2.5 GeV, is even smaller than that available from a bend source at the PF ring. In order to avoid unwanted and harmful contribution by third-higher harmonics in angiography, the acceleration energy of the ring can be suited to 5.8 GeV instead of 6.5 GeV. If the cooling efficiency of the magnets can be increased in the near future, the machine may even be run at 8 GeV, which is the energy for injection into the TRISTAN Main Ring.

The TRISTAN accelerator department has provided us with a very fine and friendly place and opportunity for users who want to do experiments with relatively high energy and/or very brilliant x-ray photons. Owing to these opportunities given, we have learned a lot. Surely these will help a great deal in the design of a future machine, such as a super-brilliant light source. That we have been utilizing this machine as a light source is quite beneficial to those who are involved in projects of any future machines. So far, in other words, that

machine has provided an outstanding contribution to synchrotron radiation sciences.

The articles in the following sections are a brief description of the operation diary of the machine AR as a light source, the status of the beamlines and the highlights of experiments. The main functioning of the AR is to accumulate electrons and positrons at 2.5 GeV for boosting up to 8 GeV, for injecting into the TRISTAN Main Ring. Improvements, such as increasing the stored current up to, say, 150mA, will be probable while the high energy program is under way. In the event of big changes of the machine, such as improving the vacuum condition, through which the beam lifetime will be much improved, further discussion will be necessary.

## B. OPERATION OF THE TRISTAN ACCUMULATION RING FOR SR EXPERIMENTS

The TRISTAN accumulation ring (AR) is a booster synchrotron of the TRISTAN main colliding ring (MR). In the interval between the beam filling in MR, AR is operated as an electron storage ring for SR experiments. The typical period of a fill is about 2 hours. Table 1 shows the parameters of the AR. Table 2 summarizes the operation statistics of the AR during this year.

An improvement of the AR during this year was replacement of seven ceramic chambers whose raise in temperature by SR limited the ring beam current to 30mA at 6.5GeV. To avoid SR irradiation of ceramics, aluminum bellows, and brazed parts between ceramics and aluminum chambers, the inner width of the new chambers was extended from 95mm to 100mm, and the chambers were moved outward by 15mm from the central beam orbit.<sup>1),2)</sup> New absorbers with larger cooling capacity were introduced to shade SR. Test operation at the current of 40mA and the energy of 6.5GeV was carried out from the second to the tenth of July 1992. No heating problem was found. Temperatures on both sides of the chambers were below 50 degrees.<sup>3)</sup>

*H. Fukuma*

- 1) T. Momose, TRISTAN memo 231 (in Japanese)
- 2) T. Momose, TRISTAN memo 274 (in Japanese)
- 3) T. Momose, TRISTAN memo 359 (in Japanese)

Table 1. General parameters of TRISTAN AR.

Energy	6.5 GeV
Number of bunch	1
Stored current	40mA
Beam life time	4-5 hr.
Natural emittance	293 nm rad
Circumference	377 m
RF frequency	508.6 MHz
Bending radius	23.2 m
Energy loss per turn	6.66 MeV
Damping time	
horizontal	2.5 ms
vertical	2.5 ms
longitudinal	1.2 ms
Natural bunch length	18.6 mm
Momentum compaction factor	0.0129
Natural chromaticity	
horizontal	-14.3
vertical	-13.1

Table 2. Operation statistics of TRISTAN AR.

AR machine study & tuning	144.0 hr.
MR machine study & injection	509.0
User time for SR research	4747.0
Machine failure	377.0
Others	187.0
Total	5964.0

## C. BEAMLINES

### 1. Present Status of the AR Beamlines

We have been operating two insertion devices and 4 beamlines and 8 associated experimental stations at the AR. Sciences under way are as follows: precision Compton scattering and magnetic Compton scattering, at NE1A1; magnetic XANES and angiography, at NE1A2; MCD (Magnetic Circularly Dichroism) and x-ray microscopy, at NE1B; Mossbauer scattering and parametric scattering, at NE3A1; surface and interface structure analysis, at NE3A2; angiography, super magnification imaging by means of SR excited fluorescence x-rays and x-ray CT, at NE5A; study of materials of all types subjected to high pressure and high temperature, at NE5C; desorption rate measurement on Al and Cu materials to be used in



the next generation machines, at NE9B. Further, in the current scheme of managing beamlines, both at the PF ring and at the AR, none of the beamlines are dedicated to development of optics and detectors. In order to fill such lack, because it is of great importance for the future program, a new beamline BL-NE9 has been fabricated so that it can accommodate two independent stations; one, to be called NE9A, for this development; and the other, NE9B, for vacuum science development. Previously the BL-NE9 has been accommodating only one station for vacuum science and technology. The NE9B will be ready for use, while the NE9A will need more work before finalizing its design.

In the summer in 1992, the "4th International Conference on Biophysics and Synchrotron Radiation (BSR 92)" was successfully held in which some of the activities at the AR participated, for instance, x-ray microscopy, angiography and x-ray CT. Not only during the conference but after that these have held either a lamp session or a workshop. Particularly the angiography group had a post conference called the "International Workshop on Medical Applications Using Synchrotron Radiation". Almost all groups all over the world that are involved in developing angiography, except from Russia, joined this workshop. That we did not have a Novosibirsk group was a pity. That Workshop was held at Daigo, 50 km north of Tsukuba, where a spa, 'Yamizo', and a sake brewery, 'Kakucho', are located. All participants enjoyed the scientific meeting and the post- and pre-conference activities. A proceedings is being printed.



Fig.1 A picture from the International Workshop on Medical Applications using SR at Daigo.

In order to house an experimental station for x-ray microscopy, which is downstream of that for MCD, a mezzanine was made. Also another

mezzanine for NE5A was constructed, to make more space on the floor there. Along with extension of beamlines and experimental stations, since more office space for staff as well as for users has been needed, two container houses were built in December 1991, just outside the experimental hall. The size of each is around 64 m<sup>2</sup>. One is for user's, while the second is for in-house staff.

The AR area does not have enough space for various kinds of preparation such as chemical, cryogenic, machine-workshop, electronics, and so on. Since we are planning installation of a cryogenic monochromator, piping for liquid nitrogen and related safety concerns will be taken care of considered.

The name of contact persons for each station are listed in Table 4, while other in-house staff who are also involved in operation and experiments at the AR are as follows: H. Fukuma and M. Yoshioka and operation group of the TRISTAN AR and S. Yamamoto, H. Kitamura, T. Shioya, and K. Tsuchiya, for ID of #NE1 and #NE3; N. Kanaya and S. Asaoka for front ends of the beamline NE1 and K. Ito, T. Kosuge and Y. Saito for interlock system. Further four Ph.D. students of the GUAS (Graduate University for Advanced Studies) are involved in the activities at the AR; their names are T. Mochizuki, for cryogenic cooling of the monochromator at BL-NE3, J. Chen, for high pressure and high temperature x-ray scattering experiment at BL-NE5C and J. Pak, for MCD experiment at BL-NE1B, J. Wang, for x-ray microscopy at BL-NE1B. We have one visiting scientist from industry, called in Japanese 'jutak kenkiu-in', named Y. Oku who is designing a compact synchrotron ring dedicated to angiography. Also one more student in a master's course from Tokyo Science University, M. Shoda is in diagnosis of a multilayer mirror for Mossbauer scattering at BL-NE3A1.

*M. Ando*

## 2. Construction of BL-NE9

A front end for the beamline NE9 has been renewed in order to accommodate two branch beamlines. Previously that had been used as a single beamline dedicated to the study of vacuum materials such as, Al and Cu by the TRISTAN vacuum group. Meanwhile no proper beamlines for developing beamline and optical components and detectors exist at the entire Photon Factory. At

least one station, if it is a bend source one, should be feasible for that purpose. In order to partially meet this requirement, a budget has been put in this beamline to install a versatile station.

A new concept that a gate valve located most upstream in the beamline should be closed and opened not manually but remotely in case of emergency and necessity so that an absorber further upstream also should be closed and opened in coincidence with a gate valve. Also improvements in interlock have been performed: a terminal CRT screen gives the current status and error messages if some failures occur. These are stored in a file and can be printed when necessary. This will be installed in January 1993. One branch of NE9B

will be operational late next fall in 1993. Figs.2 and 3 correspond to a schematic view to show how two branch beamlines are divided and a top and side view showing this beamline looks like. Further sciences using this beamline, such as use of photons in the higher energy range, up to, say, 1 MeV, can be thought, for instance Compton scattering that can provide more precision information on momentum distribution of electrons in solids, and a form factor measurement of a nucleus as well as another use of a single bunch whose shapes and features can be observed by a Hamamatsu streak camera with a temporal resolution of 1 psec.

*M.Ando*

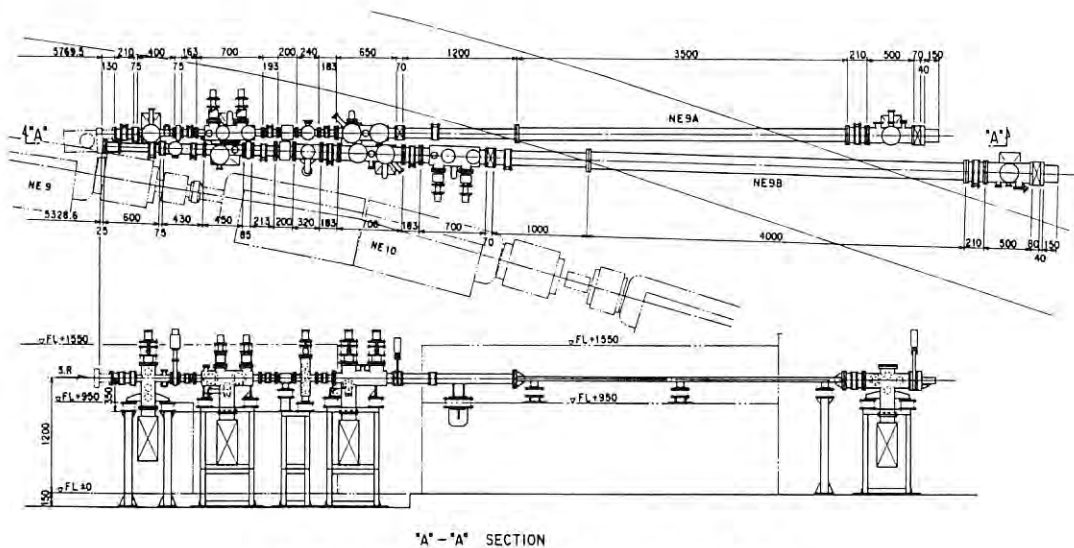


Fig.2 Schematic image of beamline BL-NE9.

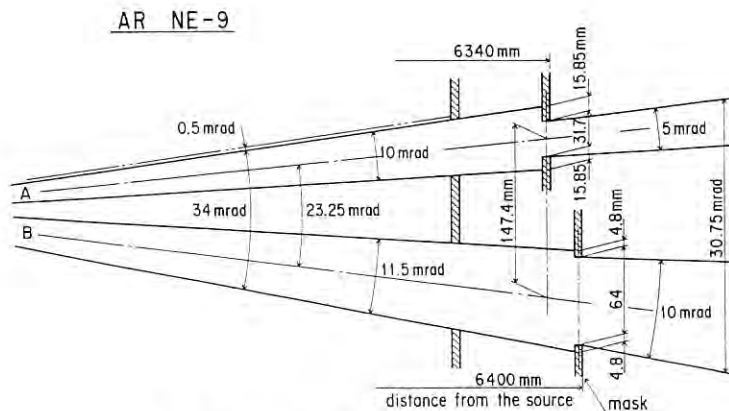


Fig.3 Layout of beamline BL-NE9.



### 3. New Monochromator System at BL- NE3

A new monochromator has installed in the beamline NE3 (Fig.4). There are several remarkable features in the new monochromator. Its mechanics are not assembled in vacuum, but in a helium gas chamber. The first crystal is mounted in a small vacuum chamber that can serve for a design of cooling the crystal using liquid nitrogen. The height of the outgoing monochromatic x-ray is 140mm higher than the incoming SR beam; it is suitable for a high energy storage ring beam line, to avoid bremsstrahlung from a long straight section. Each part of the mechanics in the first and second crystals can be controlled independently.

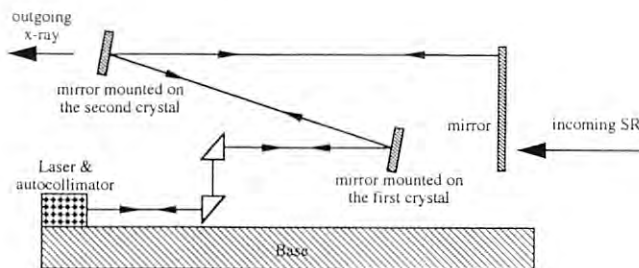


Fig. 5 A sketch of the crystals parallel monitoring optics. The optical mirrors are mounted on the crystal holders, perpendicular to the diffraction plane of the crystals.

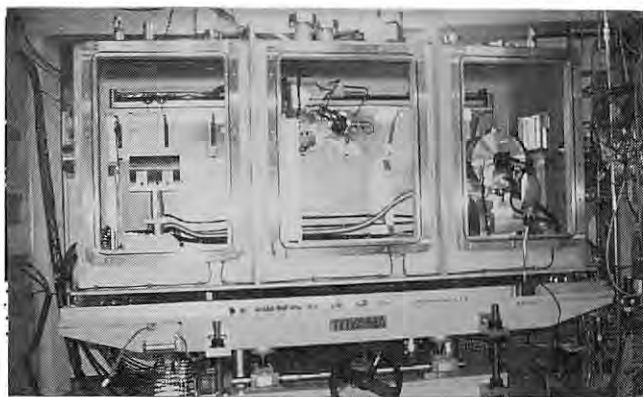


Fig. 4 A photograph of the new x-ray monochromator installed in the beamline NE3. The outgoing x-ray (left) is higher than incoming SR (right) 140mm.

Also each and both mechanisms for crystals can be controlled with constrained conditions of Bragg's law and it can provide a fixed exit beam position. The motion of the crystals can be monitored by laser optics built into the monochromator, as shown in Fig.5. Using this monitoring system, one can change the diffraction angle to select the photon energy easily, where the parallel of the two crystals is always kept within about 2 arcsec automatically.

The test running data are shown in Figs.6 and 7. The running condition of Fig.6 is a fast scan mode, where the Bragg angle was changed from 3 to 30 degrees with increments of 0.005 degrees within 12 minutes. Figure 7 shows the results of a medium scan mode within a time of 30 minutes.

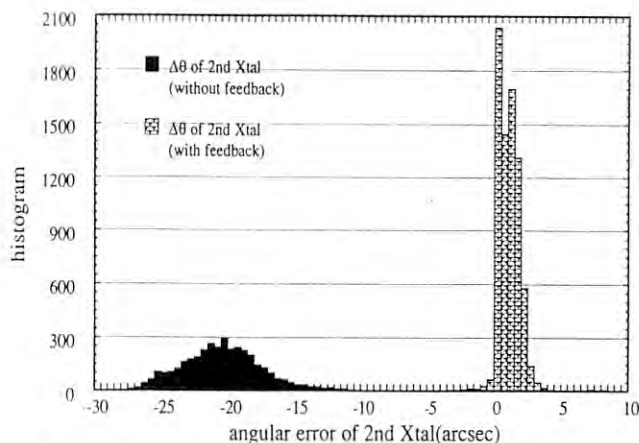


Fig. 6 Histograms of the second crystal angular error when the Bragg angle was changed from 3 to 30 degrees within 12 minutes with and without feedback. The error was recorded by an autocollimator shown in Fig.5 With feedback actions, twice standard deviations of angular error of the second crystal is lower than 4 arcsec.

Using the optical monitoring system and feedback mechanics, at most of the positions even in the motion, the crystals can be parallel within 2 arcsec. This value is smaller than the rocking curve width of silicon (111) in the range from 5 to 30 keV, which is the coverage of the x-ray undulator of NE3.

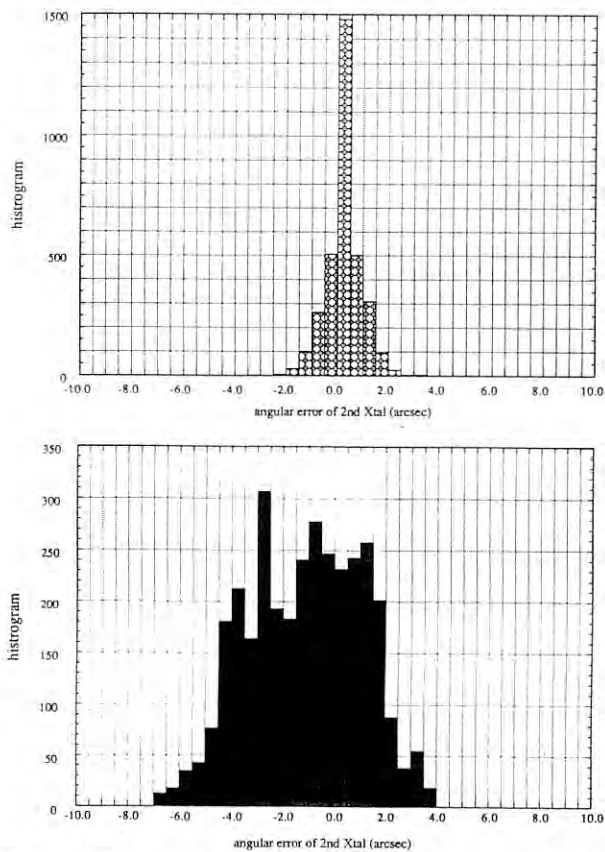


Fig. 7 Histograms of the second crystal angular error when the Bragg angle was changed from 3 to 26 degrees within 30 minutes. The top is a result after feedback actions; the bottom is a result without feedback. The twice standard deviations are 1.4 and 6 arcsec, respectively.

X. Zhang

## D. NEW RESULTS OF EXPERIMENTS

### 1. Site Specific Magnetic XANES

Magnetic X-ray Absorption Near Edge Structure (XANES) using circularly polarized X-rays gives the spin-polarized unoccupied electron states.<sup>1),2)</sup> Recently, the studies for ferro- or ferri-magnetic materials by using this experimental method have been rapidly developed. In a case of ferri-magnetic materials, however, there are two different sites for magnetic atoms; for example in the case of  $\text{Y}_3\text{Fe}_2(\text{FeO}_4)_3$  (YIG), the magnetic ions  $\text{Fe}^{3+}$  have two different sites. One is an octahedral site and the other is a tetrahedral site. The directions of magnetic moments on these sites are opposite to each other. It is naturally expected that the magnetic XANES spectra of Fe K-edge for  $\text{Fe}^{3+}$  ion at the octahedral site is different from that

for the tetrahedral site, because of the different chemical bonding and the different direction of the magnetic moment. Therefore, it is necessary to identify the site-specific magnetic in order to study these materials. At the last year, the first measurement of the site-specific magnetic XANES of YIG by mean of the following two methods.

### Magnetic XANES under a Standing Wave Field

The standing wave field method, which is obtained by exiting a dynamical Bragg diffraction in a crystal, gives us site-specific information. Therefore, magnetic XANES measurement under a standing wave field gives us the site-specific magnetic XANES.<sup>3)</sup> The experiments was carried out at the BL-NE1. Figs.8(a) and (b) show the site-specific XANES and magnetic XANES at the Fe K-absorption edge. The black dots and open circles in each figure are these of the octahedral site and tetrahedral site, respectively. As shown in this figure, the characteristic structure at the pre-edge is mainly given by the tetrahedral site.

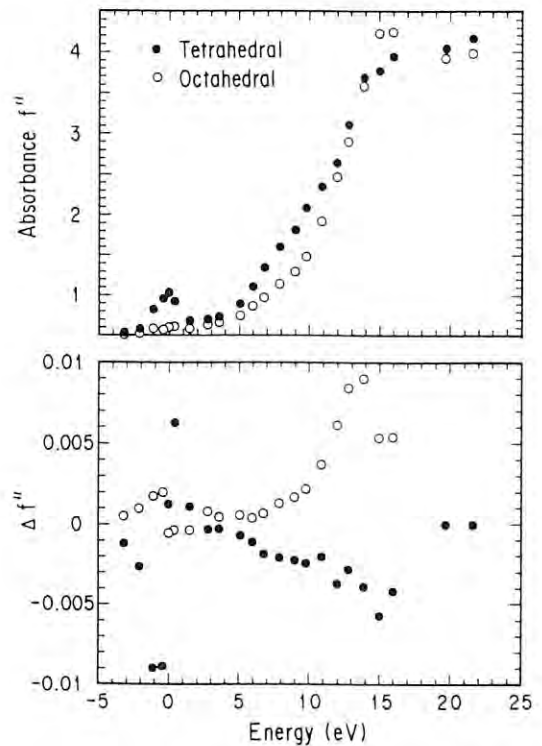


Fig.8(a)(b) The site-specific XANES and magnetic XANES at Fe K-absorption edge.

### Resonant Magnetic Bragg Scattering

Recently, the site-specific normal XANES was successfully obtained by mean of precise energy-dependent x-ray diffraction anomalous fine-structure (DAFS).<sup>4)</sup> The resonant magnetic Bragg

scattering, which is precise energy-dependent magnetic Bragg scattering around an absorption edge, just corresponds to the magnetic DAFS. Therefore, the resonant magnetic Bragg scattering from the different diffraction indexes also brings us the site-specific magnetic XANES. The experiment was carried out at BL-15B. Figs.9(a) and (b) show the results from (444) and (864) diffraction.

The structure factor of these indexes are as follows :

$$F(444) = -12f_Y + 8f_{Fe^O} - 12f_{Fe^T},$$

$$F(864) = -8f_Y - 8f_{Fe^T}.$$

Here,  $f_Y$ ,  $f_{Fe^O}$ , and  $f_{Fe^T}$  are atomic form factors of Y, Fe at the octahedral site, and Fe at the tetrahedral site, respectively. In the case of 864 diffraction, Fe at the tetrahedral site only contributes to the structure factor, and the spectrum of Fig.9(b) is well explained by the magnetic XANES of the tetrahedral site in Fig.8(b).

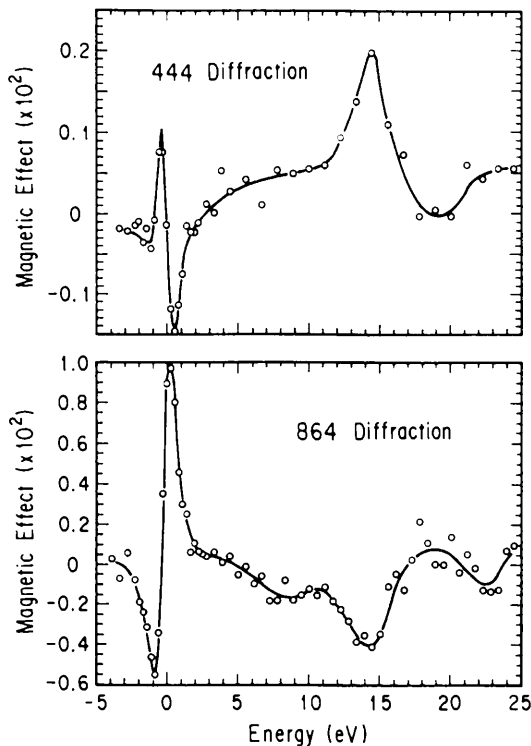


Fig.9(a)(b) The results from (444) and (864) diffraction.

H.Kawata

- 1) G. Schütz, W. Wagner, W. Wilhelm, P. Kienle, R. Zeller, R. Frahm, and G. Materik, Phys. Rev. Lett., 58(1987)737.
- 2) H. Ebert, P. Strange, and B. L. Gyorffy, J. Appl. Phys., 63(1988)3055.

- 3) H. Kawata, T. Iwazumi, N. Shiotani, and F. Itoh, The proceedings of international conference on anomalous scattering, 1992 Malente/Hamburg.
- 4) H. Stragier et al. Phys. Rev. Lett., 69(1992)3064.

## 2. MCD Measurement at BL-NE1B

The beamline, NE1B, which is for the helical undulator operation mode of the elliptical multiple wiggler EMPW#NE1 began its associated commissioning experiments in June 1992. It serves us with circularly polarized soft x rays with the photon energy ranging from 250 eV to 1500 eV. Its monochromator is an inverse Vodar type with two interchangeable gratings of 1200 *lines/mm* and 2400 *lines/mm*. The curvature of the two gratings is 10.31 m. Detail of the beamline is described in the last report.<sup>1)</sup>

The first experiment performed was the Magnetic Circular Dichroism (MCD) measurement of Ni and its alloys by using an apparatus with a permanent magnetic flipper.<sup>2)</sup> This experiment followed an original study at BL28A,<sup>3)</sup> which covers photon energies lower than those of the NE1B. In this experiment the direction of circular polarization was fixed while the magnetic field was switched at each photon energy. The frequency of the measurement per photon energy was several seconds. The maximum magnetic field at the sample position was 11 k gauss, and the sample was cooled to liquid nitrogen temperature. The basic vacuum of the chamber was better than  $4 \times 10^{-10}$  Torr during the measurement.

Figure 10 shows the total photoelectron yield spectra of the 2p-3d excitation region of Ni (a), and the MCD spectrum defined by  $\mu_{RCP} - \mu_{LCP}$  (b), where  $\mu_{RCP}$  and  $\mu_{LCP}$  are the absorption coefficients for right and left circularly polarized lights, respectively.

Two apparent peaks corresponding to L<sub>3</sub> (2p<sub>3/2</sub>-3d) and L<sub>2</sub> (2p<sub>1/2</sub>-3d) are observed in Fig.10(a). The difference in the integrated values between L<sub>3</sub> and L<sub>2</sub> in the MCD spectrum suggests that the total orbital momentum of 3d electrons does not vanish and contributes to the magnetic moment parallel to their total spin momentum. The experimental result is almost consistent with that presented by C. T. Chen et al.,<sup>4)</sup> except that the present result gives a larger MCD in spite of the poorer resolution.

The MCD spectra of Ni-Pd alloys have also been measured with the total photoelectron yield

mode, and the apparent MCD has been observed in both sites of Ni (2p-3d) and Pd (3p-4d).

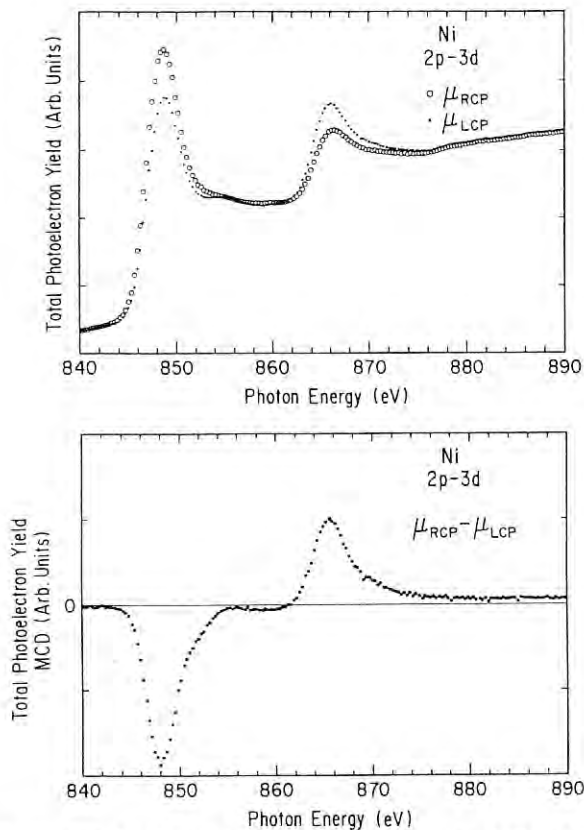


Fig.10 (a) Total photoelectron yield spectra of Ni for right and left circularly polarized light in the region of the 2p-3d excitation.  
(b) MCD spectrum defined by  $\mu_{RCP} - \mu_{LCP}$ .

*S. Muto, Y. Kagoshima and T. Miyahara*

- 1) Photon Factory Activity Report #9(1991)S-10.
- 2) S. Muto, Y. Kagoshima and T. Miyahara, Rev. Sci. Instrum., **63**(1992)1470.
- 3) S. Muto, Y. Kagoshima, T. Miyahara, S. Yamamoto and H. Kitamura, Solid State Commun., **83**(1992)41.
- 4) C. T. Chen, F. Sette, Y. Ma and S. Modesti, Phys. Rev. B, **42**(1990)7262.

### 3. Development of a Six-Circle Surface X-ray Diffractometer at BL-NE3A2

#### Design of the Diffractometer

A six-circle surface x-ray diffractometer for the structural study of surfaces and interfaces has been constructed in the beamline of NE3. A side view of the diffractometer is shown in Fig.11. In surface x-ray diffraction, x-ray intensities along the reciprocal rods have to be measured covering as wide an area as possible. Furthermore, the incident angle and the

outgoing angle of x-rays with respect to the sample surface must be controlled. Thus the conventional four-circle diffractometer is not appropriate for sophisticated surface studies.

We have designed six circles in such a way that a special five-circle diffractometer is mounted on a rotation table,  $\alpha$ . The five circles are composed of three axes for sample rotation:  $\chi$ ,  $\phi$ , and  $\omega$ , and two axes for detector rotation:  $2\theta$  and  $\beta$ , as shown in Fig.12. A pair of swivels is used for  $\chi$  axis, to make a free space on the center of rotation axis.

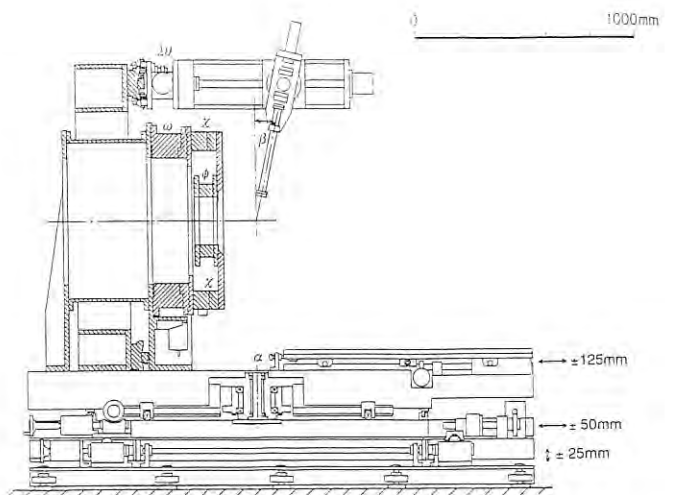


Fig.11 Side view of the six-circle surface x-ray diffractometer installed in BL-NE3.

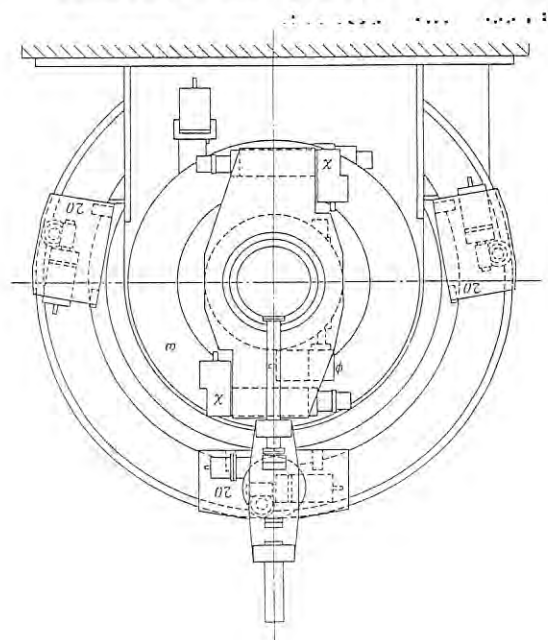


Fig.12 Side view of a five-circle part of the diffractometer.



A sample mounted on a goniometer head (not illustrated in Figs.11 and 12) is coupled tightly to the  $\phi$  circle. If the sample is mounted on a manipulator for UHV use, the five circles with the sample manipulator are loosely coupled with a vacuum chamber mounted on the rotation table a by means of a rotary feedthrough with a differential pumping system.<sup>1),2)</sup>

One of the features of the diffractometer is that three detecting systems are allowed to move independently along a  $2\theta$  circular rail to detect simultaneously diffracted beams in different directions, as indicated in Fig.12. One of the three detector tables has another axis,  $\beta$ , to detect a diffracted beam in out-of-plane measurements as shown in Fig.11. We can mount an analyzer crystal on the other two detector tables.

### Performance Test of the Diffractometer

A performance test of the diffractometer has been done using synchrotron radiation from BL-NE3. Figs.13 and 14 show an example to demonstrate high angular resolution of the diffractometer.

The (00) rod scan around the 004 Bragg point ( $L=1$ ) was performed for a so-called delta-doped sample that was epitaxially grown by evaporating a monolayer of Ge on Si(001) substrate followed by evaporation of overlayer Si of about 800Å thickness. Circles mean the integrated intensities obtained by  $\omega$ -scan with an aid of an analyzer crystal.

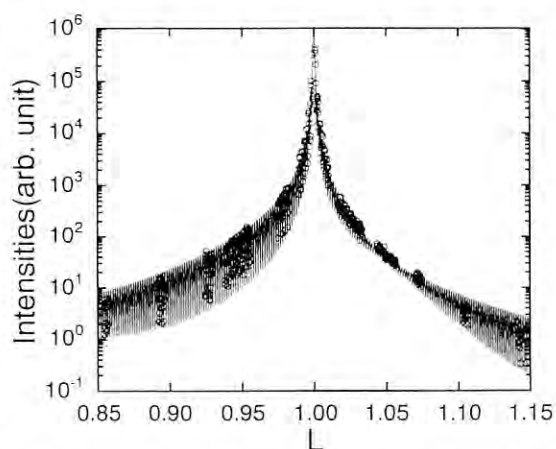


Fig.13 Overall view of the (00) rod profile around the 004 Bragg point obtained for a delta-doped sample of Si/Ge/Ge(001). Circles are observed points. The curve is a result obtained by a least-squares analysis.

Oscillations with a very short period of 0.00156 in perpendicular momentum transfer scale,  $L$ , were observed. Overall dumping of the intensity was found to be more rapid than the CTR scattering expected for a fat Si(001) crystal.

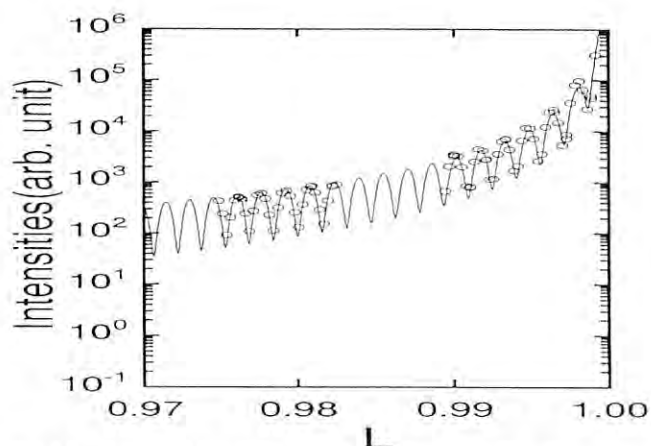


Fig.14 A part of the (00) rod profile shown in Fig.13.

From the analysis of the intensity curve, we can extract information on 1) thickness of the overlayer Si, 2) lattice distortion at the interface, 3) roughness of the interface as well as the surface. The solid curves in Figs.13 and 14 are the best fitted result using a structure model, in which the above parameters together with divergence of the incident beam and Debye-Waller factors of atoms are taken into account.<sup>3)</sup> The thickness of the overlayer was in good agreement with the sample prepared condition, 800Å. The degree of roughness toward the surface was about five times as much as that toward the substrate, which was consistent with a measurement of SIMS. The lattice distortion at the interface showed somewhat different value from that estimated from the lattice constants of Si and Ge single crystals. For more detailed and quantitative analysis, further calculations based on various models and measurements for other than (00) rods are required.

*T. Takahashi (Univ. of Tokyo) and X. Zhang*

- 1) D. Gibbs et al., Phys. Rev., **42**(1990)7330.
- 2) E. Vlieg et al., Nucl. Instrum. Methods, **A262** (1987)522.
- 3) M. Takahasi et al., Proc. Sixth Topical Meeting on Crystal Growth Mechanism, Jan. 20-22, Awara, (1993)p. 249.

#### 4. Monochromatic X-ray CT at BL-NE5A

Development of a high-resolution high-energy monochromatic x-ray CT system using SR for medical applications is under way. At present, one can get CT images in the energy range from 30keV to 75keV with a spatial resolution of  $2\mu\text{m}$  to  $8\mu\text{m}$ .<sup>1)</sup> In the near future we intend to extend the energy range up to 100keV and improve the spatial resolution better than  $1\mu\text{m}$ . The system consists of a double-crystal monochromator employing asymmetrical reflection using Ge crystals to magnify projected images, and a photodiode array detector with a phosphor screen ( $\text{Gd}_2\text{O}_2\text{S:Tb}$ ) as shown in Fig.15. The detector with size of 36mm has 512 photodiode array elements. The projection images were digitized with 16 bits and were stored in a personal computer. A CT image was reconstructed by a filtered back-projection method.

This system will be useful for investigations on brain metabolism with high resolution K-edge subtraction images utilizing contrast materials injected into vessels. Its spatial resolution of the interested region in a brain will be improved more than eight times over that of the conventional Positron Emission CT method (PET).

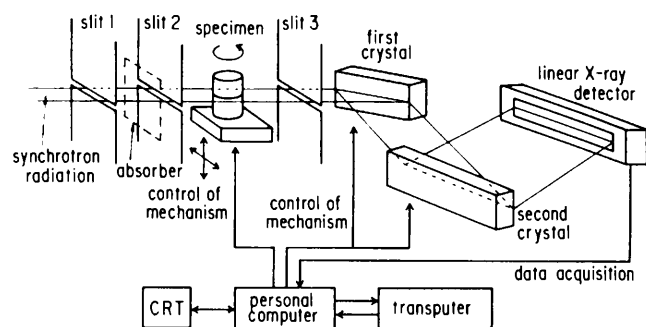


Fig.15 Schematic diagram of a monochromatic x-ray CT system using asymmetrical reflection from a crystal.

*K. Hyodo and Y. Nagata (Nippon Steel Company)*

- 1) Y. Nagata, H. Yamaji, K. Hayashi, K. Kawashima, K. Hyodo, H. Kawata and M. Ando, Res. Nondestr. Eval. 4(1992)55

## E. SPECIFICATIONS OF THE TRISTAN ACCUMULATION RING

This section summarizes principal parameters of a bend source and insertion devices and their calculated spectral performance.

Table 3. Calculated spectral performance of the bend source and insertion devices at the TRISTAN Accumulation Ring. E/I: beam energy and current,  $\lambda_u$ : period length, N: number of periods, L: length of undulator or wiggler,  $G_y$  ( $G_x$ ): minimum vertical (horizontal) gap,  $B_y$  ( $B_x$ ): maximum vertical (horizontal) magnetic field, P: pure configuration, H: hybrid configuration,  $\sigma_{x,y}$ : horizontal and vertical beam size,  $\sigma_{x',y'}$ : horizontal and vertical beam divergence,  $K_y$  ( $K_x$ ): horizontal (vertical) deflection parameter,  $\varepsilon_1/\varepsilon_c$ : photon energy of the first harmonic (critical energy in the case of bend source or wiggler),  $\Delta\varepsilon/\varepsilon$ : relative bandwidth, Pc: degree of circular polarization, D: photon flux in a unit solid angle (photons /s · mrad<sup>2</sup> · 0.1%b.w.), B: brilliance (photons/s · mm<sup>2</sup> · mrad<sup>2</sup> · 0.1%b.w.), P<sub>T</sub>: total radiated power, dP/dΩ: power in a unit solid angle. Different operation modes of a helical undulator and a wiggler are denoted by -H and -W, respectively.

Name	Bend-NE5	EMPW#NE1	-W	-H	U#NE3	
E/I GeV/mA	6.5/50	6.5/50			6.5/50	
$\lambda_u$ cm		16.0			4.0	
N		21			90	
L m		3.4			3.6	
$G_y$ ( $G_x$ )		3 (11)			1.0	
$B_y$ ( $B_x$ )		1 (0.2)			0.83	
Type of magnet		P (NdFeB)			P (NdFeB)	
$\sigma_x$ mm	0.8	1.14			1.24	
$\sigma_y$ mm	0.15	0.079			0.121	
$\sigma_{x'}$ mrad	0.45	0.14			1.24	
$\sigma_{y'}$ mrad	0.023	0.021			0.018	
$K_y$ ( $K_x$ )			15 (1)	1 (1)	1.5	3.1
$\varepsilon_1/\varepsilon_c$ keV	26.3		28 (Pc=83%)	1.2 (Pc=97%)	4.68	
$\Delta\varepsilon/\varepsilon$				0.12	0.064	
D	$3.5 \times 10^{13}$		$5.3 \times 10^{14}$	$5.4 \times 10^{15}$	$1.4 \times 10^{16}$	
B	$4.7 \times 10^{13}$		$8.8 \times 10^{14}$	$9.5 \times 10^{15}$	$1.5 \times 10^{16}$	
P <sub>T</sub> kW			4.5	0.04	0.78	3.3
dP/dΩ kW/mrad <sup>2</sup>	0.38		5.6	0.49	8.95	35

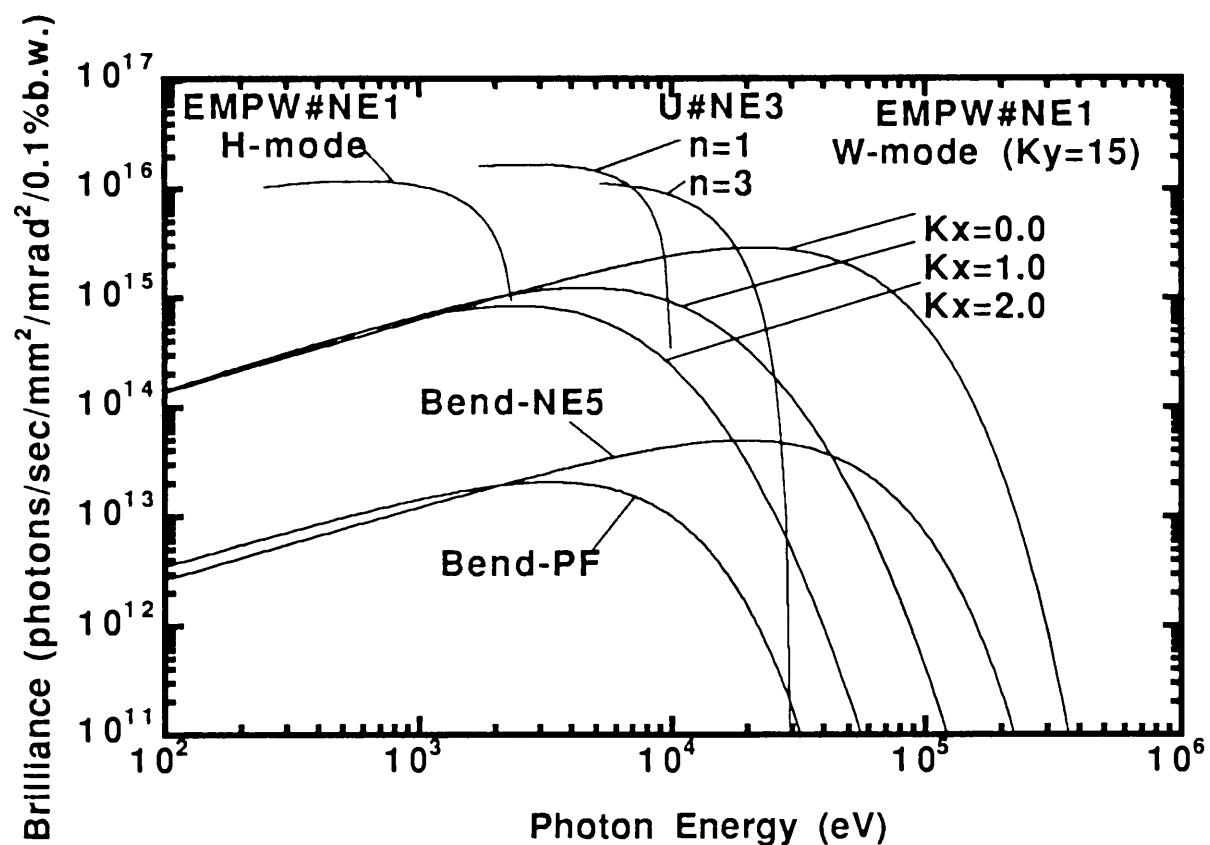


Fig. 16 Synchrotron radiation spectra.

Brilliance of radiation vs. photon energy for the insertion devices (EMPW#NE1 and U#NE3) and the bending magnet (Bend-NE5,NE9) of the AR. The name of each source is assigned in Table 3. EMPW#NE1 has both a helical undulator and a wiggler modes, which are denoted by H or W, respectively. The spectral curve of each undulator (or a helical undulator mode of EMPW) is a locus of the peak of the harmonics within the allowable range of K-parameter.



## F. SPECIFICATIONS OF EXPERIMENTAL STATIONS

This section summarizes the experimental stations with the names of the contact persons (Table 4) and the beamline optics (Table 5). Figure 17 shows a plan view of the experimental hall of the Accumulation Ring (AR).

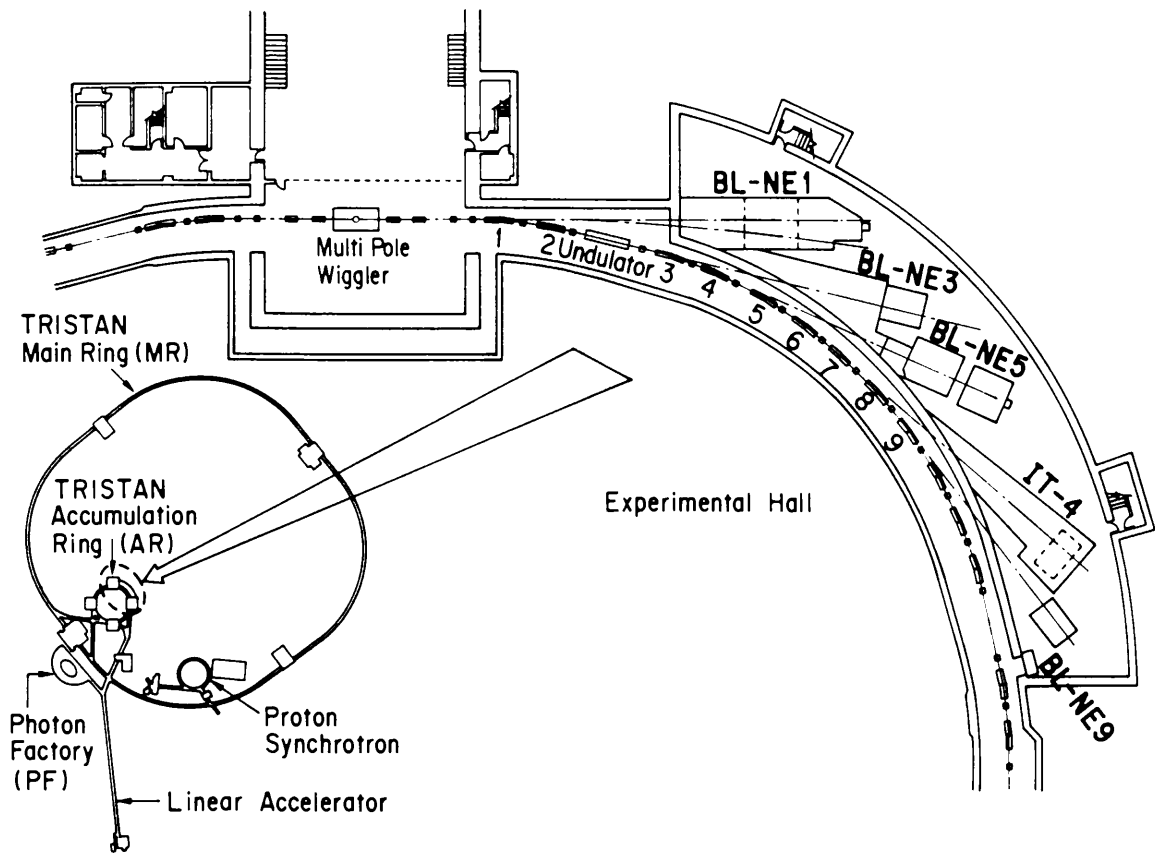


Fig.17 Plan view of the experimantal hall of the TRISTAN Accumulation Ring (AR).

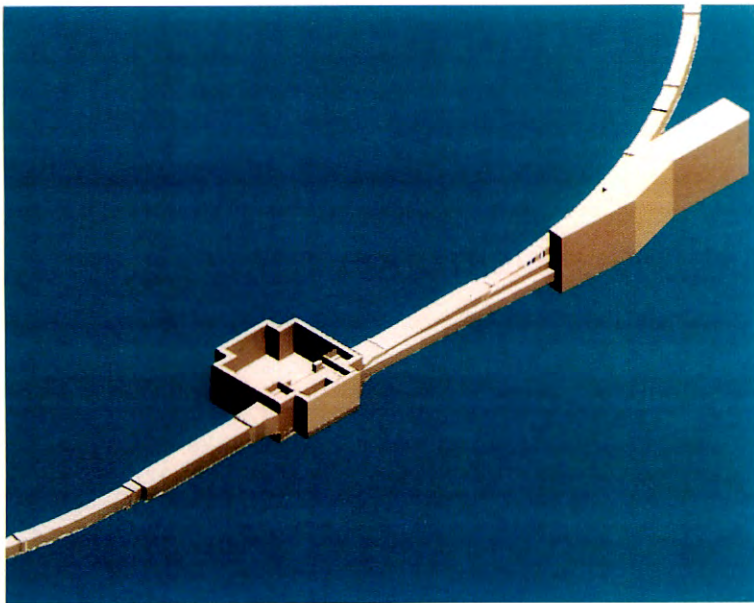
Table 4. List of Experimental Stations.

Experimental station	Source	Typical Experiments	Contact Person
BL-NE1	EMPW#NE1		
A1		Precision Compton and magnetic Compton scattering	H. Kawata
A2		Spectroscopy and scattering with circularly polarized x-rays	T. Iwazumi
B		Spectroscopy with circularly polarized soft x-rays	Y. Kagoshima T. Miyahara
BL-NE3	Undulator#NE3		
A1		Nuclear resonant scattering	X. Zhang
A2		Surface and interface diffraction	H. Sugiyama
BL-NE5	Bending-NE4		
A		Angiography. X-ray tomography	K. Hyodo
C		High pressure and high temperature x-ray diffraction	T. Kikegawa
BL-NE9	Bending-NE8		
A		In design	M. Ando
B		Vacuum science and technology	K. Kanazawa

Table 5. List of Beamline Optics.

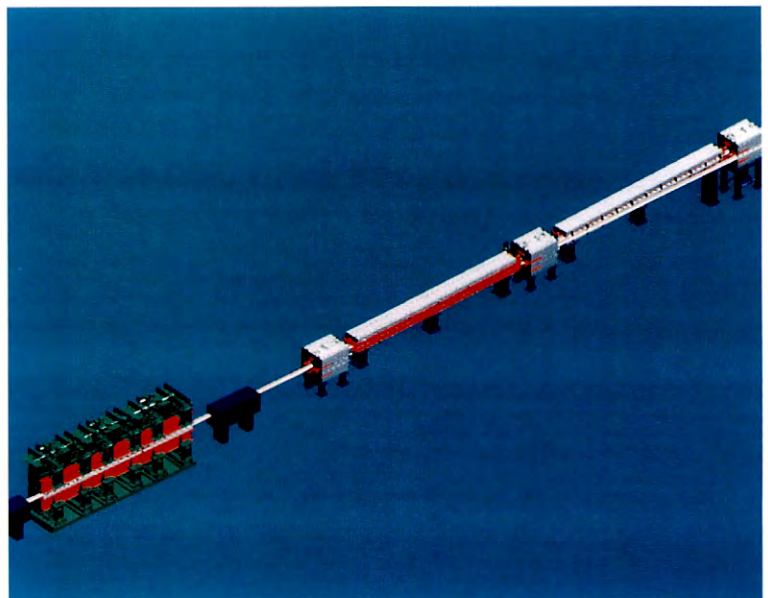
Experimental Station	Horizontal Angular Acceptance (mrad)	Typical Beam Size (hor.xver.) (mm <sup>2</sup> )	Photon Flux at Sample Position (mm <sup>2</sup> /s/mA)	Monochromator System	Energy Resolution ( $\Delta E/E$ )	Energy Range (keV)
NE1-A1	2	8×3	$1 \times 10^{10}$ (60.0keV)	Single Crystal Si(111) Double Bent Crystal Si(111)	$1.5 \times 10^{-3}$	40~70
NE1-A2	2	80×4 4×4		Double Crystal Si(111) Sagittal Focusing Si(111)	$2 \times 10^{-4}$	6~28
NE1-B	~0.2 [0.02(ver.)]	~0.3×0.1	~ $1 \times 10^{11}$ (400eV)	10m Grazing Incidence Grating (1200 or 2400lines/mm) $\beta=89^\circ$	$2 \times 10^{-3}$	0.25~1.8
NE-3A1	0.5	10×1	$1 \times 10^3$ (14.4keV)	Double Crystal Si(111) with fine monochromator of Si with Single Crystal $^{57}\text{Fe}_2\text{O}_3(777)$	$1 \times 10^{-4}$ $5 \times 10^{-7}$ $1 \times 10^{-11}$	5~25
NE5-A	10	150×10	$5 \times 10^8$ (33.2keV)	Asymmetrically Cut Single Crystal Si(311) ( $\alpha=4^\circ \sim 6^\circ$ )	$6 \times 10^{-3}$	20~40
NE5-C	3	60×5		Double Crystal Si(111) (Sagittal Focusing)	$1 \times 10^{-3}$	30~100
NE9-A	5			not fixed		
NE9-B	10	10×3		white beam	none	none

# ***The Tristan Super Light Facility***



*An example of computer-aided designs for the TSLF:  
(a) an external view of the MR tunnel equipped with a new TSLF's experimental hall, and*

*(b) a front end of a new beamline shown together with a super-brilliant-x-ray undulator and other accelerator components inside the tunnel.*



CONTENTS

<b>A. INTRODUCTION</b>	Page S – 1
<b>B. TRISTAN MR AS A VERY LOW-EMITTANCE MACHINE</b>	
1. MACHINE PARAMETERS OF THE TSLF PROJECT	S – 2
2. BEAM-EMITTANCE MONITOR FOR THE TSLF	S – 4
3. TRIAL MANUFACTURING OF A COPPER VACUUM DUCT	S – 6
<b>C. R&amp;D STUDIES ON NEW INSERTION DEVICES FOR THE PROJECT</b>	S – 7
<b>D. EXPERIMENTAL STATIONS AND INSTRUMENTATION FOR THE TSLF</b>	
1. NEW BUILDING AND EXPERIMENTAL STATIONS	S – 10
2. HEAT REMOVAL FROM BEAMLINE COMPONENTS	S – 12
<b>E. COHERENT X-RAY SOURCES</b>	S – 13
<b>F. SCIENTIFIC CASE</b>	S – 15

## A. INTRODUCTION

Director General Hirotaka Sugawara has made official announcements not only in science communities, but also in the KEK steering committees since 1989, that the Tristan Main Ring (MR) should be converted into a novel light source which is defined as a "superthird-generation" or "fourth-generation" light source. Along this line, a dedicated project called the Tristan Super Light Facility (TSLF) was born in May, 1990. Since then, during these two years the following activities, together with the budget requirement for reconstructing the MR into a new light source, have been carried out.

First of all, as activities of the TSLF project, four new members dedicated to this project have been involved. They are K.Ohsumi, S.Kamada, S.Yamamoto and H.Sugiyama. In this TSLF project K.Ohsumi is in charge of instrumentation R&D and scientific applications, S.Kamada in charge of conversion of the whole MR into a super light source, S.Yamamoto in charge of insertion devices, a key for leading this MR to a super brilliant light source and H.Sugiyama currently in charge of beamlines and optics and their associated buildings. Naturally, this should proceed as a whole KEK project. Thus, participation not only of dedicated members, but also of all possible other members from all divisions, such as the PF light source, the PF instrumentation and the Tristan accelerator are needed.

A budget for promoting this project as an international collaboration was established in fiscal year 1992, which is currently being led by H.Iwasaki, the PF director. Its first meeting was held on 2nd and 3rd of July, 1992, at KEK with the participation of some 60 persons. In that meeting, the modification of the MR into a light source together with novel insertion devices was discussed.

A committee for promoting this project was founded in June, 1992, which is chaired by S.Kikuta (University of Tokyo). This (we call it the MR committee) is under the scheme of the PF users community currently chaired by K.Hieda (St. Paul's (Rikkyo) University). This activity is also shared by its subcommittee of the PF users community, called the Utilization Subcommittee chaired by N.Shiotani (Tokyo University of Fisheries). The MR committee is in charge of establishing all probable striking topics to be fitted to the super light available from the TSLF. As a first step of its activity, a call for good proposals has been initiated.

Currently the names of the members of this Committee are as follows: M.Ando (PF), Y.Hatano (Tokyo Institute of Technology), S.Kikuta (University of Tokyo), Y.Kimura (KEK), H.Kobayakawa (PF), T.Matsushita (PF), T.Ohta (University of Tokyo), I.Sato (PF), S.Sato (Tohoku University), and N.Shiotani (Tokyo University of Fisheries).

The editing process for a conceptual design report of this project is underway. Its chapters are as follows: Chapt.1. What is leading to a Tristan super light facility (TSLF); Chapt.2. Conversion plan of Tristan to a light source; Chapt.3. Basic design of insertion devices for the project; Chapt.4. Coherent x-ray sources; Chapt.5. Beamline and experimental hall; Chapt.6. Instrumentations and experiments. Any request for this publication to be named as KEK progress report No. 92-1, January 1992 should be addressed to the library of KEK or to the office of the TSLF project. A free copy will be available.

H.Iwasaki, S.Kamada, H.Kitamura, S.Yamamoto, K.Ohsumi, S.Kikuta (University of Tokyo) and M.Ando attended the Workshop on Fourth-Generation Light Sources held at SLAC on February 24-27, 1992. Participation from KEK was of importance from the viewpoint of being involved in one of the three potentially convertible fourth-generation light sources in the world. The definition of a fourth-generation light source, the fundamental performance limits of a fourth-generation light sources and suggestions concerning R & D towards the development of the fourth-generation light sources were discussed at the meeting.

The architectural and civil engineering designs of beamline tunnels and experimental halls are in making progress by introducing a computer-aided design (CAD) system, which comprises a SPARC 2 station and a CAD software called "Medusa". In the current design a very long straight section, either at the Nikko or Tsukuba experimental station, will be modified so that one can accommodate the above-mentioned insertion device and its associated beamline. That beamline will be designed in 1993 and will be fabricated by spring 1994 so that extraction of the first synchrotron radiation will be performed in order to carry out important original experiments. The selection of research subjects which are suitable to this activity will be done soon.

The actually construction of one prototype undulator comprising three units has been initiated. That will be delivered in by the end of March,

1993. In order to economize the manpower necessary for installing and commissioning it, an in-vacuum version which has been developed for BL NE3 at the AR was not adopted. Nevertheless, its 1st higher harmonic can provide photons up to 20 keV or so under the condition that the acceleration energy of the ring is 10 GeV. This idea also seems to be quite adaptive so that any straight section can accommodate necessary the number of insertion device units.

In order to proceed with this extremely brilliant light source project, the development of tolerant x-ray optics against super power-density light must simultaneously make progress. A newly designed double-crystal monochromator in which its first Si crystal will be cooled by liquid nitrogen from its backside in a vacuum has been ordered. Its fabrication will be carried out outside of KEK. Cooling tests have already been carried out since last autumn, 1992. Since the advantages of using liquid nitrogen for cooling silicon material have been deeply appreciated, at least at the first step of utilization of the SR at the MR, this system will be adopted.

Proper monitoring of the undulator light will be one of the key technologies for controlling the orbit as well as utilizing SR. The development of this technique must therefore be carried out.

## B. TRISTAN MR AS A VERY LOW-EMITTANCE MACHINE

### 1. Machine Parameters of the TSLF Project

#### Towards a Low-Emittance Beam

A low-emittance beam and a long undulator are key issues for high brilliance; both can be readily realized in the TSLF project at the Tristan MR. The horizontal natural emittance ( $\epsilon_x$ ) is given by

$$\epsilon_x = \frac{C_q \gamma_0^2 I_5}{J_x I_2},$$

where

$$I_5 = \oint \frac{\beta \eta^2 + 2\alpha \eta \eta' + \eta'^2}{\rho^3} ds$$

and

$$I_2 = \oint \frac{1}{\rho^2} ds.$$

In the TSLF project  $\epsilon_x$  is set to a small value of around 1 nm-rad, so that  $\gamma_0$  is chosen to be smaller than the design energy of the MR as the collider,

and denominator of  $I_5$  is much larger than existing lattices for dedicated light sources in the world. The emittance-damping wigglers (EDW) to be installed in the dispersion-free section will reduce  $\epsilon_x$  further by increasing  $I_2$ , while keeping  $I_5$  at a small value.

The sextupole strength for a chromaticity correction is moderate, and a large dynamic aperture is attainable without any sophisticated correction scheme. This large dynamic aperture allows us to install very long insertion devices that are essential for producing photon beams of ultra-high brilliance.

### Principal Parameters

Table 1 lists the TSLF optics parameters for both with and without excitation of the EDW. For the sake of a comparison, the principal parameters of the MR as a collider are summarized in Table 2.

### Expected Limitations

The ultimate limit towards a low-emittance beam may be given by two features of intra-beam scattering if considerable intensity of the beam is required. One is the emittance growth. In Fig. 1 is described the effect of intra-beam scattering on the beam emittance in the case of 2% coupling between the horizontal and vertical emittances. The other is the so-called Touschek life time, which is limited by a momentum acceptance. Figure 2 shows the Touschek life for various beam energies, assuming a 2% coupling of the emittance and a momentum acceptance of 2%. These effects of the intra-beam scattering are much dependent on the beam energy, the emittance coupling ratio and the excitation of the EDW. Those parameters should thus be utilized as tuning knobs for the beam character.

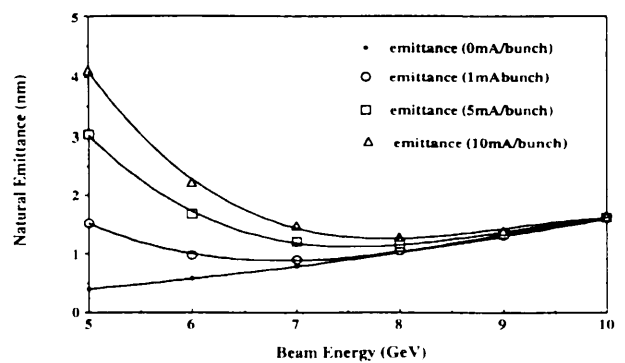


Fig. 1 Emittance enlargement caused by intra-beam scattering assuming a 2% coupling of the emittance between the horizontal and vertical planes.

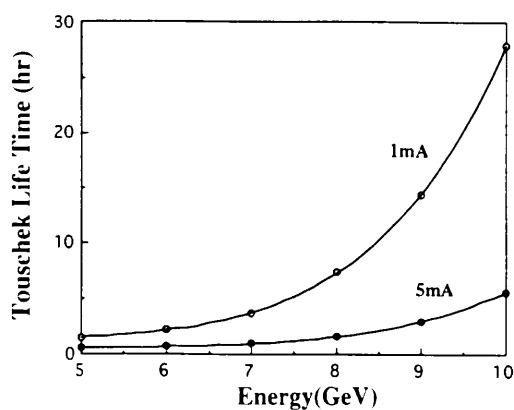


Fig. 2 Touschek lifetime as a function of the beam energy for bunch currents of 1mA (upper) and 5mA (lower). The assumed momentum acceptance ( $\Delta p/p$ ) is 2%. The effect of emittance enlargement (shown in the Fig. 1) is included here.

A series of studies revealed that the beam current will be severely limited by multi-bunch instabilities, which are mainly induced by a large impedance for the higher modes in the present APS type RF-cavities. At the early stage of TSLF operation, the available beam current may be limited to less than a few tens of mA, even when a number of cavities are reduced to the minimum. The available current will be increased later by

introducing new types of cavities with a much smaller impedance for the higher modes. They are now under development at KEK for an asymmetric B-factory project. Longitudinal and transverse feedback systems will improve the situation and may be essential in the case of low energy-operation for FEL experiments. Such a kind of feedback system is under examination at the PF ring.

*S. Kamada*

Table 1. The TSLF optics parameters.

	Emittance Damping Wigglers(EDW)		
	OFF	ON	
Circumference		3018.276	m
Nominal operation energy		10.0	GeV
Normal cell phase advance(H/V)		90°/60°	
Momentum compaction		0.000635	
Betatron tune		51.86/36.84	
RF voltage		90.0	MeV
First synchrotron integral	1.917	1.915	m
Second synchrotron integral	0.025	0.1467	m <sup>-1</sup>
Third synchrotron integral	$1.0 \times 10^{-4}$	$4.477 \times 10^{-3}$	m <sup>-2</sup>
Fourth synchrotron integral	$-1.084 \times 10^{-6}$	$-1.367 \times 10^{-6}$	m <sup>-1</sup>
Fifth synchrotron integral	$9.867 \times 10^{-7}$	$1.461 \times 10^{-6}$	m <sup>-1</sup>
Natural chromaticity(H/V)	-74.0/-55.4	-73.9/-55.3	
Synchrotron tune	0.0682	0.0673	
Radiated energy in a turn	3.52	20.65	MeV
Radiation damping time			
Transverse	57.2	9.75	msec
Longitudinal	28.6	4.88	msec
Relative energy spread	$5.42 \times 10^{-4}$	$1.50 \times 10^{-3}$	
Natural bunch length	0.24	0.68	cm
Natural emittance	5.79	1.46	nm

Table 2. Operational Parameters of the Tristan Collider.

at Injection		at Collision	
Emittance growing wiggler (EGW)	ON	OFF	
Circumference		3018	m
Bending radius		246.5	m
Total length of RF section		299.5	m
Betatron tune (H/V)	36.635/38.789	36.615 / 38.718	
Normal cell phase advance(H/V)		60°/60°	
Beta function at I.P. (H/V)	5.0/0.2	1.0 / 0.04	m
Natural chromaticity (H/V)	-48.3/-56.6	-58.5 / -105.8	
Momentum compaction factor		0.00149	
Beam energy	8	29	GeV
RF voltage	90.0	385.3	MV
RF frequency shift	0	3.0	kHz
Radiated energy in a turn	3.9	253.5	MeV
Radiation damping time			
horizontal	41.5	1.1	msec
vertical	41.5	2.3	msec
longitudinal	20.7	2.5	msec
Synchrotron frequency	11.6	10.95	kHz
Natural emittance	180	80	nm
Relative energy spread	$1.27 \times 10^{-3}$	$2.33 \times 10^{-3}$	
Natural bunch length	0.8	1.5	cm

## 2. Beam-Emittance Monitor for the TSLF

### Introduction

A very low-emittance beam in an electron storage ring has been envisaged as the next-generation synchrotron radiation source in order to deliver high-brilliance photon beams. From the point of view of accelerator operation, it is essential to have a monitor that measures the intrinsic emittance representing the phase space of the electron motion in the beam. The beam emittance in an electron storage ring has usually been deduced from measurements of the angular distribution of the synchrotron radiation by a system like a pinhole camera. In a beam profile produced by synchrotron radiation, however, the intensity distribution of the image can not represent a true projection of the electron motion, because of the diffraction and emission mechanisms. The diffraction pattern of synchrotron radiation depends on the opening angle, wavelength and photon polarization. Thus, the diffraction from a limited aperture enlarges the true beam profile. The finite length of the photon source in a bending magnet produces a spherical aberration, called the field depth, in both the horizontal and vertical planes. In the horizontal plane, further, the

curvature of the particle trajectory in the bending magnet produces an error.

The phase-space motion of electrons in storage rings can be observed by a scattering process of electrons and photons. A measurement of the angular distribution of Compton scattering provides a direct observation of the beam emittance. A laser pulse is used to produce Compton scattering by illuminating an electron beam, and backscattered  $\gamma$  rays are detected. The principle of this measurement is free from errors related to the photon source, unlike synchrotron radiation. The accuracy of the measurement is only limited by the resolution of detector for position and energy measurements of photons.

### Beam Profile Produced by Compton Scattering

We now consider the Cartesian reference system shown in Fig. 3, where the  $x_0$  and  $y_0$  axes are in the plane of the interaction point of the laser photon onto the electron beam, and the X and Y axes are in the plane of the photon detector placed at a distance L. The betatron motion of a single electron in the storage ring is expressed by

$$y_0 = \sqrt{\epsilon\beta} \cos \varphi, \quad y'_0 = -\sqrt{\frac{\epsilon}{\beta}} (\alpha \cos \varphi + \sin \varphi),$$



where  $y_0$  denotes the horizontal or vertical position relative to the equilibrium orbit and  $y'_0$  is the angle relative to the vertical or horizontal plane. At a given position (s) on the orbit, the phase-space coordinates of the electron are plotted on an ellipse:  $\gamma y_0^2 + 2\alpha y_0 y'_0 + \beta y_0'^2 = \epsilon$ ,

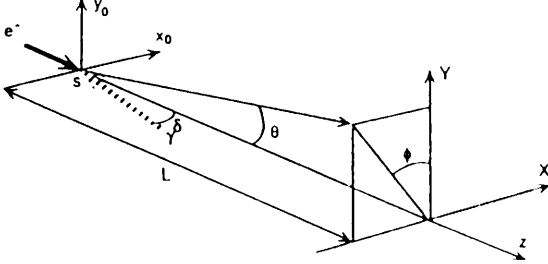


Fig. 3 Definition of the coordinates

where  $\alpha, \beta, \gamma$  are the Twiss parameters defined by the beam optics of the storage ring. They are periodic functions with the period of the machine circumference, and are related to each other by

$$\gamma = (1 + \alpha^2)/\beta, \quad \beta' = -2\alpha,$$

where  $\beta'$  represents the derivative of the  $\beta$  function with respect to position along the orbit. The beam emittance is denoted by  $\epsilon$ , and the phase-space area of the ellipse is given by  $\pi\epsilon$ , which is constant around the machine. The position of the electron projected onto the detector plane is

$$Y_0 = y_0 + Ly'_0 = \sqrt{\epsilon(\beta - 2\alpha L + \gamma L^2)} \cos(\phi + \delta),$$

where  $\delta = \tan^{-1}[L/(\beta - \alpha L)]$ .

Assuming that the amplitude of the betatron motion is a Gaussian distribution in phase space, the distribution function of the projected position on the detector plane is given by

$$P(Y_0) = \frac{1}{\sqrt{2\pi}\sigma_r} \exp\left(-\frac{Y_0^2}{2\sigma_r^2}\right),$$

$$\sigma_r = \sqrt{\langle\epsilon\rangle(\beta - 2\alpha L + \gamma L^2)},$$

and  $\langle\epsilon\rangle$  denotes the rms emittance of the beam. The probability of electron projection found on the detector plane is normalized as  $\int_{-\infty}^{\infty} P_r(Y) dY = 1$ .

Thus, the rms emittance can be obtained from a measurement of the rms width ( $\sigma_r$ ) of the beam profile projected on the detector. Projection of the beam is produced by photons scattered from electrons in the beam through Compton scattering. The position of a scattered photon on the detector is given by

$$X = X_0 - L \tan \theta \sin \phi, \quad Y = Y_0 + L \tan \theta \cos \phi,$$

where  $\theta$  and  $\phi$  are the scattering angles of a photon in the laboratory frame. The coordinates  $X$  and  $Y$  are the only measurable quantities. The distribution function of scattered photons detected on the detector is

$$\frac{d^2\sigma}{dXdY} = \int_{\Delta\Omega} d\Omega P_x(X + L \tan \theta \sin \phi) \times P_r(Y - L \tan \theta \cos \phi) \frac{d\sigma}{d\Omega}(\theta, \phi).$$

Here,  $\Delta\Omega$  is a solid angle spanned over the acceptance of the detector and  $d\sigma/d\Omega$  is the differential cross section of Compton scattering. The profile projected on the vertical ( $Y$ ) axis is given by

$$\frac{d\sigma}{dY} = \int_{-\infty}^{\infty} dX \frac{d^2\sigma}{dXdY} = \int_{\Delta\Omega} d\Omega P_r(Y - L \tan \theta \cos \phi) \frac{d\sigma}{d\Omega}(\theta, \phi).$$

The rms width of the beam profile produced by scattered photons is

$$\Sigma_r^2 = \int_{-\infty}^{\infty} dY Y^2 \frac{d\sigma}{dY} / \int_{-\infty}^{\infty} dY \frac{d\sigma}{dY} = \sigma_r^2 + \sigma_c^2,$$

where  $\sigma_c$  is the rms width produced by the angular distribution of photons due to Compton scattering from a point electron, calculated by

$$\sigma_c^2 = \int_{\Delta\Omega} d\Omega L^2 \tan^2 \theta \cos^2 \phi \frac{d\sigma}{d\Omega}(\theta, \phi) / \int_{\Delta\Omega} d\Omega \frac{d\sigma}{d\Omega}(\theta, \phi).$$

The net width of the beam profile can be obtained as

$\sigma_r^2 = \Sigma_r^2 - \sigma_c^2$ . For the distribution on the horizontal ( $X$ ) axis, the same approach as that used to measure the horizontal width of the beam profile can be carried out. The emittance is deduced from the rms width of the beam profile by using the known Twiss parameters at the interaction point:

$$\langle\epsilon\rangle = \frac{\beta}{1 + (\beta/L - \alpha)^2} \frac{\sigma_r^2}{L^2}.$$

### Layout of the System

The system used to measure the beam emittance comprises a Nd:YAG laser at 532 nm, which generates a 7 ns long, 550 mJ pulse at a 10 Hz repetition rate and the  $\gamma$  detector. The laser beam is guided through the transport optics towards the interaction point where the laser light crosses the electron beam in the vertical plane and is focused with a spot size of about 2 mm. The laser transport line is installed in the end of the Nikko straight section at the Tristan MR (Fig. 4). The backscattered  $\gamma$  rays travel along with the electron beam, then leave the beam pipe at the end of the main dipole, and reach the  $\gamma$  detector located 40 m downstream from the interaction point. The  $\gamma$  rays are detected by silicon micro-strip detectors as

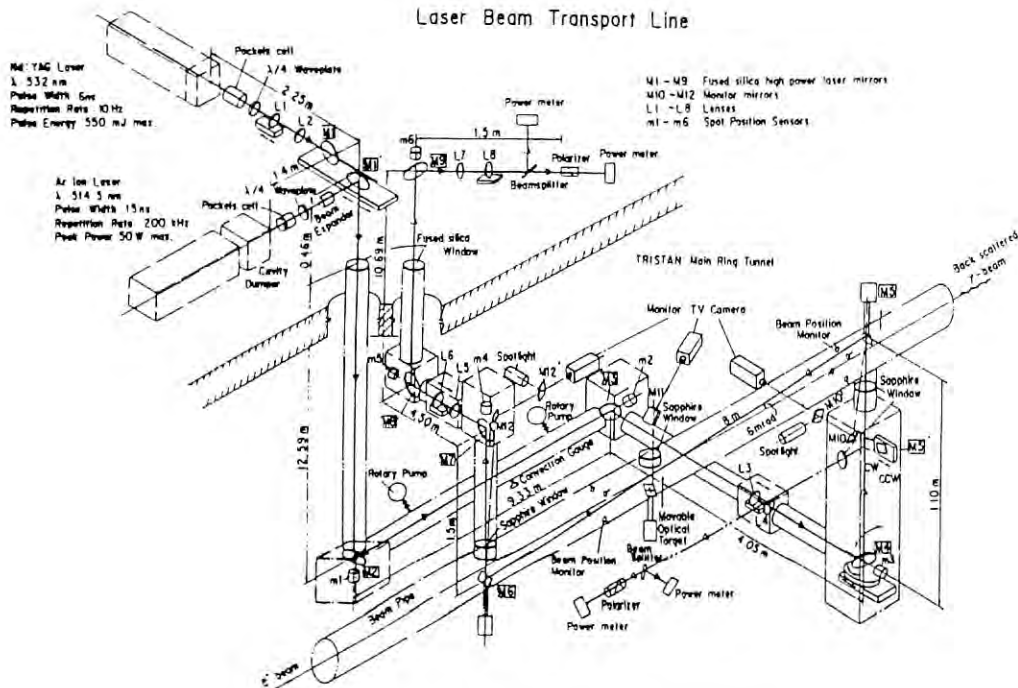


Fig. 4 Layout of the Compton emittance monitor

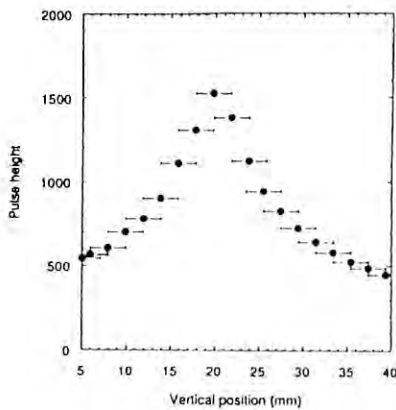


Fig. 5 Vertical profile of the backscattered  $\gamma$  beam.

electron-positron pairs created in the tungsten converter. The pulse height of the signals from the detector is read out by the CAMAC ADC system. These data are transferred to the VME memory and computer. A laser pulse can produce  $\sim 6 \times 10^5$  photons with an energy range of 2 - 15 GeV per interaction with a 1 mA electron bunch at a 29 GeV beam energy. A preliminary measurement for a low-intensity laser pulse of about 40 mJ provides a vertical beam profile projected onto the detector with a 2 mm resolution (Fig. 5). The positional resolution of the detector should be able to be improved down to 125  $\mu\text{m}$ . The background from

the synchrotron radiation and the beam-gas bremsstrahlung should be corrected. A further precise study will be continued and the new  $\gamma$  detector for imaging a spectral profile of the  $\gamma$  beam will be developed.

*K. Nakajima*

### 3. Trial Manufacturing of a Copper Vacuum Duct

To achieve the described beam emittance, an emittance damping wiggler (EDW) is planned to be installed in the converted MR for the TSLF. Although SR generated by the EDW will irradiate intensely vacuum ducts, they can not be equipped with an appropriate thermal absorber system for protecting themselves, due to the spatial restriction around the vacuum duct. Therefore, the duct material should have a high thermal conductivity and be sufficiently tough against high temperature. Oxygen-free high conductivity (OFHC) copper is one of the suitable materials as a duct material to meet the above-mentioned conditions. This material is, however, difficult and expensive to be processed, compared with stainless steel or aluminum alloy. We tried two types of manufacturing of a vacuum duct made of OFHC.

First, we tried a manufacturing method of a material pipe for the duct with welding. Two half parts of the duct, which had been made by extrusion/extraction processing, were combined along the axial direction. A cross-sectional view is shown in Fig.6. Side covers of water-cooling channels were also welded. Other components made of different materials, bellows, pumping ports and electrodes of beam position monitors, were welded using a nickel alloy (Inconel) as a transition material. In order to achieve small outgassing, caused by the SR, the inner surfaces of the duct were machined prior to welding.<sup>1)</sup> The completed duct was installed in the PF ring, and showed a satisfactory result with a small outgassing yield under the usual operation of the PF ring.<sup>2)</sup>

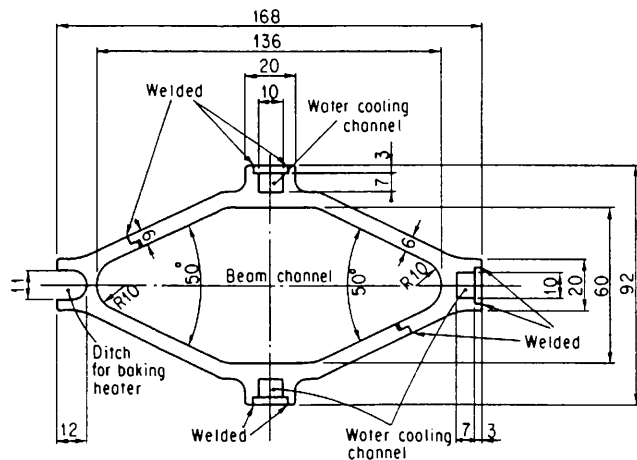


Fig.6 Cross section of the material pipe made with welding.

The second trial is to explore a method for manufacturing a material pipe other than welding or brazing. It is practically impossible with the present technology to extrude a duct having more than two channels, such as a duct including both a beam channel and water-cooling channels. We first made a material pipe having a beam channel by extrusion/extraction processing, and then made two cooling channels by gun-drilling. The cross section of the duct is shown in Fig.7. The material pipe was 2.5m long. The pipe was drilled from both ends; two drilled channels showed a deviation of several mm. This method proved to be useful, but technical improvements were found necessary for precise drilling.

Y. Hori

#### References

- 1) S.Ueda, M.Matsumoto, T.Kobari, T.Ikeguchi, M.Kobayashi and Y.Hori, Vacuum **41**, 1928 (1990).
- 2) "Installation of a copper duct", in this report.

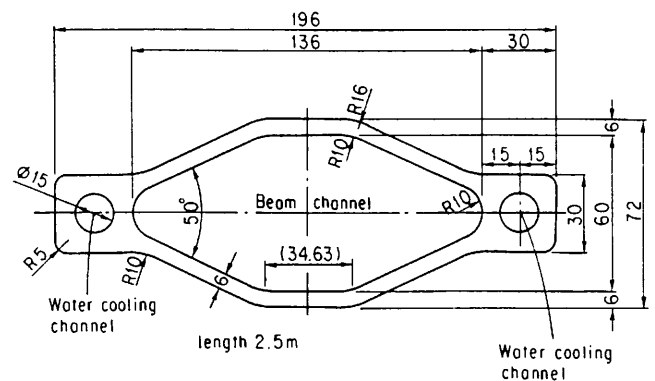


Fig.7 Cross section of the material pipe made without welding.

### C. R&D STUDIES ON NEW INSERTION DEVICES FOR THE PROJECT

When we optimize the MR for synchrotron-radiation experiments, three of four 200-m long straight sections of the present MR will be used for installing undulators by greatly reducing the number of RF cavities. Each straight section is bent slightly outward for the extraction of light beams to form a 200-m arc, and are divided into two long (70m) sections and two short (6m) ones; the 70-m and 6-m sections in an upper-stream half of the 200-m arc is to be used (Fig. 8).

Since the total length of the undulators required for a project of the TSLF amounts to 200m ( $\cong 6m \times 3 + 70m \times 3$ ),<sup>1)</sup> it is not very practical to design and construct such undulators using a device-by-device policy, from both the view-points of design and construction costs as well as from that of manpower for commissioning and operation. Here, we propose a new scheme using a standardized unit undulator, in which: (1) three unit undulators are placed very precisely on a common frame for the short undulator (5.4m long as seen below) for the TSLF; (2) for long undulators with some 70-m length, these short undulators will be connected longitudinally.

In accordance with the above-mentioned concept, we have been constructing a prototype of the short undulator (named XU#MR0) using permanent magnets, and exploring and solving

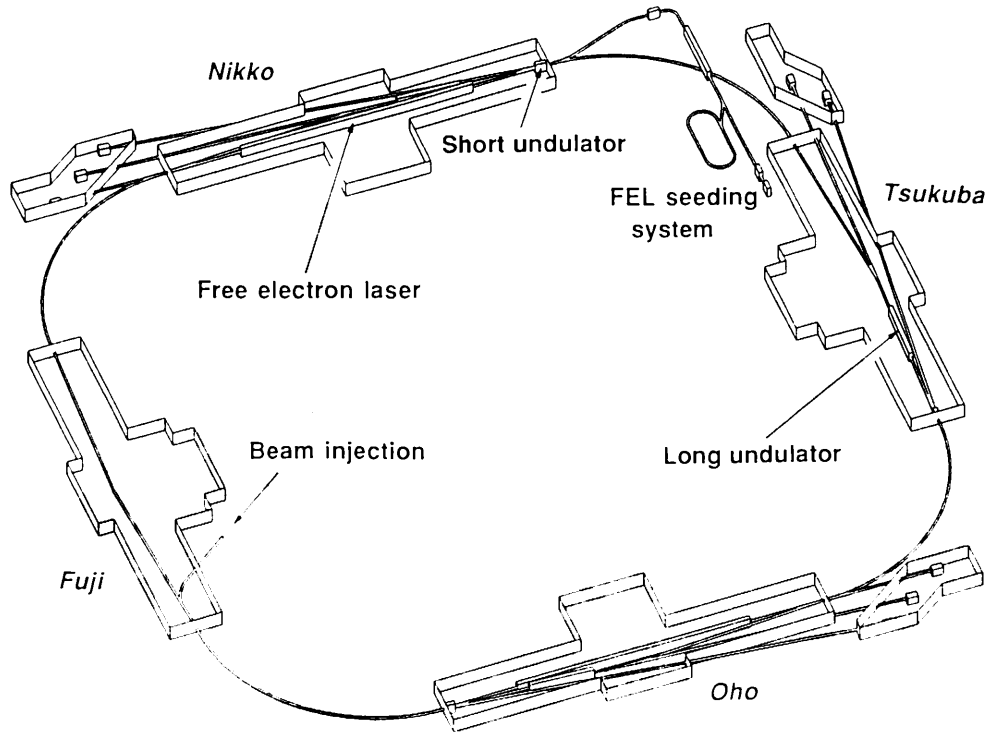


Fig. 8. Schematic view of the Tristan Super Light Facility.

Table 3. Characteristics of Tristan Super Light Source:  
E=10GeV, I=100mA,  $\epsilon=1.5\text{nm}\cdot\text{rad}$ .

	Short undulator	Long undulator
$\lambda_u$ (cm)	4.5	4.5
L (m)	5.4	70.2
N	120	1560
$\sigma_x$ ( $\mu\text{m}$ )	97	228
$\sigma_y$ ( $\mu\text{m}$ )	17	23
$\sigma_x'$ ( $\mu\text{rad}$ )	16	6.5
$\sigma_y'$ ( $\mu\text{rad}$ )	1.5	0.7
K	0.97	0.97
B (kG)	2.3	2.3
$\epsilon_1$ (keV)	14.4	14.4
$\sigma_p$ ( $\mu\text{m}$ )	1.8	6.6
$\sigma_p'$ ( $\mu\text{rad}$ )	3.8	1.0
Brilliance*	$1.9 \times 10^{20}$	$6.1 \times 10^{21}$
Angular flux	$2.0 \times 10^{18}$	$2.1 \times 10^{20}$
Density**		

\* : (photons/s/mm<sup>2</sup>/mrad<sup>2</sup>/0.1% bandwidth)

\*\* : (photons/s/mrad<sup>2</sup>/0.1% bandwidth)

Table 4. Parameters of XU#MR0.

Magnetic structure	Pure configuration
Magnetic material	NdFeB (NEOMAX41H)
Period length	$\lambda_u=4.5\text{cm}$
Number of periods	120 [=3×(40/unit undulator)]
Magnet length	5.4m [=3×(1.8m/unit undulator)]
Maximum B*	B=2.55kG
Maximum K*	K=1.07
Minimum gap*	3cm
Maximum aperture	2.5cm

\* : values estimated from the magnetic performance given in the text.

XU#MR0 is also planned to be used as the first undulator in the TSLF. A calculation shows that it is able to produce quasi-monochromatic x rays as the first harmonic with a brilliance of  $1.92 \times 10^{20}$  [photons/s/mm<sup>2</sup>/mrad<sup>2</sup>/0.1% bandwidth] in the case of K=0.97 and  $\lambda_u=4.5\text{cm}$  (120 periods) at 14.4keV, when the MR is operated at 10GeV and 100mA. Table 3 summarizes the source characteristics of the TSLF and the spectral performance of XU#MR0 and the long undulator.

various problems, including thermal expansion and alignment issues, which will arise in the actual construction of the TSLF in the near future. The

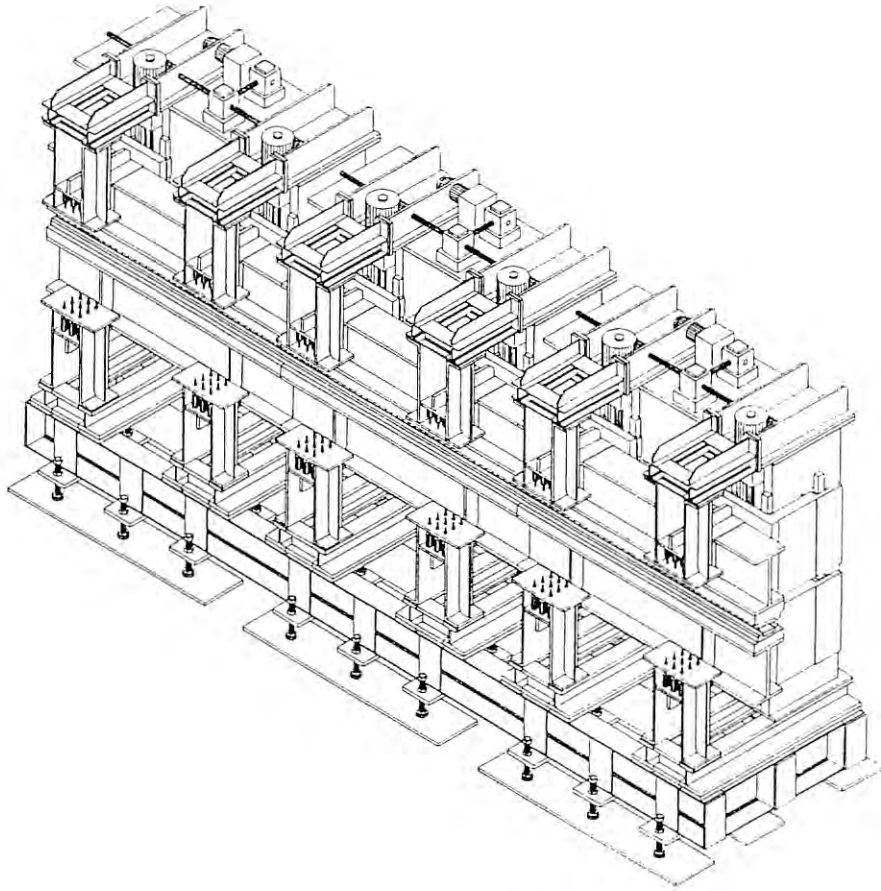


Fig.9. Basic structure of the prototype short undulator (XU#MR0) for the Tristan Super Light Facility.

### Structure of XU#MR0

Figure 9 shows the basic structure of the XU#MR0 in an out-of-vacuum configuration. The standardized unit undulator has a length of 1.8m. Three units are connected and placed on a rigid common frame to form a 5.4-m, 120-period undulator totally. In the construction of this prototype, we adopted a pure-type configuration of NdFeB magnets (remanent field,  $B_r=12.8\text{kG}$ , coercivity,  $iH_c=17\text{kOe}$ ). The basic parameters of the XU#MR0 are given in Table 4.

The support structure of the XU#MR0 has a shape like the letter "C", so that it can be installed in the MR without breaking the vacuum. In this case of the supporting structure, however, the magnetic attractive force tends to violate parallelism between the upper and lower girders on which the magnets are attached. In order to eliminate this effect, spring systems are equipped with both girders from the open side of the "C" letter to share the load of the magnetic force. The spring system has a set of

springs: the stiffer springs work at progressively closer gaps to support the load to be shared by this system for the parallelism between the upper and lower girders.<sup>2)</sup>

In the present scheme, the selection of  $\lambda_u$  is constrained by the reducibility of the fixed length of the girders with respect to  $\lambda_u/4$  for the pure configuration, and  $\lambda_u/2$  for the hybrid configuration. The girder length of the unit undulator of 1.8m was selected due to this viewpoint, so that it has as many divisors as possible in the range of  $\lambda_u$  from 4 to 12cm, under the criterion that the value of  $\lambda_u/4$  (or  $\lambda_u/2$ ) is met machinability within the present technology. A practical, but important, problem against the selectivity of  $\lambda_u$  is the constant pitch of holes through which the magnets are bolted down to the girder: once we drill the holes on the girder for a particular  $\lambda_u$ , we can not use it for other period lengths. In order to resolve this, parallel plates are embedded between the magnets and the girders,

which are bolted down tightly to the girders and have the holes with a pitch which fits the individual period lengths.

#### In-vacuum Modification of XU#MR0

An important figure of merit of the in-vacuum configuration for an undulator is the enhancement of the degrees of freedom during operation of the storage rings. This was demonstrated by the success of the U#NE3<sup>3)</sup> in the AR. The very small gap size of 1~2cm is used only for the utilization of synchrotron radiation; the gap is opened when a wide aperture is required, as in case of beam injection and a machine study. The necessity of an in-vacuum configuration becomes quite significant in the construction of the TSLF, where very fine and delicate machine tuning will be required for producing an ultra-low emittance electron beam.

Along this line, we have started design and R&D studies of an in-vacuum undulator for the TSLF. Basic ideas and a schematic cross section of this in-vacuum undulator are shown in Fig.10. It is noted that the vacuum chamber of this undulator is equipped in the same mechanical frame as the XU#MR0 with the out-of-vacuum configuration. Details concerning the design, including a sliding mechanism for the relaxation of thermal expansion occurring in a bake-out process required to make an ultrahigh vacuum, will be reported elsewhere, together with related R&D studies.

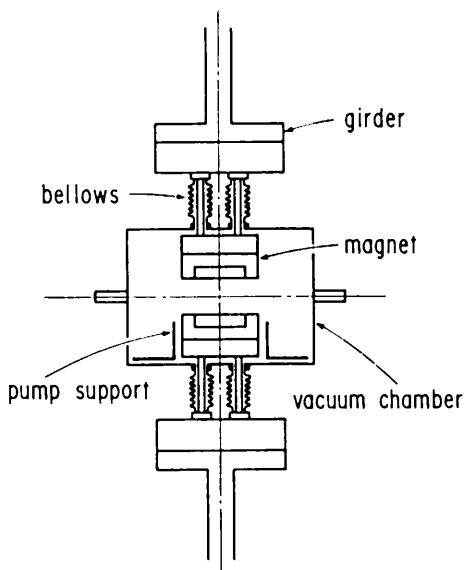


Fig.10. Schematic cross section of an in-vacuum version of the XU#MR0.

*S. Yamamoto*

#### References

- 1) The Tristan Super Light Facility; Conceptual Design Report 1992, KEK Progress Report No. 92-1 (1993).
- 2) Yamamoto, S., Renovation of undulator#2, Photon Factory Activity Report 1990, R-11.
- 3) Yamamoto, S., et al., Rev. Sci. Instrum., **63**, 400 (1992).

## D. EXPERIMENTAL STATIONS AND INSTRUMENTATION FOR THE TSLF

### 1. New Buildings and Experimental Stations

In this section we describe the design of new architecture (experimental hall and beamline tunnels) and experimental stations for SR experiments. More detailed reports are presented in the reference.<sup>1)</sup>

#### The Ground Plan of New Buildings for the TSLF

The MR as a high-energy-physics machine has four colliding experimental halls called "Nikko", "Tsukuba", "Oho", and "Fuji". In the present plan of the TSLF, the Nikko and the Oho are to be furnished with three beamlines (for short and long undulators and an FEL), and the Tsukuba is to have two beamlines (for short and long undulators), respectively. Below, the design of new buildings at the Nikko region is discussed as a typical example.

#### Experimental Hall

For SR experiments in the TSLF, a new experimental hall is planned to be constructed (Fig. 11) under the following conditions:

- 1) The new experimental hall must be separated from the site boundary of KEK by at least 3m due to technological restrictions for architecture. It must also be separated from the existing MR tunnel by 10m for the sake of reducing the distortion of the existing tunnels.
- 2) The distance between the emission point and experimental hall is preferred to be as short as possible. Due to condition 1), however, the distance should be 250m for the short- and long-undulator beamlines, and 200m for the FEL beamline.
- 3) The area of the experimental hall is set to be 600m<sup>2</sup> per beamline. This value is estimated from the area (about 200m<sup>2</sup> per a beamline) of the present SR experimental hall at the Tristan AR.

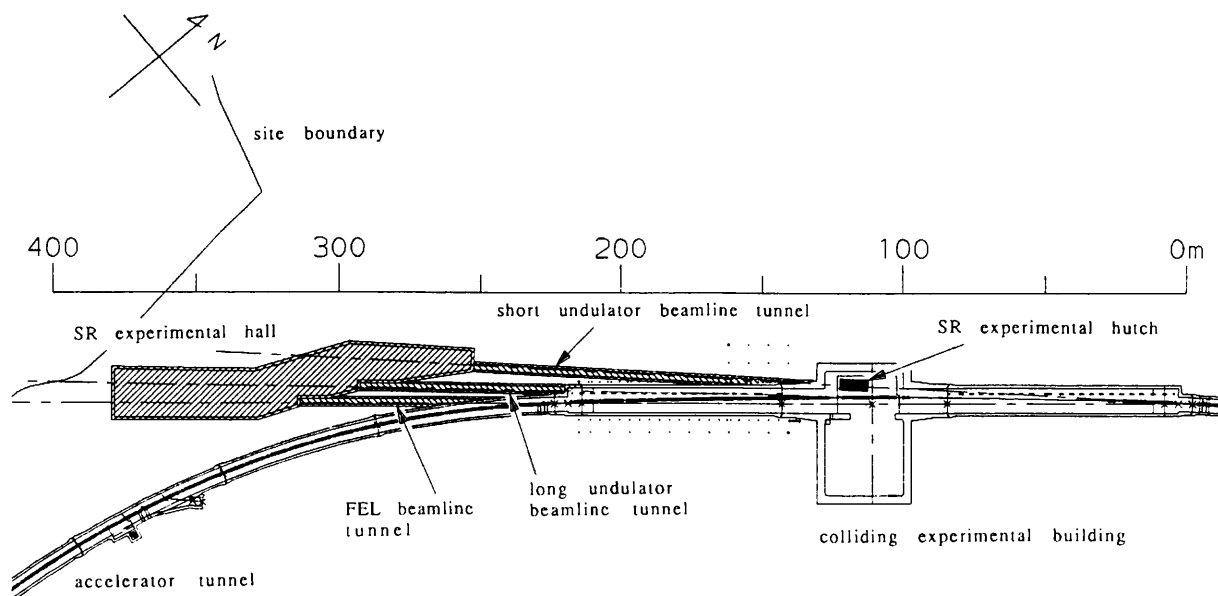


Fig. 11 Design of new buildings at the Nikko. The hatched regions are new experimental hall, beamline tunnels and experimental hutches for the TSLF. The scale describes the distance from the emission point of the short undulator. The array of rectangles on the straight section outside of the electron orbit is an array of pillars. The arrays of circles are also pillars for an electric-power-supplying building on the ground.

We decided that the experimental hall at the TSLF should have a space three times as large as that at the AR, since the present AR's hall is so congested that adjacent experimental hutches obstruct each other, and the experimental apparatus used at the TSLF will be much bigger.

4) The experimental hall is extended along the SR beam. The length of the hall along the optical axis at each beamline is more than 60m in this design.

The ground part of the experimental hall building is assigned as a preparatory space for experiments, though it is not shown in Fig. 11.

Preliminary and day-one use of SR on the MR will be attempted in an experimental hutche constructed in the colliding experimental hall of Tristan, as shown in Fig. 11. This plan is described in the reference.<sup>1)</sup>

### Beamline Tunnel

The beamline tunnels are constructed under the following conditions:

1) Since the tunnels are in the radiation-controlled region and are also completely buried under the ground, a system for preventing disasters is more complicated than that in the experimental hall. The tunnels should be structurally separated from the existing buildings and the SR experimental hall.

Further, in order to minimize hazards, it is desirable that equipment which must be manually operated or require frequent and long-time maintenance, such as monochromators, is not installed in the tunnel.

2) From the viewpoints of construction cost, and the influence to the accelerator, the cross section of the tunnel is designed so as to be as small as possible. This is because the new tunnel is constructed by digging from the SR experimental hall under the ground, and is placed very close to the existing accelerator.

Considering the above conditions, the appropriate width of the tunnels is 2m, as shown in Fig. 11. The center line of the tunnel is shifted one-sided by 0.5m from the SR beam to maintain the working area.

### **Basic Concepts of the Experimental Station**

The basic concepts and specifications for individual components of the experimental station in the TSLF are summarized below.

### Monitors of the Beamline

The SR experimental station should be equipped with many kinds of monitors, as follows:

- 1) Beam-position monitors.
- 2) Timing and bunch-purity monitors using detectors, such as an avalanche photodiode.
- 3) Radiation power monitors, such as a calorimeter.

- 4) Monochromatic photon intensity monitors using detectors, such as a PIN photodiode.
- 5) Fluorescence screens with a TV system.

Although the beam-position monitors are most important among the above-mentioned items, no proper monitors for undulator radiation have been established so far. At present, a beam position monitor using a carbon wire probe, and another based on the scattering phenomena of electrons or ions by the SR beam, are under development. The positional resolution of these monitors is expected to be about 1  $\mu\text{m}$ . By using two monitors placed at a few meters interval, we can obtain directional changes of the beam with an accuracy of less than 1 arcsec.

### Beamline Vacuum and Disposition of Its Components

The optical path can be constructed by using suitable pipes with ICF70 or ICF114 flanges, since the beam size of undulator radiation is sufficiently narrow. In addition, the distance is very long between the isolation valve and the beryllium windows, which separate the vacuum of the MR from the vacuum of the beamline. Thus, it is possible to exclude fast closing valves and related components from the beamline.

It is important that a set of water-cooling X-Y slits are disposed on the forehead of a monochromator and a thermal protector for the beryllium windows. They are used to fix the beam size and energy resolution, and to reduce the heat power of radiation, except for its coherent part.

Because of the long distance and the small diameter of the optical path, the beamline must be arranged much more accurately. It is necessary to develop a method of beamline alignment and realignment, since the floor level of the hall and the tunnel is subject to change in the long term. The development of fixed and stable marks using an optical system, such as a laser beam, should be included in these efforts.

### Shield and Shutter

The chamber of an absorber which protects a  $\gamma$ -ray shutter from a thermal load and its associated controller units in the MR tunnel should be covered with a few millimeters-thick layer of lead. The experimental hutch to which a white beam is introduced should be covered with a shield of 20 mm-thick lead.

The  $\gamma$ -ray shutter must be designed to work well even when the MR is operated at 20 GeV.

### Other Necessary Items for the Experimental Hutch

It is necessary for application experiments that the terminals of the electric power supply, cooling water, compressed air, and nitrogen gas etc. are introduced in the experimental hutch. For the precise experiments, temperature of the hutch should also be controlled.

### Software on the Experimental Station

Several kinds of software should be equipped at each station, for example, a standard security logic, controllers of experimental apparatus and software to analyze the experimental data. This software should be linked to each other.

### Safety Systems

Safety systems are necessary against a fire, radiation hazards and chemical hazards. Equipment for safety measures must cope with the worst situation and must be easy to operate and maintain. The safety systems are described in detail in the design report.<sup>1)</sup>

*H. Sugiyama*

### Reference

- 1) The Tristan Super Light Facility, Conceptual Design Report 1992, KEK Progress Report No. 92-1 (1993).

## **2. Heat Removal from Beamline Components**

### **Short Undulator Beamline Components**

In beamlines for the TSLF short Undulator, the beamline components are exposed to a radiation power of 1.5kW (200kW/mrad<sup>2</sup> in terms of the peak power density). We have carried out design studies for a short-undulator beamline having a length of 100m, since this case corresponds to the shortest-length version of the beamline and gives the most disadvantageous situation concerning thermal problems to the beamline components. A photon beam shutter, which is the most upstream component in the beamline, is irradiated by the photon beam with a peak power density of 500W/mm<sup>2</sup> at a distance of 20m from the source point. Thermal analyses using a finite element method (FEM) show that the water-cooled shutter of copper withstands the above-mentioned condition when it is slanted by 5° with respect to the direction of the photon beam.

In order to intercept low-energy photons and to reduce the heat load on the window, several thin films of graphite are placed in front of beryllium



windows, which separates the beamline from the MR. Our estimation shows that the effect of the absorption of the low-energy photons in the graphite films reduces the heat load on the first beryllium window to less than 30W, when the graphite film has a thickness of 0.2mm. Once the heat load is reduced to this level, the beryllium window is durable against the load if the window is welded to a copper block having water-cooling channels.

The first crystal of a double-crystal monochromator is exposed to a peak power density of 2.8W/mm<sup>2</sup> at a photon beam incidence angle of 7.9° when it is located at a distance of 100m from the source point. This value of the power density is 3- or 4-times higher than the allowable one for water-cooled Si crystals (finned), such as those of the monochromator used in the AR-NE3 beamline.

### Long Undulator Beamline Components

The long undulators generate a total power of 23kW (3500kW/mrad<sup>2</sup> in terms of peak power density). The beamline length is estimated to be 250 m long in the preliminary design. The photon beam shutter is irradiated by the photon beam with a peak power density of 550W/mm<sup>2</sup> at a distance of 80m from the source point. The thermal analysis with FEM shows that the water-cooled shutter of copper can handle the heat load when its surface is slanted by 2° with respect to the photon beam.

The first crystal of a double-crystal monochromator for the long undulator beamline is exposed to a peak power density of 7.7W/mm<sup>2</sup> at a incidence angle of 7.9°, which is 10-times higher than the allowable value of the water-cooled Si crystals. The development of the Si crystal cooling systems, which employ water and liquid nitrogen as coolants, is in progress at the AR-NE3 in order to overcome this situation.

*T.Mochizuki and X.Zhang*

### E. COHERENT X-RAY SOURCES

The Tristan MR has great potential for attaining to a very low emittance beam of sub nm radian when operated at 4 GeV. This indicates the possibility of a self-amplified spontaneous emission (SASE) FEL in the water window region. At KEK, another accelerator with a beam energy of 1.54 GeV has been constructed in order to study the technical feasibility on damping rings. Since the emittance of the ring, called the ATF damping ring

at KEK, is designed to be as low as 1 nm-rad, an SASE-FEL in the VUV region above 50Å would be possible.

The first phase of the TSLF aims at a super 3rd-generation light source. The ultra-high brilliance of 10<sup>22</sup> photons/sec/mm<sup>2</sup>/mrad<sup>2</sup> in 0.1% bandwidth would be obtained at 14.4 keV from a 70-m undulator. The first phase would be completed around 1996. After that, the second phase would start aiming at a 4th-generation light source in the water window region. Since the beam emittance designed for the first phase is 1.5 nm-rad at 10 GeV, the natural emittance at 4 GeV is estimated to be 0.24 nm-rad. However, it would be increased by intra-beam scattering. The principal parameters of the MR for FEL operation are summarized in Table 5. In the case of full emittance coupling, the emittance is estimated to be 0.5 nm-rad at a beam current of 1 mA/bunch. Therefore, an FEL would be possible in the wavelength region above 30Å. The MR has four long straight sections, 200m long each, so that modification is possible for dividing each straight section for installations of undulators or damping wigglers. In order to install a very long undulator for an FEL system, a bypass of 180m long would be constructed, as shown in Fig. 12. The possible parameters of the SASE-FEL are summarized in Table 6.

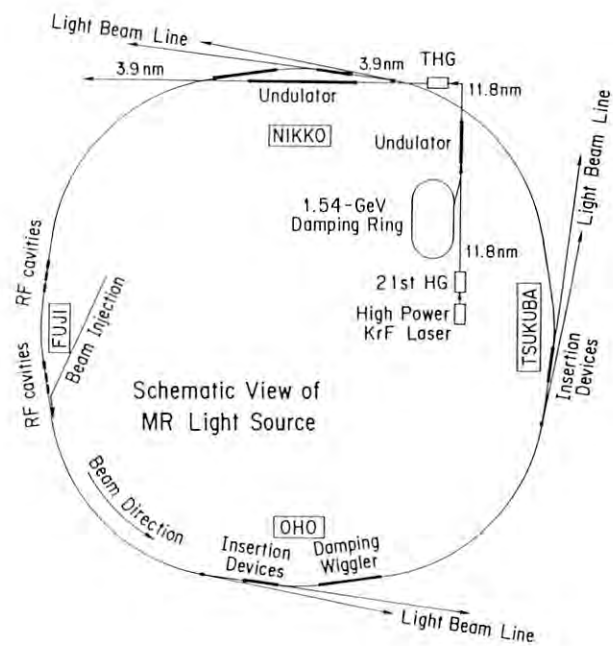


Fig. 12. SASE-FEL at TSLF

The coherence length of the SASE-FEL at 40Å is estimated to be as short as 2 μm, which is much shorter than the bunch length of 6 mm. The requirement to narrow the line width of SASE-FEL will arise in the future. To obtain a long coherence length up to the Fourier transform limit, an optical cavity or seeder laser system is required. However, the approach using an optical cavity is almost impossible in the X-ray region. Further, it is also very difficult to obtain 40-Å coherent radiation as seeder light by up-conversion using conventional lasers. We know that the coherent radiation around 100Å has been obtained using a high-power KrF excimer laser. For example, the 21st harmonic of KrF excimer laser may be obtained at 118Å. If this 118-Å radiation could be amplified so as to produce sufficient coherent power using the SASE-FEL installed in another accelerator with lower

beam energy, 39-Å coherent radiation could be obtained as seeder light by the third-harmonic generation of 118-Å radiation with an appropriate gas target. Of course, nonlinear optics in the above-mentioned region need to be developed.

Table 5. Beam parameters for a SASE-FEL at the TSLF

Beam energy	4 GeV
Horizontal emittance	0.5 nm-rad
Vertical emittance	0.5 nm-rad
Relative energy spread	$6 \times 10^{-4}$
Beam current	1 mA/bunch
Number of bunches	4
Bunch length	20 psec(2σ)
Peak current	400 A

Table 6. Possible SASE-FEL parameters at the TSLF

$\lambda$ Å	$\lambda_u$ cm	K	$\beta_{x,y}$ m	$L_g$ m	$z_R$ m	$\rho$ $10^{-3}$	$\rho_{eff}$ $10^{-3}$	$N_{sat}$	$L_{sat}$ m	$P_{sat}$ GW	RLW* $10^{-3}$
40	15	2.1	10	6.5	8.0	1.25	1.06	944	142	1.7	1.1
25	10	2.5	8	8.0	9.9	1.02	0.79	1260	126	1.27	0.8
14	8.0	1.5	9	8.3	2.0	0.71	0.44	2260	180	0.7	0.44

\*relative line width

Table 7. Beam parameters of the ATF damping ring

Beam energy	1.54 GeV	
Repetition rate	200 Hz	
Number of particles/bunch	$1 \times 10^{10}$	
Number of bunches/train	10	
Number of trains	8	
Circumference	138 m	
Field of damping wigglers	2.0 tesla	
Period length of wiggler	42.5 cm	
Length of wigglers	40 m	
Horizontal emittance	1 nm-rad	→0.5 nm-rad(for FEL)
Vertical emittance	0.01 nm-rad	→0.5 nm-rad(for FEL)
Bunch length	33 psec(2σ)	
Relative energy spread	$7.9 \times 10^{-4}$	
Peak current	39	→500 A(for FEL)

Table 8. Possible SASE-FEL parameters at the ATF damping ring.

$\lambda$ Å	$\lambda_u$ cm	K	$\beta_{x,y}$ m	$L_g$ m	$z_R$ m	$\rho$ $10^{-3}$	$\rho_{eff}$ $10^{-3}$	$N_{sat}$	$L_{sat}$ m	$P_{sat}$ GW	RLW $10^{-3}$
114	10	1.47	5	2.2	2.7	2.20	2.12	472	47	1.63	2.1
303	10	3.0	12	1.9	2.5	2.45	2.37	422	42	1.83	2.4
999	12	5.34	40	2.2	2.5	2.62	2.55	392	47	2.0	2.0
38	4	1.2	2.5	1.5	4.1	1.35	1.22	822	33	0.94	1.2

At KEK, an R&D study concerning the Japanese Linear Collider (JLC) project has started. Although the targeted final beam energy of the JLC is 0.5+0.5 TeV, the energy of the injector (damping ring) for the X-band linac is planned to be 1.54 GeV, and the natural emittance of a beam extracted from the damping ring (DR) is designed to be 1 nm-rad. At present, the DR of a test type (the ATF-DR) is under construction. The design parameters of the ATF-DR are summarized in Table 7. As shown in Table 7, a very small emittance coupling ratio is planned. Although it is suitable for the colliding experiments, it restricts the beam current. If the emittance coupling could be increased up to 100% (full coupling) for the SASE-FEL, the horizontal emittance would be decreased to 0.5 nm-rad, half the original value; the peak beam current could thus be increased up to 500A. Therefore, we would obtain a great possibility for the SASE-FEL by the above-mentioned modification in the design of the ATF-DR. The possible SASE-FEL parameters calculated on the basis of the modified ATF-DR are summarized in Table 8.

*H. Kitamura*

## F. SCIENTIFIC CASE

Workshops on possible basic sciences and industrial applications by utilizing the MR as a synchrotron light source were held over several years in various occasions such as the PF symposia, or meetings financially supported by the Ministry of Education, Science and Culture (Monbusho).<sup>1,2)</sup> This year, our proposal to hold workshops was granted by the Monbusho, which encourages the SR community to discuss SR utilization and possible scientific subjects in the MR. Also this year the TSLF proposed chances to the PF users' community to discuss the projects among users of wide regions, and the committee, called the MR committee, was organized.

In this year six workshops for the TSLF were held and the subjects which were proposed are classified into five categories below. Some of these subjects were described elsewhere.<sup>3)</sup>

### Nonlinear quantum optics

- Two-photon absorption
- Higher harmonic generation
- Stimulated x-ray parametric scattering

### Mössbauer source

#### Resonant type experiments:

- Increasing of the number of isotopes for Mössbauer experiments
- Studies on surfaces and interfaces
- Coherent-SR-induced excitation of cascade of gamma transitions in a single crystal

#### Non-resonant type experiments:

- Energy analysis with ultra-high resolution x-ray phase optics
- Statistical optics in the x-ray region
- Standard sources of electromagnetic radiation in the x-ray region
- Gravitational red-shift experiments

### Time resolved studies

- Protein crystallography
- Muscle fibers
- Chemical reactions

### X-ray microprobe

- Elemental analysis
- Absorption mapping
- Scanning topography
- Micro x-ray diffraction
- Micro XAFS
- Magnetic x-ray microscopy
- Micro fabrication

### Zone plate microscopy

- Transmission x-ray microscopy
- Spectromicroscopy

The workshops on these subjects including other subjects are further scheduled to be held in the next year, and the priority order of each subject will be settled through discussions given at those workshops.

*K. Ohsumi*

### Reference

- 1) Research on the future plans of SR sciences, edited by J. Chikawa (1987), in Japanese.
- 2) Report of the Plan Meeting on Use of Synchrotron Radiation from the Tristan Main Ring, KEK Report 88-16, edited by M. Ando, H. Kobayakawa and K. Ohsumi (1989), in Japanese.
- 3) The Tristan Super Light Facility; Conceptual Design Report 1992, KEK Progress Report No. 92-1 (1993).





# ***PHOTON FACTORY ACTIVITY REPORT***

**1992**

PHOTON FACTORY ACTIVITY REPORT 1992

**#10**

**#10**